Past, present and future volcanic activity at restless calderas in the Main Ethiopian Rift

William Hutchison

University College and the Department of Earth Sciences,
University of Oxford

Thesis submitted for the degree of Doctor of Philosophy

July 2015

Supervisors: Prof. David M. Pyle, Prof. Tamsin A. Mather,

Dr. Juliet Biggs and Prof. Gezahegn Yirgu

Abstract

Past, present and future volcanic activity at restless calderas in the Main Ethiopian Rift

William Hutchison, University of Oxford

There is growing recognition that magma plays a key role in the extension and eventual break-up of the continental lithosphere. One of the most intriguing aspects of magmatism during the transition from continental rifting to sea-floor spreading is that large silicic magmatic systems develop within the rift zone. However, the processes by which these silicic magmatic centres develop as well as their larger role in rift development remains poorly understood.

This thesis focuses on silicic volcanism in the Main Ethiopian Rift; the most extensive active continental volcanic field in the world, and home to over 10 million people. I use a variety of geological, geochemical, geophysical and geochronological techniques to explore spatial and temporal variability in volcanism in this active rift segment. In particular I focus on Aluto volcano, a restless caldera volcano just ~ 200 km south of Addis Ababa, but by extension I make inferences about what this means for past, present and future volcanism at other caldera systems in East Africa.

Aluto has been active for over 300,000 years, and has overwhelming erupted chemically-evolved peralkaline rhyolites that are derived through protracted (>80%) fractional crystallisation. Tectonic faults dissect the volcanic complex, and along with an underlying caldera ring fault provide key pathways for fluid release. Episodic ground deformation events occur at Aluto, and are characteristic of a coupled magmatic-hydrothermal system, where faults networks connecting the surface and deep reservoirs play an important role in the deflation. Finally, new $^{40}Ar/^{39}Ar$ geochronology support a new paradigm that silicic volcanism in this segment of the rift is pulsed, not steady, on human evolutionary timescales.

Extended abstract

Past, present and future volcanic activity at restless calderas in the Main Ethiopian Rift

William Hutchison, University of Oxford

Magma plays a fundamental role in the initiation and evolution of continental rifts. Knowledge of the processes that generate melt beneath rift zones and govern its pathway to the surface are central to our understanding of how tectonic plates break apart and new ocean basins form. Furthermore, by understanding the journey magma takes from source to surface beneath a rift we can determine its physical and chemical evolution, which set the scene for its eventual eruption style. The East African Rift System (EARS) represents a unique natural laboratory to study the role of magma in rifting, not only because this is a an active geological process, but because the long-term geochemical records required to probe the spatial and temporal evolution of magmatism are preserved in volcanic products at the surface of the rift.

Recent volcanism in the EARS has been marked by the eruption of cubic kilometres of evolved silicic magmas. These volcanoes are a ubiquitous feature of continental rift volcanism; many show evidence of large, geologically young (<500 ka), caldera-forming eruptions, several show signs of unrest, and in almost all cases they are located close to densely populated areas (> 9 million people in Ethiopia live within 30 km of an active volcano). Our understanding of the evolution and eruptive histories of these complexes is poor, for most there has been no modern geological mapping or any geochemical characterisation of the erupted products, and thus there is a critical lack of knowledge about the volcanic hazards they may pose, as well as their larger role in continental rift development. This thesis has sought to address these key questions by investigating temporal and spatial controls on magmatism

and volcanic processes in the Main Ethiopian Rift (MER) using a variety of field, geochemical, geochronological and geophysical techniques.

Integrating new high-resolution airborne data (lidar and imagery) with soil-CO_2 flux measurements shows that Aluto volcano, a typical restless silicic complex, and the main study area of this thesis, is dissected by rift-related extensional faults and underlain by an elliptical caldera ring fracture. These pre-existing structures impart fundamental controls on active volcanism, governing the pathways that gas, hydrothermal fluids and magma ascend to the surface. This provides important insights into future volcanic hazards, but also reveals the importance of structural mapping for successful development of geothermal resources at rift volcanoes. We estimate the total CO_2 emission from Aluto to between 250 and 500 t d^{-1}. Diffuse degassing of magmas in rifting environments has been little studied, but yet these measurements suggest that rift volcanoes could represent a globally significant source of atmospheric CO_2.

On decadal timescales, a number of volcanoes in the EARS undergo episodic ground deformation. The cause of these unrest events is unclear, and the key question is whether they represent a magmatic or hydrothermal deformation signal. We use soil-gas CO_2–$\delta^{13}C$ measurements to chemically fingerprint a magmatic signal in gas emissions and demonstrate that the magmatic and hydrothermal systems of Aluto must be physically connected. We also investigate the spatial and temporal nature of uplift events using a joint inversion of Envisat and ALOS InSAR data. Deformation events at Aluto show accelerating uplift with time, and can be modelled by a spherical source at ~5 km. A key feature of the deformation events is that they show a roll-over from uplift to subsidence; consistent with a coupled magmatic- hydrothermal system where faults and fractures allow for efficient fluid release.

On geological timescales, new $^{40}Ar/^{39}Ar$ geochronology and geochemical data, supplemented by a new geological map, have been used to constrain the volcanic edifice growth and magmatic evolution of Aluto. This volcano has been active for over 300 ka, initially built as a trachytic edifice before

undergoing large-volume ignimbrite eruptions. Geochemical modelling is consistent with peralkaline rhyolite genesis from protracted fractionation (>80 %) of basalt that is compositionally similar to rift-related basalts found east of the complex. Based on the style and volume of recent eruptions we suggest that silicic eruptions occur at an average rate of 1 per 1000 years, and that future eruptions of Aluto will involve explosive emplacement of localised pumice cones and effusive obsidian coulees of volumes between 1–100 x 10^6 m^3.

Finally, at the rift segment scale, new radiometric dating suggests that the MER experienced a major pulse of explosive volcanic activity between 320–170 ka. During this period, at least four distinct volcanic centres (Aluto, Gedemsa, Corbetti and Shala) underwent large volume (> 10 km^3) caldera-forming eruptions, with eruptive fluxes elevated five times above the average eruption rate for the past 700 kyr. The temporal clustering of the ignimbrite eruptions suggests that development of large volume silicic magma reservoirs was closely synchronous. We suggest that a pulse of mantle-derived basalt was delivered to the crust, after c.a. 2 Ma, and that stalling of magma at favourable structural loci was critical in generating the flare-up ignimbrites. Explosive silicic volcanism in the Ethiopian rift valley appears to be episodic, creating geologically brief intervals of environmental change that would have remodelled landscapes and ecosystems occupied by early hominin populations.

Acknowledgements

First of all I would like to thank my supervisors David Pyle, Tamsin Mather and Juliet Biggs who have provided support, advice and encouragement over the last four years. This DPhil would not have been completed without their ideas, endless reading of manuscripts and attention to detail. Gezahegn Yirgu (Addis Ababa University) has been a fantastic colleague to work with over the last four years supplying me with a wealth of knowledge on geology in Ethiopia and logistical support throughout the field campaigns (helping me to bring gas equipment in and rocks out).

For technical assistance I am indebted to Nick Marsh and Rob Kelly at Leicester (XRF), Karen Fontijin, Steve Wyatt and Phil Holdship (ICP-MS), Owen Green and Jeremy Hyde (rock prep). Ben Cohen and Dan Barfod at SUERC were instrumental in getting the $^{40}Ar/^{39}Ar$ geochronology done, and Stefano Caliro, Giovani Chiodini and Tobias Fischer kindly analysed our volcanic gases. Airborne data was expertly acquired by the NERC-ARSF team. Gary Llewellyn provided a calming voice when equipment was impounded and clouds appeared. Ben Taylor at the NERC-ARSF Data Analysis Node helped out with initial processing and provided fantastic tutorials on how to generate digital elevation models.

My field assistants: Tulu Bedada, Amde Zafu, Fekadu Aduna, Elspeth Robertson and Michael Hutchinson were enthusiastic, hard-working and fun (the best I could have hoped for). Girma Andarge provided vital assistance throughout the campaigns, always smiling and keeping us up to date with drilling on Aluto. Elias Lewi and Atalay Ayele (IGSSA) helped immensely throughout the field work and provided great conversations and coffee. In Oxford, Postgrads11 and my COMET office mates have kept me smiling. Sarah Dixon-Clarke, Julia Schollick and Harry McClelland extracted me from the desk from time to time to have dinner and a beer; this was much appreciated.

Finally I would like to thank Tess, Mum, Dad and Alasdair, whose support, humour and encouragement have kept me together over the last four years.

Funding

Funding for the project has been provided by a Natural Environmental Research Council (NERC) studentship grant (NE/J5000045/1). Airborne data were collected on NERC Airborne Research and Survey Facility (ARSF) flight ET12-17-321. $^{40}Ar/^{39}Ar$ chronology at SUERC was supported by a NERC Argon Isotope Facility grant (IP-1506-1114). Additional funding for fieldwork was generously provided by University College (University of Oxford), the Geological Remote Sensing Group, the Edinburgh Geological Society, and the Leverhulme Trust. It is hoped that much of the work conducted as part of this thesis will form a useful initial contribution to the NERC funded RiftVolc project (NE/L013932/1, Rift volcanism: past, present and future).

Contents

Chapter 1

Introduction

1.1 Continental rifting in East Africa

The East African Rift System (EARS) is one of the most extensive geologically active features on Earth (Chorowicz, 2005). It forms a series of segmented tectonic basins that extend from the Afar triangle, at the Red Sea-Gulf of Aden junction, southwards through to Mozambique (Fig. 1.1). The EARS represents the major divergent boundary between the Nubian and Somalia plates which are currently extending at rates of 1–10 mm yr^{-1} (Fig. 1.1, Stamps et al., 2008). From the Afar triple junction ~1000 km south to southern Ethiopia the rift forms a single segment before dividing into two major Eastern and Western branches, around the mechanically strong and thick Tanzanian Craton (TC in Fig. 1.1, Petit and Ebinger, 2000; Nyblade and Brazier, 2002).

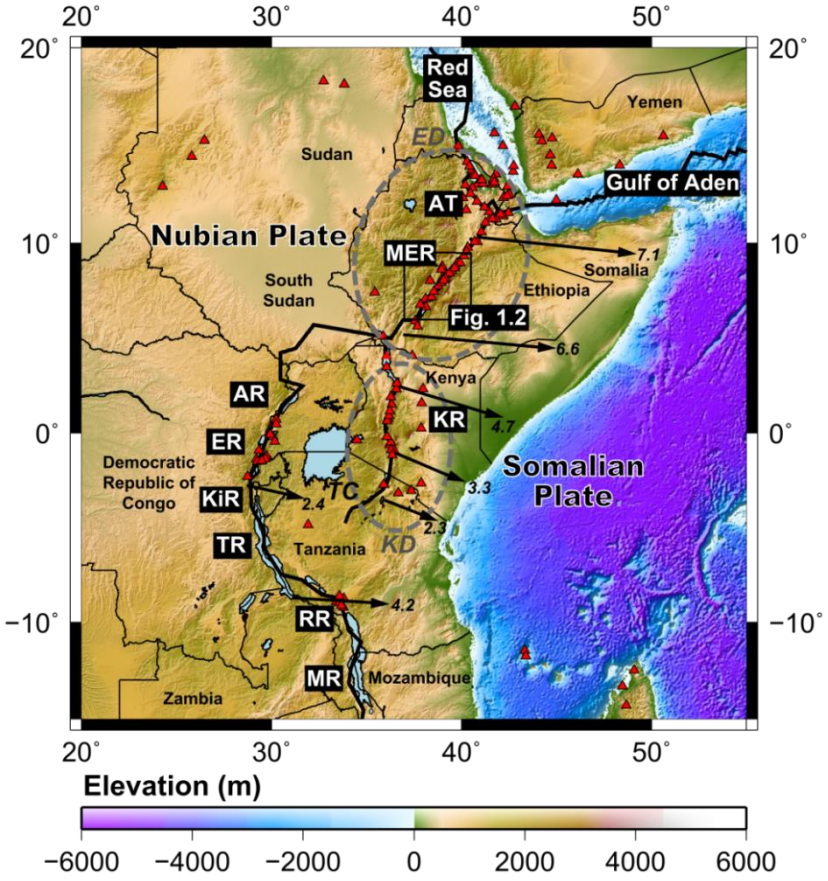

Figure 1.1: *Topographic map of the East African Rift System (EARS). Rift names are abbreviated as follows: AT: Afar triangle; MER: Main Ethiopian Rift; KR: Kenyan Rift; AR: Albertine Rift; ER; Edward Rift; KiR: Kivu Rift; TR: Tanganyika Rift; RR: Rukwa Rift and MR: Mozambique Rift. The black line running from AT to MR shows the major divergent boundary between the Nubian and Somalian plates. Red triangles mark all Holocene volcanoes (after Siebert and Simkin, 2002).Plate velocities are calculated using the Euler poles of Stamps et al. (2008). Plateaux regions of the Ethiopian and Kenyan domes, ED and KD respectively, are marked by grey dashed ellipses. TC identifies the Tanzanian Craton which divides the east and west branches of the EARS.*

Continental break-up in the EARS is achieved by both tectonic faulting and magmatism, which together mechanically weaken the lithosphere by stretching and intrusive heating (e.g., Ebinger and Casey, 2001; Buck, 2004, 2006; Ebinger, 2005; Kendall et al., 2005; Corti, 2009; Rooney et al., 2011). Initiation of the major rift segments was diachronous. While the earliest surface volcanism dates from ~45 Ma in Southern Ethiopia (George et al., 1998), rifting phases began at: ~35 Ma in the Gulf of Aden (d'Acremont et al., 2005); ~28 Ma in the Red Sea (Wolfenden et al., 2005); 25 Ma in northern Kenya (Morley et al., 1992; Hendrie et al., 1994) and 15–18 Ma in the Main Ethiopian Rift (Wolfenden et al., 2004).

One of the most prominent mantle plumes on Earth is found in East Africa. Seismic imaging of the East African mantle (e.g., Ritsema et al., 1999; Nyblade et al., 2000) reveals the existence of a large, continuous, thermochemical mantle plume, originating at the core-mantle boundary. This plume provides dynamic support to the lithosphere as evidenced by the two prominent plateaux of the Ethiopian and Kenyan domes (ED and KD in Fig. 1.1). It has been suggested that this deep mantle plume not only initiated rifting (Pik et al., 1999) but has provided heat and mass which have helped to drive rift-related magmatism throughout the Cenozoic (since ~30 Ma, Furman et al., 2006; Pik et al., 2008). More recent He-Ne-Ar noble gas isotopic studies, which appear to be unambiguous identifiers of plume involvement and provenance, suggest that there is a plume signature across the entire EARS (Hilton et al., 2011) and that this is consistent with a single mantle plume source (Halldórsson et al., 2014).

The role of the mantle plume in generating melt beneath the EARS remains contentious. Decompression melting is typically linked with magma production in rift environments (White and McKenzie, 1989), however, the presence of a mantle plume can have a profound impact on the thermo-chemical conditions of the mantle and can significantly perturb melting conditions in the ambient upper mantle (potentially adding volatiles and generating more fertile melts). There is

ongoing debate as to the role this plume may play now (e.g., Rychert et al., 2012; Ferguson et al., 2013), and also the extent to which the EARS upper mantle has been contaminated by plume materials (e.g., Rooney et al., 2012).

The EARS also hosts a rich hominin fossil record and there is substantial paleontological evidence to suggest that many of the major events in hominin evolution occurred here (Maslin et al., 2014, 2015). The unusual geology and climate of East Africa created a complex, environmentally variable setting (Bailey et al., 2011), and it has long been hypothesised that periods of environmental change were an important driver for human evolution, dispersal and cultural development (Maslin and Christensen, 2007). While there has been considerable work to investigate how the EARS environment has changed over the last 10 Myr (e.g., deMenocal, 2004; Trauth et al., 2007, Maslin et al., 2014), major questions remain about how global climate and physical processes (i.e., tectonics and volcanism) have shaped this region and the direct impacts this would have had for flora and fauna living in the EARS (Basell, 2008; Bailey et al., 2011).

1.2 The Main Ethiopian Rift (MER)

The ~500 km long MER (Fig. 1.2) is considered to be the type example of a continental rift (Ebinger, 2005). It extends from the Afar triple junction in the north, to the Turkana basin in the south (Fig. 1.1). The MER is traditionally separated into three main sectors (Northern, Central, and Southern), which display along axis variations in fault architecture (Hayward and Ebinger, 1996; Agoistini et al., 2011), lithospheric characteristics (Keranen et al., 2004), crustal thickness and modification (Keranen and Klemperer, 2008).

It is commonly assumed that these changes reflect a spatial variation in rift evolution, from mature rifting in the Northern MER to less evolved rifting southward (e.g., Hayward and Ebinger, 1996; Corti, 2009; Agostini et al., 2011). The changing architecture of the MER has been used by Ebinger (2005) and Corti (2009) to define the classic model of how continental rifts evolve; where early stages of extension are fault-controlled but over time deformation narrows and magma-assisted rifting becomes more dominant (Fig. 1.3). The major transition in rifting dynamics, from fault-dominated extension to localized axial volcanic segments (Fig. 1.3 b to c), appears to take place in the Northern and Central MER at around 3–2 Ma (Boccaletti et al., 1998; Ebinger and Casey, 2001; Keir et al., 2015), while in the Southern MER active deformation is still largely fault-controlled (Corti et al., 2013a).

A strong theme to have emerged from recent studies is that pre-existing lithospheric weaknesses have played an important role in the initiation and development of the MER. Fundamental to this argument is that extension vectors are not orthogonal to the rift axis (Fig. 1.2), and thus the MER can be regarded as an oblique rift (Bonini et al., 1997, Corti et al., 2013b). Oblique extension may be related to the localisation of extensional deformation along a NE–SW-trending lithospheric scale pre-existing heterogeneity (Bastow et al., 2008; Corti, 2008); potentially a Neoproterozoic suture zone separating two distinct Proterozoic basement terranes underlying the Ethiopian and Somalian plateaus (Keranen and Klemperer, 2008; Keranen et al., 2009; Corti, 2009). Ultimately, a more comprehensive understanding of the time-space evolution of tectonics and volcanism in the MER is required to evaluate the role pre-existing structures have played, and more generally, to refine our conventional models of rift evolution (Fig. 1.3).

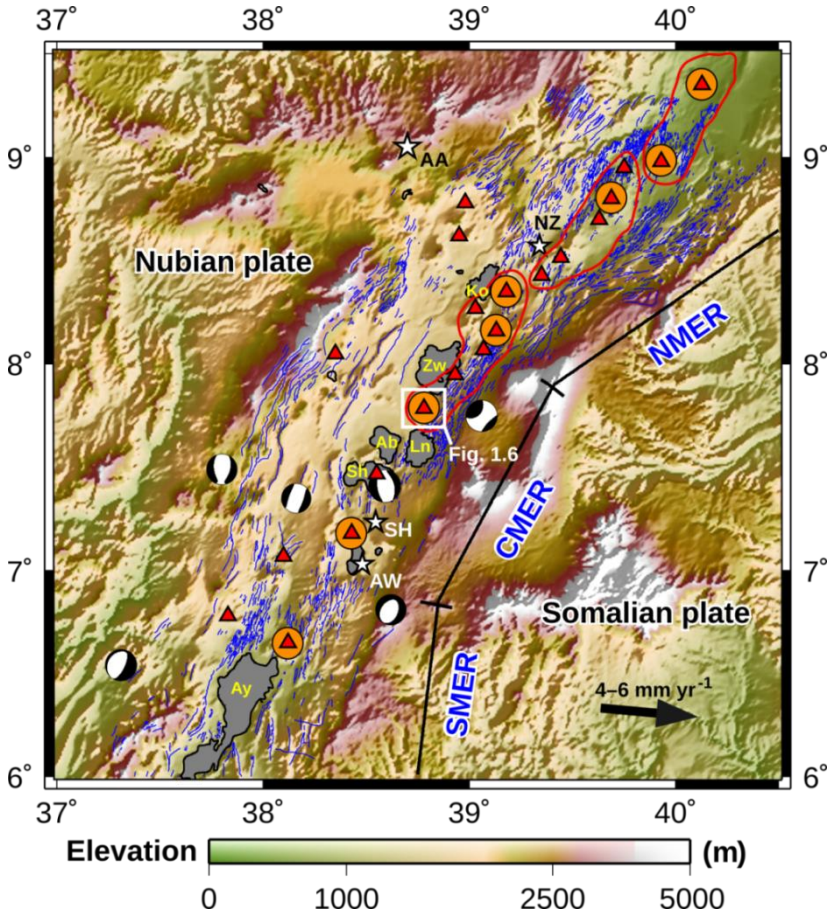

Figure 1.2: *Topographic map of the Main Ethiopian Rift. The three main sectors (northern, central and southern, i.e., NMER, CMER, and SMER) of the MER are delineated after Corti (2009). The surface faults (mapped by Agostini et al., 2011) are shown in blue. Earthquake locations and focal mechanisms for the region are from the Global Centroid Moment Tensor Project catalogue (http:// www .globalcmt .org; 1976–2012; M > 5). Red triangles identify volcanic centres thought to have been active in the Holocene (Siebert and Simkin, 2002); those that host geothermal prospects are shown by the orange circles. Red lines indicate Quaternary-Recent volcanic segments from Ebinger and Casey (2001). White stars identify major centres of population (after the Socioeconomic Data and Applications Center, http:// sedac .ciesin .columbia .edu/): AA—Addis Ababa; NZ—Nazareth; SH—Shashemene; AW—Awassa. Lakes in the MER are shown in grey and include: Ko—Lake Koka; Zw—Lake Ziway; Ln—Lake Langano; Ab—Lake Abijta; Sh—Lake Shala; Ay—Lake Abaya. The Aluto volcanic complex is located within the white rectangle (Fig. 1.6).*

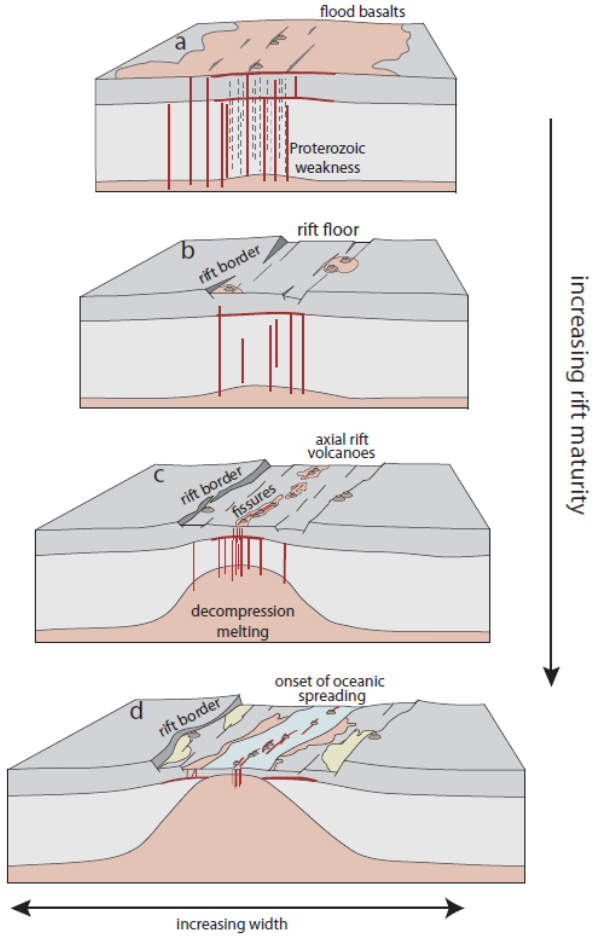

Figure 1.3: *Schematic model of rift evolution in the MER, modified after Corti (2009) and Robertson (2015).* ***a)*** *Flood-basalt volcanism affecting Ethiopia prior to the main rifting phase. A zone of pre-existing in weakness localizes strain and rifting in the subsequent deformation phases.* ***b)*** *Activation of the rift boundary faults, these lead to subsidence of the rift floor and facilitate diffuse volcanism across a broad footprint of the rift. The lithosphere begins to thin, stretch and heat.* ***c)*** *Boundary faults are abandoned and deformation shifts to the centre of the rift valley. Volcano-tectonic activity is localised within volcanic segments (Fig. 1.2), and a strong feedback between deformation and magmatism develops. The thinned lithosphere is strongly modified by the extensive magma intrusion, and further extension is facilitated and accommodated by a combination of magmatic intrusion, dyking and faulting.* ***d)*** *Tectonically and magmatically thinned lithosphere ruptures in the heavily intruded zones, and new oceanic lithosphere can be created along the volcanic segments.*

The MER exhibits a variety of surface volcanism, ranging from large silicic calderas (the focus of this thesis) to basaltic fissure swarms and monogenetic cone fields (Abebe et al., 2007; Rooney et al., 2011). The silicic volcanoes are geologically young (<500 ka), many have undergone large caldera-forming eruptions and a number of them also host large geothermal fields (Fig. 1.2, Di Paola, 1972; Mohr et al., 1980; Le Turdu et al., 1999; Peccerillo et al., 2003, 2007; Rampey et al., 2010; 2014).

1.3 Ethiopia's power demand

The power sector in sub-Saharan Africa (including Ethiopia) is significantly underdeveloped in terms of energy access, installed capacity and overall consumption (Eberhard et al., 2008). In both residential and industrial sectors electricity supply in these countries does not meet demand (Eberhard and Shkaratan, 2012). This problem is illustrated in Figure 1.4a, which shows that almost half of the population of sub-Saharan Africa has no access to grid electricity. Ethiopia's electrification rates are among some of the lowest at 23 % (i.e., 77 % of the population has no access to grid electricity, International Energy Agency, World Energy Outlook 2014).

Electricity shortages are a major hindrance to long-term economic growth (Eberhard et al., 2008), and in Figure 1.4b, the general relationship between electricity consumption and gross domestic product (GDP) is clearly demonstrated. Many of the countries in sub-Saharan Africa have the lowest GDP and electricity consumption; only those with significant wealth in natural resources are elevated in GDP when electricity consumption is low (e.g., Angola, Fig. 1.4b). The crux of this issue is that businesses and individuals must rely on generators, and on average generator power is four times the price of grid power (McKinsey Global Institute, 2015). This means that comparable businesses operating in sub-Saharan Africa will have much higher relative energy expenses than their counterparts in more developed countries. High local energy costs and unreliable grid power are a major discouragement for investors and enterprises hoping to bring business to sub-Saharan Africa.

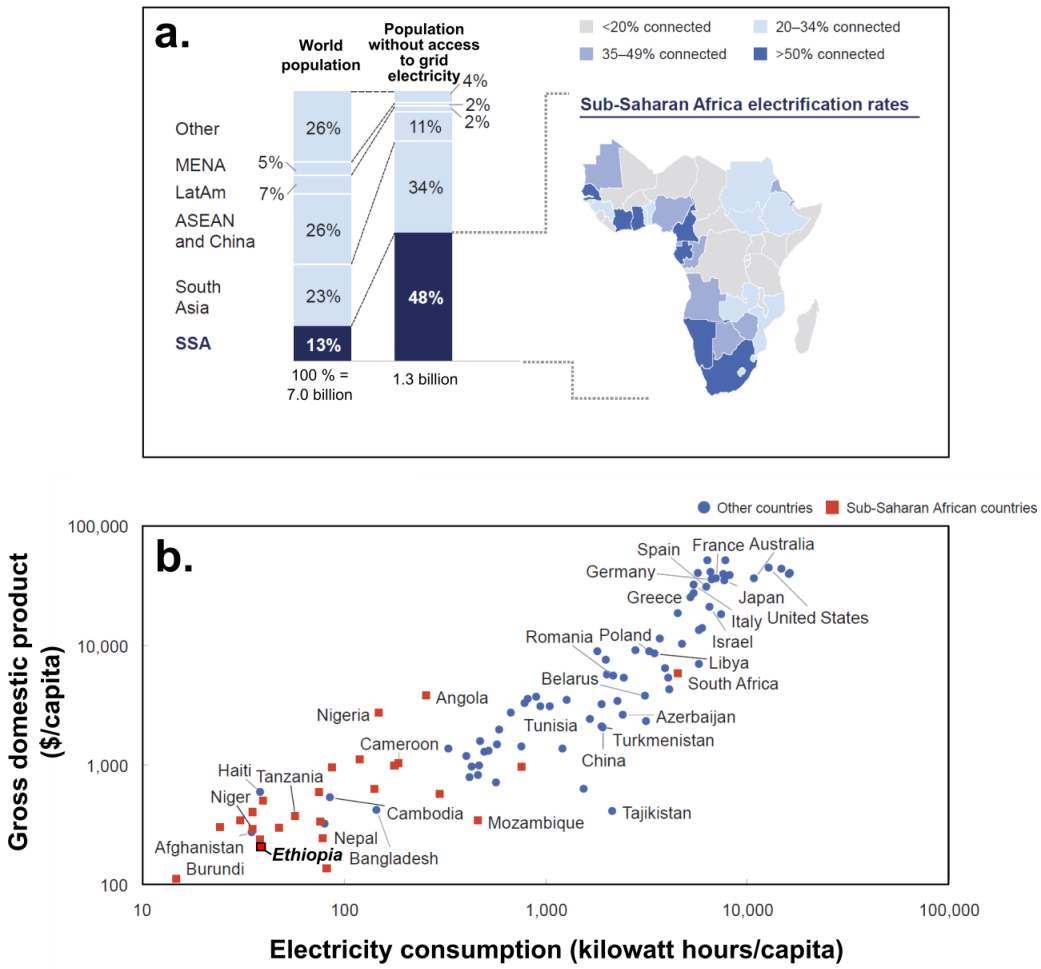

Figure 1.4: ***a)*** *Electrification rates in sub-Saharan Africa, modified after McKinsey Global Institute, 2015. Data from Electricity Access Database, World Energy Outlook, International Energy Agency, 2011, worldenergyoutlook.org. Sub-Saharan Africa is faced with a challenge that most of the rest of the world has resolved: almost half the population has no access to grid electricity. MENA: Middle East and North Africa, ASEAN: Association of Southeast Asian Nations, SSA: sub-Saharan Africa. South Asia includes Bangladesh, India, Nepal, Pakistan and Sri Lanka.* ***b)*** *Correlation between gross domestic product (GDP) and electricity consumption. Data from the Electricity Access Database, World Energy Outlook, International Energy Agency, 2011, worldenergyoutlook.org and World Development Indicators, World Bank Group, July 2014, worldbank.org.*

Geothermal resources hosted in the EARS (Figure 1.2) offer the potential for secure, low-carbon renewable energy, and present a solution to this energy shortfall (Younger, 2014). In Kenya major geothermal production is being carried out at Olkaria volcano and it now contributes ~15 % of the country's total energy mix (Fridriksson, 2009) equivalent to ~290 MW. In Ethiopia geothermal has yet to be effectively exploited and development is limited to one power plant on Aluto volcano which is currently only producing 7 MW. There has, however, been a considerable drive to develop these resources in Ethiopia over the last few years and multi-billion dollar investments from the World

Bank aim to stimulate a 10-fold expansion in the geothermal industry over the next decade. In real terms, volcanoes such as Aluto are being developed to increase capacity from 7 MW to 70 MW, and at Corbetti volcano a 1000 MW power plant has recently been commissioned (Kebede, 2012).

1.4 Volcanic hazard

Despite the recent drive to develop geothermal power in Ethiopia, very little is known about the eruptive histories of the volcanoes that host these resources and none of them have permanent monitoring infrastructure (Aspinall et al., 2011). While there have been a number of recent eruptions in the Afar region of Ethiopia (Nabro in 2011: Pyle, 2012, Hamlyn et al., 2014; Alu-Dalafilla in 2008: Pagli et al., 2012; Dabbahu between 2005–2009: Ferguson et al., 2010), the only historical eruptions that have been documented in the MER occurred at Kone and/or Fentale volcanoes in 1820-1830's (Gibson, 1970; Rampey et al., 2010). Recent regional surveys of ground deformation (Biggs et al., 2011) and seismicity (Keir et al., 2006) have however detected signs of unrest beneath a number of the MER volcanic complexes over the last decade.

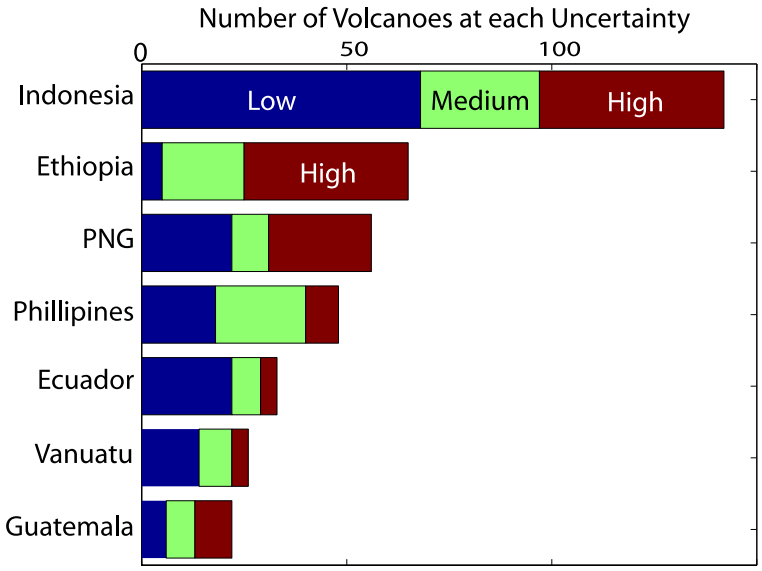

Figure 1.5: *Bar graph showing number of volcanoes at each uncertainty level after analysis of Aspinall et al. (2011). Almost all of Ethiopia's volcanoes fall in the highest uncertainty level (red, 3), and Ethiopia has almost as many high uncertainty volcanoes as Indonesia.*

The hazard and population exposure of these volcanoes was assessed by Aspinall et al. (2011) and Brown et al. (2015), for the World Bank and Global Volcano Models, respectively. These authors showed that in Ethiopia, forty million people live within 100 km of a volcano (roughly half of the total population), one million live with 10 km, and to give an example of a specific hazard, ~4 million people live in regions at risk from pyroclastic density currents. A key feature of the hazard analyses of Aspinall et al. (2011) and Brown et al. (2015) is that a high level of uncertainty was assigned to the 49 Ethiopian volcanoes that lack eruptive histories (Fig. 1.5). Almost two thirds of Ethiopia's volcanoes fall in the highest uncertainty level (Fig. 1.5), and from a global perspective Ethiopia has almost as many high uncertainty volcanoes as volcanic arc settings such as Indonesia. Many of Ethiopia's high-uncertainty/high-population exposure volcanoes are located within the MER (Aspinall et al., 2011).

It is also important to recognize that the majority of general models for magmatic systems are based on sub-alkaline silicic rocks. The silicic volcanic systems of the EARS are peralkaline in composition; oversaturated with alkalis, $Na_2O + K_2O$, and thus undersaturated with respect to Al_2O_3. While peralkaline volcanic systems tend to be smaller and less voluminous than their sub-alkaline counterparts (e.g., Mahood, 1984), their low viscosity and volatile-rich nature lead to petrogenetic processes which are arguably more complex (Macdonald, 2012).

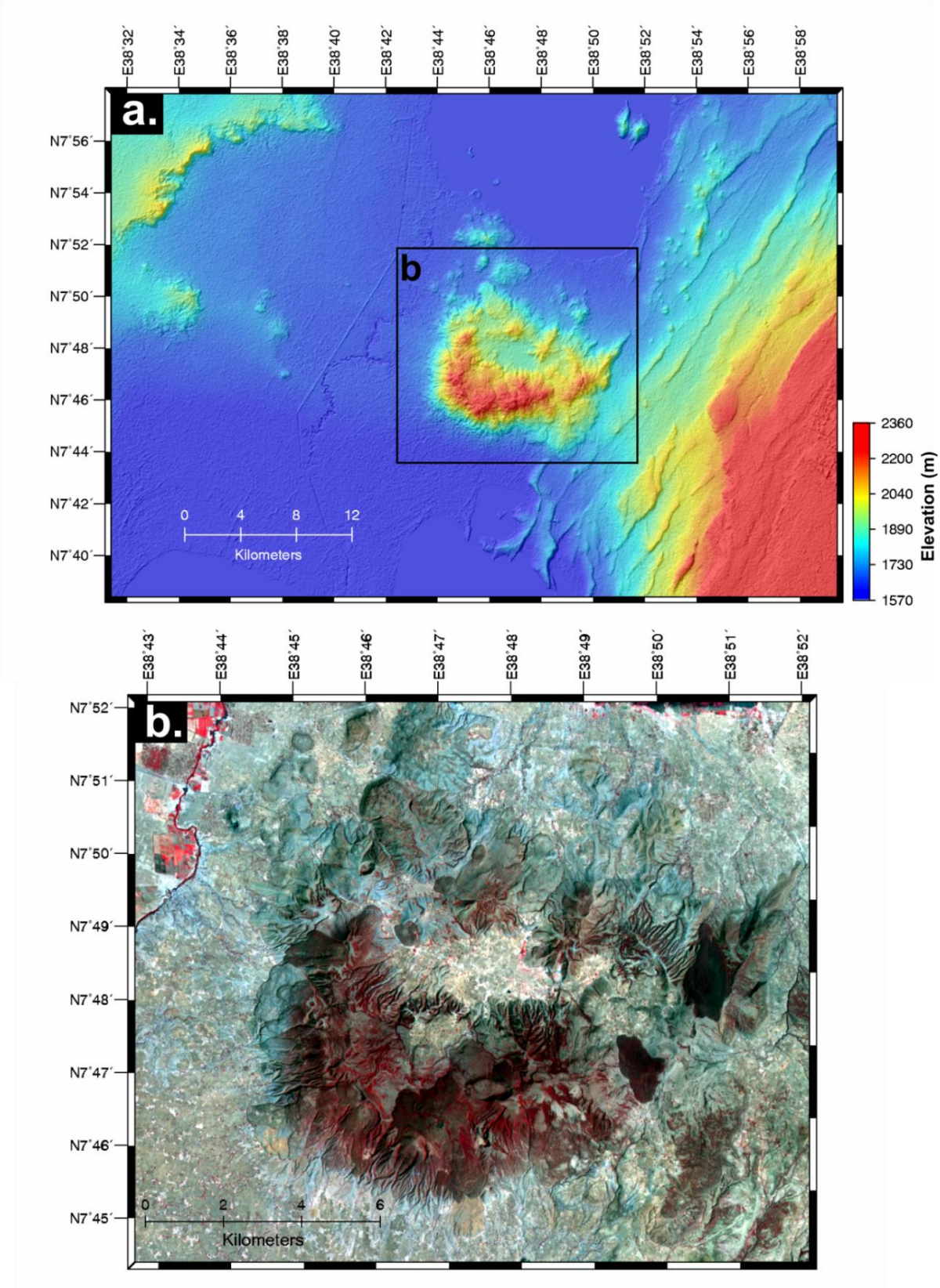

Figure 1.6: *Shaded relief map (a) and false-colour satellite image (b, RGB321) of Aluto volcano, Ethiopia. The elevation data was acquired by the Shuttle Radar Topography Mission (SRTM), while the imagery was acquired by the Advanced Spaceborne Thermal Emission and Reflection Radiometer (ASTER) instrument. The Aluto volcanic complex (centre) largely comprises a pile of coalescing obsidian coulees and volcaniclastic deposits. Obsidian coulees (dark black and grey colours in b) can be seen fanning off the complex; darkest colours represent the least weathered and hence more recent flows. In (b) the red colours typically represent dense vegetation. Aluto is located on the eastern margin of the MER (Fig. 1.2) and on the east of the complex NE-SW trending regional fault structures can be identified in (a).*

1.5 Thesis overview

The overarching goal of this thesis is to achieve a more thorough understanding of silicic volcanism in the MER and the timescales and processes of magmatism and volcanism. We have targeted Aluto volcano (Fig. 1.6), a typical silicic complex which has a high proximal population (300,000 people live within 30 km, Siebert and Simkin, 2002), geothermal resources set for further development (Section 1.4), an InSAR deformation signal (Biggs et al., 2011), and a largely unknown eruptive history. We adopt a multidisciplinary approach involving remote sensing, degassing, petrology, geochronology and geochemistry, and use these techniques to learn more about past, present and future volcanism at Aluto and, by extension, other restless caldera systems in East Africa.

The main research themes covered in this thesis are as follows:

- **Past** – ***How have the MER silicic volcanic complexes evolved? Have the rates of silicic volcanism been steady or pulsed over geological timescales?***

- **Present** – ***What volcanic processes are taking place today? What can we learn about MER geothermal systems, and how can we best exploit these resources?***

- **Future** – ***What are the recent rates of volcanism? What hazards can we foresee?***

These key questions will be considered throughout the individual chapters, and the thesis is structured as follows:

Chapter 2: Structural controls on volcanism and hydrothermal processes. In this chapter, we integrate observations from field campaigns, airborne remote sensing (lidar, aerial photos) and soil-

gas CO_2 surveys to examine how magma, hydrothermal fluid and gas pathways are coupled to the major structural features on Aluto. We show that each data set provides unique information about the complex and the links between volcanic activity and pre-existing volcanic and tectonic structures. From these data, we develop a conceptual model that captures both the volcanic evolution and the role these major structures play in controlling fluid pathways.

Chapter 3: New constraints on causes of episodic unrest. In this chapter we combine measurements of ground displacement and degassing to understand more about magmatic-hydrothermal interactions and unrest events at Aluto volcano. We use interferometric synthetic aperture radar (InSAR) to investigate the spatial and temporal patterns of deformation and establish simple constraints on the volume of fluids involved in the unrest events. We also report new soil-gas CO_2 isotopic data which shed light on the links between the magmatic and geothermal reservoirs of Aluto. We suggest episodic uplift is caused by magmatic and/or fluid intrusion in the cap of a magmatic reservoir at ~5 km and that subsequent deflation is related to magmatic degassing and cooling of the hydrothermal reservoir.

Chapter 4: The volcanic and magmatic evolution of Aluto volcano. In this chapter, field studies, remote sensing, $^{40}Ar/^{39}Ar$ geochronology and geochemical techniques are integrated to document the volcanic and magmatic evolution of the Aluto volcanic complex. We reconstruct the eruptive history of Aluto and present a new geological map; we present the first dedicated whole-rock geochemical study of the volcano, and assess magma petrogenesis, and finally, we develop a conceptual model of the eruptive history and magmatic evolution of the complex within the context of the evolving rift.

Chapter 5: Silicic eruptive fluxes in the Main Ethiopian Rift. In this final chapter we present new age data for caldera-forming eruptions at Aluto and Corbetti volcanoes as well as an analysis of eruption scales. We use these to evaluate the Middle Pleistocene (300–200 ka) flare-up hypothesis of

Mohr et al., (1980) who speculated that a paroxysm of crustal extension and silicic volcanism took place at this time. Our results suggest that the onset of the Middle Stone Age in Ethiopia (c.a. 300 ka) was indeed a period of elevated magmatic flux and caldera-forming volcanism. We consider the causes for the flare-up, the broader implications of this mode of activity, and the potential impacts both for early hominin populations living in the MER, and for current volcanic hazards in the region.

Chapter 6: Conclusions. In this final chapter I provide an overall summary of the results, show how this new work ties into the past, present and future research themes discussed previously, and also outline future avenues for research.

Chapter 2

Structural controls on volcanism and hydrothermal processes

A version of this chapter has been published as: Hutchison et al. 2015. Structural controls on fluid pathways in an active rift system: A case study of the Aluto volcanic complex. Geosphere, 11, doi:10.1130/GES01119.1. Authors as follows:

William Hutchison*[1], Tamsin A. Mather[1], David M. Pyle[1], Juliet Biggs[2] and Gezahegn Yirgu[3]

1. COMET, Department of Earth Sciences, University of Oxford, South Parks Road, Oxford OX1 3AN, UK
2. COMET, School of Earth Sciences, University of Bristol, Wills Memorial Building, Queens Road, Bristol BS8 1RJ, UK
3. School of Earth Sciences, University of Addis Ababa, P.O. Box 1176, Addis Ababa, Ethiopia

---

Abstract

In volcanically and seismically active rift systems, pre-existing faults may control the rise and eruption of magma, and direct the flow of hydrothermal fluids and gas in the subsurface. Using high-resolution airborne imagery, field observations and CO_2 degassing data on Aluto, a typical young silicic volcano in the Main Ethiopian Rift, we explore how pre-existing tectonic and volcanic structures control fluid pathways and spatial patterns of volcanism, hydrothermal alteration and degassing. A new lidar digital elevation model and evidence from deep geothermal wells show that the Aluto volcanic complex is dissected by rift-related extensional faults with throws of 50-100 m. Mapping of volcanic vent distributions reveals a structural control by either rift-aligned faults or an elliptical caldera ring fracture. Soil-gas CO_2 degassing surveys show elevated fluxes (>>100 g m^{-2} d^{-1}) along major faults and volcanic structures, but significant variations in CO_2 flux along the fault zones reflect differences in near-surface permeability caused by changes in topography and surface lithology. CO_2 emission from an active geothermal area adjacent to the major fault scarp of Aluto amounted to ~60 t d^{-1}, we estimate the total CO_2 emission from Aluto to be 250-500 t d^{-1}. Pre-existing volcanic and tectonic structures have played a key role in the development of the Aluto volcanic complex and continue to facilitate the expulsion of gases and geothermal fluids. This case study emphasises the importance of structural mapping on active rift volcanoes to understand the geothermal field as well as potential volcanic hazards.

2.1. Introduction

Existing fault structures can play a significant role in the development of a volcanic complex, ultimately providing high permeability pathways that magma, hydrothermal fluids and gas can ascend to the surface (e.g., Arnórsson, 1995; Rowland & Sibson, 2004; Caliro et al., 2005; Fridriksson et al., 2006). Understanding how pre-existing structures such as regional tectonic faults and caldera ring faults impact fluid flow to the surface is a major task in defining the evolution of rift zones and has important implications for mineralisation, geothermal exploration and the assessment of volcanic hazard.

Recent work, specifically focused on hydrothermal venting and volcanic degassing (Schöpa et al., 2011; Pantaleo & Walter, 2013), has shown that while pre-existing structures may control permeability at the edifice scale, at smaller scales these structural controls may be obscured by localized near surface permeability variations. These local influences may include: (1) lithological variations: where fluids will preferentially migrate along high permeability layers (e.g., poorly consolidated tephra layers) and (2) topographic controls: where the stress field induced by gravitational loading causes fracturing parallel to topography, and focuses pathways for steam and other gases towards topographic highs (Schöpa et al., 2011). To understand how large-scale structures influence active volcanic processes it is useful to look at the surface expression of different volcanic fluids (i.e., magma, hydrothermal fluids and gas) across a variety of scales to disentangle large scale structural controls from these localized near-surface permeability variations.

Both direct and remote measurements can be used to assess the spatial distribution of fluids and fluid pathways. Remotely sensed data such as lidar and aerial photography (e.g., Pyle & Elliott, 2006; Cashman et al., 2013) are powerful tools to analyse volcano morphology, map sites of eruption and extrusion, and distinguish zones of hydrothermal alteration and fluid upwelling (e.g.,

Crowley & Zimbelman, 1997). On the other hand, volcanic gases (e.g., CO_2) that may be hard to detect remotely, can be readily measured in the field using modern surveying techniques (Chiodini et al., 1998) and gridded to produce detailed maps of gas flux across a volcanic edifice (Cardellini et al., 2003; Parks et al., 2013). These techniques allow us to build up detailed pictures of how different fluids are released from active volcanoes; the challenge for volcanologists is integrating these observations to unravel the sub-surface structure and the processes controlling fluid pathways.

The Main Ethiopia Rift (MER) provides an ideal natural laboratory to study how pre-existing structural features (of both volcanic and tectonic origin) influence active volcanic processes. Firstly, the MER hosts a number of young silicic peralkaline volcanoes, allowing investigation of active magmatic and geothermal systems. Secondly, extension in the MER has generated abundant faults and fracture networks (e.g., Keir et al., 2006; Corti, 2009) through which magma can ascend and erupt. Finally, many of the MER volcanoes have undergone caldera collapse (Cole et al., 2005) and thus are likely to have established ring fault systems (Cole, 1969; Gibson, 1970; Mohr, 1980; Acocella et al., 2003; Rampey et al., 2010).

The silicic peralkaline volcanoes of the MER are among the least studied on Earth: few have detailed geological maps and significant knowledge gaps exist regarding their past and current activity (Aspinall et al., 2011). More generally, detailed studies of peralkaline volcanic systems are limited to a few key complexes (e.g., Pantelleria, Mahood & Hildretth, 1983, 1986; Civetta et al., 1988; White et al., 2009; Neave et al., 2012; Williams et al., 2013) despite the fact that they appear to be a ubiquitous feature of continental rift zones (Mahood, 1984; Cole et al., 2005). The caldera structures produced at peralkaline volcanic centres in the East African Rift system (EARS) are also of note because many appear elliptical in map view (e.g., Acocella et al., 2003; Bosworth et al., 2003; Holohan et al., 2005). While several recent publications have emphasised

the role of elongate magma chamber collapse in generating elliptical calderas in the EARS (e.g., Acocella et al., 2003; Bosworth et al., 2003), there is a lack of consensus regarding the exact mechanism in the MER. Establishing the controls on magma rise and ponding in tectonically thinned crust is fundamental to understanding how continental rift zones evolve (Ebinger et al., 2010).

In this paper, we integrate observations from field campaigns, airborne remote sensing (lidar, aerial photos) and soil-gas CO_2 surveys to examine how magma, hydrothermal fluid and gas pathways are coupled to the major structural features on Aluto, a typical young peralkaline volcanic complex of the MER. We show that each data set provides unique information about the complex and the links between volcanic activity and pre-existing volcanic and tectonic structures. From these data, we develop a conceptual model that captures both the volcanic evolution and the role these major structures play in controlling fluid pathways.

2.1.1 Main Ethiopian Rift – Regional setting

The Main Ethiopian Rift (MER), Fig. 2.1, is a zone of active extension in the EARS that connects the Afar depression to the north with the Turkana depression and Kenyan rift to the south. The MER is an oblique rift, exhibiting an overall NE-SW trend, formed by east-west extension between the Nubia and Somalia plates via both magmatic intrusion and tectonic faulting (Ebinger, 2005; Corti, 2009; Corti et al., 2013a). Geodetic and seismic data (Bendick et al., 2006; Keir et al., 2006; Stamps et al., 2008) indicate that the current east-west (~N100°E) extension rates are 4-6mm yr^{-1}. The MER is usually divided into three sectors (northern, central and southern), that reflect differences in terms of the spatial pattern of the faulting (Agostini et al., 2011); the timing of the major faulting episodes (WoldeGabriel et al., 1990; Wolfenden et al., 2004; Bonini et al., 2005) and the thermal-mechanical state of the lithosphere (e.g., Keranen & Klemperer, 2008). This pattern is consistent with rift maturity increasing northward along the

MER towards Afar where the overall physiology changes from continental rifting to incipient 'oceanic' spreading (Beutel et al., 2010; Ebinger et al., 2010; Ferguson et al., 2013).

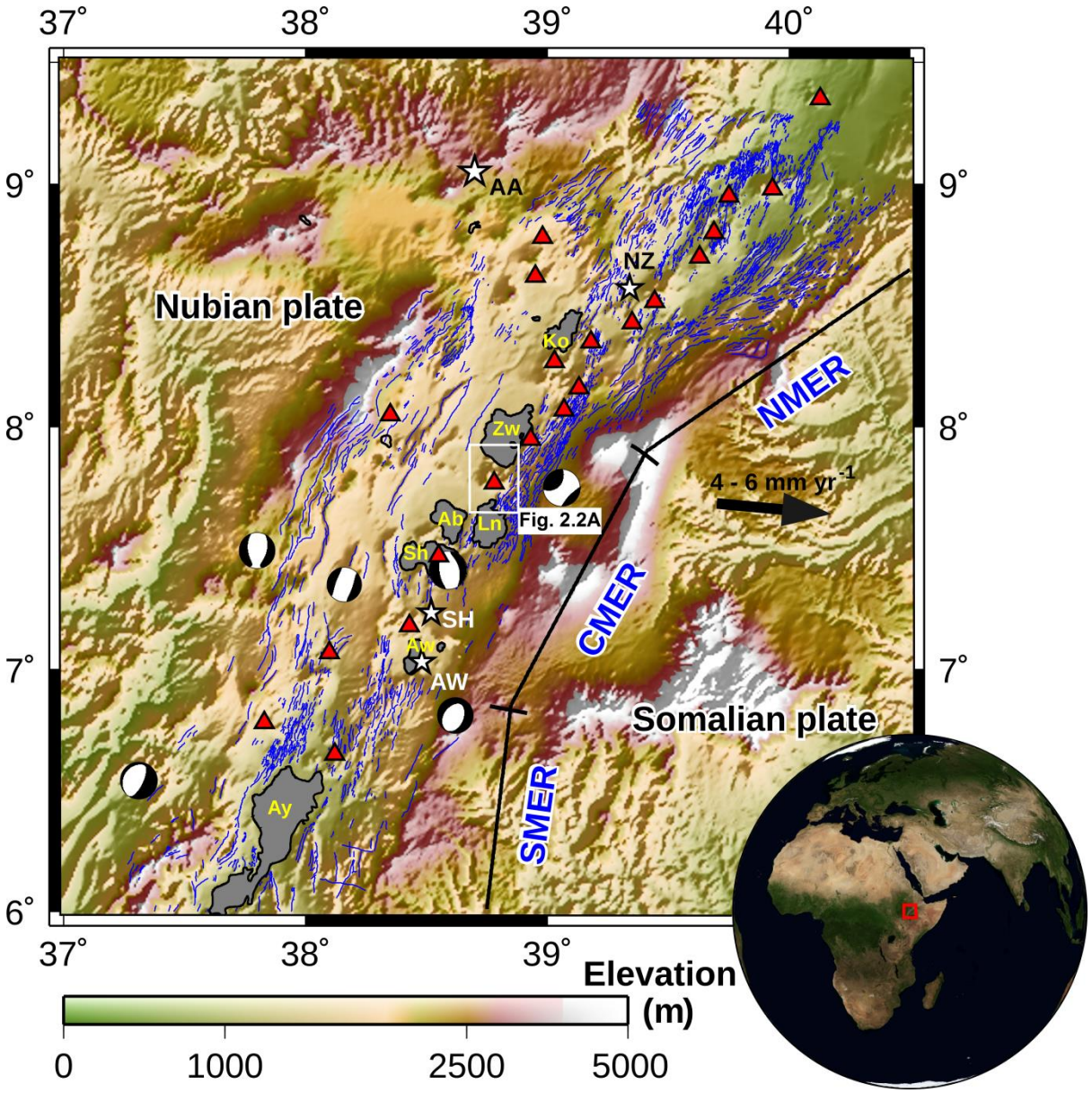

Figure 2.1: *Topographic map of the Main Ethiopian Rift (MER) indicating the three main sectors (northern, central and southern MER marked NMER, CMER and SMER respectively). The surface faults (mapped by Agostini et al., 2011) are shown in blue. Earthquake locations and focal mechanisms for the region are from the GCMT catalogue (1976-2012, M>5). Red triangles identify volcanic centres thought to have been active in the Holocene (Siebert & Simkin, 2002). White stars identify major centres of population (after the Socioeconomic Data and Applications Center), including AA: Addis Ababa; NZ: Nazareth; SH: Shashemene and AW: Awassa. Lakes outlined in the MER include: Ko: Lake Koka; Zw: Lake Ziway; Ln: Lake Langano; Ab: Lake Abijta; Sh: Lake Shala; Aw: Lake Awasa and Ay: Lake Abaya. The Aluto volcanic complex is located within the white rectangle (Fig. 2.2a).*

The MER possesses two distinct fault sets: (1) NE-SW oriented border faults with large vertical offsets (>100 m) on the boundaries of the rift and (2) a set of closely spaced internal faults, the Wonji faults, with smaller vertical offsets (<100 m) oriented NNE-SSW and concentrated on the rift floor (Chorowicz et al., 1994; Boccaletti et al., 1998). In the central MER (CMER), the focus of this paper, the border faults formed at 6-8 Ma (WoldeGabriel et al., 1990; Bonini et al., 2005), while the Wonji faults initiated at ~2 Ma (Boccaletti et al., 1998; Ebinger & Casey, 2001). These observations support models of rift initiation and continental extension (Hayward & Ebinger, 1996; Ebinger, 2005; Corti, 2008) whereby border faults are progressively abandoned and strain becomes localised to active segments central to the rift zone. This focusing of strain has resulted in discrete narrow zones (~20km wide) where extension is accommodated by Wonji faults as well as magmatic intrusion (Keranen et al., 2004; Keir et al., 2005; Kendall et al., 2005; Mackenzie et al., 2005). In the CMER, while the border faults are still seismically active (Keir et al., 2006; Pizzi et al., 2006), much of the active tectonic deformation occurs in the magmatic segments via the NNE-SSW Wonji faults (Keir et al., 2006).

Magmatic intrusion within the active segments has produced abundant surface volcanism. Basalts are associated with scoria cones and eruptive fissures whereas rhyolitic volcanism has produced a series of peralkaline volcanoes comprising both silicic lava flows, domes, and coulees, and extensive pyroclastic products (Gibson, 1969; Di Paola, 1972).

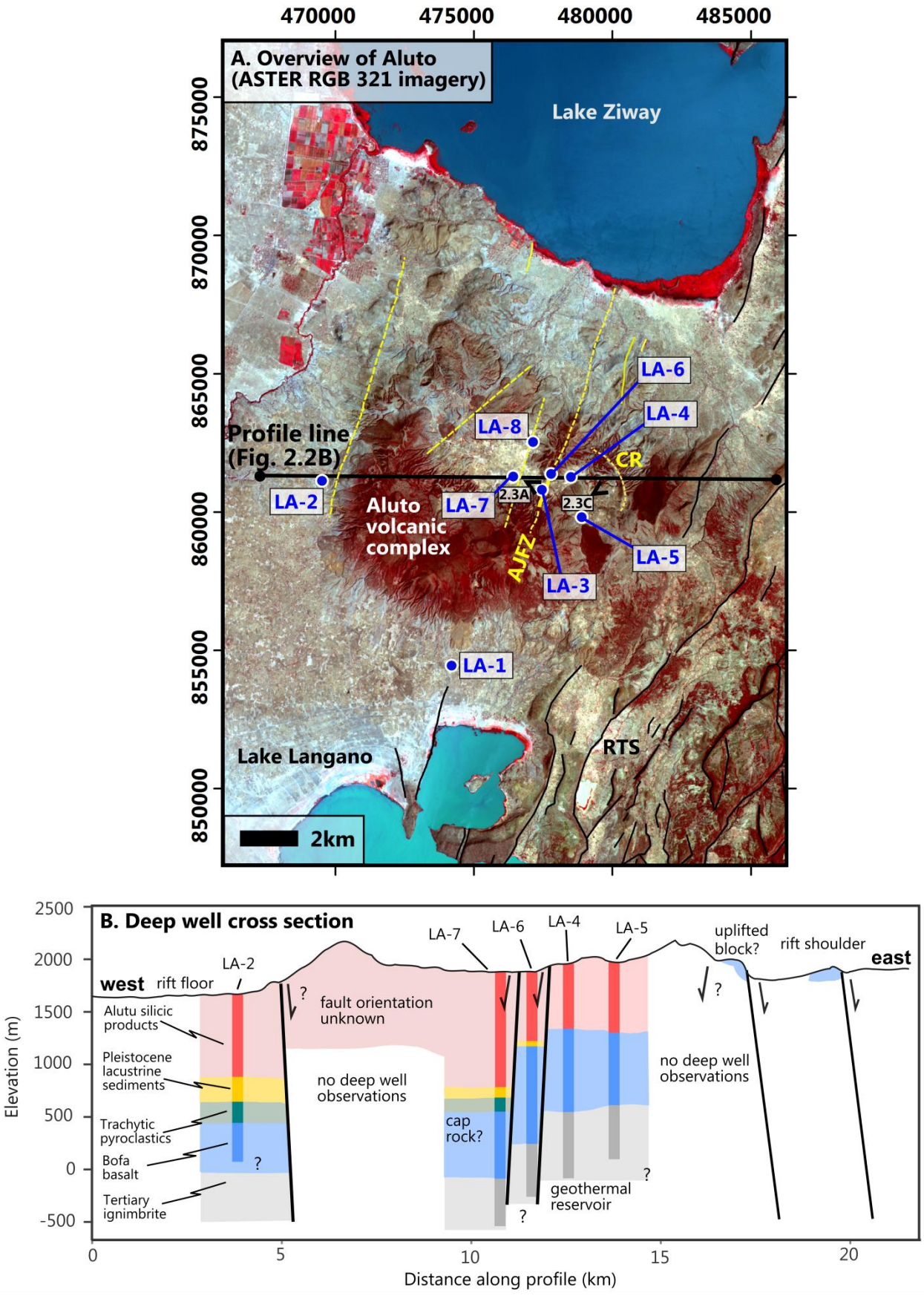
A. Overview of Aluto
(ASTER RGB 321 imagery)
Lake Ziway
Lake Langano
Aluto
volcanic
complex
Profile line
(Fig. 2.2B)
LA-1
LA-2
LA-3
LA-4
LA-5
LA-6
LA-7
LA-8
2.3A
2.3C
AJFZ
CR
RTS
2km
470000
475000
480000
485000
875000
870000
865000
860000
855000
850000
B. Deep well cross section
west
rift floor
LA-2
LA-7
LA-6
LA-4
LA-5
uplifted
block?
rift shoulder
east
fault orientation
unknown
Alutu silicic
products
Pleistocene
lacustrine
sediments
Trachytic
pyroclastics
Bofa
basalt
Tertiary
ignimbrite
no deep well
observations
cap
rock?
geothermal
reservoir
no deep well
observations
Elevation (m)
2500
2000
1500
1000
500
0
-500
0
5
10
15
20
Distance along profile (km)

2.1.2 Aluto volcano – Geological overview and deep well observations

Aluto is a silicic peralkaline volcano located in the CMER (Fig. 2.1). The complex (outlined by the white box in Fig. 2.1 and detailed in Fig. 2.2a) is dominated by a ~14 km wide, 700m high edifice composed of a thick pile of coalescing rhyolitic lava flows and domes, pumice cones and ignimbrite deposits. There are a significant number of smaller volcanic vents and domes formed off the main edifice, particularly to the north-west of the complex. Aluto has an internally drained central depression (herein referred to as a caldera floor, Section 2.4.2) that has been partially in-filled by alluvium and reworked material from the surrounding surface volcanic deposits. While there are no detailed accounts of the eruptive history of the complex, descriptions of the geology of Aluto are given in regional scale mapping reports (e.g., Dakin & Gibson, 1971; Di Paola, 1972; Kebede et al., 1985); studies of the Ziway-Shala lake basin system (Gasse & Street, 1978; Street, 1979; Le Turdu et al., 1999; Benvenuti et al., 2002; Gibert et al., 2002) and publications related to geothermal development on Aluto (Gebregzabher, 1986; Valori et al., 1992; Gizaw, 1993; Ginaelli & Teklemariam, 1993; Teklemariam et al., 1996; Saibi et al., 2012). This work and our own field investigations, suggest that the Aluto volcanic complex has undergone several cycles of explosive and effusive volcanism throughout its history and that these eruptive phases have been dominantly silicic in composition.

Figure 2.2: ***(a)*** *ASTER RGB321 image of Aluto volcano and the surrounding area. Geothermal wells on Aluto are labelled in blue (note only wells LA-3 and LA-6 are productive). Yellow lines indicate the location of faults mapped in previous studies (Kebede et al., 1985; Electroconsult, 1986) or indicated by deep well data (Fig. 2.2b). Black open arrowheads/view lines indicate viewing direction for photographs in Fig. 2.3. As for subsequent figures maps are shown in Universal Transverse Mercator (UTM) coordinates, in UTM Zone 37N with the WGS84 datum. AJFZ is Artu Jawe fault zone. RTS indicates regional tectonic structures visible east of Aluto.* ***(b)*** *West-east cross-section showing the deep stratigraphy and hypothesised sub-surface structure. Well data represents the synthesis of a number of previous publications (Gizaw, 1993; Gianelli & Teklemariam, 1993; Teklemariam et al., 1996) and drilling reports provided by the Geological Survey of Ethiopia (Yimer, 1984; Mamo, 1985; Electroconsult, 1986; Teklemariam, 1996). The geological units shown have been correlated between the different wells on Aluto (Gizaw, 1993; Gianelli & Teklemariam, 1993) and indicate a prevailing mode of deposition rather than a single homogeneous unit (e.g., palaeosols occur within the Bofa basalt and ash horizons occur within lacustrine sequences). The section line is shown on Fig. 2.2a. Note also that data from well LA-5 have been collapsed on to the section line.*

There are few constraints on the ages of the erupted products of Aluto. A single K/Ar date from a geothermal feasibility study gives an age of 155±8 ka for the "Hulo-Seyno ignimbrite" which is taken as one of the first products of the silicic complex (Electroconsult, 1986). The most recent volcanic activity on Aluto is represented by a series of obsidian lava flows, the youngest of which likely erupted within the last 2000 years (Gianelli & Teklemariam, 1993). Aluto remains an active volcanic system. Across the complex, hydrothermal manifestations include fumaroles and hot springs (Kebede et al., 1985). Interferometric synthetic aperture radar (InSAR) studies show that Aluto has undergone several uplift and subsidence events on the order of 10-15 cm over the last decade (Biggs et al., 2011). While the exact mechanism driving deformation is uncertain, the source characteristics and timescale are indicative of shallow magmatic processes active beneath the complex (Biggs et al., 2011).

Eight exploration wells have been drilled on Aluto (LA-1 to 8 on Fig. 2.2a). From these a deep stratigraphy of Aluto has been assembled that forms the model for the geothermal field (Gizaw, 1993; Ginaelli & Teklemariam, 1993). A geological cross-section compiled from these previous studies, as well as various drilling reports provided by the Geological Survey of Ethiopia, is given in Fig. 2.2b. The deep well stratigraphy reveals firstly, that there are substantial offsets in the units between the wells. This is taken as evidence that faults, shown on the map in Fig. 2.2a, dissect the complex. Secondly, there are thickness variations in units between the wells; this is particularly evident in a Pleistocene lacustrine horizon that shows a stepped thinning pattern from west to east (i.e., from the rift centre, towards the rift margin). The abrupt changes in thickness of this unit suggest that deposition took place on an uneven surface, given the rift geological setting this is likely to be associated with faulting, however other processes such as wedging out of the layer on a previous erosive surface cannot presently be ruled out. The Pleistocene lacustrine horizon pre-dates the Aluto silicic products, so if deposition of this unit was fault controlled this would imply that significant faulting preceded volcanic activity at Aluto. Of the 8 wells drilled,

only two (LA-3 and LA-6) are productive to date. The sustained production in these wells is linked to their location along a major NNE-SSW fault on Aluto (herein referred to as the Artu Jawe fault zone, AJFZ, Fig. 2.2a). Well temperatures (Gizaw, 1993), alteration mineral assemblages (Gebregzabher, 1986; Gianelli & Teklemariam, 1993) and the Na/K ratio of geothermal fluids from these deep wells (Gizaw, 1993) all support the hypothesis that this faulted zone is the main upflow zone through which high-temperature fluids ascend to the surface.

2.2. Methods

2.2.1 Remote sensing and GIS analysis

Mapping of the volcanic and tectonic landforms on Aluto was carried out using airborne and satellite remote sensing, complemented by 8 weeks field mapping to "ground-truth" these interpretations. High spatial resolution topography and imagery of the volcanic edifice were acquired on the 16th November 2012 by the UK Natural Environmental Research Council's Airborne Research and Survey Facility (NERC-ARSF). The aircraft was equipped with a Leica ALS50 Airborne Laser Scanner, AISA Eagle and Hawk hyperspectral instruments and a Leica RCD105 39 megapixel digital camera. The lidar system acquired first, second and last returns for ~140 million discrete points and was operated with a pulse repetition frequency of 46200 kHz and scan frequency of 29.9 Hz. The last-return data points were combined into a single point cloud and a 2-m resolution digital elevation model (DEM) was generated using GRASS GIS (Grass Development Team 2009). The Aluto DEM and full lidar datasets is available from: http://dx.doi.org/10.6084/m9.figshare.1261646. The DEM was also used to orthorectify aerial photos acquired by the digital camera. Orthorectification was performed with the Leica Photogrammetry Suite in ERDAS Imagine software using camera calibration information provided with the photographic data. Orthophotos reveal valuable surface and morphological information and have a resolution of 0.25-0.50 m.

Using the airborne data we mapped: (1) volcanic vent locations, the site of an effusive vent of a lava flow and the centre of a crater (or set of nested crater features), represented by points (Figs. 2.4, 2.5), and (2) volcanic lineaments, crater rims and other linear fissures represented by line features (Fig. 2.5b). We could only map volcanic lineaments on the main edifice of Aluto (i.e., the area covered by the lidar DEM), off the main edifice Google Earth and ASTER satellite imagery were used and owing to their lower resolution, and the generally greater erosion of the volcanic landforms beyond the main edifice, only vent locations could be accurately mapped (Fig. 2.4).

The spatial distribution of volcanic vents and the orientation of elongate vents and fissures can be used to make inferences about geometry of feeder dykes and ultimately evaluate the underlying structural or stress field controls on magma pathways (e.g., Nakamura, 1977; Tibaldi, 1995; Paulsen & Wilson, 2010). On the main edifice, we used crater rim and fissure line data (Fig. 2.5) to investigate whether these features exhibited any prevailing orientations and alignments with regional faults (Fig. 2.8). To do this we analysed the orientation of all individual segments of the digitised crater and fissure line data and length-weighted our results (Fig. 2.8c). The results are illustrated for an individual elongate crater in Fig. 2.6a with the inset clearly demonstrating that a rose plot with prevailing east-west orientation is obtained. This method is similar to that employed previously (e.g. Trippanera et al., 2014) but has the advantage that rather than taking one averaged elongation direction all mapped segments that make up the crater and fissures are used and can be compared together. Beyond the coverage of the lidar-DEM, where it was not possible to carry out detailed volcanic lineament mapping, an azimuth-based method was used to assess vent alignments (Lutz, 1986; Wadge & Cross, 1988; Lutz & Gutmann, 1995; Cebriá et al., 2011). Vents are treated as discrete points and the azimuth (or alignment direction) between a vent and its neighbours is determined for a given separation distance. When vent locations (or

magma pathway to the surface) are controlled by faulting then neighbouring vents will have similar orientations relative to each other. However, as the distance between vents increases then so too does the likelihood that the vents will not be located on the same fracture. Thus, alignments need to be assessed within a specific separation window to best expose regional structural trends (Cebriá et al., 2011). Ultimately, these numerical interpretations of the volcanic vents and structural data (Fig. 2.8) are considered in the context of the physical observations from the remote sensing, field observations and the CO_2 degassing measurements to assess their real geological significance (Sections 2.4.1 and 2.4.2).

Hydrothermal fluid upwelling on Aluto causes visible alteration of the surface volcanic products, producing red and orange clays over areas >>10m^2, which can be mapped using aerial photographs (Fig. 2.6b). While an automated mapping approach using the spectral signature of these alteration facies (e.g., Crowley & Zimbelman, 1997) would be feasible given our dataset, for the purposes of this study the resolution of the aerial photos is sufficiently high that major altered zones can be approximately mapped, and their locations can be linked with structural interpretations and CO_2 degassing results. Our assessment of hydrothermal alteration made using the orthophotos (Section 2.3.4) correlates well with fumarole vents mapped on the ground by the Geological Survey of Ethiopia (Kebede et al., 1985), and for hot spring locations that were beyond the coverage of our remote sensing data we have used Kebede et al. (1985) to constrain their location.

2.2.2 Soil CO_2 flux

Measurements of soil CO_2 flux on Aluto were undertaken in three surveys between January 2012 and February 2014. The first survey was conducted in January 2012 and sought to transect large-scale structures and identify whether they provided key permeability pathways for CO_2-rich geothermal fluids and magmatic gases to upwell. Degassing surveys were next conducted in

November 2012 and February 2014 and focused on producing a detailed map of spatial degassing patterns along the major tectonic fault (Artu Jawe fault zone, Section 2.3.2). A 1000 m x 800 m study area (outlined in black in Fig. 2.5a) was chosen to cover both the major fault scarp (shown in the photograph in Fig. 2.3a) and the productive geothermal wells (LA-3 and LA-6). A 30 m sampling grid was used; a compromise between attaining spatial coverage of the fault zone at sufficient sampling resolution. In total 560 sites were visited (424 in November 2012 and 136 in February 2014). Those that fell in geothermal effluent ponds, areas of dense vegetation or hazardous slopes were excluded, and in some instances extra measurements were made off the pre-defined sampling grid to help characterize the highest values in the degassing regions.

CO_2 flux was measured directly using two portable closed system gas analyser units (a LICOR LI-8100 automated soil CO_2 flux system and a PP-systems SRC-1 chamber with EGM-4 analyser). Both instruments have an in built infra-red gas analyser and use the accumulation method (Parkinson, 1981; Chiodini et al., 1998) to measure CO_2 flux. Measurements were consistent between the instruments; comparisons made at identical sites showed variations of 10-25% between the two instruments (significantly less than the variation seen across the complex, Section 2.3.5). Repeated site measurements showed variations of ~25% in low flux zones (<10 g m^{-2} d^{-1}) and less than 10% in high flux zones (>100 g m^{-2} d^{-1}), consistent with random error in natural emission rates (Carapezza & Granieri, 2004; Viveiros et al., 2010) and in line with the quoted reproducibility of each instrument (5-10%, Chiodini et al., 1998; Giammanco et al., 2007).

To generate maps of soil CO_2 flux from the discrete point measurements the sequential Gaussian simulation (sGs) method was used (Cardellini et al., 2003). A simulation grid was defined (at higher spatial resolution than the sampling grid) and 100 sequential Gaussian simulations were performed using the sgsim code (Deutsch & Journel, 1998) available in the Stanford Geostatistical Modeling Software (SGeMS) open-source geostatistics package (Remy et al.,

2009). A CO_2 flux map was constructed from these simulations taking the arithmetic mean of each individual cell across all simulations, equivalent to the E-type soil flux map proposed by Cardellini et al. (2003). The total CO_2 flux was calculated for each simulation and finally the mean and standard deviation of all simulations was computed and used to estimate total CO_2 release as well as the associated uncertainty (Cardellini et al., 2003).

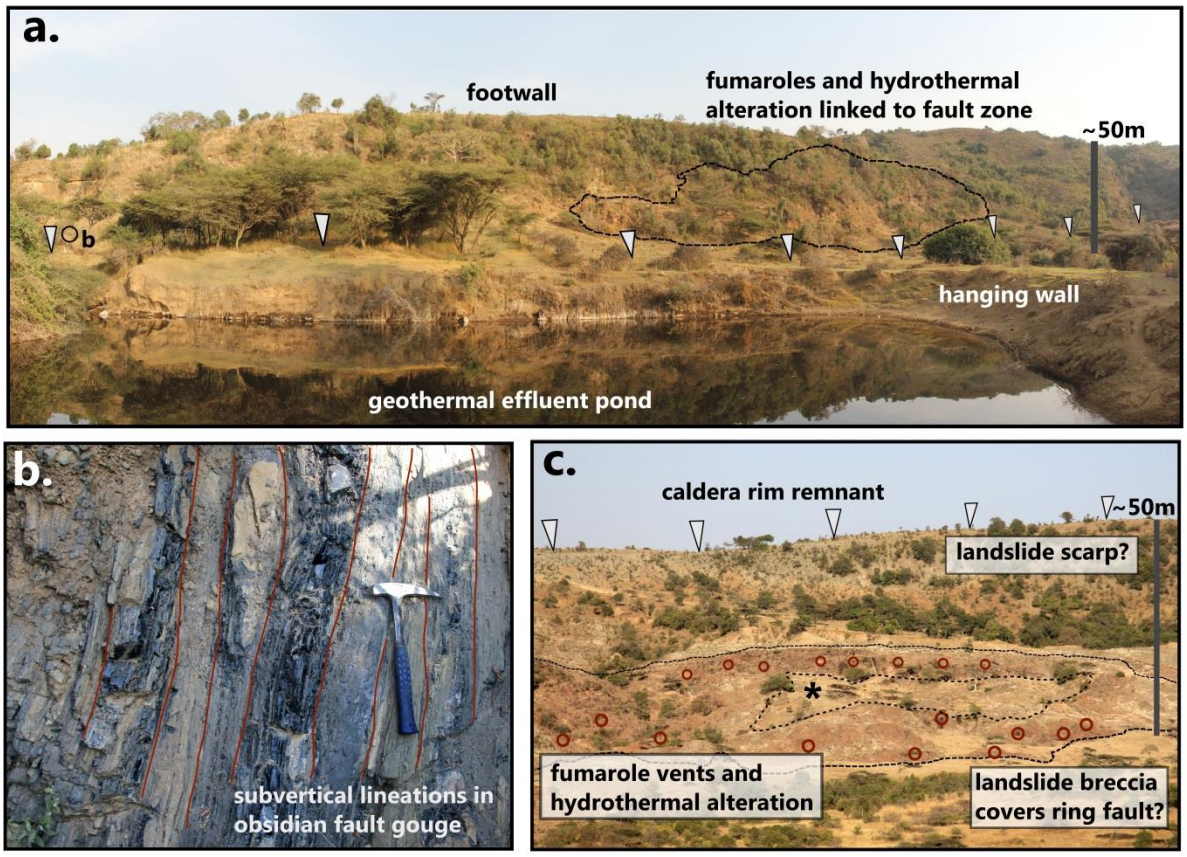

Figure 2.3: *Photographs of major volcanic and tectonic structures on Aluto.* ***(a)*** *The Artu Jawe fault scarp viewed from the west (located in Fig. 2.2a). Along the escarpment fumaroles are visible at the base of the structure and there is evidence of hydrothermal alteration at the surface.* ***(b)*** *Sub-vertical foliations developed in obsidian in crush zone of Artu Jawe fault scarp (located in Fig. 2.3a). Hammer is 30 cm in length.* ***(c)*** *The caldera wall of Aluto, identifying fumarole vents (red circles) and hydrothermal alteration at the base of the structure. The starred (*) zone in the centre of the fumarole field does not show any surface alteration and has low ground temperatures and CO_2 gas flux relative to the surroundings (see Section 2.3.5.1).*

2.3. Results

2.3.1 Recent volcanism and links to a ring fracture system

The spatial distribution of volcanic vents on Aluto is shown in Fig. 2.4. Vents are largely restricted to the main edifice and a roughly NNE-SSW trending zone to the north-west of this. A detailed map of volcanic vents, lava flows, craters and fissures overlain on the lidar DEM is given in Fig. 2.5. Lava flows on the central edifice are rhyolitic; Fig. 2.6a shows shaded relief and slope maps for a typical obsidian lava deposit. Craters are predominantly <1 km in diameter and <100 m deep, many are elliptical (e.g., Fig. 2.6a) or are composed of nested structures (Fig. 2.5).

On the north-east flank of Aluto, several lines of evidence support the existence of a caldera rim structure. From remote sensing data we identify a 2.5 km long arcuate structure (Fig. 2.2a 'CR' and also Figs. 2.4, 2.5) that is orthogonal to the regional NNE-SSW tectonic structures (Fig. 2.2a, 'RTS'). Viewed from south-west (Fig. 2.3c), the rim comprises a steep wall 50-60 m in height. Fumaroles and hydrothermal alteration are picked out at the base of the structure (Fig. 2.3c), and tentatively correlated with a buried ring fault. North-east of the rim (Fig. 2.2a and Fig. 2.5) the topography gently slopes away from the edifice and is incised by numerous gullies and channels. The morphology of this structure is characteristic of a volcanic caldera (Lipman, 1997; Cole et al., 2005) including: a caldera rim, curving landslide scarp and possible landslide breccia that conceals the ring fault (labelled on Fig. 2.3c).

Figure 2.4: *Map of volcanic vents, hydrothermal alteration, active fumaroles and hot springs on the Aluto volcanic complex. Faults on the complex have either been mapped using remote sensing data sets (this study) or have been suggested by previous geological mapping reports and deep well data (Kebede et al., 1985; Electroconsult, 1986; Gizaw, 1993; Gianelli & Teklemariam, 1993). Regional faults were mapped by Agostini et al. (2011). The dashed ellipses show the size and orientation of a buried ring fault that we propose may explain the distribution of volcanic vents on the main edifice, the fine dashed ellipses represent ±500 m uncertainty bounds on the central ellipse. The mapped caldera rim (Section 2.3.1) overlaps the proposed ring structure. Major hydrothermal zones are labelled and link to the summary in Table 2.1 where the abbreviations used in the figure are expanded.*

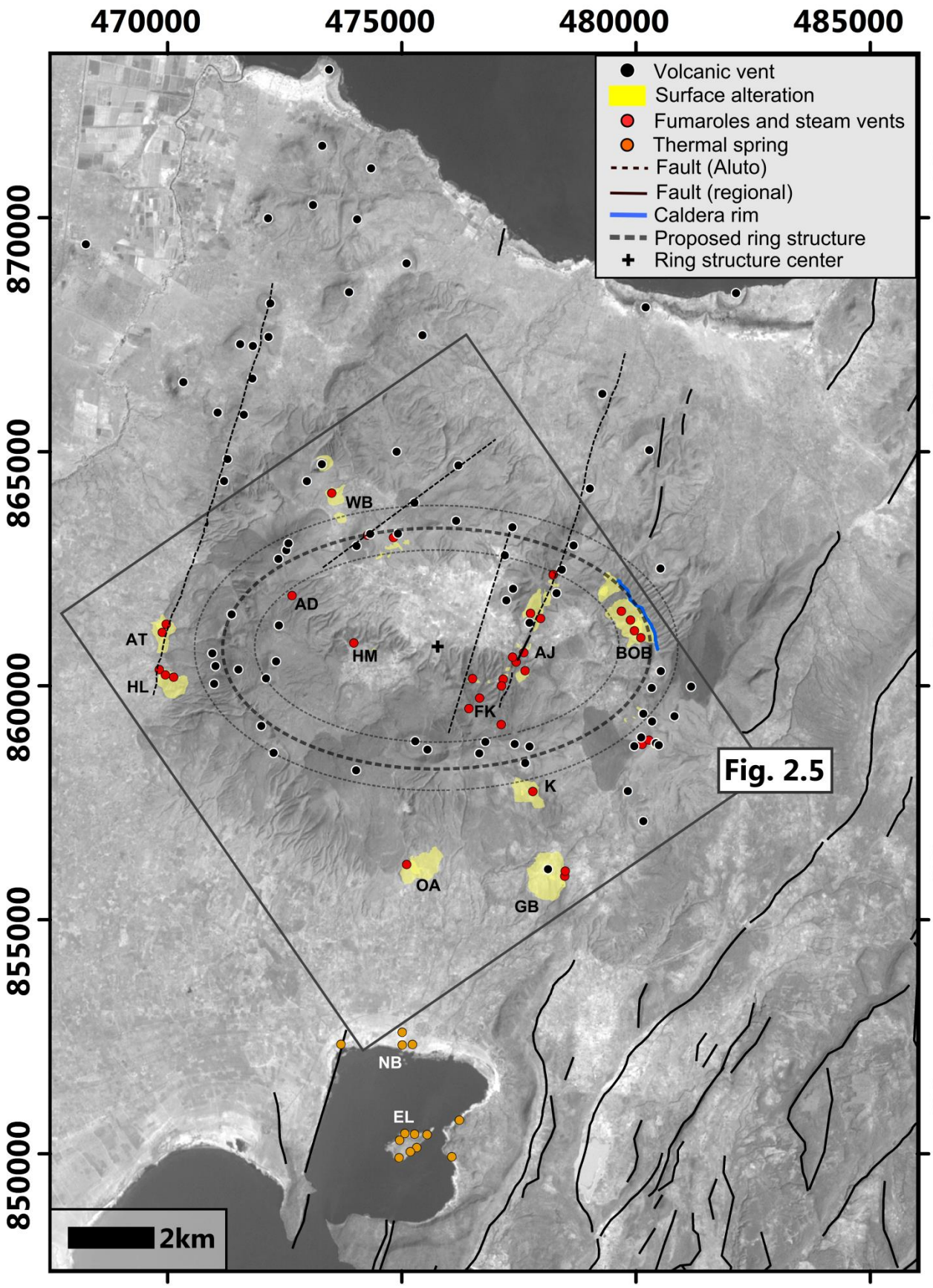
470000
475000
480000
485000
870000
865000
860000
855000
850000
Volcanic vent
Surface alteration
Fumaroles and steam vents
Thermal spring
Fault (Aluto)
Fault (regional)
Caldera rim
Proposed ring structure
Ring structure center
WB
AD
AT
HL
HM
AJ
BOB
FK
K
OA
GB
NB
EL
Fig. 2.5
2km

An underlying caldera ring fault (east-west oriented ellipse, Figs. 2.4 and 2.5) centred on the floor of the main edifice may explain a number of aspects of the young volcanism. Assuming vent and fissure elongation parallels the orientation of subsurface fractures (Paulsen and Wilson, 2010), then crater rim and fissure lineations in Fig. 2.5 can be used as proxy for the underlying structures feeding surface eruption. Vent elongations on the southern rim of Aluto show clear east-west orientations (e.g., Fig. 2.6a, and the nested crater structures east of this in Fig. 2.5b) indicative of an east-west oriented fissure feeding surface eruptions. In Fig. 2.5b it is also clear that mapped crater rims on the western margin of the edifice show approximate elongation north-south, and likewise on the east of the complex a group of clustered craters show overall elongations in north-south and NE-SW directions. The distribution of volcanic vents (Figs. 2.4, 2.5) also shows a dominantly elliptical ring distribution on the main edifice with a marked absence of vents within the centre of the caldera. Fig. 2.4 shows that a number of vents on the main edifice (62% of total mapped using the lidar) fall within ±500 m uncertainty of the proposed ring structure. Vents that do not fall within this structure, may have been controlled by other structures (e.g., the Artu Jawe fault zone, Section 2.3.2), or alternatively the caldera ring fault may be more structurally complex than the proposed ellipse. Caldera ring faults are unlikely to truly approximate an ellipse in shape; however this is the simplest first-order model of a ring fault in the absence of other evidence concerning its structure.

Taken together, the vent elongations and distributions match orientations that would be expected for a mature caldera structure feeding eruptions at the surface. We assume that feeder dykes here are either elongate in response to the local stress field set up on the caldera or are directly exploiting an existing ring fracture. The ellipse fit is ~5 km in north-south diameter and ~8 km in east-west diameter, with ellipticity (short/long axis ratio) of 0.63 and long axis elongation of N090°E. Importantly, the mapped caldera rim remnant corresponds closely to the proposed ring fracture although it only overlaps ~8% of the whole ellipse (Figs. 2.4, 2.5).

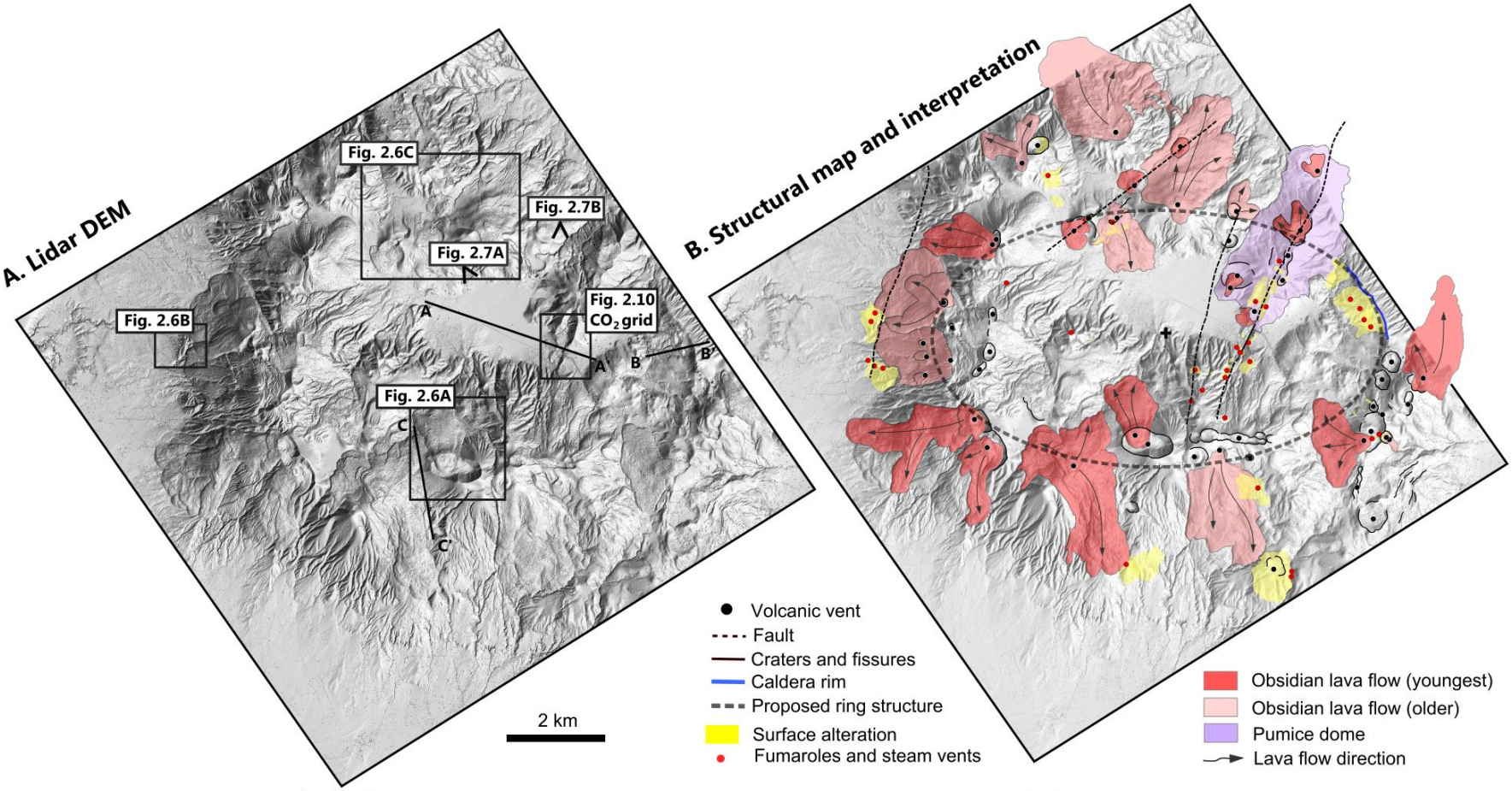

Figure 2.5: ***(a)*** *lidar hillshade DEM covering the main edifice of Aluto volcano (black box shown in Fig. 2.4). Black box insets link to Fig.6 and Fig. 2.10 where detailed imagery and interpretation of the volcanic features is given. Black triangular features show the viewing direction for the 3D DEM imagery given in Fig. 2.7. The light blue lines A-A', B-B' and C-C' correspond to the CO_2 degassing transects given in Fig. 2.9.* ***(b)*** *Structural map and interpretation of the DEM imagery. A key to the mapped features is given below the figure. The older, more weathered, obsidian lava flows of Aluto (shown in rose colour) are covered in a thin shower of grey pumice unlike the younger obsidian lavas (shown in red). The different colours are used for display purposes. The lidar dataset used in this study has a doi: 10.6084/m9.figshare.1261646.*

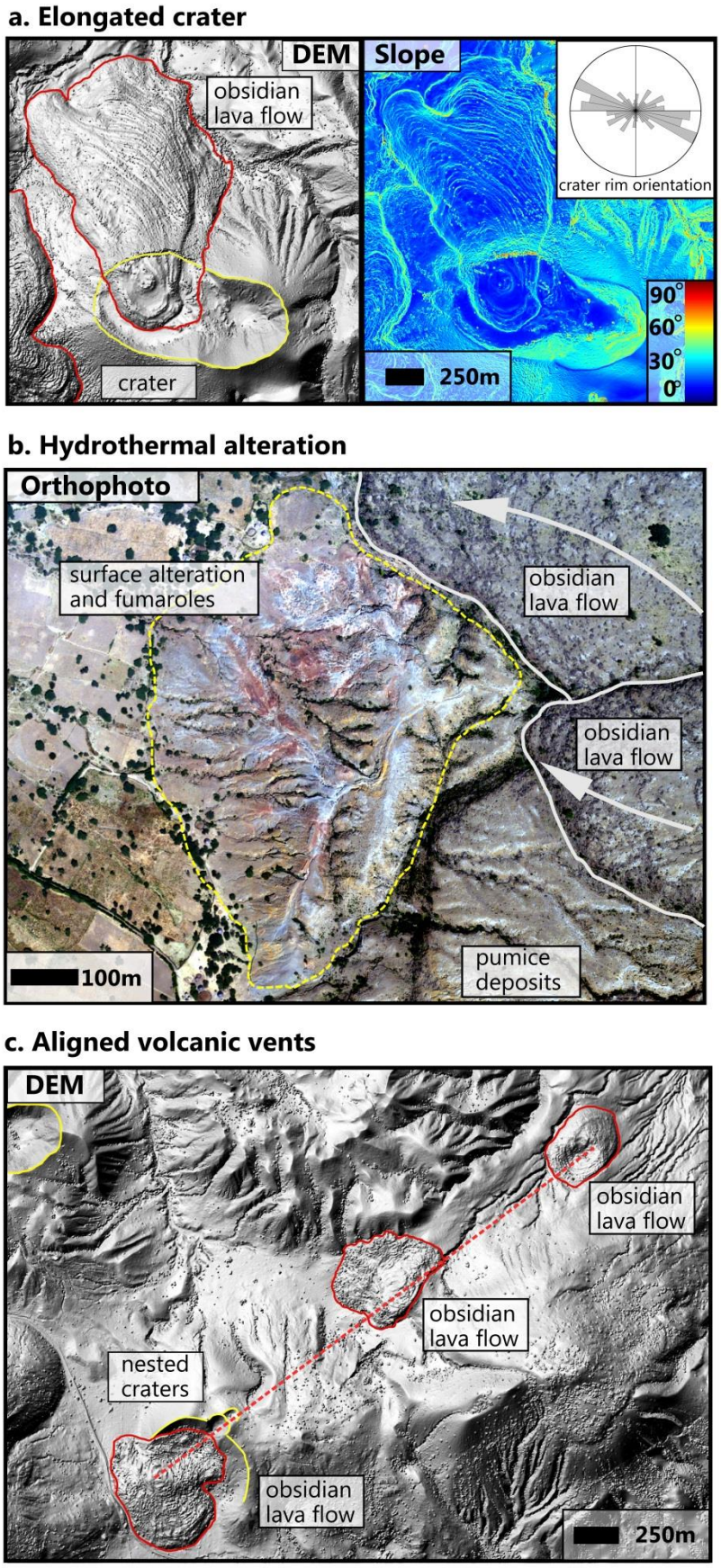

Figure 2.6: *Examples of volcanic features mapped using the airborne data sets.* ***(a)*** *Hillshade DEM and slope map showing a typical obsidian lava flow vent and elongate crater. These flows often preserve compression folds on the surface that are characteristic of viscous silicic lavas (e.g., Fink, 1980; Gregg et al., 1998; Pyle & Elliott, 2006). On the top right of the Figure 2.we show the length-weighted rose diagram generated by analysing the orientation of all the individual segments that compose the crater feature (yellow outline); the dominant ESE-WNW orientation is clearly identified (N.B. for a circular crater rim a radial distribution would be generated).* ***(b)*** *Aerial photograph of the Auto fumarole zone on the west of Aluto. Hydrothermal alteration of pumiceous deposits produces bright red clays adjacent to active fumaroles.* ***(c)*** *Hillshade DEM identifying a set of three aligned obsidian domes and nested craters on the west of the caldera floor suggestive of an underlying tectonic control.*

2.3.2 Evidence for faulting

The deep well stratigraphy (Section 2.1.2, Fig. 2.2b) reveals several major fault zones, aligned with regional tectonic trends, dissecting the Aluto volcanic complex. However, few of these structures have a clear surface expression, due to the large volumes of young volcanic and lacustrine sediment cover. On the edifice itself, the surface is mantled by tephra and obsidian lava flows, while to the north, west and south of Aluto there are substantial lacustrine deposits (including: gravels, sands, muds and diatomite) that have been deposited throughout the Late Pleistocene and Early Holocene (Grove & Goudie, 1971; Grove et al., 1975; Gasse & Street, 1978; Street, 1979; Gillespie et al., 1983; Le Turdu et al., 1999; Benvenuti et al., 2002).

The only major fault scarp visible on Aluto is exposed in a 500 m long segment on the east of the caldera, the NNE-SSW Artu Jawe fault zone (Figs. 2.2a, 2.3a). Topographic profiles across the fault show a typical profile expected for a normal fault down throwing to the west (with a maximum throw of 50 m measured at the surface, Section 2.3.5.1). The scarp is, for the most part, covered by recent slumped clastic material but in a more pristine deeper exposure a highly brecciated aphyric obsidian lava is visible (Fig. 2.3b). The poorly consolidated texture and thin (1-10 cm) sub-vertical banding of the deposit is very different from obsidian lavas encountered elsewhere on the complex and therefore may represent fault gouge. The near vertical dip and approximate north-south strike of the foliations (Fig. 2.3b) closely match the overall trend of the fault scarp.

To the north, the fault scarp is covered by an elongate dome of pumice and obsidian lava units (Figs. 2.5b, 2.7). This elongate dome is 2 km (east-west) by and 4 km (north-south), ~180 m high, and lies close to the trend of the Artu Jawe fault scarp. We infer that these volcanic deposits have erupted along the fault zone building up the elongate pumice dome. To the south of the Artu Jawe fault scarp the surface rupture is again obscured by mantling tephra, however 3D views of the

fault zone (Fig. 2.7) show a gorge following the same trend supporting its continuation into the volcanic pile. Finally, ~500 m west of the main scarp there is evidence of a secondary less pronounced break in topography (Fig. 2.7). The surface topography data alone are not sufficient to classify these faults separately. Owing to their proximity to the main scarp, we group these structures together as the Artu Jawe fault zone.

There are no clear fault traces exposed on the caldera floor (Fig. 2.7, 'CF') suggesting that either the material infilling the caldera is very young and/or there has been no significant recent displacement on faults within the caldera. Previous workers (Kebede et al., 1985; Electroconsult, 1986) have suggested that a fault gorge runs through the southern rim ('SFG' in Fig. 2.7). A line of fumaroles running parallel to this gorge (Fig. 2.7b) provides qualitative evidence to support existence of this fault (see Section 2.3.4).

On the northwest of the caldera floor a set of three obsidian domes and nested craters were identified (Fig. 2.6c). The domes are of comparable size (150-400 m diameter) and are aligned along a trend of N050°E. In the field the domes appear compositionally similar and display similar weathering characteristics, suggesting that they share a common source and erupted at a similar time. Taken together these observations suggest an underlying tectonic control on the eruption of these lavas at the surface.

Figure 2.7: *3D view of the hillshade DEM covering the Artu Jawe fault zone,* ***(a)*** *identifies the faults scarps and their possible continuation into the volcanic pile (indicated by deep gorges), geothermal wells are also shown (note the only productive wells are located adjacent to the major fault scarp,* ***(b)*** *shows fumaroles identified either in the field or using locations reported from field mapping by the Geological Survey of Ethiopia (Kebede et al., 1985). The pink shaded area and dashed line delimits the pumice dome (Fig. 2.5), the elongate nature of the dome is interpreted to reflect the underlying tectonic control feedings the eruptions.*

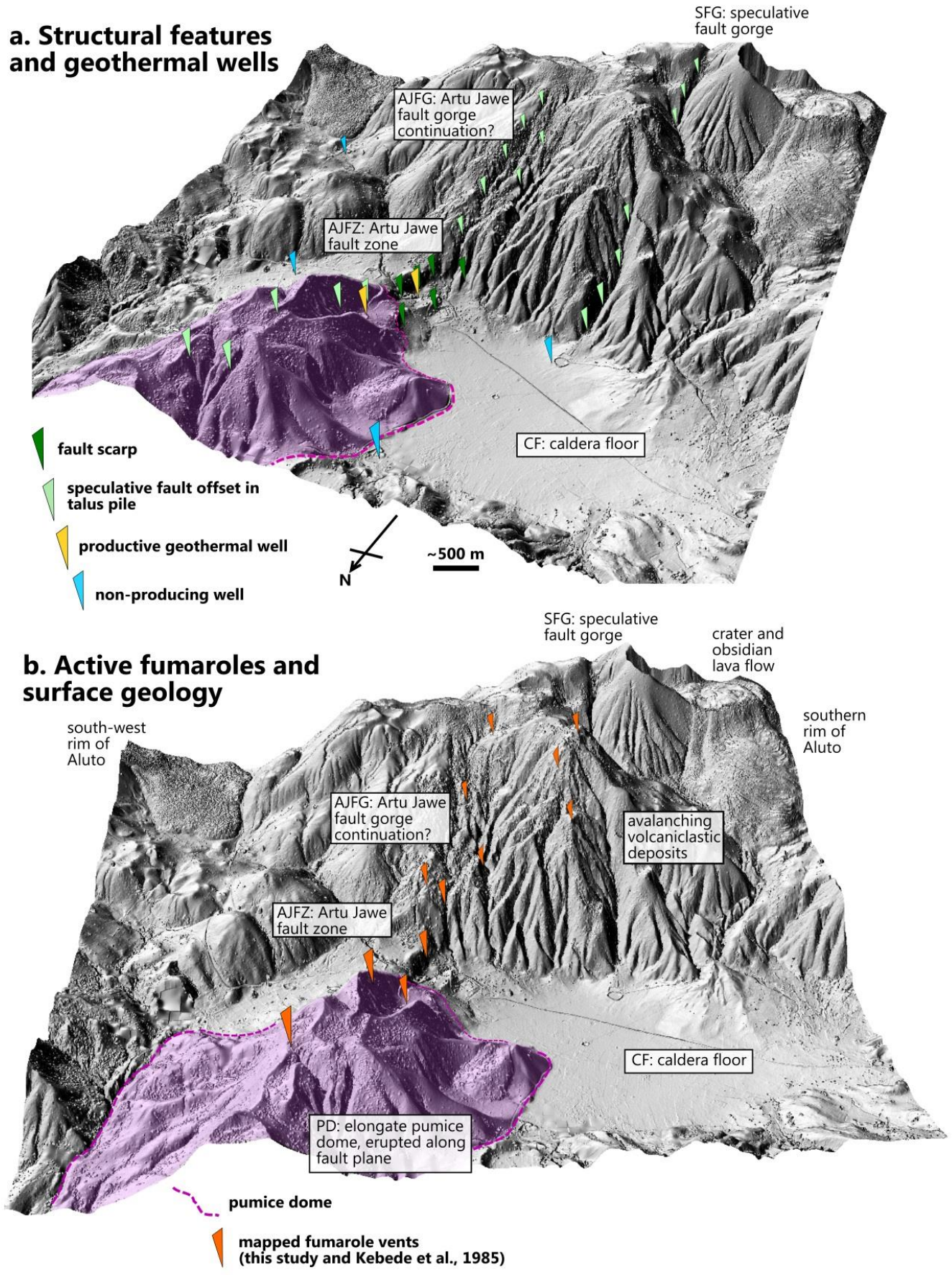
a. Structural features and geothermal wells
SFG: speculative fault gorge
AJFG: Artu Jawe fault gorge continuation?
AJFZ: Artu Jawe fault zone
CF: caldera floor
fault scarp
speculative fault offset in talus pile
productive geothermal well
non-producing well
N
~500 m
b. Active fumaroles and surface geology
SFG: speculative fault gorge
crater and obsidian lava flow
southern rim of Aluto
south-west rim of Aluto
AJFG: Artu Jawe fault gorge continuation?
avalanching volcaniclastic deposits
AJFZ: Artu Jawe fault zone
CF: caldera floor
PD: elongate pumice dome, erupted along fault plane
pumice dome
mapped fumarole vents (this study and Kebede et al., 1985)

From remote sensing (Figs. 2.2a, 2.4) there is a clear prevalence of volcanic vents aligned NNE-SSW north-west of the edifice but yet there is no evidence for large fault structures at the surface. High stands in the lake system since 10 kyr BP have reached maximum lake levels of 1660-1680 m above sea level (Street, 1979; Gillespie et al., 1983; Benvenuti et al., 2002, 2013) sufficient to isolate these vents. We therefore assume that these young lacustrine sediment deposits have masked any surface fault breaks.

2.3.3 Volcanic alignments

In Fig. 2.8 we compare the orientations of volcanic features and vent alignments with regional fault trends. As expected (e.g., Agostini et al., 2011), we can distinguish two distinct fault systems in the CMER: border faults and the younger internal faults (referred to as Wonji faults from here onwards). There is a marked difference in strike between the two groups (Fig. 2.8a, b). Wonji faults have a NNE-SSW strike (mean value of N012°E) while in contrast border faults have a more NE-SW orientation (mean value of N032°E).

Fig. 2.8c shows a length-weighted rose plot for all crater rim and fissure line segments mapped on the main volcanic edifice (identified in Fig. 2.5). Unlike tectonic fault trends these features display preferential orientations along both north-south and east-west alignments. Crater rim and fissure line orientations are also skewed to NE-SW rather than NW-SE alignments (Fig. 2.8c). Figs. 2.8d and 2.8e show the azimuth between volcanic vent locations (i.e. point features, Section 2.2.1) on and off the main edifice of Aluto respectively. On the main edifice the volcanic vents alignments (Fig. 2.8d) show equivalent results to Fig. 2.8c; there is a pronounced NNE-SSW alignment (N010-020E° bin), secondary east-west alignment and also a general skew to NE-SW rather than NW-SE alignments. Off the main edifice (Fig. 2.8e) the results show the prevailing vent alignment is between N000-020E°.

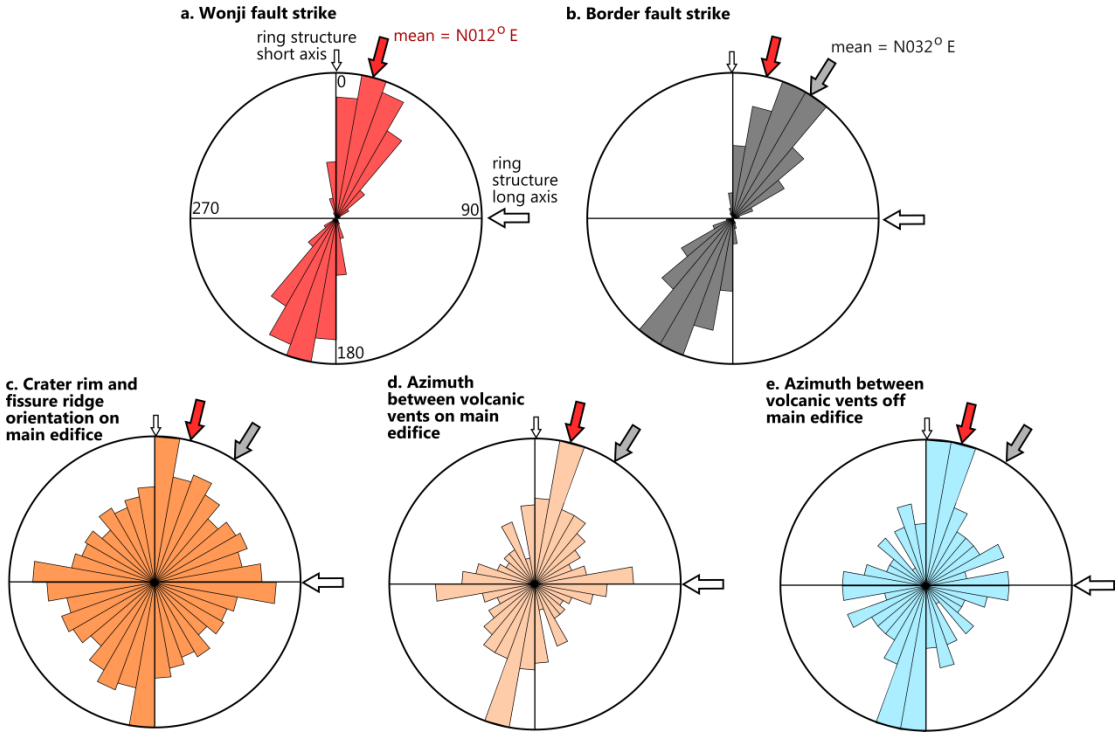

Figure 2.8: *Rose plots comparing regional fault trends, volcanic crater rim and fissure orientation and vent alignments, shown as trends in degrees from north (i.e., 0°=north; 90°=east; 180°=south).* ***a), b)*** *provide regional fault strike for the Wonji and border faults of the CMER (Section 2.1.1) analysed using the Agostini et al. (2011) database (available online at http://ethiopianrift.igg.cnr.it/utilities.htm).* ***c)*** *length-weighted rose plot that analyzes the orientation of all crater rim and fissure line segments mapped using the lidar data set (shown in Fig. 2.5b) to identify prevailing orientations of elongate vents and fissure features.* ***d), e)*** *the azimuth between neighbouring volcanic vents, analysed using the vent locations (black point features) in Figs. 2.4, 2.5. Vent azimuth is analysed both on and off the main edifice (i.e. the area covered by the lidar, Fig. 2.5). The data are filtered such that only those vents separated by 0.2 to 2 km are analysed. A number of different distance filter windows were explored and while the 0.2 – 2 km filter window is shown here the results of similar size windowing methods between 0.1 km and 4 km tended to produce comparable results. Arrows are used to identify: the long and short axis of the ring structure (white) which has an approximately east-west elongation; the mean trend of the Wonji faults (red) and the mean trend of the border faults (grey).*

The preferential east-west orientations observed in Fig. 2.8c arise due to the large number of elongated craters (clearly present on the southern rim of the complex, Fig. 2.5). Figs. 2.8c and 2.8d both support the existence of east-west oriented structures feeding surface eruptions; following analysis in Section 2.3.1 it is assumed this is the surface manifestation of an underlying elliptical caldera structure. Crater and fissure line orientations (Fig. 2.8c) as well as vent alignments (Fig. 2.8d) also show north-south and NNE-SSW orientations, these are representative of aligned elongate craters on the east and west margins of the caldera ring structure (Fig. 2.5) but also alignments along the major tectonic fault structure (Artu Jawe fault zone, Section 2.3.2). Off

the main edifice (Fig. 2.8e) vent alignments are very close to the observed fault strike of the Wonji faults (Fig. 2.8a), strengthening the case that beyond the caldera tectonic fault structures are the dominant control on magma pathways.

2.3.4 Hydrothermal features

Fig. 2.4 shows the zones of hydrothermal alteration, fumaroles and hot springs mapped using the aerial photos and supplemented by mapping reports from the Geological Survey of Ethiopia (Kebede et al., 1985). A summary of the main hydrothermal features and their links to the volcanic and tectonic structures is provided in Table 2.1.

The sites of hydrothermal activity are confined to the summit and flanks of Aluto, as well as the region of hot springs around the north bay of Lake Langano (Fig. 2.4). There is no evidence of active or fossil hydrothermal activity on the northern and eastern flanks of the Aluto edifice. Along the Artu Jawe fault zone (Fig. 2.5) fumaroles continue both north and south of the fault scarp (Figs. 2.5, 2.7b) indicating that the fault continues beneath the young volcanic cover (Fig. 2.7a). Hydrothermal alteration is also found at the base of the remnant caldera rim (Fig. 2.4) where several zones of fumaroles are seen emanating from fractures in altered lava (Fig. 2.3c and Bobesea, Table 2.1). The lines of fumaroles (identified in Fig. 2.3c) follow a NW-SE trend, identical to the orientation of the caldera rim and thus are linked to a buried ring fault.

Not all hydrothermal features on Aluto can be correlated with mapped structures. For example, on the west flank of Aluto fumaroles occur over a large area at Hulo and Auto (HL and AT, respectively in Fig. 2.4) and while these may link to structures and aligned volcanic vents north-west of the edifice, as shown in Fig. 2.4, evidence for a tectonic control at the surface is absent (Fig. 2.6b). On the southern flank of Aluto fumaroles at Kore and Gebiba (K and GB, Fig. 2.4) also show no clear structural association.

Area	Easting (m)	Northing (m)	Max temperature at 5-15cm	Max CO_2 flux (g m^{-2} d^{-1})	Structural association	Notes
Hulo (HL)	469800	860300	95†	ND	West Aluto fault	Large area of hydrothermal alteration with several groups of fumarole vents
Auto (AT)	470000	861300	94†	ND	West Aluto fault	Fumaroles located south-east of LA-2 on west flank of Aluto (Fig.2d), significant alteration of pumice to red/orange clays
Adonshe (AD)	472700	861900	85†	ND	Continuation of NE-SW fault?	Altered pumiceous ground through which fumaroles are issued
Humo (HM)	474000	860900	77†	ND	Unknown	Low temperature fumarole outlets running along gorge
Worbota (WB)	474300	863200	85*	2300	NE-SW fault or ring fault?	Steaming ground found in small crater and patches of orange/brown altered ground within 1km
North Bay (NB)	475000	852300	67†	ND	Outflow along water table	Several springs located along the northern shore of Lake Langano
Oitu Artu (OA)	475100	856200	94†	ND	Continuation of Artu Jawe fault zone?	Fumaroles exposed in gorge running north-south, fumaroles emanate from rhyolite lava units at base of gorge, surrounding pumices is altered to yellow/red clay, fumaroles have H_2S smell
Edo Laki (EL)	475100	850400	95†	ND	Unknown	Hot springs and mud pools along the shore of the island
Artu Jawe (AJ)	476500	860200	95*	10000 - 40000	Artu Jawe fault zone	Large groups of fumaroles located east of power plant, steam has H_2S smell, alteration of rhyolite and pumice surface lithologies
Finkilo (FK)	477100	859200	85†	ND	Artu Jawe fault zone	Groups of fumaroles emanating from rhyolitic lava units in north-south running gorge, H_2S smell, alteration of surface rocks to red-brown clays
Kore (K)	477800	857700	95†	ND	Hidden NNE-SSW trending fault or lateral outflow from Artu Jawe fault zone?	Fumaroles aligned in north-south running gorge, issued through rhyolite lava
Gebiba (GB)	478500	855900	95*	5400	Hidden NNE-SSW trending fault or lateral outflow from Artu Jawe fault zone?	Fumaroles at base of gorge running NNE, H_2S smell, alteration of pumice to red/grey clays
Bobesea (BOB)	480100	861000	93*	1850	Ring fault	Fumarole vents run in several NW-SE trending ridges (parallel to remnant caldera rim), large area of hydrothermal alteration where pumices are altered to red/grey clays

Table 2.1: *Summary of the main hydrothermal features on the Aluto volcanic complex, locations shown in Fig. 2.4. Localities given in UTM coordinates (UTM Zone 37N, WGS84 datum). Ground temperatures measurements were made in the field with thermocouple either during this study, shown as *, or by Kebede et al. (1985), shown as †. ND: no data.*

2.3.5 CO_2 degassing

CO_2 flux values measured on Aluto span several orders of magnitude, varying between 0.5 and 40,000 g m^{-2} d^{-1}. Background CO_2 flux measurements at locations 10-20 km away from Aluto ranged from 0.5 g m^{-2} d^{-1} in rocky organic-poor soils to 6 g m^{-2} d^{-1} in darker organic-rich soils (vegetated areas with more abundant leaf litter). A flux of 6 g m^{-2} d^{-1} was taken as the upper limit for a purely biogenic background CO_2 flux in the study area. These fluxes are low when compared to values that characterize soils in less arid climates, 10-30 g m^{-2} d^{-1} (Mielnick & Dugas, 2000; Rey et al., 2002; Cardellini et al., 2003).

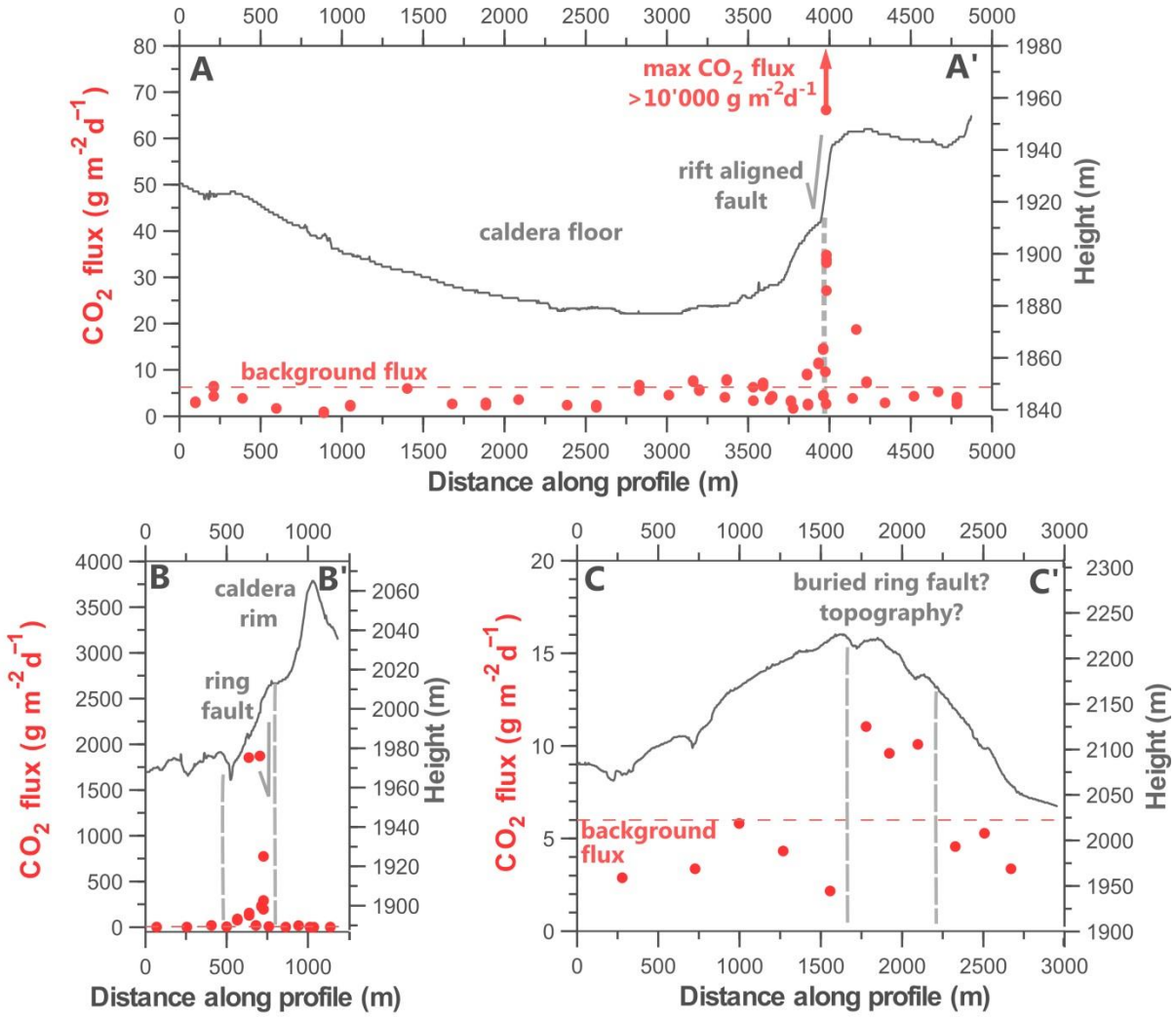

Figure 2.9: *CO_2 degassing transects across the major structural features (Fig. 2.8) including: the Artu Jawe fault zone, A-A'; the remnant caldera rim, B-B' and the southern rim of the complex, C-C'. The red points give the observed CO_2 flux (left axis) and the grey line gives the topography (right axis). Note differences in vertical scales between plots.*

2.3.5.1 Transects across major structures

CO_2 degassing transects across the main structural features (A-A', B-B' and C-C', shown in Fig. 2.5a) correspond with lidar-derived topography and soil CO_2 flux profiles shown in Fig. 2.9. A-A', is a profile along the centre of the volcanic complex across the caldera floor and intersecting the Artu Jawe fault zone to the east. The topography reveals the smoothly downward curving caldera floor and the well-defined ~50 m offset across the fault zone. CO_2 flux through the caldera floor is below or very close to the background biogenic flux value. The absence of significant degassing through the caldera floor is in line with remote sensing observations that did not indicate any clear fault offsets (Section 2.3.2). Adjacent to and within ±500 m of the fault scarp the CO_2 flux is significantly above the background levels. The scale in Fig. 2.9 A-A' was chosen to illustrate the small variations in the low fluxes and in fact maximum values measured along the fault zone were >10,000 g m^{-2} d^{-1} (N.B. a higher resolution transect showing the full range of flux values is given in Section 2.3.5.2, Fig. 2.11 W-W').

Profile B-B' transects the remnant caldera rim structure (Section 2.3.1). The CO_2 flux shows greatest values (up to 1850 g m^{-2} d^{-1}) at the base of the caldera rim with lower values (2-7 g m^{-2} d^{-1}) to the south-west and on the caldera rim itself. The area of anomalous degassing is defined by several sets of fumaroles (Section 2.3.4), CO_2 flux values are greatest on fumaroles (500-1850 g m^{-2} d^{-1}) and lower in cohesive soils between the open fractures (15-240 g m^{-2} d^{-1}, Fig. 2.3c).

C-C', profiles the topographic high on the southern rim of the complex. CO_2 flux values increase from low background values (<6 g m^{-2} d^{-1}) up to 11 g m^{-2} d^{-1} at the peak and immediately south of the rim. Elevated CO_2 flux values coincide with the hypothesised location of the ring fault (Section 2.3.1). However, the maximum values encountered at the peak were significantly lower than B-B' and no evident structural feature was exposed at the surface.

2.3.5.2 The Artu Jawe fault zone

In Fig. 2.9 A-A' there are considerable CO_2 flux variations encountered in the fault zone. To better constrain these variations along the fault, we undertook a high-resolution (30-m) sampling survey. Fig. 2.10 provides: topography; surface geology and soil CO_2 flux results for the survey area (outlined in Fig. 2.5b). The shaded relief DEM (Fig. 2.10a) identifies the main ~50 m high fault scarp (Section 2.3.2, Fig. 2.3a) and its projected (dashed) continuation north where it is obscured by pumice dome deposits (identified also in Figs. 2.5b, 2.7). To the west of the main fault scarp there are a number of smaller breaks in topography (10-20 m high) marked by white dashed lines in Fig. 2.10a.

Fig. 2.10b shows the surface geology map. The area is largely covered in young tephra (pumice fall and pyroclastic deposits) sourced either from the pumice dome to the north of the study area (Figs. 2.5b, 2.7) or from eruptive vents on the southern rim of the caldera complex. At the base of these slopes, tephra have been reworked by fluvial processes and are represented by fine-grained alluvium and gravel deposits. A porphyritic obsidian flow is encountered on the west of the grid. The obsidian flow is likely sourced from a vent at the base of the cliff, however recent avalanching of the volcaniclastic deposits in the cliff has obscured the exact position of the vent.

The soil CO_2 flux map (Fig. 2.10c) shows that the flux varies by several orders of magnitude across the survey area, while a log probability plot (Fig. 2.10d) shows a bimodal distribution confirming the existence of two distinct CO_2 sources (i.e., background-biogenic and volcanic-hydrothermal; Chiodini et al., 1998) that contribute to the degassing. The highest CO_2 flux values are found close to fumarole vents suggesting that in those areas CO_2 travels mostly with hydrothermal steam. From the mean of the simulations the total diffuse CO_2 emission for the 800,000 m^2 grid (Fig. 2.10c) is calculated at 62 ± 12 t d^{-1}.

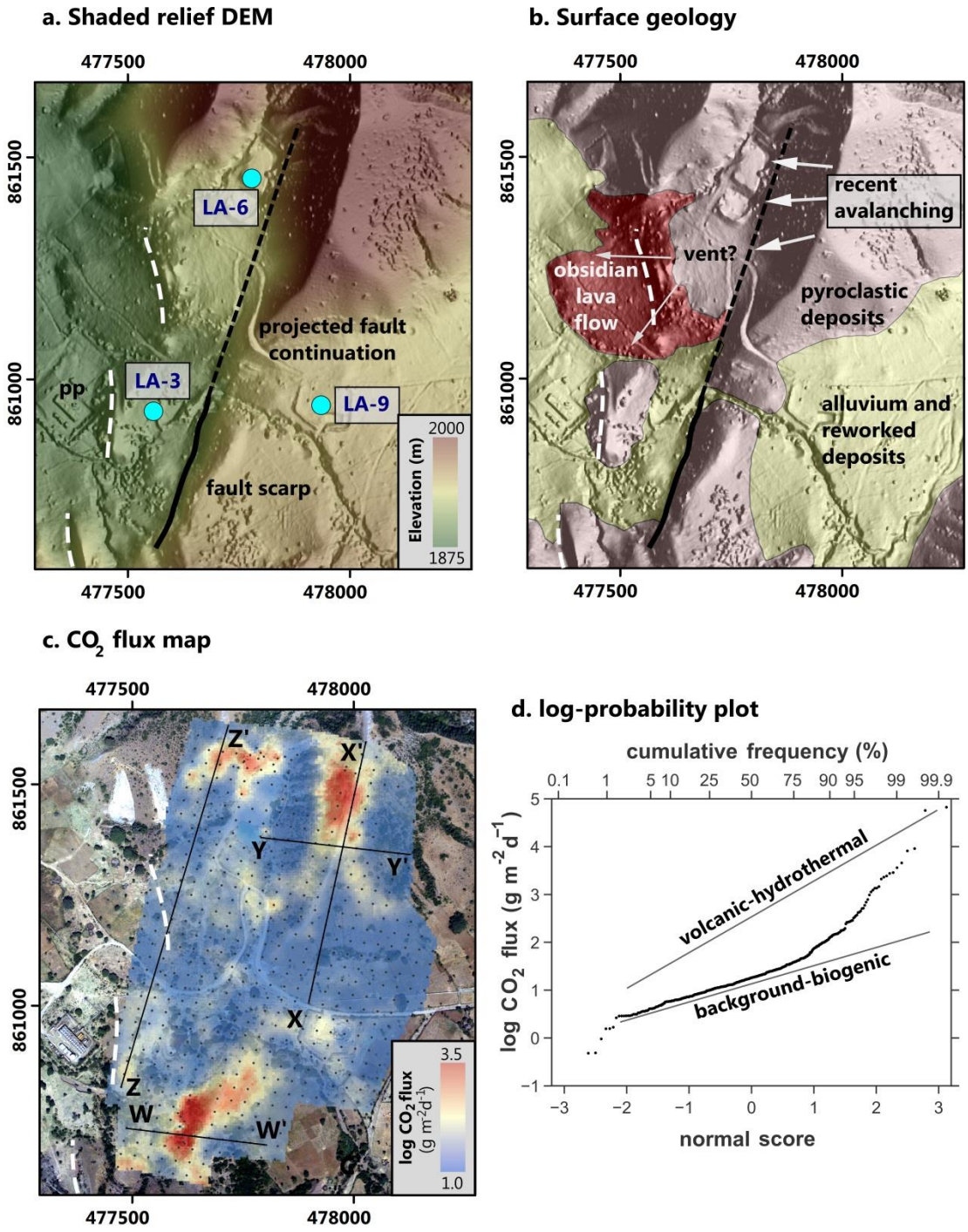

Figure 2.10: *Focused study of degassing along the Artu Jawe fault zone.* ***a)*** *Shaded relief DEM showing the Artu Jawe fault scarp (black) and its projected continuation north (dashed), less pronounced breaks in topography (10-20 m high) west of the main fault scarp are marked by white dashed lines (these are also visible in in Fig. 2.7). Blue points identify the location of the productive geothermal wells (LA-3 and LA-6), as well as the site of the new well (LA-9). The Aluto-Langano geothermal power plant (pp) is located on the west of the image.* ***b)*** *Surface geology map constructed from the observations of the exposure noted at each grid locality and further discriminated using the aerial photos. Surface geology consists of: pyroclastic deposits (pink); alluvium (yellow) and obsidian lava (red).* ***c)*** *CO_2 flux map derived using the sGs approach. Grey points represent a discrete flux measurement. The lines (W, X, Y and Z) link to transects given in Fig. 2.11.* ***d)*** *Probability plot of soil CO_2 flux values from the survey grid identifying background and volcanic-hydrothermal populations in the distribution (for detailed explanation of application of probability plots to CO_2 flux data sets see Chiodini et al., 1998).*

Transect lines shown in Fig. 2.10c link to Fig. 2.11, which show the topography and flux measurements along the profile line. In W-W', peak flux values occur at the base of the main cliff, associated with a fault plane. Profiles X-X' and Y-Y' (Fig.11) cross the ridge of pyroclastic deposits east of the fault and also show a relationship between CO_2 flux and topography, with peak values in CO_2 flux close to but slightly displaced from the absolute topographic high. Profile Z-Z' crosses several lithologies on the west of the grid, CO_2 flux values are on average lower on the obsidian lava flow deposits compared to the tephra deposits to the north and south.

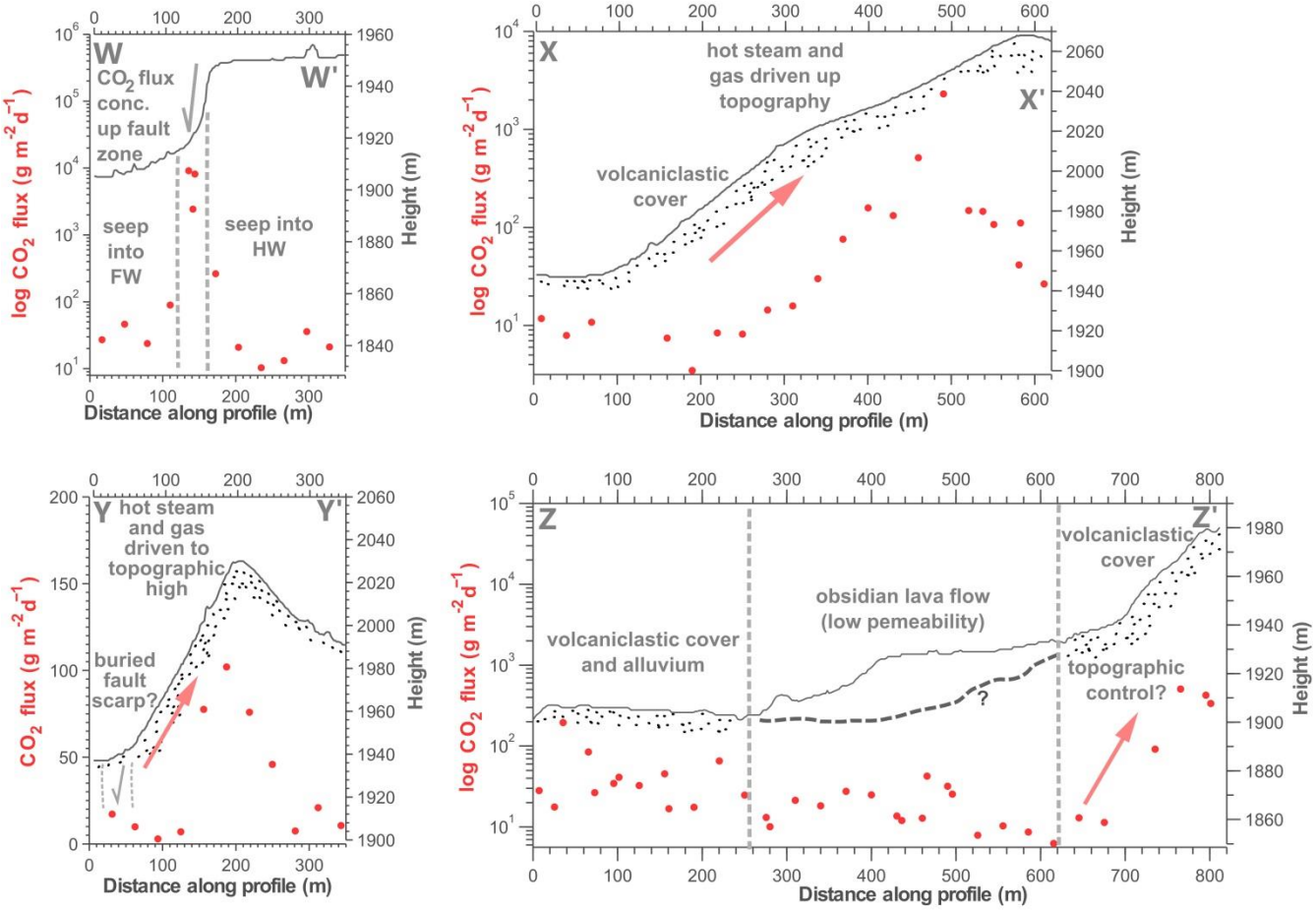

Figure 2.11: *CO_2 degassing transects across the Artu Jawe fault zone that link to the lines (W, X, Y and Z) shown in Fig.10c. Abbreviations, HW: hanging wall, FW: footwall. The red points give the observed CO_2 flux (left axis) and the grey line gives the topography (right axis). Note differences in vertical scales between plots.*

2.4. Discussion

2.4.1 Tectonic features dissecting the volcano

The results of this study, combined with prior mapping and geothermal well data (Dakin & Gibson, 1971; Di Paola, 1972; Kebede et al., 1985; Gebregzabher, 1986; Valori et al., 1992; Gizaw, 1993; Ginaelli & Teklemariam, 1993), show that the Aluto volcanic complex has been dissected by normal faults related to the regional extensional tectonics, which have in turn influenced the distribution of volcanic products. The aligned vent trains that cross Aluto reflect magma pathways controlled by faults. Young vents and craters on and off the main edifice show a prevailing alignment to the regional NNE-SSW strike of the Wonji faults (Fig. 2.4, Fig. 2.8), although there is field evidence that minor NE-SW oriented structures may also exist (Fig. 2.6c).

Physical evidence for the link between faults and volcanic activity is particularly clear along the Artu Jawe fault zone, where magma has erupted along the fault, building an elongate pumice dome (Fig. 2.5b, Fig. 2.7). The Artu Jawe fault zone remains a high permeability pathway through which steam (Fig. 2.4) and CO_2 (Fig. 2.10c) ascend to the surface as evidenced by the zones of fumarolic alteration and peaks in CO_2 flux along the fault structure (Fig. 2.7, Fig. 2.9 A-A'). Our work shows that hydrothermal mapping (Fig. 2.4, Fig. 2.7) and CO_2 soil-gas surveys (Fig.10c) can be used to identify high permeability zones, revealing the locations of hidden fault structures when multiple observational data sets are considered together (e.g., Fig. 2.7, Fig. 2.10).

Understanding the initiation and growth of these faults is critical to address the development of the Aluto volcanic complex. At present the best evidence for major fault zones on Aluto, and the only constraints on their development are provided by the deep wells. Of particular significance is a Pleistocene lacustrine horizon that can be correlated between wells (Fig. 2.2b, Gianelli & Teklemariam, 1993; Gizaw, 1993) and shows a stepped west to east thinning suggestive of faulting. This unit lies beneath the volcanic products of Aluto (Fig. 2.2b), implying that

significant faulting preceded surface silicic volcanism, and hence these pre-existing faults may have controlled magmatic processes throughout the growth of Aluto. Recent investigations of the Soddo region in the southern MER by Corti et al. (2013b) find a similar relationship, with both basaltic and rhyolitic volcanic centres following closely pre-existing border faults.

2.4.2 The Aluto caldera

Several previous studies have suggested that Aluto has undergone a caldera forming event (Dakin & Gibson, 1971; Le Turdu et al., 1999), and our observations help to confirm this. Taking together the presence of a remnant caldera rim (Figs. 2.2a, 2.4, 2.5), the occurrence of eruptive vents on an elliptical (ring) structure (Figs. 2.4, 2.5) and the correspondence of this to zones of hydrothermal alteration (Fig. 2.4) and local peaks in CO_2 degassing (Fig. 2.9, B-B' and C-C'), we propose that an underlying ring fracture system that matches the mapped caldera rim remnant can explain these observations.

A major challenge in defining this structure is that the exposure of the remnant caldera rim is limited to the north-east of the complex (only covering ~8% of the ellipse, Fig. 2.4). We assume that the rest of the structure has been covered by post-caldera volcanic deposits, or eroded. This is typical of peralkaline volcanic edifices which undergo repeated phases of caldera collapse and caldera-filling volcanism (Cole et al., 2005), that overspill the caldera rim and mask its surface expression (Mahood, 1984). The size (~8 km x ~5 km) and shape of the proposed Aluto ring structure (Figs. 2.4, 2.5b) is similar to other peralkaline complexes in the MER (Cole, 1969; Mohr, 1980; Acocella et al., 2003; Rampey et al., 2010), and within the upper range of other peralkaline calderas worldwide (Mahood, 1984; Cole et al., 2005). The caldera wall on Aluto (> 50-60 m in height) is comparable to other peralkaline calderas where subsidence is on the order of a few hundred metres (Mahood, 1984).

The elliptical caldera form is typical of continental rift volcanoes worldwide (e.g., Wilson et al., 1984; Acocella et al., 2003; Bosworth et al., 2003; Casey et al., 2006; Geyer & Marti, 2008). Elliptical calderas may be produced by a number of different mechanisms (Holohan et al., 2005), including: 1) collapse of an elliptical magma reservoir; 2) nesting: where multiple collapse structures overlap and give rise to an elongate geometry; 3) shallow crustal processes: where asymmetric collapse, or distortion of caldera faults leads to an asymmetric caldera above a circular magma chamber and 4) post-caldera modification: where a circular caldera is distorted by erosion or regional deformation. Ultimately, the infilling of the Aluto caldera has left little information concerning the original collapse structure, and the nature of the collapse event. In particular, it is unclear whether the caldera collapse comprised one or multiple events, to create a nested structure (as is typical for peralkaline volcanic complexes, Mahood and Hildreth, 1983; Mahood, 1984; Rampey et al., 2010). It is also not possible to infer whether collapse was asymmetric or whether subsidence was accommodated by existing tectonic faults. Assuming collapse took place at 155 ka, the only age constraint for the major ignimbrite deposits of Aluto (Electroconsult, 1986), and assuming current extension rates of 5mm yr^{-1} (Bendick et al., 2006; Stamps et al., 2008) then this would generate <1km of extension since caldera formation (i.e., not sufficient to explain all of the east-west elongation).

Several recent publications have emphasised the role of elongate magma chamber collapse in generating elliptical calderas in the EARS (e.g., Bosworth et al., 2003; Acocella et al., 2003). The genesis of elongate magma chambers in a continental rift currently revolves around two distinct models, one related to the regional extensional stress field causing differential spalling of the walls of the magma reservoir (Bosworth et al., 2003), the other related to pre-existing structural weaknesses, such as pre-rift faults, facilitating preferential magma chamber development (Acocella et al., 2003). To explain caldera elongation using the pre-existing structures model requires a detailed understanding of the evolution and orientation of regional fault patterns. For

example, Acocella et al. (2003) identified a number of east-west oriented pre-rift tectonic structures on the flanks of the MER and invoked these to explain elongate calderas at Fentale, Kone and Gedemsa. We investigated fault maps of the MER presented by Acocella et al. (2003), Abebe et al. (2007) and Agositini et al. (2011) as well as our own satellite imagery and could not highlight any clear east-west structures on the rift plateau adjacent to Aluto. On the other hand, the east-west elongation of the Aluto caldera is almost orthogonal to the active Wonji faults of the CMER (Fig. 2.8a) and parallel to the Nubia-Somalia displacement vector (~N100°E, Bendick et al., 2006; Keir et al., 2006, Pizzi et al., 2006; Stamps et al., 2008). This observation is consistent with the idea that the regional stress field played a role in magma reservoir development at Aluto (c.f. Bosworth et al., 2003).

Compared to neighbouring MER volcanoes, Aluto has undergone considerable post-caldera volcanism. Shalla (Mohr et al., 1980), Gedemsa (Peccerillo et al., 2003) and Kone (Cole, 1969; Rampey et al., 2010) volcanoes have all undergone caldera forming eruptions however, post-caldera activity has been modest, building up small domes of pumice and obsidian (within the caldera and adjacent to the caldera ring fault). At Corbetti, two silicic cones (Chabbi and Urji) have built up within the caldera (Mohr, 1966; Di Paola, 1971). Chabbi, the larger and more voluminous of these, has built up on the east of the caldera floor and now completely covers the caldera wall on the eastern side of the complex (Di Paola, 1971). This may provide a possible analogue to Aluto, which has undergone widely distributed post-caldera volcanism along the ring fracture and thus only a small segment of the caldera wall is retained (Fig. 2.4).

2.4.3 Controls on CO_2 degassing and the hydrothermal system

2.4.3.1 Volcanic CO_2 degassing

At the edifice scale, both regional tectonic faults (such as the Artu Jawe fault zone, Fig. 2.9 A-A') and the volcanic ring fracture (Fig. 2.9 B-B') have a strong control on diffuse CO_2 emissions. The escarpment of the Artu Jawe fault zone (Fig. 2.11 W-W') shows that CO_2 gas is concentrated along the fault plane and that flux values remain high over a ~50 m wide high-permeability crushed zone across the fault. Across the southern rim of the complex we find elevated CO_2 fluxes spread over a ~500 m wide zone (Fig. 2.9 C-C'). Here, we infer that a ring fault is deeply buried beneath a thick pile of volcanic deposits. Without deep penetrating structures, connecting reservoir to surface, significant soil-flux degassing peaks (such as Fig. 2.9: A-A', B-B') are unlikely to be observed.

Substantial variations in the spatial pattern of CO_2 degassing are evident both parallel and transverse to the major structures when observed at scales <100 m (Fig. 2.10c). These are linked to permeability variations in the near surface (Schöpa et al., 2011; Pantaleo & Walter, 2013) potentially caused by changes in lithology or changes in the topography-induced stress field (that focuses the permeable pathways toward the morphological crests). A correlation between local topography and degassing flux (Fig. 2.11: X-X', Y-Y') in the pumice dome (Fig. 2.10). Our interpretation is that the pumice dome deposits have buried the Artu Jawe fault scarp (Section 2.3.2), and thus, steam and gas rising up along the fault plane enter the base of the dome and become focused towards the morphological ridge crest. A similar morphological control has been observed at Vesuvius, where CO_2 anomalies are concentrated in the inner slopes of the crater rim (Frondini et al., 2004). The key difference on Aluto is that CO_2 gas and steam are fed into the base of the volcanic pile from a tectonic fault rather than a volcanic conduit.

Several previous authors (e.g., Peltier et al., 2012; Pantaleo & Walter, 2013) have studied the influence of surface lithology and soil texture on permeability, and our data set permits a qualitative assessment for Aluto. Profile Z-Z' (Fig. 2.11) crosses several contrasting lithologies west of the Artu Jawe fault scarp, CO_2 fluxes are on average lower on the obsidian lava flow deposits compared to pumiceous deposits north and south. This could be evidence that the lower permeability obsidian lava flow restricts or deflects gas flux relative to the more permeable, poorly consolidated clastic deposits.

The total CO_2 flux value of 62 t d^{-1} calculated along the 0.8 km^2 section of the Artu Jawe fault zone represents both the volcanic-hydrothermal and biogenic CO_2 flux. Assuming that a mean biogenic flux of 6 g m^{-2} d^{-1} (Section 2.3.5) is constant over the survey area then subtracting this contribution from the total CO_2 release would give the total volcanic-hydrothermal CO_2 emission as 57 t d^{-1}. This is comparable to other sites of volcanic CO_2 degassing worldwide (Table 2.2), and when standardised to a flux per unit area (i.e. 71 t d^{-1} km^{-2}) it is similar to geothermal sites in other rift zones such as Reykjanes geothermal area, Iceland (Fridriksson et al., 2006) and Taupo Volcanic Zone, New Zealand (Werner & Cardellini, 2006). Given that the total area of hydrothermal alteration and degassing features on Aluto (Fig. 2.4) is 5-10 times larger than the area covered by the CO_2 flux survey (Fig.10c) we may then expect total CO_2 emission from Aluto to be on the order of 250-500 t d^{-1}. This magnitude of diffuse CO_2 release is comparable to a number of other volcanoes that have either undergone Holocene eruptions and/or show signs of unrest, e.g. Pululahua caldera (Ecuador), Vesuvius (Italy), Teide (Canary Islands) and Rotorua (New Zealand), Table 2.2. The estimated CO_2 flux for Aluto is also comparable to mean volcanic plume CO_2 fluxes measured at active volcanoes such as Merapi (Indonesia), Vulcano (Italy), Sierra Negra (Ecuador) and Villarrica (Chile), see Burton et al. (2013) and references therein. Degassing measurements at continental rift zone volcanoes are sparse, especially soil CO_2 surveys (Koepenick et al., 1996) and no such surveys have been undertaken at the silicic caldera-

forming volcanoes of the EARS, like Aluto, which constitute an important class of rift volcanism. This highlights the significance of the CO_2 degassing surveys presented here and future surveys of the EARS volcanoes to constrain carbon and other volatile element fluxes are to be encouraged.

Study area	CO_2 flux ($t\ d^{-1}$)	Area (km^2)	CO_2 flux density ($t\ km^{-2}\ d^{-1}$)	Reference
Cuicocha caldera, Ecuador	106	13.3	8	Padròn et al. (2008)
Pululahua caldera, Ecuador	270	27.6	10	Padròn et al. (2008)
Pantelleria island, Italy	989	84	12	Favara et al. (2001)
Oldoinyo Lengai, Tanzania [a]	100	3.14	32	Koepenick et al. (1996)
Satsuma-Iwojma volcano, Japan	80	2.5	32	Shimoike et al. (2002)
Iwojima volcano, Japan	760	22	35	Notsu et al. (2005)
Vesuvius, Italy	193.8	5.5	35	Frondini et al. (2004)
Mt. Epomeo, Italy (western flank)	32.6	0.86	38	Chiodini et al. (2004b)
Vulcano island, Italy (western and southern slopes)	75	1.9	39	Chiodini et al. (1998)
Nisyros caldera, Greece	84	2	42	Cardellini et al. (2003)
Yanbajain geothermal field, China	138	3.2	43	Chiodini et al. (1998)
Reykjanes geothermal area, Iceland	13.5	0.22	61	Fridriksson et al. (2006)
Rotorua geothermal system, Taupo Volcanic Zone, New Zealand	620	8.9	70	Werner and Cardellini (2006)
Aluto, Ethiopia (Artu Jawe fault zone)	57	0.8	71	*this study*
Miyakejima volcano , Japan (summit)	100–150	0.6	167	Hernández et al. (2001a)
Furnas volcano, São Miguel Island, Azores	968	5.2	186	Viveiros et al. (2010)
Hakkoda volcanic area, Japan (localised flank area)	127	0.58	219	Hernández et al. (2003)
Methana volcanic system, Greece	2.59	0.01	259	D'Alessandro et al. (2008)
Hot Spring Basin, Yellowstone	60	0.16	387	Werner et al. (2008)
Mud volcano, Yellowstone	1730	3.5	494	Werner et al. (2000)
Liu-Huang-Ku hydrothermal area, Taiwan (phreatic crater)	22.4	0.03	659	Lan et al. (2007)
Teide volcano, Spain (summit area)	380	0.53	717	Hernández et al. (1998)
Mammoth Mountain, Horseshoe Lake (flank area)	104.3	0.13	802	Cardellini et al. (2003)
Nea Kameni, Santorini, Greece (summit area) [b]	21 - 38	0.02	1050 - 1900	Parks et al. (2013)
Solfatara volcano, Italy	1500	1	1500	Chiodini et al. (2001)
Cerro Negro volcano, Nicaragua	2800	0.58	4828	Salazar et al. (2001)

Table 2.2: *Compilation of diffuse CO_2 emissions from selected volcanic degassing areas of the world (after Viveiros et al., 2010; Burton et al., 2013)*

[a] Measurements assume CO_2 emission restricted to the summit and flank area with diameter of 2 km (Koepenick et al., 1996).

[b] Measurements made across a period of volcanic unrest (Parks et al., 2013)

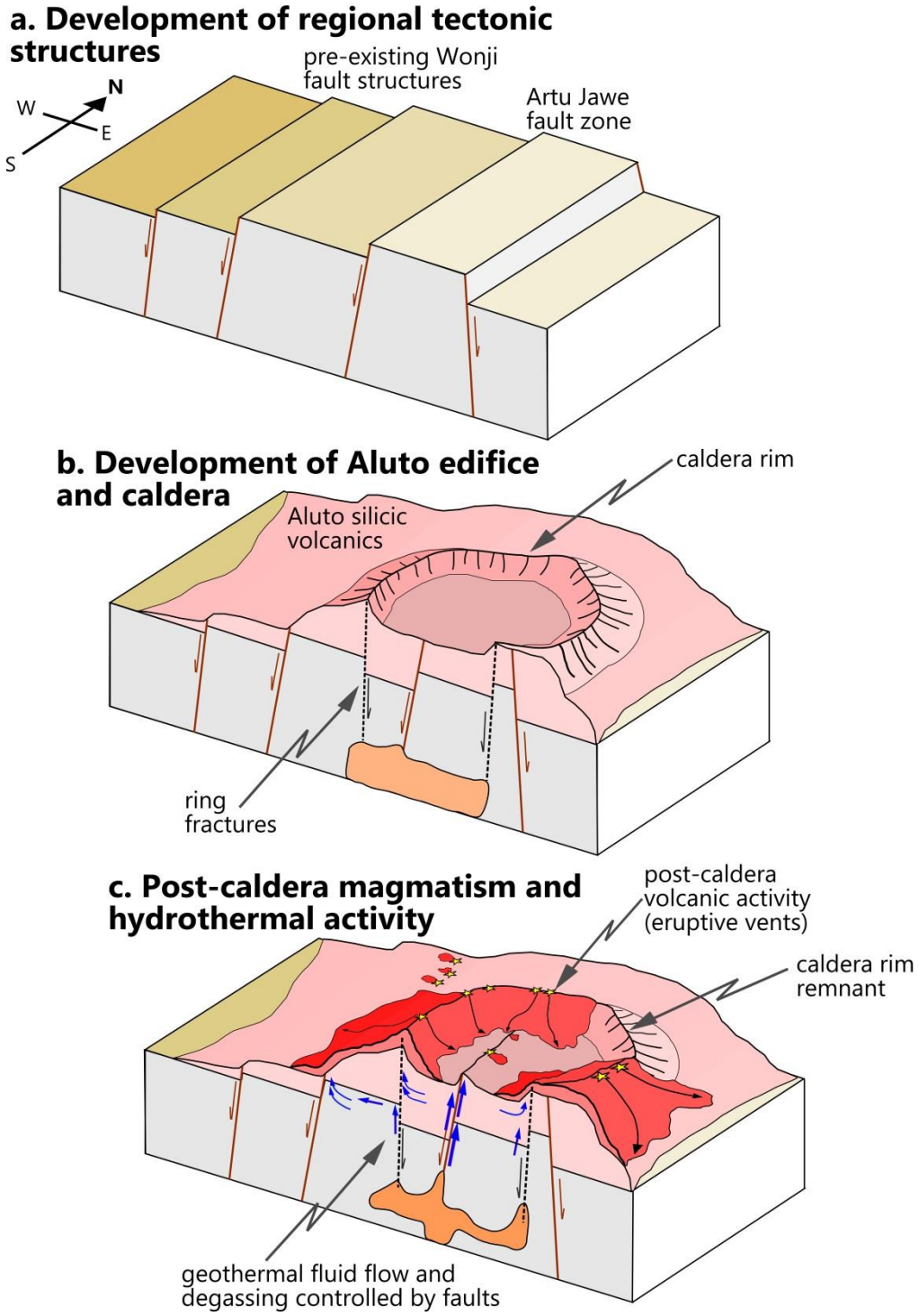

Figure 2.12: *Conceptual model summarising the evolution of the major structures on Aluto and their controls on surface volcanism, geothermal fluids and degassing.* ***a)*** *Regional tectonic structures aligned with the Wonji faults develop prior to surface volcanism, creating fault bounded blocks over which abrupt lateral thickness variations in the deep well lacustrine sediments occur (Fig. 2.2b).* ***b)*** *Surface volcanism at Aluto build up a silicic shield which then undergoes caldera collapse. The dynamics of caldera formation remain unclear as most of the structure has either been removed by erosion or buried by subsequent volcanic deposits.* ***c)*** *Post-caldera volcanic eruptions, as well as ongoing geothermal activity and degassing processes exploit the existing volcanic and tectonic fault network. While various fault structures provide high permeability zones for fluid flow (Fig. 2.9: B-B'), the Artu Jawe fault zone appears to represent the main pathway connecting the hydrothermal reservoir to the surface (Teklemariam et al., 1996)*

2.4.3.2 Hydrothermal system

Our observations of hydrothermal features on Aluto (Fig. 2.4) confirm that the mapped faults (Sections 2.3.1 and 2.3.2) provide key pathways for the upflow of geothermal fluids. A number of the fumarole sites do not align with these structures, which suggests that they are controlled by otherwise hidden fractures or are influenced by other subtle permeability parameters (e.g., topography or lithological controls, Schöpa et al., 2011). Hot springs located along the shore of Lake Langano (Fig. 2.4) likely mark the outflow of the hydrothermal fluids at the water table. This is supported by shallow temperature data from well LA-1 on the south flank of Aluto (Gizaw, 1993), and evidence of silicified beach sediments 100 m north of present springs that indicate these springs follow lake levels and hence are tied to the level of aquifer (Kebede et al., 1985). Despite the close proximity of Aluto to the lakes of Ziway, Langano and Abijta (Fig. 2.1) oxygen isotope measurements of geothermal fluids conducted by Darling et al. (1996) show that >90% of the water in the Aluto geothermal system is derived from rainfall from the rift shoulders with a minimal component (<10%) derived from lake waters. The geothermal fluids are of alkali-chloride-bicarbonate type, and display geochemical evidence for interaction with rhyolitic volcanic products (Gianelli & Teklemariam, 1993). This observation along with deep well temperature and stratigraphy data (Gizaw, 1993; Ginaelli & Teklemariam, 1993; Teklemariam et al., 1996) support the Tertiary ignimbrite deposit (Fig. 2.2b) as the reservoir for the geothermal field.

2.4.4 Conceptual model

A conceptual model is provided in Fig. 2.12 that captures both the evolution of the complex and the role the major structures have on controlling fluid pathways. While the timing of the initiation of the tectonic fault structures remains poorly constrained, the existing evidence from deep well lacustrine sequences (Fig. 2.2b, Gianelli & Teklemariam, 1993; Gizaw, 1993) suggests that prior to surface volcanism fault structures were active, leading to fault bounded blocks (Fig. 2.12a).

The Aluto volcanic complex developed before 155 ka (Electroconsult, 1986) building a substantial silicic volcanic shield on the faulted surface. The complex then underwent a large caldera-forming eruption developing a caldera rim structure (Figs. 2.4, 2.5) and ring fault (Fig. 2.12b). Following collapse significant post-caldera volcanism has taken place at Aluto (Fig. 2.12c) and the caldera structure and regional tectonic faults that dissect the volcano have provided magma pathways to the surface, resulting in the development of aligned volcanic domes in NNE-SSW orientations (close to the strike of the Wonji faults, Fig. 2.8) and to a prevalence of recent volcanic activity around the rim of the volcano (Fig. 2.5b). Latterly a geothermal field has developed on Aluto (Fig.12c). Fluids are capped in an ignimbrite reservoir beneath the complex (Ginaelli & Teklemariam, 1993), and the Artu Jawe fault zone provides the major pathway where hydrothermal fluids and gases ascend to the surface (Fig. 2.9: A-A', Fig. 2.10c).

Recent InSAR evidence (Biggs et al., 2011) has shown that Aluto has undergone a number of ground deformation events over the last decade. No evidence exists to suggest that this activity correlates with any changes in industrial geothermal power development on the complex, and so at present we assume deformation is of natural magmatic or hydrothermal origin. Comparing the InSAR deformation pattern identified by Biggs et al. (2011) to our structural interpretation, we note that: 1) deformation shows an east-west elongation; 2) the deformation is approximately centred on the caldera structure centre, and 3) deformation extends beyond the proposed ring fault and mapped caldera rim remnant (Figs. 2.4, 2.5), and does not show elongation along the mapped tectonic fault structures. While the magmatic and/or hydrothermal processes driving ground deformation events on Aluto remain uncertain, an important conclusion from this study is that tectonic/volcanic structures do not appear to influence these deformation events. For example, tectonically aligned faults on Aluto do not play a role in storing fluids as has been shown at other volcanic complexes (e.g., Yellowstone, Vasco et al., 2007, where elongate deformation patterns align with mapped faults). In addition, the ring structure does not constrain the area over which

deformation occurs. If deformation is of hydrothermal origin this may be explained by fluid expansion/contraction in a reservoir unit which extends beyond the confines of a ring structure (as shown in Fig. 2.2b). Alternatively if the deformation is magmatic then it suggests the source may be a deep intrusion unaffected by these structures. We conclude that the mapped faults simply act as pathways facilitating shallow fluid release.

The results of this study have relevance to understanding the geothermal resources and volcanic hazards at active rift volcanoes. Firstly, regarding the geothermal field, it is clear that the Aluto complex is heavily fractured by both tectonic and volcanic structures. Of the eight exploration wells initially drilled on Aluto only two, those on the Artu Jawe fault zone, continue to be productive. This underscores the importance of undertaking detailed geophysical surveys and structural mapping to constrain hydrothermal flow along the major structures prior to drilling. For similar structurally complex rift volcanoes that are also targets of future geothermal exploration (e.g., Corbetti, Fentale and Dofen in the MER) it is critical to understand the key structures and their impact on subsurface fluid flow in order to maximise productivity of the field. Although these structures introduce significant complexities, fractured geothermal fields may also present new opportunities for exploitation, for example, Curewitz & Karson (1997) show that the intersection of faults may provide efficient conduits to concentrate hydrothermal upflow. On Aluto the intersection between the ring fault and Artu Jawe fault zone might therefore provide a suitable target for future geothermal exploration.

Whilst the size and frequency of past eruptive activity on Aluto is poorly constrained (Section 2.1.2) recent evidence from InSAR (Biggs et al., 2011) suggests that the complex is still restless. A major result of this study is that a significant amount of recent volcanism on Aluto exploits pre-existing structures. Recent volcanism at other MER complexes such as Kone (Rampey et al., 2010) and Corbetti (Mohr, 1966; Di Paola, 1971) as well as other silicic volcanic centres in the

southern MER (Corti et al., 2013b) also appear to exploit existing fault structures (Section 2.4.2). Future volcanic eruptions at Aluto, and elsewhere in the MER, are therefore likely to be facilitated by existing structures, and therefore detailed structural maps will provide an invaluable tool to assess future volcanic hazards alongside conventional geological mapping and geochronology.

2.5. Conclusions

A combination of high-resolution airborne remote sensing, field mapping and soil CO_2 degassing surveys provide new insights into how pre-existing volcanic and tectonic structures facilitate active volcanic processes in the Main Ethiopian Rift. The main outcomes of this study are:

1. Digital mapping of Aluto volcano reveals evidence for various structures on the complex. The two major structures are: the Artu Jawe fault, a NNE-SSW tectonically-aligned ~50 m high fault scarp, and a 2.5 km long caldera rim remnant which has been deeply eroded and otherwise obscured by the young post-caldera volcanic products.

2. These structures provide high permeability zones that have facilitated magma ascent and recent volcanism on Aluto leading to vent alignments in an overall NNE-SSW orientation as well as a prevalence of vents on elliptical ring distribution pattern. These structures have facilitated past volcanic eruptions and remain open at present controlling geothermal upwelling and volcanic degassing.

3. CO_2 degassing surveys conducted along the major fault zone reveal that while these structures control the ascent of gas from the deep reservoir near surface permeability complexities, linked to lithological variations and changes in the volcanic morphology, play an important role in determining the final surface expression of degassing.

4. Overall these different observations of how lava, steam and gas reach the surface are complementary and when integrated provide a strong case for the overarching structural controls on volcanic fluid pathways.

Chapter 3

New constraints on causes of episodic unrest

A version of this chapter is in preparation for submission to a journal as: Hutchison et al. Episodic ground deformation at Aluto volcano, Ethiopia: new constraints from InSAR and soil-gas chemistry. Authors as follows:

William Hutchison[1], Juliet Biggs[2], Tamsin A. Mather[1], David M. Pyle[1] Elias Lewi[3], Gezahegn Yirgu[4], Stefano Caliro[5], Giovanni Chiodini[5] and Tobias Fischer[6]

1. COMET, Department of Earth Sciences, University of Oxford, South Parks Road, Oxford OX1 3AN, UK
2. COMET, School of Earth Sciences, University of Bristol, Wills Memorial Building, Queens Road, Bristol BS8 1RJ, UK
3. IGSSA, Addis Ababa University, PO Box 1176, Addis Ababa, Ethiopia
4. School of Earth Sciences, Addis Ababa University, P.O. Box 1176, Addis Ababa, Ethiopia
5. Istituto Nazionale di Geofisica e Vulcanologia (INGV), Osservatorio Vesuviano, Via Diocleziano 328, Napoli, Italy
6. Department of Earth and Planetary Sciences, MSC03 2040, 1 University of New Mexico, New Mexico 87131-0001, USA

Abstract

Ethiopia hosts a number of young silicic volcanoes that hold significant untapped geothermal resources. However, a number of these complexes are also undergoing episodic ground deformation, and this raises a number of concerns for both local populations and geothermal developers hoping to safely exploit the resources. In this study we target the Aluto volcanic complex in the Main Ethiopian Rift, and combine geodetic and degassing observations to shed light on magmatic-hydrothermal processes and causes of unrest. We process multiple tracks of Interferometric Synthetic Aperture Radar (InSAR) data and use these to investigate the temporal and spatial characteristics of a deformation pulse that took place at Aluto between 2008 and 2010. All SAR data sets reveal ~10 cm of inflation, and Envisat Wide Swath Mode data, which provide the greatest number of acquisitions across the uplift period, are consistent with a two-step accelerating trend. In February 2014 diffuse degassing sites along a major fault zone of Aluto were sampled for bulk gas chemistry and CO_2–$\delta^{13}C$ analysis. We found that while spatially separated fumaroles show distinct CO_2–$\delta^{13}C$ values that can vary on short-timescales, the highest CO_2 flux sites clearly indicate a magmatic carbon contribution ($\delta^{13}C$ of –4.2 to –4.5 ‰). This provides compelling evidence that the magmatic and hydrothermal reservoirs of the complex are physically connected. We consider the evidence from degassing and deformation together, and suggest that a coupled magmatic-hydrothermal system can explain the uplift-subsidence signals at Aluto. We suggest episodic uplift is caused by magmatic intrusion and/or fluid injection in the cap of a magmatic reservoir at ~ 5 km, and that subsequent deflation is related to magmatic degassing and/or cooling of the hydrothermal reservoir. We posit that monitoring changes in gas flux and composition along the major fault zone, which acts as an important conduit for fluid upflow from the geothermal reservoir, will be central to unravelling how the magmatic and hydrothermal systems interact during future unrest events at Aluto.

3.1. Introduction

Young magmatic systems in active rifts offer ideal targets for geothermal exploration. Firstly, they host shallow magma reservoirs at depths of 5–10 km (e.g., Biggs et al., 2009, 2011; Ebinger et al., 2010; Rowland et al., 2010); secondly, rift architecture causes internal drainage and groundwater flow from the elevated rift margins towards axial volcanic centres (e.g., Darling et al., 1996); and finally, rift-related faulting can help concentrate fluid flow along major structural features (Giordano et al., 2013; Egger et al., 2014; Hutchison et al., 2015). In volcanically active rift zones, such as Reykjanes (Iceland) and Taupo (New Zealand), substantial progress has been made at exploiting geothermal resources and delivering power to national grids. In Iceland for example, geothermal is now a major contributor towards the country's total electricity production (25 %), and geothermal water is used to heat ~90 % of homes (National Energy Authority of Iceland, 2015). By contrast, geothermal exploration in the East African Rift System (EARS) is still at an early stage but could offer significant economic benefits for developing nations that host these resources (e.g., Ethiopia, Kenya and Tanzania, Fridriksson, 2009; Kebede, 2012; Younger, 2014).

The key requirements for a geothermal field to exist are a fluid supply, a heat source and a structural trap (Anderson et al., 2000). For a conventional rift geothermal field, the heat source will be provided by an axial volcanic system with a shallow magma reservoir (Wohletz and Heiken, 1992). Fluids will be meteoric in origin, sourced either from rainfall on the rift margins or from rift lakes, and groundwater flow delivers this to the axial volcanoes (Darling et al., 1996). To make the field commercially viable it is essential that the geothermal reservoir is sealed from above, allowing hot pressurised fluid to accumulate at depths accessible to modern drilling (typically up to 3 km, Wohletz and Heiken, 1992). The conventional models assume that hot fluids circulating within the hydrothermal system significantly alter the volcanic and sedimentary rocks that typically dominate the surrounding strata, creating extensive layers of clay minerals

(e.g., smectite, kaolinite and chlorite, Johnston et al., 1992). Alteration will be particularly pervasive in fine-grained sediments and volcanoclastic material, and it is in these layers that lenses of clay minerals can form (commonly referred to as the clay cap). The clay lenses effectively seal and help pressurise the hydrothermal system (Johnston et al., 1992; Arnason et al., 2000; Cumming, 2009). Geothermal prospects are traditionally imaged using magnetotelluric (MT) surveys (e.g., Pellerin, 1996) which can identify clay cap layers (low resistivity) overlying the geothermal reservoir rock (high resistivity).

Ground deformation events have been documented at volcanoes across the globe (Sparks et al., 2012; Biggs et al., 2014; Pinel et al., 2014) and are a common feature of volcanoes that host large hydrothermal systems (Chiodini et al., 2003; Wicks et al., 2006). Campei Flegrei (Italy) is a well-documented example of an active caldera system that hosts a major geothermal field (e.g., Chiodini et al., 2001, 2008; Todesco et al., 2003; Caliro et al., 2007). Here it has been observed that slow long-term subsidence and uplift patterns (1984–2005, and 2005–present, respectively) are periodically interrupted by episodic uplift and accompanying microseismicity (Orsi et al., 1999; Troise et al., 2007; D'Auria et al., 2011). Regional ground deformation surveys conducted by Biggs et al. (2009, 2011) have recently identified similar patterns of episodic uplift at a number of important geothermal prospects in the EARS (e.g., Kenya: Paka, Longonot, Menegai and Suswa volcanoes, and Ethiopia: Aluto and Corbetti volcanoes, Fig. 3.1).

Understanding the causes of unrest at active magmatic-hydrothermal systems is of real importance to both local populations and geothermal developers, but establishing the physical mechanism is often ambiguous when based on ground deformation data alone. While InSAR and GPS observations can be used to infer the volumes and timescales of fluid movement in the subsurface (e.g., Biggs et al., 2010; Parks et al., 2012, 2015) they provide limited information on

the fluid composition and how the magmatic and hydrothermal systems interact (e.g., Gottsmann and Battaglia, 2008).

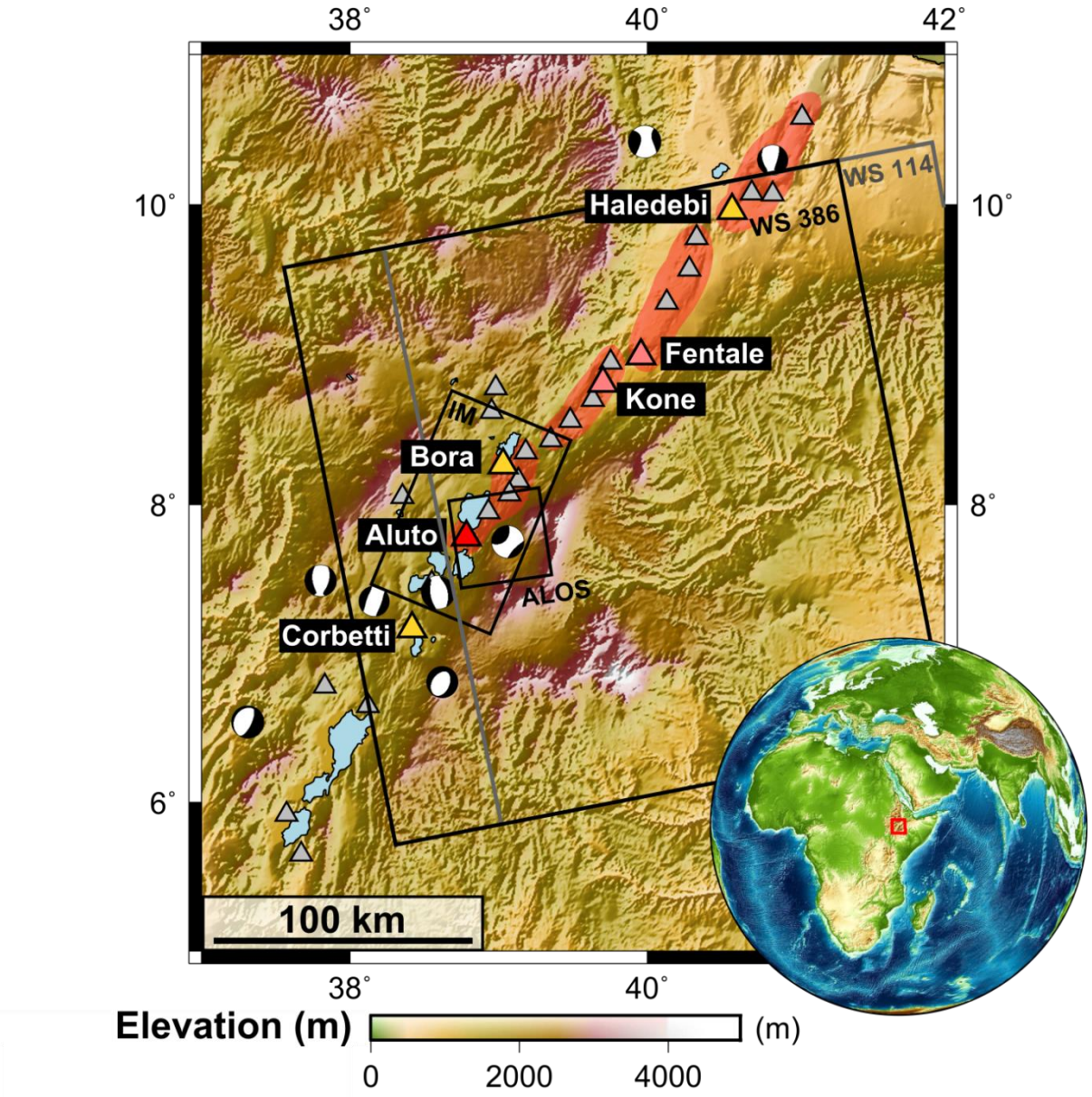

Figure 3.1: *Shaded relief map of the Main Ethiopian Rift (MER). Holocene volcanic centres are shown as triangles (after Siebert and Simkin, 2002). Aluto volcano, the focus of this study, is shown in red, other deforming volcanoes (after Biggs et al., 2011) are shown in yellow, and those that have undergone historical eruption are shown in pink. Note that ground deformation has not been detected at volcanoes that have undergone historical eruptions. Earthquake locations and focal mechanisms for the region are from the Global Centroid Moment Tensor Project catalogue (http:// www .globalcmt .org; 1976–2012; M > 5). The red coloured area marks the extent of volcanic segments of the MER (Casey et al., 2006; Beutel et al., 2010; Keir et al., 2015). Rectangles indicate the coverage of the four SAR data sets used in this study. WSM: Envisat Wide Swath Mode and IM: Envisat Image Mode.*

Further insight into subsurface processes at restless volcanic systems can be gained from geochemical monitoring of gas and fluid effluent. These techniques provide vital additional constraints on the sub-volcanic system, and by identifying spatial and temporal variations in the concentration and isotopic characteristics of geochemical tracers, volcanologists can gain insight into magmatic-hydrothermal interactions, degassing behaviour of magmatic bodies, geothermal reservoir evolution and earthquake effects (e.g., Oppenheimer et al., 2003; Hilton et al., 2010; Parks et al., 2013; Tassi et al., 2013; Rizzo et al. 2015). In the case of Campi Flegrei caldera, geochemical time series of H_2O, CO_2 and CH_4 ratios and concentrations have shown that repeated injection of magmatic fluids into the hydrothermal reservoir shows close temporal correlation with ground displacement, and this ultimately provides a mechanism to explain pulses of uplift (e.g., Chidoini et al., 2010, 2012, 2015).

In this contribution, we combine geophysical observations of ground displacement with geochemical constraints from degassing to understand more about magmatic-hydrothermal interactions and unrest events at Aluto volcano, Ethiopia (Fig. 3.1). Aluto presents a suitable target for this study because it is showing signs of unrest (identified by InSAR, Biggs et al., 2011), and it also hosts a major geothermal field which has been and is being drilled; allowing us to place some constraints on the subsurface structure. We use Interferometric Synthetic Aperture Radar (InSAR) to investigate the spatial and temporal patterns of deformation and establish simple constraints on the volume of fluids involved in the unrest events. We also report new soil-gas chemical data which help confirm physical connections between the magmatic and geothermal reservoirs of Aluto. Together, these techniques shed light on the sub-surface of a restless caldera system, and reveal important coupling between magmatic and hydrothermal processes.

3.2. Methods

3.2.1 InSAR

InSAR is a geodetic technique that measures phase difference between two Synthetic Aperture Radar (SAR) acquisitions (e.g., Simons and Rosen, 2007, and references therein). InSAR has been successfully applied in a number of volcanic settings (e.g., Andes: Pritchard and Simmons, 2004; Indonesia: Chaussard and Amelung, 2012; Central America: Ebmeier et al., 2010, 2012, 2013; Iceland: Sigmundsson et al., 2010, 2014; East Africa: Biggs et al., 2009, 2011).

A number of factors contribute to changes in phase including: differences in satellite position ($\delta\Phi_{orbit}$) and viewing geometry ($\delta\Phi_{topo}$); variations in atmospheric composition ($\delta\Phi_{atm}$); changes in the scattering properties of the ground ($\delta\Phi_{pixel}$) and deformation of the ground ($\delta\Phi_{defo}$). Thus, the total phase change is determined by the sum of all these processes,

$$\delta\Phi_{topo} = \Phi_{orbit} + \Phi_{topo} + \Phi_{atm} + \Phi_{pixel} + \Phi_{defo} \quad (3.1)$$

With precise information on the satellite orbital trajectory, Φ_{orbit} effects can be removed. Φ_{topo} can be corrected for by using a Digital Elevation Model (DEM) to calculate the phase due to topography. Atmospheric errors (Φ_{atm}) result from changes in the pressure, temperature and water vapour contents between SAR acquisitions (e.g. Li et al., 2005). Tropospheric water vapour content is often the major contributor to atmospheric variability and may be correlated with topography, such that phase variations will be correlated with topography (e.g., Ebmeier et al., 2013). Turbulent water vapour errors are also common but can be easily identified in pairs of interferograms that share common image date by using "pair-wise logic" (Massonnet and Feigl, 1998). Incoherence in interferograms is caused by distinct changes in the surface property of radar scatterers (Φ_{pixel}) between satellite image acquisitions, and often changes in vegetation density are the major cause of incoherence. With increasing time between acquisitions, the

likelihood of incoherence increases due to changes in the pixel scatterer properties. In Ethiopia, water vapour effects (Φ_{atm}) are generally minor and those interferograms that have been affected are straightforward to identify and remove from the data set. Likewise the low rainfall and limited vegetation growth means that pixel scattering properties (Φ_{pixel}) do not change significantly over monthly timescales (i.e., coherence between imagery is high).

Here, we use four sets of SAR data acquired by Envisat and ALOS satellites between 2002 and 2012 (summarized in Table 3.1, and in Figure 3.1 where swath coverage is shown). We have generated ~100 interferograms in total and have focused on producing greatest coverage between 2007 and 2010 as this covers a major pulse of uplift at Aluto (Biggs et al., 2011) during which time both satellites were operational.

Satellite	Operation mode	Operational period	Wavelength (cm)	Repeat interval (days)	Swath (km)	Orbit	Tracks processed	Heading angle (°)	Look angle (°)
Envisat (ESA)	Image mode (IM)	2002–2012	5.65 (C-band)	35	58–100	descending	321	-167	22
	Wide swath mode (WSM)	2007–2012[a]	5.65 (C-band)	35	~400	ascending	386 & 114 (both IS1 sub-swath)	-12	18 & 24
ALOS (JAXA)	PALSAR*	2007–2011	23.6 (L-Band)	46	70	ascending	605	-12	40

Table 3.1: *Summary of satellite data sets used in the study. ESA (European Space Agency); JAXA (Japanese Aerospace Exploration Agency); PALSAR (Phased Array type L-band Synthetic Aperture Radar).* [a] *Data covering the Ethiopian Rift extends until December 2008.*

The majority of our data was acquired by the European Space Agency's Envisat satellite. Envisat carries an Advanced Synthetic Aperture Radar (ASAR) instrument that operates at a wavelength of 5.65 cm (C-band) and has several modes of operation. In this study we use data collected in Image Mode (IM) and Wide Swath Mode (WSM). IM is Envisat's conventional operation mode and provides descending data across a swath of 58–110 km (Table 3.1). The Scanning Synthetic Aperture Radar (ScanSAR) technique of the Enivsat ASAR instrument, hereafter referred to as

the WSM mode permits radar observations with a much larger swath of ~400 km (Table 3.1) but with a reduced spatial resolution compared to IM. The swath widening in the WSM is achieved by the use of an antenna beam that is capable of rapid electronic steering in elevation and covers the extended area by using five different overlapping antenna beams (sub-swaths) (Moore et al., 1981). The theoretical and technical aspects of ScanSAR interferometry are further detailed in Guarnieri and Prati (1996) and Guarnieri et al. (2003). We also processed SAR data from the ALOS satellite which acquires data at a longer wavelength of 23.6 cm (L-band, Table 3.1).

Interferograms for Envisat IM and ALOS data were generated using the Repeat Orbit Processing software (ROI_PAC) (Rosen et al., 2004). For the Envisat WSM data we processed the interferograms using Gamma software (Wegmüller and Werner, 1997). For all data sets we removed the topographic contribution using an identical 90 m SRTM DEM. Linear ramps were found in the phase data for several interferograms and were likely caused by inaccuracies in the satellite orbital positions. In these cases, orbital ramps were sampled, modelled (fitting a linear or quadratic surface), and then subtracted from the interferogram (e.g., Ebmeier et al., 2010).

Line of sight (LOS) deformation time series were constructed by using a least squares inversion of the displacements for each interferogram to find incremental displacements between the acquisition dates (e.g., Lundgren et al., 2001; Berardino et al., 2002; Biggs et al., 2010).

3.2.2 Joint inversion

We used a joint inversion technique (after Biggs et al., 2010 and Parks et al., 2015) to combine SAR data acquired from the different satellites and tracks, and produce a time series of subsurface volume change. The main advantage of this method is that it provides an estimate of the volumes and fluxes that are required to generate the observed volcanic deformation signals (Parks et al., 2015). Furthermore, by combining InSAR measurements from different satellite

viewing geometries this allows the deformation source to be independently verified and more confidently constrained (Pritchard and Simons, 2004; Biggs et al., 2010).

We defined a series of linear equations in the form $\mathbf{Ax} = \mathbf{b}$ where **A** is the temporal design matrix, **x** is the model vector for the incremental displacements, and **b** is a vector containing the measured displacements (Biggs et al., 2010). For a series of satellite images acquired at different times (e.g., C, D, E and F) we solve for displacements in a series of small steps, whereby the matrix equation can be represented by:

$$\begin{pmatrix} 1 & 0 & 0 \\ 0 & 1 & 0 \\ 0 & 1 & 1 \\ 0 & 1 & 0 \end{pmatrix} \begin{pmatrix} \mathbf{X}_{,CD} \\ \mathbf{X}_{,DE} \\ \mathbf{X}_{,\boldsymbol{EF}} \end{pmatrix} = \begin{pmatrix} \mathbf{b}_{,CD} \\ \mathbf{b}_{,DE} \\ \mathbf{b}_{,DF} \\ \mathbf{b}_{,CE} \end{pmatrix} \tag{3.2}$$

Following the method of Biggs et al. (2010) we treat the displacements as arising from a spherical point source pressure variation at depth within an elastic crust. We used a simple Mogi source (Mogi, 1958) to convert our displacement time series to volume change. Penny-shaped crack geometries were previously used by Biggs et al. (2011) but we found that when combining images from different viewing geometries, the penny-shaped crack geometry tended to produce worse fits than for a Mogi model. We also recognize that the shallow depth (typically < 2 km) and large radius (5–10 km) required for the penny-shaped crack extends beyond the known limits of the geothermal field (Section 3.5), and thus we restrict discussion to the spherical source.

We estimate the incremental volume change of the Mogi source, using equations 3.3 and 3.4 (Biggs et al., 2010).

$$\begin{pmatrix} m_x \\ m_y \\ m_z \end{pmatrix} = (1 - v) \frac{\Delta V}{\pi} \begin{pmatrix} \frac{x}{R^3} \\ \frac{y}{R^3} \\ \frac{z}{R^3} \end{pmatrix} \tag{3.3}$$

$$\begin{matrix}(\mathbf{l_n} \cdot \mathbf{M_n})\mathbf{A_n} \\ (\mathbf{l_p} \cdot \mathbf{M_p})\mathbf{A_p} \\ \vdots \end{matrix}\begin{pmatrix} V_{12} \\ V_{23} \\ V_{34} \\ \vdots \end{pmatrix} = \begin{pmatrix} \mathbf{b_n} \\ \mathbf{b_p} \\ \vdots \end{pmatrix} \quad (3.4)$$

where v is Poisson's ratio, R is the distance from the source to the observation, subscripts $\mathrm{n}, \mathrm{p}\ldots$ represent the observation group (e.g. $\mathbf{b_n}$ may represent the measured LOS displacements from a series of interferograms from the same satellite track, and $\mathbf{b_p}$ all the observations from a second track), then $\mathbf{l_n}$ is the LOS unit vector from the first InSAR track and $\mathbf{l_p}$ is LOS unit vector from the second InSAR track. $\mathbf{M_n}$ and $\mathbf{M_p}$ are the 3 component displacement vectors (mx, my, mz) predicted by the Mogi model and $\mathbf{A_n}$ and $\mathbf{A_p}$ are the temporal design matrices illustrated in equation 3.1. The incremental volumes are then integrated to provide a time series of volume change (Biggs et al., 2010). We solved for several different sources of noise or nuisance parameters: those that were temporally and spatially correlated and those that were uncorrelated. More detailed information regarding both the inversion technique and error estimation may be found in Biggs et al. (2010).

We carried out a three-dimensional grid search to find the best-fitting source location and depth by minimizing the misfit between the observations and model. We consider all deformation to be related to a single point source, on the grounds that Envisat IM interferograms suggest the deformation centre is constant through time (Fig. 3.2 C–F), and when we attempted to model the uplift and subsidence separately using the inversion both solutions converged at a depth interval of 4.9–5.4 km depth (Section 3.3.4).

3.2.3 Gas chemistry and CO_2–$\delta^{13}C$ analysis

Diffuse degassing through soil and fumarole vents is the main outlet for volatiles on Aluto (Hutchison et al., 2015, Chapter 2). In February 2014 we collected ~100 soil-gas samples from nine sites along the main fault zone of Aluto (Artu Jawe fault zone, AJFZ) whilst conducting

diffuse CO_2 degassing surveys (described in Hutchison et al., 2015). We adopted the method of Chiodini et al. (2008) to sample gas for laboratory analysis. At each measurement station we set up an accumulation chamber (Chiodini et al., 1998) and inserted a T-connector with a pierceable septum in the flowline just after the infrared gas analyser. During the CO_2 flux measurements we pierced the septum with a syringe and extracted 12 ml of gas. The syringe had a built-in shut off valve, and so the sample gas was sealed, and then subsequently injected into a 12 ml evacuated vial through a pierceable butyl rubber septum. Two gas samples were extracted from the line during each measurement. The first was taken after a few seconds allowing homogenisation of gases within the chamber; the second sample was collected some 40 seconds later, at higher CO_2 concentration. The first sample (0 second) allows localized air pollution effects to be characterized (e.g., Chiodini et al., 2008; although this was minimal at Aluto), and more importantly, it can be used to distinguish contributions from other sources (e.g., biogenic) before volcanic gases swamp the chamber.

Bulk gas chemistry was measured for seven samples (Table 3.2) at the Department of Earth and Planetary Sciences at University of New Mexico (UNM). A combination of gas chromatography (GC) and quadrupole mass spectrometry (QMS) were used to measure the composition of gases (de Moor et al., 2013). CH_4, CO_2, H_2, and CO concentrations were measured using GC, whilst Ar, He, N_2, and, O_2 were determined using QMS. de Moor et al. (2013) used identical measurement apparatus and procedure at UNM and reported analytical uncertainty for the GC measurements at ± 5%, and QMS analyses at <0.1 % (concentration). It is important to recognize that the pierceable glass vials are not designed for storage of hydrogen and helium gas species and although these were analysed at UNM we believe that these species were likely to have been lost either by diffusion through glass or through the rubber septum.

Carbon isotope measurements of gas (CO_2–$\delta^{13}C$) were made for the majority of samples at the Geochemistry Laboratory of INGV-Osservatorio Vesuviano (Naples). The gases were analysed within a few days of sampling; well within the time period of isotopic fractionation through the septum (Tu et al., 2001). The samples were analysed using a continuous flow isotope ratio mass spectrometer (Thermo-Finnigan Delta XP) interfaced with a Gasbench II device equipped with autosampler. CO_2–$\delta^{13}C$ measurements were also made by mass spectrometer for seven samples at the Stable Isotope Lab at UNM (the same samples that were also analysed for bulk gas chemistry, Table 3.2). Results for all CO_2–$\delta^{13}C$ measurements are shown in delta notation as per mil values (δ‰) relative to PDB (Pee Dee belemnite) using an internal standard and are characterised by a $\delta^{13}C$ standard error of ± 0.1‰.

It was not possible to make a direct comparison of an identical soil-gas sample measured for CO_2–$\delta^{13}C$ between the different laboratories at UNM and Naples. However, at site 06A (Table A1.1) where the natural CO_2–$\delta^{13}C$ variation was well constrained by samples analysed in Naples, all nine gas samples were between –4.5 and –4.2 ‰, we found that the corresponding measurements made at UNM were –4.2 and –4.3 ‰ (Table 3.2). The overlapping values suggest that any systematic error in isotopic measurements between the different laboratories were within the natural variability of the soil-gas sampling sites on Aluto.

3.3. InSAR observations

In this section we present interferograms and deformation time series that cover the main periods of unrest between 2003 and 2011. In particular we focus on the time period between 2007 and 2011 when both satellites were operational and acquiring data. In Figure 3.2A the main structural features on and around the Aluto volcanic complex are highlighted, as well as the extent of volcanic deposits from the complex. Major tectonic faults in the region generally follow a NNE-SSW trend and have vertical offsets of 50–100 m (Agostini et al., 2011). An elliptical caldera rim

and ring fault is hypothesized to underlie the Aluto complex and is shown by the black dotted line in Figure 3.2A (Hutchison et al., 2015).

Each displacement time series is referenced to a pixel (asterix, Fig. 3.2A) located beyond any of the young volcanic deposits and assumed not to be deforming. Note that as surface displacements are measured in the satellite LOS, the difference in the apparent location of the centre of uplift, and the magnitude of the signal in Figures 3.2–3.5, primarily results from differences in the satellite azimuths and incidence angles of the radar pulse.

3.3.1 Envisat IM

The Enivsat IM data suggest there have been two major uplift events at Aluto between 2004 and 2011; in both cases these were followed by a period of slow subsidence (Fig. 3.2B). The displacement time series reveal that deformation in 2004 was ~+15 cm and ~+10 cm in 2008. Data spanning the periods in between the uplift events are sparse but generally supportive of a subsidence signal of ~5 cm following maximum uplift (Biggs et al., 2011). The temporal resolution of the Enivsat IM data during the periods of deformation is also limited and the simplest assumption is that deformation is linear throughout (Fig. 3.2B). This would support a minimum rate of uplift of ~10 cm yr^{-1} in 2004 and ~6 cm yr^{-1} in 2008.

The airborne mapping conducted by Hutchison et al. (2015) allows us to consider the deformation signals on Aluto with respect to the major structural features. The uplift signals detected by Enivsat IM extend beyond the main edifice but are contained within the area covered by volcanic deposits (Fig. 3.2C, E). The uplift patterns clearly extend well beyond the proposed ring fault of Hutchison et al., (2015), and there is no apparent elongation or termination in deformation along the major tectonic structures. The subsidence deformation field (Fig. 3.2D, F) also shows no alignment with fault patterns.

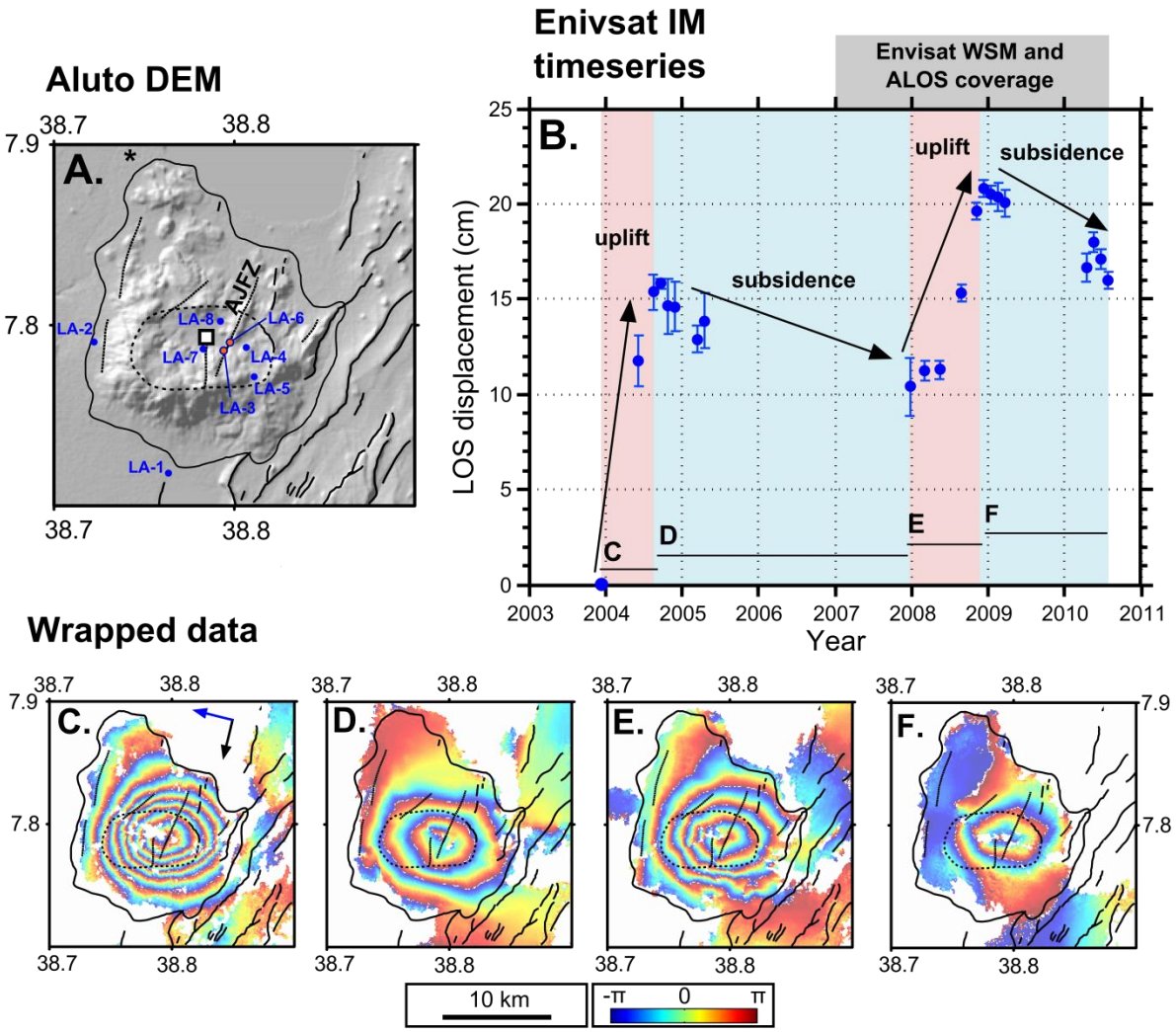

Figure 3.2: ***A)*** *Hillshade DEM of Aluto volcano. Black outline marks the extent of volcanic deposits, dashed line delineates the hypothesised ring fracture beneath Aluto (after Hutchison et al., 2015), and NNE-SSW trending lines indicate tectonic faults (after Agostini et al., 2011). The major tectonic fault that dissects Aluto is referred to throughout at the Artu Jawe fault zone (AJFZ) and is labelled in the figure.* ***B)*** *Enivsat IM line of sight (LOS) displacement time series (after Biggs et al., 2011). The black asterix locates the reference pixel. The white square contains pixels used to generate the time series.* ***C–F)*** *Example interferograms, covering the period indicated by the black horizontal lines in the time series. Note that in* ***C–F*** *each colour fringe represents 2.58 cm of LOS displacement. Black arrow indicates orientation of satellite orbit, and blue arrow indicates the look direction of the satellite.*

In all interferograms the signal is elliptical, showing an E-W to ESE-WNW elongation. The centre of the deformation (for both uplift-subsidence events) is also remarkably consistent throughout the observation period and from the Envisat IM look direction is located a few kilometres east of the caldera centre.

3.3.2 ALOS

ALOS data also capture the period of uplift at Aluto between 2008 and 2009. The results are consistent with the Enivsat IM mode data and suggest a maximum of ~+9 cm uplift centred on the caldera (Fig. 3.3A). The data following the peak uplift on the LOS time series are scattered but suggest a subsidence of ~–2 cm (Fig. 3.3A). The ALOS interferograms also clearly indicate that there was no deformation prior to 2008 (Fig. 3.3B). The uplift signal is circular (Fig. 3.3C), shows no alignments to major structures, and was observed across the main edifice (Fig. 3.3C). The pattern of subsidence shows slight elongation E-W and is largely focused within caldera (Fig. 3.3D).

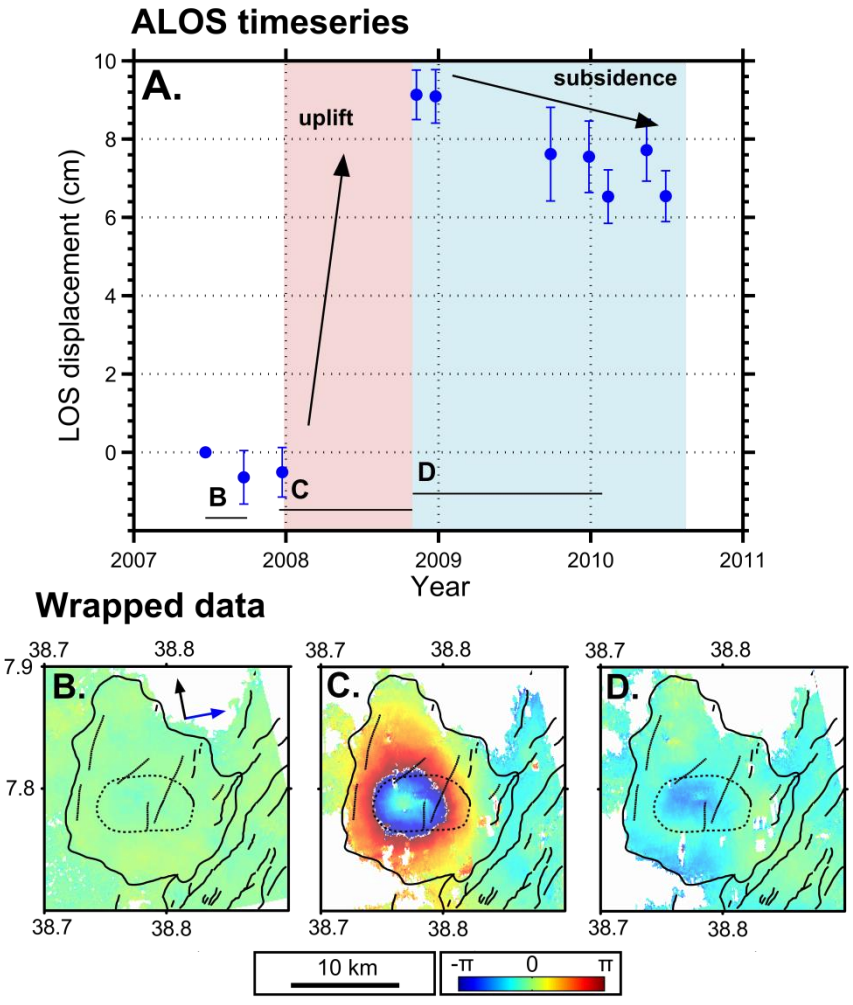

Figure 3.3: ***A)*** *ALOS line of sight (LOS) displacement time series.* ***B–D)*** *Example interferograms, covering the period indicated by the black horizontal lines in the time series. Each fringe represents 11.8 cm of LOS displacement (note that this is different from the Envisat data presented elsewhere in the chapter). Tectonic and volcanic structures are overlain, and can be linked back to the DEM in Fig. 3.2A. Black arrow indicates orientation of satellite orbit, and blue arrow indicates the look direction of the satellite.*

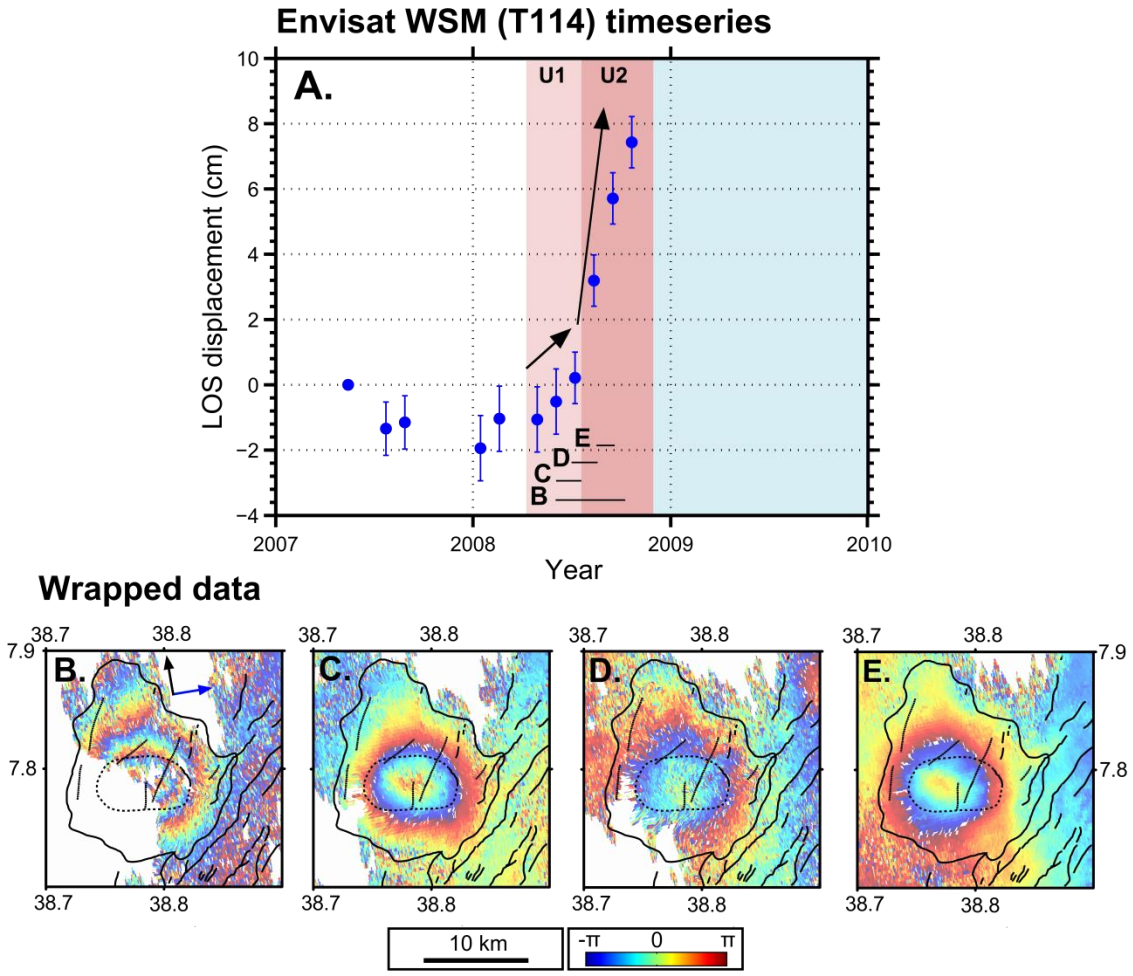

Figure 3.4: ***A)*** *Envisat WSM track 386 line of sight (LOS) displacement time series.* ***B–E)*** *Example interferograms, covering the period indicated by the black horizontal lines in the time series. Each fringe represents 2.58 cm of LOS displacement. Tectonic and volcanic structures are overlain, and can be linked back to the DEM in Fig. 3.2A. Black arrow indicates orientation of satellite orbit, and blue arrow indicates the look direction of the satellite.*

3.3.3 Enivsat WSM

Envisat WSM data were available between 2007 and 2009 (Table 3.1), and provide the highest number of acquisitions over the uplift. Time series are consistent in magnitude with the other data and suggest a maximum of LOS displacement of +8.5 and +9.5 cm for tracks 114 and 386, respectively (Figs. 4A and 5A). The signals also suggest there are two phases to the uplift pulse (marked U1 and U2, on Figures 3.4A and 3.5A). The initial phase (U1) has a displacement of 2–3 cm over a three month period between April and July 2008, the rate then increases between July

and October (U2) where 5 cm of deformation occurs over three months. We suggest that the WSM imagery indicate a two-step accelerating deformation trend. Similar to the IM and ALOS interferograms we find that the WSM deformation centre is also located within the centre of the caldera. For both WSM tracks there is no compelling evidence that the uplift patterns are tied to any of the major fault traces (Figures 3.4 and 3.5 B–E).

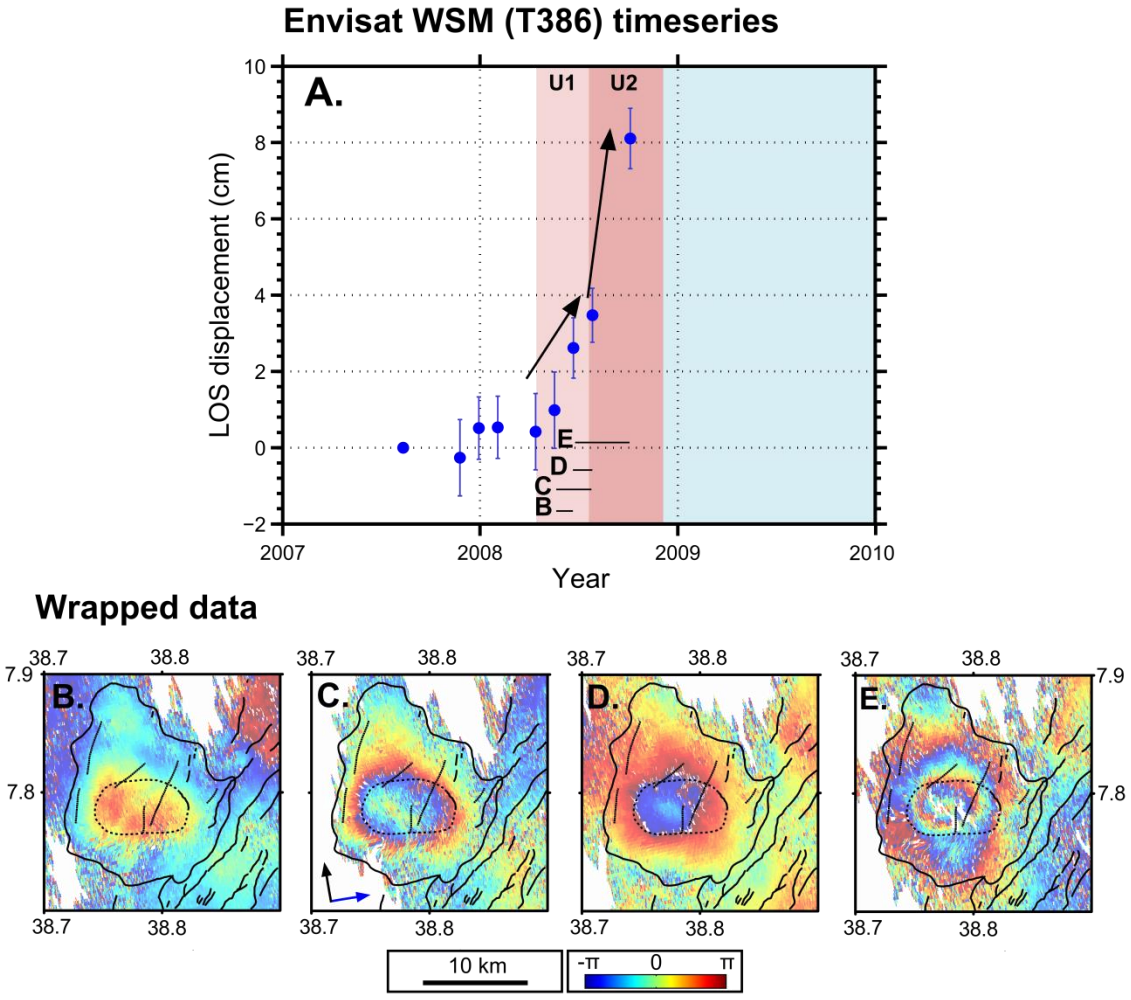

Figure 3.5: *Envisat WSM track 114 line of sight (LOS) displacement time series.* ***B–E)*** *Example interferograms, covering the period indicated by the black horizontal lines in the time series. Each fringe represents 2.58 cm of LOS displacement. Tectonic and volcanic structures are overlain, and can be linked back to the DEM in Fig. 3.2A. Black arrow indicates orientation of satellite orbit, and blue arrow indicates the look direction of the satellite.*

3.3.4 Joint inversion

We have used the ~50 interferograms covering the uplift-subsidence period between 2008 and 2010 to establish a time series of sub-surface volume change (Fig. 3.6). The best fitting spherical source location and optimum depth was found by carrying out a grid search (Fig. 3.6A) and finding the minimum weighted residual for each inversion (Fig. 3.6B, C).

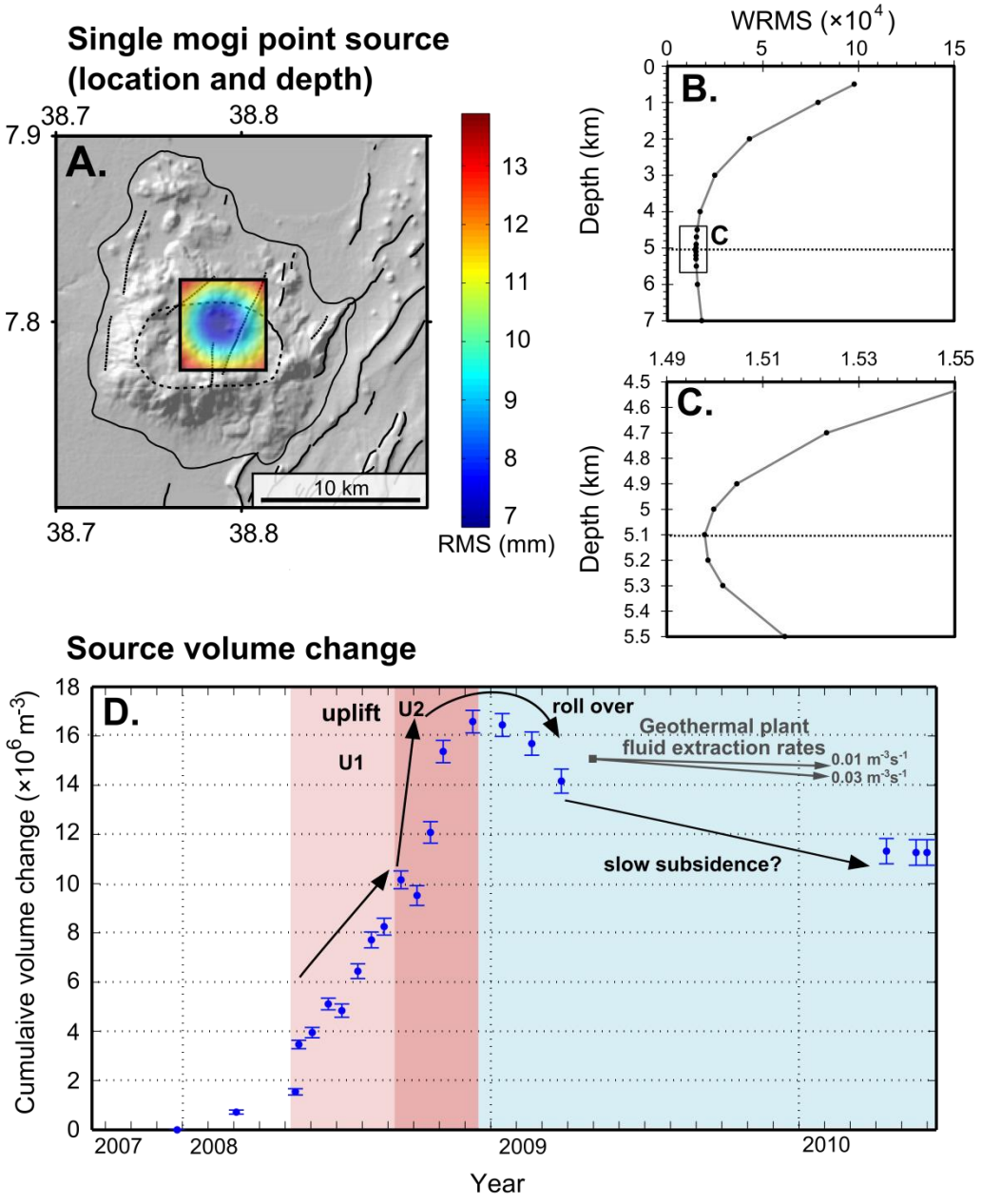

Figure 3.6: *Joint inversion models of InSAR data and cumulative volume time series.* ***A)*** *Grid search to find minimum RMS misfit (blue) and best source location.* ***B and C)*** *Source depth versus minimum weighted residual for each inversion (WRMS). The best fit depth is found to be at 5.1 km.* ***D)*** *Cumulative variation in volume change derived from the joint inversion of InSAR measurements covering the period of September 2007 – June 2010 (blue). Geothermal plant extraction rates are calculated based on known well flow rates of 10–25 kg s^{-1} (Teklemariam and Beyene, 1999). Assuming that these values correspond to water in the deep geothermal reservoir, these equate to extraction rates of 0.01–0.03 m^3 s^{-1}, or 0.3–1 × 10^6 m^3 yr^{-1}.*

The best source is shown to be at a depth of 5.1 km. The total volume increase for the uplift period is +12–16 × 10^6 m^3, and this is then followed by –5 × 10^6 m^3 of volume decrease between the end of 2009 and 2010 (subsidence period).

Bringing together the individual interferograms from the different tracks demonstrates an accelerating (or two step) uplift pattern through 2008 which is in line with the LOS displacement time series from WSM data (Figs. 4A and 5A). At the point of maximum source volume change the time series shows a distinct 'roll over' into negative volume change (i.e., deflation). This pattern could relate to two competing processes, whereby fluid flux into source region initially causes expansion but is then matched and subsequently overtaken by fluid loss. While there is a significant data gap during the presumed slow subsidence (deflation) period between mid-2009 and early-2010, the volume time series in Figure 3.6D does indicate that ~50 % of the source deflation (equivalent to –2.3 × 10^6 m^3 volume change) took place in the 3 months following peak uplift.

3.4. Degassing constraints and $\delta^{13}C$ isotopes

3.4.1 Overview

The chemical composition of the dry (water-free) gas-phase in the soil-gas samples are reported in Table 3.2, and summarized in the CO_2–O_2–N_2 triangular diagram in Figure 3.7. The gas sampling sites are also shown as coloured symbols in Figure 3.8A where they are overlain on aerial imagery and gridded soil-CO_2 flux (measured at that time, Hutchison et al. 2015).

Sample ID	H_2 ppm	He ppm	CH_4 ppm	N_2 %	CO ppm	O_2 %	Ar %	CO_2 %	$\delta^{13}C$ ‰	N_2/O_2	N_2/Ar	CO_2/N_2
01-A3 40s	6.11	23.10	25.53	78.75	33.62	18.17	0.76	2.31	-4.41	4.3	103	0.03
01-B1 40s	9.82	28.72	nd	76.21	37.26	20.72	0.86	2.20	-3.44	3.7	89	0.03
01-B4 40s	8.33	32.74	nd	80.05	47.25	17.43	0.72	1.79	-4.26	4.6	110	0.02
01-B7 40s	7.75	46.63	nd	76.67	45.15	21.01	0.87	1.45	-6.08	3.6	88	0.02
01-C1 40s	9.34	19.27	nd	77.05	35.34	20.84	0.87	1.23	-3.89	3.7	88	0.02
03-A3 40s	9.06	24.86	nd	77.27	35.00	21.02	0.90	0.81	-5.93	3.7	86	0.01
06-A1 40s	9.60	18.36	1053.00	72.19	64.44	16.93	0.73	10.03	-4.26	4.3	99	0.14
06-A4 40s	10.02	21.86	621.51	69.89	35.70	19.12	0.80	10.12	-4.22	3.7	88	0.14

Table 3.2: *Composition of soil-gas efflux from the Artu Jawe fault zone. Measured at University of New Mexico using a combination of gas chromatography (GC) and quadrupole mass spectrometry (QMS) techniques (Section 3.2.3). All samples were extracted after the accumulation chamber had been closed for 40 seconds.*

The gas samples are dominated by N_2 (69–80 %) and O_2 (16–21 %), clearly demonstrating that they are heavily mixed with air (Table 3.2). From the triangular diagram in Figure 3.7 it is clear that most of the samples have N_2/O_2 ratios of air (3.7) or slightly higher, and that they fall on a mixing line between air and a pure-CO_2 end member. The CO_2 concentrations in the gas samples are between 1–10 %; much higher than present-day atmospheric concentrations of ~400 ppm, and strong evidence that magmatic-hydrothermal gases have been sampled. The air saturated water N_2/O_2 ratio is temperature dependent (e.g., 1.9 at 25 °C; 1.6 at 100 °C) but is evidently lower than any of the Aluto samples (Fig. 3.7); further confirmation that our soil-gas samples are predominantly mixed with air. N_2/Ar ratios for the Aluto samples (88–110, Table 3.2) are slightly higher than air (84), and above that of the typical mantle-derived gases (80, Marty and Zimmermann, 1999) and air saturated water (~40, temperature dependent, de Moor et al., 2013). CH_4 was above detection only in the samples with the highest CO_2 concentrations (Table 3.2) and in these cases was well above present-day atmospheric values of 1.8 ppm. CO was between 33 and 65 ppm; again significantly above typical atmospheric values of 0.2 ppm.

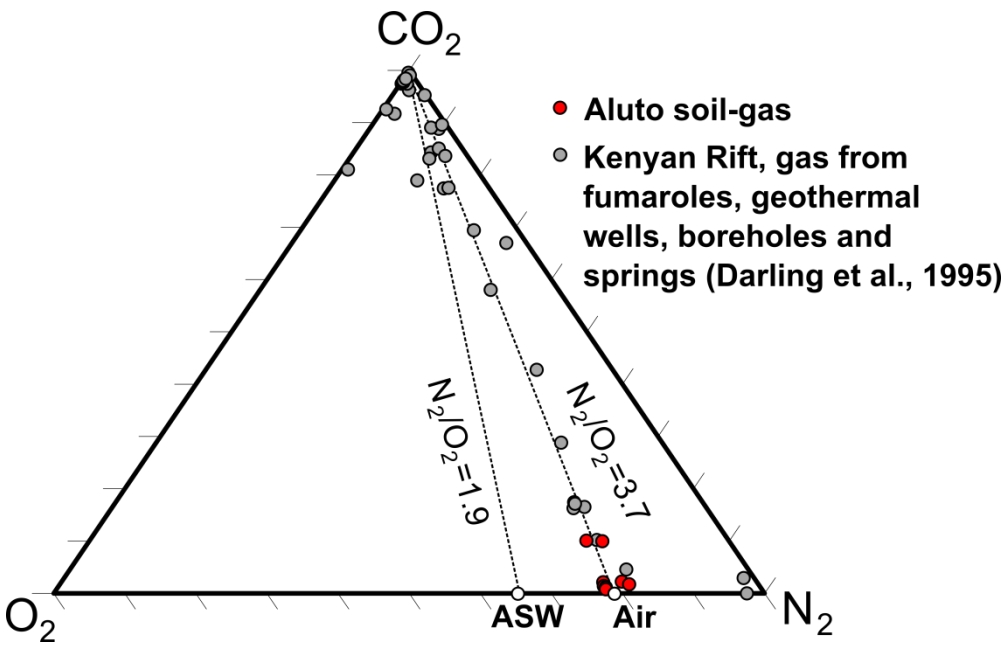

Figure 3.7: *CO_2-O_2-N_2 triangular plot for soil-gas samples collected in this study at Aluto volcano (red), gas phase samples collected throughout the Kenyan Rift (grey; Darling et al., 1995). The Aluto samples fall on a mixing line between air and pure CO_2, although are evidently dominated by air.*

In Figure 3.7 we also show gas-phase analyses made at fumaroles, geothermal wells, springs and boreholes, at active geothermal areas along the Kenyan Rift (after Darling et al., 1995). While there are no analogous data sets currently available for Ethiopia, this comparison quite clearly demonstrates that geothermal gases from across the EARS can be broadly defined by mixing between air, air saturated water and a CO_2-rich end-member that is of magmatic/mantle origin (e.g., Darling et al., 1995; Barry et al., 2013).

CO_2–$\delta^{13}C$ data from the AJFZ of Aluto are presented in Figure 3.8B (symbols are linked to the CO_2 flux map in Fig. 3.8A). The values span a range between –21.2 and –2.5 ‰, and define a triangular array when plotted as the reciprocal of CO_2 concentration (Fig. 3.8B; after Parks et al., 2013). Overall the CO_2–$\delta^{13}C$ array (Fig. 3.8B) can be defined by three end-member components: magmatic $\delta^{13}C$ values (between –3 ‰ and –8 ‰, Gerlach and Taylor 1990; Javoy et al. 1991; Macpherson and Mattey 1994; Sano and Marty, 1995); atmospheric $\delta^{13}C$ values (–8 ‰, Darling et al. 1995; Tedesco et al. 2010) and biogenic $\delta^{13}C$ values (–20 to –25 ‰, Cheng, 1996; Chiodini et al., 2008).

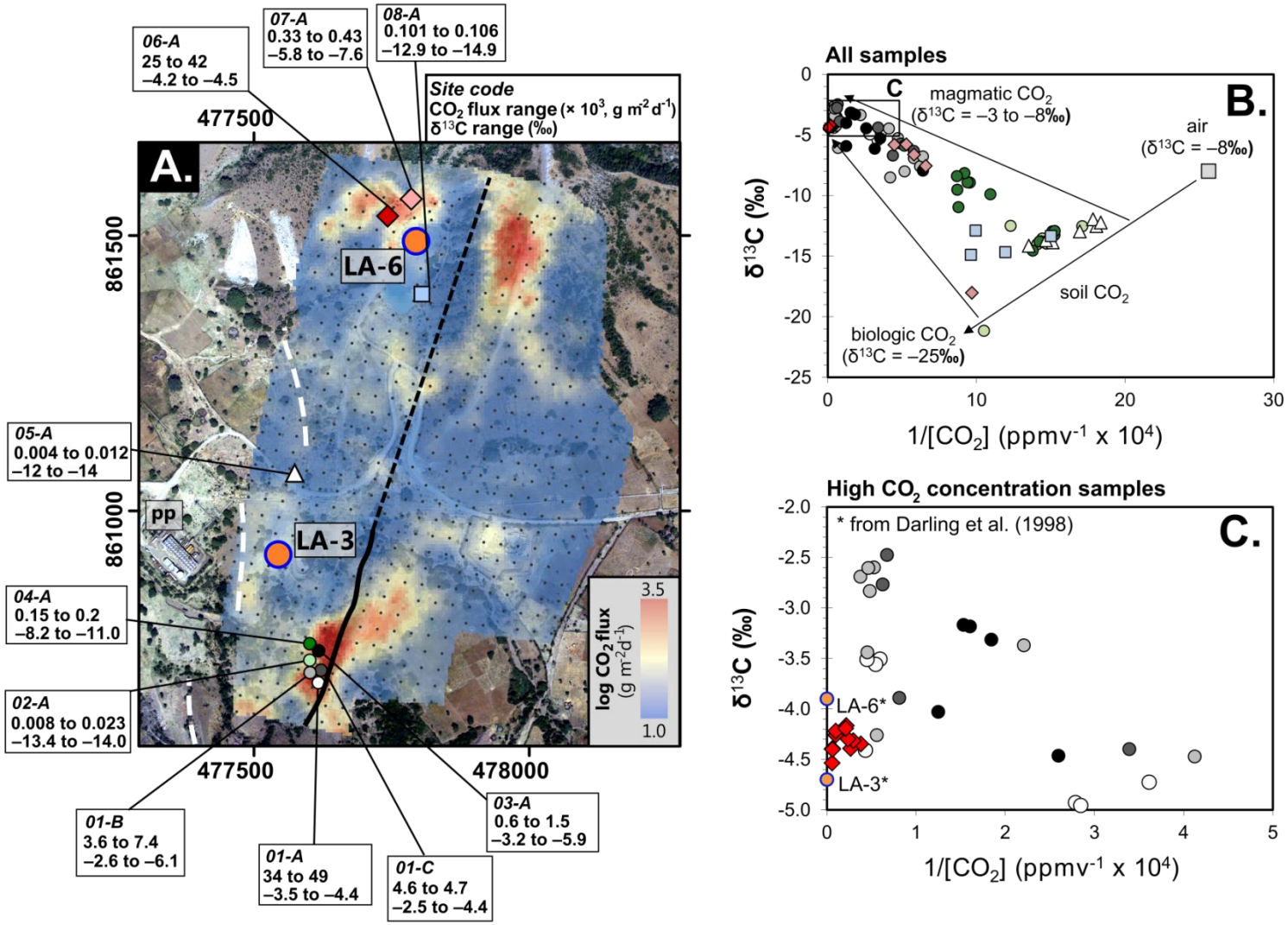

[68]

Figure 3.8: *Degassing sites along the Artu Jawe fault zone (AJFZ).* ***A)*** *Gas sampling sites along are shown as coloured symbols. Orange circles with blue outlines identify the location of the productive geothermal wells (LA-3 and LA-6). The sampling locations are overlain on an aerial photo and CO_2 flux map (blue to red colours, described by Hutchison et al., 2015). Small grey points represent discrete flux measurements. The black line indicates the Artu Jawe fault scarp (black) and its projected continuation north (dashed). Less-pronounced breaks in topography (10–20 m high) west of the main fault scarp are marked by white dashed lines. pp: the Aluto-Langano geothermal power plant. The range of soil CO_2 flux and CO_2–$\delta^{13}C$ (for the 40 second samples, Section 3.2.3) at each site are shown in the white boxes around the grid.* ***B)*** *Carbon isotopic composition ($\delta^{13}C$) of soil CO_2 efflux plotted against the reciprocal of CO_2 concentration in the gas samples (symbol are linked to map view in Fig. 3.8A). This plot shows all samples that were collected and analysed for CO_2–$\delta^{13}C$ (both the 0 second and 40 second samples, Section 3.2.3). The data define a triangular array that can be defined by mixing between between air, an endmember characterised by high CO_2 concentrations and light $\delta^{13}C$ values approaching −25 ‰ (i.e., biogenic CO_2) and an endmember characterised by high CO_2 concentrations and heavier $\delta^{13}C$ values (i.e., magmatic CO_2).* ***C)*** *Inset of Fig. 3.8B showing CO_2–$\delta^{13}C$ for the highest concentration samples. CO_2–$\delta^{13}C$ of gases from geothermal wells on Aluto are shown after Darling et al., (1998). Note that deep well samples contain ~98 % CO_2 (dry gas phase).*

We find that the samples with highest CO_2 concentrations (sample site 06-A, Fig. 3.8A and Table 3.2) show a narrow range of CO_2–$\delta^{13}C$ values from –4.2 to –4.5 ‰, strongly supporting a magmatic origin (Fig. 3.8C). The key inference that the CO_2–$\delta^{13}C$ allow us to make is that the magmatic and geothermal reservoirs of Aluto are connected. Volatiles released by the magma reservoir degas into a deep geothermal reservoir at > 2 km (Section 3.5, Gizaw, 1993; Teklemariam et al., 1996). While CO_2 and other magmatic volatiles may be scrubbed via interaction with fluid in the geothermal reservoir or by mineralization (e.g., Werner et al., 2012), ultimately the CO_2–$\delta^{13}C$ of the efflux measured at surface clearly fingerprints this deep magmatic signal. There are several subtle features to note regarding the CO_2–$\delta^{13}C$ data set and these are explored in the following sections.

3.4.2 Spatial variations

Firstly, there are clear spatial variations in CO_2–$\delta^{13}C$ at the different sample sites along the fault zone (Fig. 3.8C). For example, fumarole vents at sites 06-A and 07-A at the northern end of the grid show distinct isotopic differences from fumaroles at sites 01-A, B and C at the southern end; the latter show values that are up to ~2‰ heavier (Fig. 3.8A, C). While variations in soil-gas flux along the AJFZ have previously been linked to the presence of deep structures and changes in near-surface permeability (Hutchison et al., 2015), the distinct CO_2–$\delta^{13}C$ at different sites suggests that there is limited mixing and homogenization of the gases along the fault zone.

3.4.3 Temporal variations

Short-timescale variations are also seen in soil-gas flux and CO_2–$\delta^{13}C$ at the measurement sites. For example, sites 01-A, B and C, though only separated by a few 10's of meters, show clear differences both in terms of absolute magnitude of soil-gas flux (~45, ~7 and ~5 × 10^3 g m^{-2} d^{-1}, respectively) but also how much it oscillates between measurements (30%, 50% and 5%, respectively, Fig 8A). Similarly, there is no clear correlation between soil-gas flux and CO_2–$\delta^{13}C$ at these three measurements sites; site 01-C, for example, shows a near constant soil-gas flux but

~2 ‰ range in CO_2–$\delta^{13}C$ (Fig. 3.8A). Overall this reveals a fairly complex picture of gas flux at the surface of the fault zone, where short-timescale variations can occur in both the gas flux and its carbon isotopic composition.

3.4.4 High CO_2–$\delta^{13}C$ values

High CO_2 concentration samples (Fig. 3.8C) also collected from sites 01 B and C, show a cluster of CO_2–$\delta^{13}C$ values between –2.5 and –3.0 ‰, above the range normally associated with magmatic gases (–3 ‰ to –8 ‰). There are a number of explanations as to why these values are slightly heavier than typical magmatic values, we outline these processes first and then consider their relevance at Aluto:

i) Crustal contamination: CO_2 gas could be released by decarbonation of limestone in the sub-volcanic system, induced either by heating, or reaction with magma. These gases would yield a CO_2–$\delta^{13}C$ of 2–6 ‰ (Lollar et al., 1997; Tassi et al., 2010; Darrah et al., 2013; Parks et al., 2013), and when mixed with magmatic gases could explain the values of –2.5 ‰ observed.

ii) Calcite precipitation: loss of CO_2 due to calcite precipitation has the potential to fractionate CO_2–$\delta^{13}C$. This process is highly temperature-dependent, such that at temperatures <192 °C, calcite is enriched in ^{13}C relative to residual dissolved CO_2 in geothermal fluids, whereas at higher temperatures >192 °C calcite becomes depleted in ^{13}C relative to residual CO_2 (Bottinga, 1969). To explain the values on Aluto the latter case would have to be true, i.e., temperatures >192 °C would enrich residual CO_2 in ^{13}C and result in higher CO_2–$\delta^{13}C$.

iii) Phase partitioning and hydrothermal degassing: Vapour partitioning can be caused by either boiling (>100 °C) and/or hydrothermal degassing due to supersaturation of a

particular gas species. The loss of CO_2 from geothermal fluids via these processes will cause isotopic fractionation between ^{13}C and ^{12}C (e.g., Vogel, 1970; Mook, 1974). These processes are also temperature dependent and it has been shown by Szaran (1977) that at temperatures <110 °C dissolved carbon species will be enriched in ^{13}C, leaving ^{13}C relatively depleted in the residual gas phases. At higher temperatures (>110 °C), the isotopic fractionation is in the opposite sense and residual gases will consequently be enriched in ^{13}C. This latter case would again have to be true to explain the observed values of ~–2.5 ‰ at Aluto (Fig. 3.8C).

To interrogate these processes further, as has been done at other volcanic systems (e.g., Barry et al., 2013, 2014), would require $\delta^{13}C$ analyses of the geothermal fluids, and also additional tracers, such as He, which is much less soluble in aqueous solutions compared to CO_2 (Ellis and Golding, 1963; Weiss, 1971). Until this data is available we can, however, make several simple arguments. Firstly, there is no evidence from the petrography or geochemistry of the Aluto rock samples (Hutchison et al., in review, Chapter 4) to suggest that there is any carbonate assimilation beneath the complex. In addition, lacustrine sediments that do underlie the Aluto complex are relatively thin (50–100 m, Fig. 3.9) and significant carbonate horizons have yet to be described in deep wells (Yimer, 1984; Mamo, 1985; ELC Electroconsult, 1986; Gianelli and Teklemariam, 1993; Teklemariam et al., 1996). If decarbonation is taking place it would more likely be sourced from Jurassic-Palaeogene sedimentary rocks that make up basement lithologies in the MER (e.g., Cornwell et al., 2009), however, beneath Aluto their thickness and composition is completely unknown.

On the other hand, it is known from deep well data that beneath our sampling area temperatures exceed 300 °C, and that boiling conditions occur along the AJFZ (from at least 2100 m up to 700 m depth, Gizaw, 1993). Calcite is also one of the main hydrothermal mineral precipitates, along

with epidote, quartz and chlorite, and has been identified in deep wells cores collected along this fault zone (Teklemariam et al., 1996). These simple constraints are consistent with both scenarios ii) and iii), and favour carbon isotope fractionation by calcite precipitation, boiling and degassing within the geothermal system. These scenarios explain why some of our CO_2–$\delta^{13}C$ values are slightly heavier than the magmatic range without invoking crustal contamination by unknown carbonate material.

Overall the picture that we develop from the new gas data is of a connected magmatic-hydrothermal system where the magmatic reservoir supplies a continuous input of heat and volatiles to the deep geothermal fluid. The AJFZ provides an important pathway for fluid upflow and migration from the geothermal reservoir to the surface (Section 3.5). It is likely that upflow rates, as well as boiling, degassing and mineral precipitation vary along the fault zone, and that these processes (once over-printed on the near-surface permeability variations, Hutchison et al., 2015) produce the complex spatial and short-timescale variations in both CO_2 flux and $\delta^{13}C$ (Sections 3.4.2 and 3.4.3).

3.5. Constraints on the magmatic-hydrothermal system

The new and existing constraints on the subsurface structure and geothermal field of Aluto are now used to develop a simple conceptual model of the magmatic and hydrothermal systems (Figure 3.9), and this is developed further in terms of the causes of unrest in Section 3.6.

The CO_2–$\delta^{13}C$ results (Section 3.4), high CO_2 flux measurements (Hutchison et al., 2015) and young volcanism (<10 ka, Hutchison et al., in review, Chapter 4) at Aluto are all strongly supportive of the heat source for the geothermal system being magmatic in origin (Fig. 3.8). The recent eruptive products of Aluto are peralkaline rhyolites (Hutchison et al., in review, Chapter 4) and we envisage a crystal-melt mush zone at ~5–6 km to be the most plausible configuration of

the magmatic system; as has been suggested at other peralkaline systems in the EARS (e.g., Macdonald et al., 2008). Based on the CO_2–$\delta^{13}C$ established in Section 3.4 it is evident also that the magmatic and hydrothermal systems of Aluto are connected. Volatiles are transferred from the magmatic reservoir through fractures to the geothermal fluids, which then migrate along fault conduits to the surface where they boil and degas (e.g., de Moor et al., 2012).

$\delta^{18}O$ measurements of waters extracted from the deep wells reveal that the fluid contained within the geothermal reservoir of Aluto is largely meteoric in origin (>90 %); derived from rainfall on the rift margin (Darling et al., 1996). Despite the close proximity of the lakes of Ziway, Langano, and Abijata, Darling et al. (1996) demonstrated that these sources supply only a minimal component (<10%) of water to the reservoir. It has also been established that groundwater beneath the Aluto complex flows towards the south, consistent with the hydraulic gradient, and thus hot spring discharges largely are focussed along the shore of Lake Langano (Kebede et al., 1984; Darling et al., 1996; Hutchison et al., 2015).

The sub-surface structure of Aluto and lithological relationships have been constrained by deep well cores and cuttings and have been presented previously by Gizaw (1993), Gianelli and Teklemariam (1993), Teklemariam et al. (1996). These authors suggest that geothermal reservoir is > 2 km deep and that the main aquifer is a sequence of ignimbrites referred to as the 'Tertiary' ignimbrites. For consistency with accepted chronostratigraphic terminology we refer to these units as Neogene ignimbrites (Fig. 3.9). The reservoir fluids sampled from the deep wells are of alkali-chloride-bicarbonate type, with near-neutral pH, and display geochemical evidence for interaction with rhyolitic volcanic products (Gianelli and Teklemariam, 1993). This final observation would corroborate the Neogene ignimbrite deposit (Fig. 3.8) being the reservoir for the geothermal field.

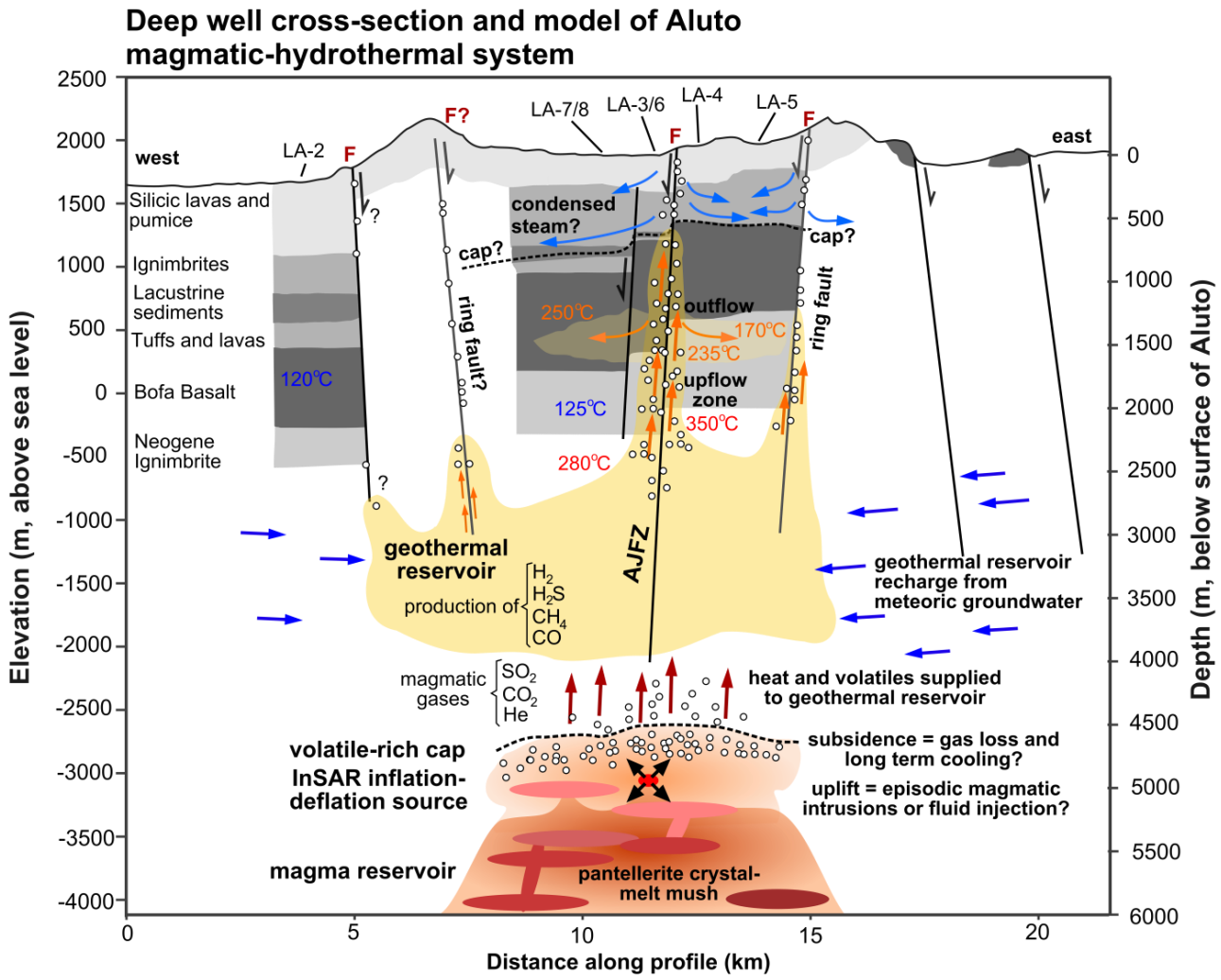

Figure 3.9: *Schematic west-east cross section of the Aluto geothermal system. Deep stratigraphy and hypothesized subsurface structures on Aluto are summarized after Hutchison et al. (2015). The deep stratigraphy summarizes results from several publications (Gizaw, 1993; Gianelli and Teklemariam, 1993; Teklemariam et al., 1996) and drilling reports provided by the Geological Survey of Ethiopia (Yimer, 1984; Mamo, 1985; ELC Electroconsult, 1986; Teklemariam, 1996). Red 'F' labels indicate major fumarole and degassing regions mapped at the surface of the volcano (after Hutchison et al., 2015). The unit colours from light to dark grey provide a simple qualitative interpretation of permeability of the geological unit (after Gizaw, 1993); the least permeable units are shown in darkest grey. In line with observations from other geothermal field s (e.g., Tassi et al., 2013) we assume that H_2, H_2S, CH_4 (and other light hydrocarbons) are produced within the reservoir. Our main interpretation is that the magmatic and hydrothermal reservoirs of Aluto are connected, and that magmatic volatiles are channelled to the surface by faults and fracture pathways.*

Above the Neogene ignimbrites a thick sequence of basalt lavas (Bofa Basalts) 500–1000 m thick are identified (Teklemariam et al., 1996). The basalts are pervasively altered and sealed by deposition of hydrothermal alteration minerals (e.g., Gianelli and Teklemariam, 1993; Teklemariam et al., 1996), as a result they exhibit poor permeability (Gizaw, 1993). Overlying the basalts lavas are layers of interbedded sediment and volcanic tuff, that are also highly altered

and sealed by deposition of clay minerals (Teklemariam et al., 1996). It is unclear whether the cap rock for the geothermal reservoir comprises the Bofa Basalt or the altered tuffs and sedimentary layers. It is possible that the Bofa Basalt unit serves as a reservoir along the contacts and where it is fractured and brecciated, but ultimately we consider that together the basalts and altered sediments-tuffs provide a capping lithology for the system (Fig. 3.9). Above the cap layers peralkaline rhyolite volcanics erupted from the Aluto volcanic complex are encountered and comprise alternating layers of rhyolite lavas and volcaniclastic deposits. The ignimbrite at the base of these units (Fig. 3.9) is permeable and appears to provide a cool shallow aquifer that has been identified in a number of the deep wells at ~700 m (Gizaw, 1993).

The main feature of the Aluto geothermal field is that it is characterized by an upflow zone that coincides with the major NNE-trending AJFZ (Fig. 3.2A). Along this fault zone the in-hole temperatures (in excess of 300 °C), water chemistry (elevated Na/K ratios, Gizaw, 1993), and the presence of high-temperature calc-silicate minerals (e.g., epidote, garnet, prehnite, tremolite-actinolite) all support upflow from the reservoir towards the surface. Temperature profiles from the bottom of these wells (~2100 m) up to 700 m show this interval is characterized by boiling (Gizaw, 1993). Either side of this boiling zone lateral outflow of the reservoir fluid takes place. This is confirmed firstly, by temperature profiles in wells LA-4, LA-5 and LA-7 that show lower temperature (≤ 250 °C) waters infiltrating at ~1500 m (Fig. 3.9), and secondly by water chemistry which shows the fluids are more concentrated and distinct from the reservoir fluid. (i.e., waters have already boiled before entering the wells). Steam also condenses within the upflow zone and this likely supplies water to the cooler shallow (~700 m) aquifer (Fig. 3.9, Gizaw, 1993).

3.6. Causes of unrest

Understanding the triggering of ground deformation at active calderas is a key challenge in modern volcanology (Lowenstern et al., 2006; Poland et al., 2006; Gottsmann and Battaglia, 2008). In particular, interpreting the cause as magmatic intrusion versus aqueous hydrothermal fluid and gas movement has been a major topic of debate at other well studied caldera systems such as Campi Flegrei and Yellowstone (e.g., Wicks et al., 2006; Lowenstern et al., 2006; Caliro et al., 2007; Battaglia et al., 2006; Chiodini et al., 2012, 2015). In this section we summarise the main observations we can draw from our data and build a simple testable hypothesis for the causes of unrest at Aluto.

Ground surface displacement at Aluto is characterised by episodic uplift that causes edifice-wide inflation, followed initially by rapid subsidence and then by slower more gradual deflation (Section 3.3.1, Figs 2–6). The uplift location is centred within the caldera and is constant through time (between 2004–2011, Fig. 3.2). Our joint inversion of the available SAR data sets for the 2008–2010 uplift-subsidence event with a single spherical point source (Fig. 3.6) suggests a best fit depth of ~5.1 km. In Section 3.5 we suggested that all available evidence from the geothermal development on Aluto places the main geothermal reservoir at a depth of 2 km, and we infer that ~5 km deformation source is most likely located between the upper boundary of the magmatic reservoir and base of the geothermal system.

The uplift of active caldera systems is typically linked to fluid injection from depth to an inflating source region (Pritchard & Simons, 2002; Battaglia et al., 2006; Wicks et al., 2006 Hurwitz et al., 2007; Parks et al., 2012, 2015). At Aluto there is no evidence from any of the individual interferograms to suggest contracting sources elsewhere around the complex, so in line with these other studies, we infer that the inflation was fed from a depth greater than 5 km. The uplift (inflation pulse) shows two steps, suggestive of an accelerating deformation trend (Section 3.3.4,

Fig. 3.6D). This could either be explained by two pulses of fluid input to this source region, or alternatively damage and fracturing, increasing permeability and allowing a greater rate of fluid supply. Deformation data alone do not allow us to investigate these possibilities, nor do they unambiguously differentiate between whether the composition is gas, aqueous fluid or magma, or a combination of these.

At the point of peak uplift (maximum source inflation) subsidence (deflation) begins at Aluto (Fig. 3.6D). The subsidence of large calderas has been attributed to a number of factors including: local or regional tectonic earthquakes (Dzurisin et al., 1994), removal and migration of magmatic or hydrothermal fluids (e.g., Todesco et al., 2004; Wauthier et al., 2013), magma crystallization and thermal contraction and degassing (e.g., Caricchi et al., 2014; Parker et al., 2014), cooling and contraction of young volcanic deposits (Ebmeier et al., 2013; Parks et al., 2015), and/or a combination of all of the above (Mann and Freymueller, 2003; Acocella et al., 2015). Based on the pattern of deformation fringes at Aluto and close temporal relation with the uplift we exclude regional earthquake activity. Migration of magma can also be excluded because no eruption took place nor was any deformation source identified outside the caldera. The observed subsidence is also not due to the thermoelastic contraction of the recent lavas or pyroclastic material (e.g., Ebmeier et al., 2012); as these would show a spatially patchy distribution.

Ground subsidence is commonly observed during extraction of geothermal fluids (e.g. Massonnet et al., 1997; Carnec and Fabriol, 1999; Fialko and Simons, 2000; Vasco et al., 2002, 2013; Allis et al., 2009; Keiding et al., 2010). In Figure 3.6D we show the typical geothermal fluid extraction rates from the Aluto-Langano plant production. The productive geothermal wells LA-3 and LA-6 extract a two phase fluid (water and steam) with a total flow rate of 10.4–25.6 kg s^{-1} (Teklemariam and Beyene, 2001). Aluto geothermal reservoir is water dominated (e.g., Giannelli and Teklemariam, 1993), and so assuming that all extracted fluid is stored as water in the

reservoir then the total extraction rates are between –0.01 to –0.03 $m^3 s^{-1}$, or –0.3 to –1 × 10^6 m^3 yr^{-1}. Compared to the subsidence volumes estimated from the joint inversion (Fig. 3.6D) it is clear that geothermal fluid extraction does not match this, either for the roll-over period (–9 × 10^6 $m^3 yr^{-1}$) nor for the slower subsidence period (–3 × 10^6 $m^3 yr^{-1}$). In other words, rates of geothermal extraction from the deep wells are much lower than the volumes of deflation modelled (Fig. 3.6D), and on their own cannot account for the observed deflation signal. It is also worth noting that deformation related to ground-water extraction is often spatially irregular, localised across a few subsidence peaks and most-importantly fault controlled (e.g., Amelung et al., 1999; Fialko and Simons, 2000; Vasco et al., 2002; Samsonov et al., 2011; Sarychikhina et al., 2011); at odds with the caldera-wide, non-fault controlled, deflation patterns seen here (e.g., Fig. 3.2F).

Our favoured mechanism for the ground deformation at Aluto is that it represents a coupled magmatic-hydrothermal process. Peralkaline volcanoes are often considered to have a volatile-rich cap at around 5–6 km depth (e.g., Leat et al., 1984; Mattia et al., 2007; Biggs et al., 2009; Neave et al., 2012; Macdonald et al., 2014) consistent with our modelled source depth (Fig. 3.6C). Our interpretation is that magmatic intrusion and/or fluid injection into this zone provides the source for the uplift (Fig. 3.9). It is worth highlighting that recent silicic eruption deposits on Aluto have volumes between 1–100 × 10^6 m^3 (Hutchison et al., in review), overlapping with the volume of the observed inflation pulse (12–16 × 10^6 m^3, Fig. 3.6D). A key feature of the deformation pattern is the roll-over from inflation to deflation (Fig. 3.6D) which suggests that two competing processes are pressurising and depressurising the source region. Our main observation from the CO_2–$\delta^{13}C$ data was that the magmatic reservoir and hydrothermal reservoirs of Aluto are physically connected (Section 3.4), and we suggest that the major faults provide an efficient conduit for degassing and fluid release. Therefore our preferred interpretation is that the physical mechanism for uplift is a fresh magmatic intrusion or magmatic fluid input into a

shallow crustal reservoir at ~5 km (Fig. 3.9). The source region is not well sealed and gases leak into the geothermal reservoir and are rapidly lost causing ground the initial sharp deflation ('roll over', Fig. 3.6D, e.g., Caricchi et al., 2014; Girona et al., 2014). Slow long term subsidence over the following years may then be caused by gradual cooling of the magmatic intrusion and hydrothermal system (e.g., Mattia et al., 2007; Caricchi et al., 2014).

3.7. Testing the hypothesis

The new InSAR observations provides further evidence that accelerating uplift pulses and subsequent subsidence are taking place at Aluto (Section 3.3), supporting the previous conclusions of Biggs et al. (2011). A joint inversion method was used to determine the best-fitting spherical point source (Section 3.3.4), and this analysis suggested that a source located within the caldera at ~5 km depth produced the closest match to the InSAR data. It is important to realize that the Mogi model is set up to calculate surface deformation due to a point source in an elastic homogenous half-space. From our synthesis of the geothermal field (Section 3.5, Fig. 3.9) it is evident that sub-surface of Aluto is far from homogeneous and that there are significant vertical and lateral variations in parameters such rock permeability, compressibility and structural weaknesses. Numerical models of geothermal fields highlight that even small changes in permeability and anisotropy of the geothermal reservoir rock, and the depth and rate of hydrothermal fluid injection can result in to significant variations in ground surface displacement (e.g., Hurwitz et al., 2007; Hutnak et al., 2009). As the Aluto magmatic and hydrothermal systems are connected (Section 3.5) we posit that the true geodetic uplift and subsidence signal will certainly represent a more complex interaction than a simple Mogi model can capture. Consequently, future modelling efforts should be undertaken to investigate how parameters such as rock permeability, compressibility and structural weaknesses might affect the deformation signal at Aluto. This will allow a better understanding of how the initial magmatic and/or fluid injection goes on to affect a 'physically realistic' geothermal system.

Our hypothesis that the unrest events link to magmatic injection at ~5 km and subsequent degassing can be tested in a number of ways. Firstly, if the uplift is associated with an injection of magmatic fluid rather than magma then the density difference (~1000 kg m^{-3} for hydrothermal fluids versus ~2500 kg m^{-3} for silicate melts) could be distinguished from time-lapse using gravity measurements. Combining time series of geodetic and gravity measurements, and with knowledge of the natural changes in water table, it may be possible to infer the density of the intrusive fluids and their relation to the deformation source (e.g., Gottsmann and Battaglia, 2008). These methods have been exploited both at Campi Flegrei caldera (Battaglia et al., 2006) and Long Valley caldera (Battaglia et al., 2003; Tizzani et al., 2009).

Long-term geochemical monitoring may also shed light nature on the causes of unrest. For example, if the uplift was caused either by hydrothermal fluid injection or magma intrusion, then these should produce distinct chemical signals as the fluid and/or gas effluent is released into the geothermal reservoir. For a pure magmatic intrusion there should be significant increases in He, while if the injection was entirely fluid then this would not be seen (due to He being highly insoluble). Therefore monitoring gas ratios, e.g., He/CH_4 (e.g., Chidoini et al., 2015), could be used to confirm arrival of new magmatic gases at the surface. Further, our suggestion that the roll over from uplift to subsidence is caused by degassing along faults pathways could also be tested by making repeat CO_2 flux surveys at sites along the AJFZ (e.g., Parks et al., 2013), we hypothesize that peak degassing would follow maximum inflation.

Finally, we re-emphasize that comparable uplift-subsidence events are taking place at a number of active volcanoes in EARS (Biggs et al., 2009, 2011). Deformation signals at Paka and Longonot (Biggs et al., 2009, in review) show similarities in terms of the magnitude of uplift (10–15 cm) and the temporal ‘roll-over’ from uplift to subsidence. This raises important

questions as to whether the same physical process is active at all of these volcanoes, and if so whether a single monitoring proxy (e.g., He/CH_4 as suggested above) could be quickly adopted at each complex to provide insight into the state of the system. However, as we have shown in Sections 3.4.2 and 3.4.3, measureable geochemical parameters (e.g., CO_2–$\delta^{13}C$) vary spatially and on short-timescales even during a single survey; careful characterization of the 'background' variability (e.g., Tassi et al., 2013) should be undertaken before useful interpretations can be made across a period of active deformation.

3.8. Conclusions

The Aluto magmatic and hydrothermal systems are physically connected by faults and fractures, such that deep (> 2km), hot (>250°C) geothermal fluids receive a continuous input of magmatic volatiles. Fluids migrate along major tectonic faults that dissect the complex and ascend to the surface. These fluids degas and high-concentrations of magmatic CO_2 ($\delta^{13}C$ of –4.2 to –4.5 ‰) are released. Episodic uplift-subsidence events also typify the Aluto volcanic system. A joint inversion of new and existing InSAR data suggest that the source is located at ~5 km, and requires an inflationary volume change of $+12–16 \times 10^6$ m^3. These volumes are well below those associated with geothermal production at Aluto and are more typical of recent eruptive volumes. Deformation events play out in a style characteristic of a coupled magmatic-hydrothermal system, and on this basis we propose that uplift is caused by a deep magmatic intrusion or magmatic fluid injection, and that faults provide key pathways for gas and fluid leakage into the geothermal reservoir. This hypothesis can be tested by monitoring changes in gas flux and composition along Aluto's main fault zone, which provides an important conduit for fluid upflow and sampling of the deeper reservoirs.

Chapter 4

The volcanic and magmatic evolution of Aluto

A version of this chapter has been submitted as an article to the Journal of Volcanology and Geothermal Research: Hutchison et al. *in review*. The eruptive history and magmatic evolution of Aluto volcano: new insights into silicic peralkaline volcanism in the Ethiopian rift. Authors as follows:

William Hutchison[1], David M. Pyle[1], Tamsin A. Mather[1], Gezahegn Yirgu[2], Juliet Biggs[3], Benjamin E. Cohen[4], Dan N. Barfod[4] and Elias Lewi[5]

1. COMET, Department of Earth Sciences, University of Oxford, South Parks Road, Oxford OX1 3AN, UK
2. School of Earth Sciences, Addis Ababa University, P.O. Box 1176, Addis Ababa, Ethiopia
3. COMET, School of Earth Sciences, University of Bristol, Wills Memorial Building, Queens Road, Bristol BS8 1RJ, UK
4. NERC Argon Isotope Facility, Scottish Universities Environmental Research Centre, Rankine Avenue, East Kilbride G75 0QF, UK
5. IGSSA, Addis Ababa University, PO Box 1176, Addis Ababa, Ethiopia

---

Abstract

The silicic peralkaline volcanoes of the East African Rift are some of the least studied and yet potentially most dangerous volcanoes in the world. We present the first detailed account of the eruptive history of Aluto, a restless silicic volcano located in the Main Ethiopian Rift, using new constraints from fieldwork, remote sensing, $^{40}Ar/^{39}Ar$ geochronology and geochemistry. Prior to the growth of the Aluto volcanic complex (before 500 ka) the region was characterized by a significant period of fault development and mafic fissure eruptions. The earliest volcanism at Aluto built up a trachytic complex over 8 km in diameter. Aluto then underwent large-volume ignimbrite eruptions at 316 ± 19 ka and 306 ± 12 ka developing a ~42 km^2 collapse structure. After a hiatus of ~250 kyr, post-caldera volcanism has taken place between 55 ± 19 ka and 16 ± 14 ka. During this period highly-evolved peralkaline rhyolite lavas, ignimbrites and pumice fall deposits have erupted from vents across the complex. Geochemical modelling is consistent with rhyolite genesis from protracted fractionation (>80 %) of basalt that is compositionally similar to rift-related basalts found east of the complex. Based on the style and volume of recent eruptions we suggest that silicic eruptions occur at an average rate of 1 per 1000 years, and that future eruptions of Aluto will involve explosive emplacement of localised pumice cones and effusive obsidian coulees of volumes between 1–100 x 10^6 m^3.

4.1. Introduction

Quaternary volcanism in the Ethiopian Rift has been marked by the eruption of hundreds of cubic kilometres of highly evolved silicic magmas (e.g., Mohr, 1971; Di Paola, 1972; Barberi, et al., 1975; Lahitte et al., 2003; Peccerillo et al., 2003, 2007; Field et al., 2012, 2013). Silicic volcanoes have produced extensive rhyolitic lavas as well as pyroclastic density current (PDC) and tephra fall deposits; many show evidence of large (>10 km^3), geologically young (<500 ka), caldera-forming eruptions (e.g., Shala, Mohr et al. 1980; Gedemsa, Peccerillo et al., 2003 and Kone, Rampey et al., 2010; 2014) and several show signs of unrest (e.g., Corbetti, Aluto, Bora and Haledebi; Biggs et al., 2011). Many of these volcanoes are located in densely populated regions (Fig. 4.1A), and it is estimated that over 10 million people in Ethiopia live within 30 km of a Holocene volcanic centre (Brown et al., 2014). Our understanding of the eruptive histories of the silicic complexes is poor and hence there are large uncertainties as to the volcanic hazards they may pose in the future (Aspinall et al., 2011).

The focus of this study is the Aluto volcanic complex (Fig. 4.1B), a silicic peralkaline volcano which lies in the central sector of the Main Ethiopian Rift (MER), and for which few details of its eruptive past are known. Aluto is currently restless, having undergone episodic ground deformation for at least the past decade (Biggs et al., 2011). This is of particular concern given that several thousand people live on the volcano as well as in the nearby towns of Ziway, Adami Tullo and Bulbula (each with populations in the range of 10,000–50,000, Central Statistical Agency of Ethiopia, 2012), and according to the Smithsonian Global Volcanism Program (Siebert and Simkin, 2002) 6.8 million people live within 100 km of the volcano. Aluto also hosts Ethiopia's only geothermal power plant (e.g., Gizaw, 1993; Gianelli and Teklemariam, 1993; Teklemariam et al., 1996), and while the plant is only producing 7 MW at present there are plans for significant expansion. Locating this major infrastructure on a volcanic edifice where eruptive frequency is unknown poses inherent risks (e.g., Wilson et al., 2012; Wilson et al., 2014).

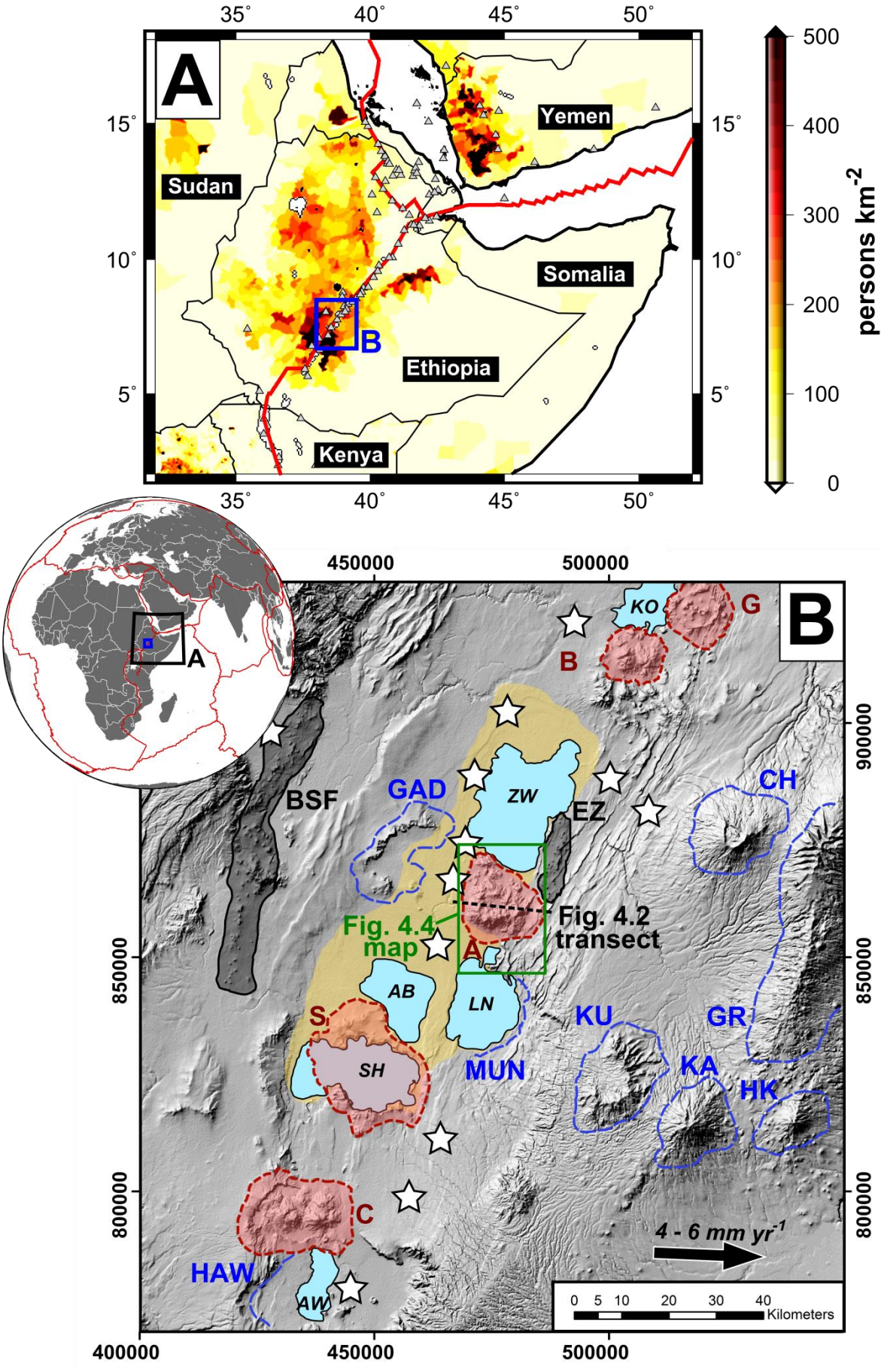
A
35˚
40˚
45˚
50˚
15˚
10˚
5˚
Yemen
Sudan
Somalia
Ethiopia
Kenya
B
500
400
300
200
100
0
persons km-2
A
B
450000
500000
900000
850000
800000
400000
KO
G
B
BSF
GAD
ZW
EZ
CH
Fig. 4.4
map
Fig. 4.2
transect
A
AB
LN
S
SH
MUN
KU
GR
KA
HK
C
HAW
AW
4 - 6 mm yr-1
0 5 10 20 30 40
Kilometers

[110]

Knowledge of Aluto's eruptive history is also of considerable importance for regional palaeoclimate and palaeoanthropological studies. Aluto lies in the centre of the Ziway-Shala lake basin (Fig. 4.1B), a key East African intracontinental rift basin that preserves palaeoclimate proxy records (e.g., Gasse and Street, 1978; Street, 1979; Le Turdu et al., 1999; Benvenuti et al., 2002, 2013; Gibert et al., 2002) as well as archaeological records of Middle and Later Stone Age (280–11 ka) hominin populations (e.g., Laury and Albritton, 1975; Morgan and Renne 2008; Sahle et al., 2013, 2014; Ménard et al., 2014; Benito-Calvo et al., 2014). An understanding of volcanism in this basin is complementary to these studies, because edifice development will change the rates and spatial patterns of sediment accumulation which preserve palaeoclimate records (Le Turdu et al., 1999); widely dispersed tephra derived from these volcanoes form the key marker horizons that constrain the rates of hominin evolution and dispersal (e.g., Morgan and Renne 2008; WoldeGabriel et al., 2005); and volcanoes have provided important resources (e.g., obsidian) that hominin populations have worked and transported since the earliest Palaeolithic, 1.7 Million years ago (e.g., Piperno et al., 2009).

Figure 4.1: ***A)*** *Map of Ethiopia and neighbouring countries overlain with population density. Red lines indicate major plate boundaries and grey triangles show Quaternary volcanic centres (after Siebert and Simkin, 2002). Population data are estimates for 2015 provided by Socioeconomic Data and Applications Center (SEDAC), http://sedac.ciesin.columbia.edu. Population values are extrapolated based on a combination of national growth rates from United Nations statistics and sub-national growth rates from census dates. The blue rectangle marked B, shows the area covered by the DEM in Fig. 4.1B.* ***B)*** *Hillshade SRTM DEM showing the location of the Aluto volcanic complex (marked A) within the central segment of the Main Ethiopian Rift (MER). Quaternary silicic volcanic complexes are shaded red, and include: Corbetti (marked C), Shala or O'a caldera (marked S); Bora-Bericcio (marked B) and Gedemsa (marked G). Recent mafic cinder cones and lavas of East Ziway (marked EZ) and the Butajira-Silti field (marked BSF) are shown by the dark grey shaded areas. Silicic volcanic complexes that became extinct prior to 1 Ma are outlined by the blue dashed lines, and include: Hawasa (marked HAW), Munesa (marked MUN), Gademotta (marked GAD), Kubsa (marked KU), Kaka (marked KA), Chilalo (marked CH), Hunkuolo (marked HK) and the Galama Range (marked GR). The beige shaded area identifies the maximum extent of the Ziway-Shala lake system that developed in the Mid–Late Pleistocene (Le Turdu et al., 1999; Benvenuti et al., 2002, 2013). The major present-day lakes are identified as: Ko: Lake Koka; Zw: Lake Ziway; Ln: Lake Langano; Ab: Lake Abijta, Sh: Lake Shala and AW: Lake Awasa. White stars identify centres of population with >10,000 inhabitants. Current extension of the MER, after Keir et al. (2006), Bendick et al. (2006) and Stamps et al. (2008), is indicated by the black arrow with motion relative to a fixed Nubian plate. The black and blue outlined areas on the globe inset correspond to the regions covered in Figures 4.1A and 4.1B, respectively.*

In this paper, field studies, remote sensing, $^{40}Ar/^{39}Ar$ geochronology and geochemical techniques are integrated to document the volcanic and magmatic evolution of the Aluto volcanic complex. We reconstruct the eruptive history of Aluto and present a new geological map (Section 4.5); we present the first dedicated whole-rock geochemical study of the volcano, and assess magma petrogenesis (Section 4.6), and finally, we develop a conceptual model of the eruptive history and magmatic evolution of the complex within the context of the evolving rift (Section 4.7).

4.2. Regional tectonic and volcanic overview

The MER is an active continental rift that forms the northernmost section of the East African Rift System (see reviews by Ebinger, 2005; Corti, 2009). It is a classic example of an oblique rift (Corti et al., 2013) and is traditionally sub-divided into northern, central and southern segments that reflect prominent spatial variations in fault architecture and lithospheric characteristics (e.g., Hayward and Ebinger, 1996; Bonini et al., 2005; Keranen and Klemperer, 2008; Agostini et al., 2011). Aluto lies in the central MER (CMER) where the pattern of faulting is characterized by two distinct groups: (1) boundary faults located on the margins of the rift, and (2) localized internal faults, mapped as 'Wonji' faults (Agostini et al., 2011, Keir et al., 2015). The boundary faults formed during the initial stages of rifting (at 8–6 Ma in the CMER, WoldeGabriel et al., 1990; Bonini et al., 2005) and appear to facilitate very limited tectonic extension at present (Keir et al., 2006; Pizzi et al., 2006; Agostini et al., 2011). The Wonji faults, located in the ~15 km wide axial zone of the rift, are short, right-stepping en-echelon features that developed after ~2 Ma (Boccaletti et al., 1998 and Ebinger and Casey, 2001) and are the focus of present-day tectonic strain (Keir et al., 2006, 2015; Agostini et al., 2011).

There has been surface volcanism throughout the development of the MER (WoldeGabriel et al., 1990, 1992, 2000; Abebe et al., 2007) but full understanding of the links between volcanic evolution and rift development is still hampered by a lack of detailed eruption chronologies for

many individual volcanoes (Corti, 2009). Prior to development of the silicic volcanoes exposed along the rift axis today (including: Gedemsa, Bora-Berrecio, Aluto, Shala and Corbetti, Fig. 4.1B), several large silicic caldera-forming volcanoes were active in the MER during the Early Pliocene–Early Pleistocene (4–1 Ma, Fig. 4.1B). Tuff deposits from these volcanoes are often found in fault sections on the margins of the rift (e.g., WoldeGabriel et al., 1990, 1992), while the associated caldera structures are deeply eroded or otherwise completely covered by younger basin-filling sediments (WoldeGabriel et al., 1990; Le Turdu et al., 1999). Three of the largest silicic caldera-forming volcanoes (Munesa, Awassa and Gademotta) formed within the axial region of the CMER (Fig. 4.1B), and are now extinct. At Munesa caldera climactic eruptions are dated at ~3.5 Ma (WoldeGabriel et al., 1990, 1992; Le Turdu et al., 1999), at Awassa caldera major eruptions took place at 1.85–1.1 Ma (WoldeGabriel et al., 1990) and at Gademotta, ~20 km NW of Aluto the final phase of activity is dated to ~1.3 Ma (Vogel et al., 2006). Volcanism in the MER, prior to 1 Ma, was diffuse and encompassed a wide footprint of the rift zone (Boninin et al., 2005; Corti, 2009), as evidenced by off-axis trachytic and basaltic volcanic centres (e.g., Chilalo, Hunkuolo, Kaka, Kubsa, Fig. 4.1B; Mohr and Potter, 1976; WoldeGabriel et al., 1990).

Since 0.65 Ma, eruptive activity has been focused within right-stepping, en-echelon volcanic segments along the axis of the rift that are co-located with the zones of Wonji faulting (Abebe et al., 2007; Corti, 2009; Beutel et al., 2010; Keir et al., 2006, 2015). Volcanism has been strongly bimodal (Abebe et al., 2007). Mafic rocks form cinder cone fields and lava flow deposits that are often aligned along Wonji fault networks (e.g., East Ziway, Fig. 4.1B, Abebe et al., 2007; Rooney et al., 2007). Silicic rocks are peralkaline and represented by large complexes 10–20 km in diameter located along the axis of the rift (Di Paola, 1972). The silicic volcanoes have compositionally zoned magma chambers (Peccerillo et al., 2003, 2007; Ronga et al., 2009), and the majority have undergone large-volume ignimbrite eruptions, creating calderas that scar the present day rift zone (e.g., Acocella et al., 2002; Rampey et al., 2010). Basaltic and silicic

volcanism in the MER appears to be spatially-separated and there is limited evidence to suggest that these compositions erupt contemporaneously from the same vent system (unlike magmatic systems in the Afar, e.g., Dabbahu: Barberi, et al., 1975; Field et al., 2013). Only in the waning stages of silicic magmatic activity in the MER do basaltic lavas erupt directly through the floor of the caldera systems (e.g., at Gedemsa: Pecerrilo et al., 2003).

There are limited accounts of historical volcanic activity in the MER and the only reported eruptions occurred at Fentale and Kone volcanoes in the 1800–1830's (Williams et al., 2004; Rampey et al., 2010). Not one of the MER complexes is routinely monitored (Aspinall et al., 2011), and so to assess the probabilities of future unrest volcanologists must rely on observations of the rates and volumes of past eruptive activity (e.g., Pyle and Elliott, 2006; Nomikou et al., 2014)

4.3. Previous studies of Aluto

The earliest geological descriptions of Aluto come from regional scale mapping reports (e.g., Dakin and Gibson, 1971; Di Paola, 1972). These studies identified that the bulk of recent volcanic products of Aluto are rhyolitic PDC deposits and obsidian coulees. Di Paola (1972) recognized that various craters and lava flow deposits exist along predominantly NNE-SSW orientations, parallel to the Wonji fault structures, while Dakin and Gibson (1971) postulated that there had been a caldera-forming event at Aluto based on field evidence for a ~1 km long segment of the caldera wall visible on the north-east of the complex.

In 1970 the Aluto-Langano region was identified as a site for geothermal development and eight exploratory wells were completed between 1981 and 1985 (ELC Electroconsult, 1986). Geological mapping was undertaken at the same time (Kebede et al., 1985), and lithological descriptions were also completed for deep wells LA-4 and LA-8, see Tables A2.1 and A2.2,

respectively (Yimer, 1984; Mamo, 1985). Using the cores and cuttings collected during deep well drilling several previous publications (e.g., Gizaw, 1993; Gianelli and Teklemariam, 1993; Teklemariam et al., 1996), and drilling reports (Yimer, 1984; Mamo, 1985; ELC Electroconsult, 1986; Teklemariam, 1996) have established a deep stratigraphy of the complex. In Figure 4.2 we summarize the Aluto deep well stratigraphy and also overlay major structural features recognized by Hutchison et al. (2015). Lithological descriptions of the units are provided in Section 4.5.1 and Figure 4.3.

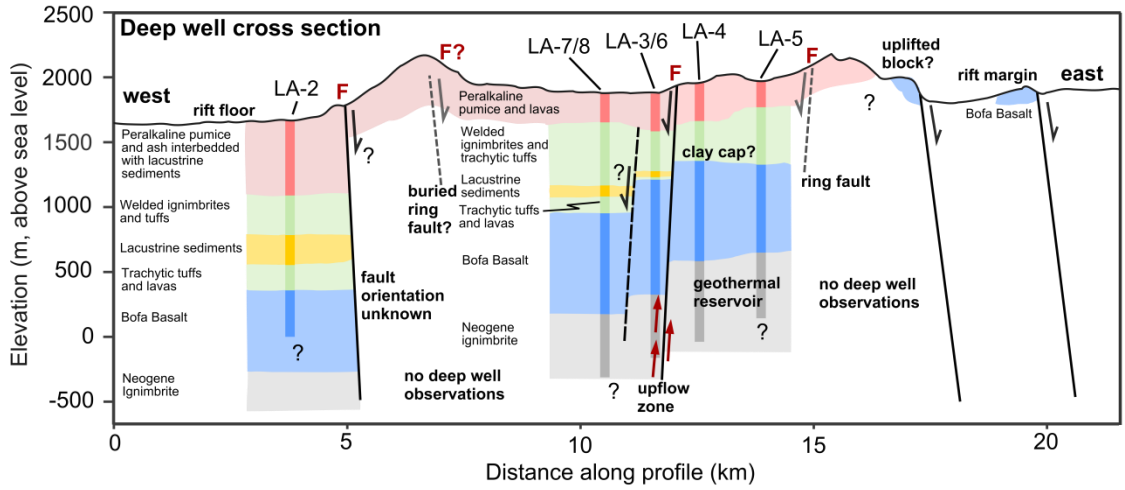

Figure 4.2: *West-east cross section showing the deep stratigraphy and hypothesized subsurface structures on Aluto (after Hutchison et al., 2015). Note that the transect line is shown in Figure 4.1B. Well data represent the synthesis of several publications (Gizaw, 1993; Gianelli and Teklemariam, 1993; Teklemariam et al., 1996) and drilling reports provided by the Geological Survey of Ethiopia (Yimer, 1984; Mamo, 1985; ELC Electroconsult, 1986; Teklemariam, 1996). The geological units shown have been correlated between the different wells on Aluto (Gizaw, 1993; Gianelli and Teklemariam, 1993) and indicate a prevailing mode of deposition rather than a single homogeneous unit (e.g., paleosols occur within the Bofa Basalt, see Section 4.5.1 for detailed descriptions). Red arrows indicate main upflow zone of geothermal reservoir along the Artu Jawe fault zone (Gianelli and Teklemariam, 1993; Teklemariam et al., 1996; Hutchison et al., 2015). Red 'F' labels indicate major fumarole and degassing regions mapped at the surface of the volcano (after Hutchison et al., 2015).*

The only previous interpretations of the eruptive history of Aluto were made by Kebede et al. (1985) and ELC Electroconsult (1986). They each proposed a period of sub-aerial basaltic eruptions (Bofa Basalts, at 1.6 ± 0.5 Ma, Table 4.1) prior to the first silicic volcanism. Silicic eruptions at Aluto then built up an early dome complex, culminating in several large ignimbrite

eruptions and caldera collapse. K/Ar dates (cited in Teklemariam et al., 1996) suggested that the climactic phases of eruption took place at ~155 ka (Table 4.1). Subsequent investigations of Aluto have focussed on the geothermal field (e.g., Gebregzabher, 1986; Valori et al., 1992; Gizaw, 1993; Ginaelli and Teklemariam, 1993; Teklemariam et al., 1996; Saibi et al., 2012) and the outline eruptive history proposed by Kebede et al. (1985) and ELC Electroconsult (1986) has not been seriously re-evaluated within the last forty years.

4.4. Sampling and analytical techniques

Our stratigraphy was established from 8 weeks of field mapping conducted during 2012–2014. Further, the Natural Environment Research Council's Airborne Research and Survey Facility (NERC-ARSF) acquired high-spatial resolution topography (lidar), hyperspectral data and aerial photographs of the complex on 16th November 2012. Digital geological mapping was carried out in ArcGIS and involved analysis of orthorectified aerial photos, the lidar DEM as well as Google Earth and ASTER satellite imagery for regions beyond coverage of the lidar DEM. Volcanic and tectonic fault structures were mapped by Hutchison et al. (2015) using remote sensing techniques and soil-CO_2 degassing surveys. The volumes of recent volcanic deposits (obsidian coulees and pumice cones) were estimated using the lidar DEM following the methods of Nomikou et al. (2014). In brief, we use polygons to outline and mask out the deposit from the DEM. After removing this region from the DEM we then interpolated a smoothed near-flat pre-eruption surface across the masked area (processing was carried out in GMT software using a variable tension parameter, Nomikou et al., 2014). We then subtracted the present day DEM from the interpolated DEM to calculate the residual volume between the surfaces, thus providing a volume estimate for the volcanic deposit. An example of this technique is given in Figure A2.1. As the internal structure of the silicic domes on Aluto is poorly constrained we simply present the total volume of the deposit rather than a dense rock equivalent. Maximum and minimum volumes

calculated by Nomikou et al., (2014) for different sub-aerial lava flows at Santorini volcano are typically within 25 % and provide an estimate for the volume uncertainty using this method.

We obtained high-precision $^{40}Ar/^{39}Ar$ age determinations at key points in the stratigraphic sequence (Fig. 4.3). Unweathered lava and bulk ignimbrite samples were collected in the field and pulverised in a jaw-crusher. Sanidine phenocrysts (250–500 μm in diameter) were separated from the crush using magnetic and LMT heavy liquid density separation techniques. The phenocrysts were then leached ultrasonically in 5 % HF for ~3 minutes to remove adhering glass and groundmass. Grains were rinsed in distilled water and dried, followed by handpicking under a binocular microscope to remove any remaining contaminant phases (fluid/melt inclusions or quartz crystals). Samples were irradiated in the Cd-lined facility at the Triga Reactor, Oregon State University, and subsequently analysed at the NERC Argon Isotope Facility, Scottish Universities Environmental Research Centre (SUERC). Five $^{40}Ar/^{39}Ar$ ages determined for Aluto were reported by Hutchison et al. (in review), who used these ages to examine silicic magma fluxes in the MER. In this study we use these five published $^{40}Ar/^{39}Ar$ ages, plus an additional two ages, to examine stratigraphic relationships and the rates of recent volcanism at Aluto. A full description of the methods is given in Hutchison et al. (in review). A limited number of geochronological data have been presented previously for Aluto; these are shown alongside our new $^{40}Ar/^{39}Ar$ ages in Table 4.1.

A total of 36 lava and pumice samples were selected for whole-rock chemical analysis. Samples were trimmed of weathered material, and powdered in an agate ball mill. Major and selected trace element analysis was conducted at the Department of Geology at the University of Leicester by X-ray fluorescence (XRF) using a PANalytical Axios-Advanced XRF spectrometer (glass fusion beads were prepared for major elements, and powder pellets were prepared for trace elements). A complete suite of trace elements were also analysed by Inductively Coupled Plasma-Mass

Spectroscopy (ICP-MS) at the Department of Earth Sciences, University of Oxford. For this, solutions of powdered samples were produced in a multi-stage method, involving initial hot, low-pressure digestion in HF and HNO_3, followed by multiple drying and dissolution steps using HNO_3, before final dilution in HNO_3. Standard analyses for both XRF and ICP-MS methods were within 10% of their reference values. This project has also compiled previous published and unpublished element data for the Aluto volcanic complex (from Di Paola, 1972; Yimer, 1984; Mamo, 1985 and Teklemariam, 1996). Both previous and new bulk major and trace element data, a total of 45 samples, are presented in Table A2.3a–d.

4.5. Volcanic stratigraphy

We have divided the stratigraphic relations as follows: Section 4.5.1 presents the deep well stratigraphy compiled from previous publications; Section 4.5.2 presents our field stratigraphy from surface mapping, and Section 4.5.3 presents age constraints and correlations between the surface and subsurface stratigraphy.

4.5.1 Deep well stratigraphy

Previous publications on the geothermal field of Aluto (Gizaw, 1993; Gianelli and Teklemariam, 1993; Teklemariam et al., 1996) and drilling reports provided by the Geological Survey of Ethiopia (Yimer, 1984; Mamo, 1985; Electroconsult, 1986; Teklemariam, 1996) have been used to establish a composite deep stratigraphy for Aluto (Fig. 4.3, right-hand column). In the following sections the unit name of previous authors is shown first, followed by our revised classification in brackets (justified in Section 4.5.3).

Sample	Sample location		Rock type	Unit	Method	Age	Reference	Additional notes
	Lat (°N)	Lon (°E)						
18 11 07a	7.69173	38.79719	ignimbrite	Qgyi	$^{40}Ar/^{39}Ar$ (sanidine)	316 ± 12 (316 ± 19) ka	Hutchison et al., in review	
13 05 04	7.84068	38.73031	ignimbrite	Qgei	$^{40}Ar/^{39}Ar$ (sanidine)	306 ± 8 (306 ± 12) ka	Hutchison et al., in review	
18 02 04	7.74193	38.80486	comenditic rhyolite	Qcr	$^{40}Ar/^{39}Ar$ (sanidine)	55 ± 9 (55 ± 19) ka	Hutchison et al., in review	
18 01 08	7.83245	38.74576	obsidian	Qpo	$^{40}Ar/^{39}Ar$ (sanidine)	18 ± 10 (22 ± 14) ka	this study	
30 01 LNE	7.81176	38.79360	obsidian	Qpo	$^{40}Ar/^{39}Ar$ (sanidine)	18 ± 8 (19 ± 5) ka	Hutchison et al., in review	
01 02 14	7.77725	38.76988	obsidian	Qpo	$^{40}Ar/^{39}Ar$ (sanidine)	61 ± 8 (62 ± 13) ka	this study	
31 01 LE	7.78321	38.82680	obsidian	Qpoy	$^{40}Ar/^{39}Ar$ (sanidine)	12 ± 7 (16 ± 14) ka	Hutchison et al., in review	
unknown	unknown (south of Gademotta)		ignimbrite	unknown	K/Ar (phase unknown)	155 ± 8 ka	ELC Electroconsult, 1986	dating procedure and error on age not reported, ignimbrite apparently overlain by the lacustrine sediments
29 BT82	7.81667	38.75833	obsidian	Qpo?	K/Ar (groundmass)	42 ± 10 ka	WoldeGabriel et al., 1990	
30 BT79A	7.74167	38.79167	rhyolite	Qao?	K/Ar (groundmass)	78 ± 20 ka	WoldeGabriel et al., 1990	
31 LA3	7.79167	38.80000	ignimbrite	Nqui	K/Ar (feldspar)	1390 ± 100 ka	WoldeGabriel et al., 1990	Crystal rich welded tuff from deep well, pervasive hydrothermal alteration of sample
33 BT92	7.86667	38.90833	basalt	Nquw	K/Ar (groundmass)	290 ± 100 ka	WoldeGabriel et al., 1990	Hawaiite from east of Lake Ziway
S-1	rift escarpment near Munesa		ignimbrite	Nqui	K/Ar (sanidine)	2300 ± 300 ka	Teklemariam, 1996	
S-1	rift escarpment near Munesa		ignimbrite	Nqui	K/Ar (glass)	2300 ± 500 ka	Teklemariam, 1996	
S-2	eastern flank of Aluto		basalt	Nqub	K/Ar (plagioclase)	1600 ± 500 ka	Teklemariam, 1996	
Abernosa pumice (Deka Wede)	7.79249	38.68877	tephra	Qpo tephra?	^{14}C (lacustrine silt and charcoal)	27670–25162 to 14809–13106 Cal BP	Street, 1979; Le Turdu et al., 1999; Benvenuti et al., 2002; Menard et al., 2014	thick volcaniclastic sequence with ~13 distinct tephra layers
Pumice lapilli (Deka Wede)	7.79249	38.68877	tephra	Qup?	^{14}C (lacustrine marl and charcoal)	15018–13704 to 9964–9074Cal BP	Street, 1979; Le Turdu et al., 1999; Benvenuti et al., 2002; Menard et al., 2014	pumice overlying fluvial sands, above the Abernosa pumice
Pumice (Deka Wede)	7.79249	38.68877	tephra	Qup?	^{14}C (charcoal and melanoides shells)	9964–9074 to 6860–6390 Cal BP	Street, 1979; Le Turdu et al., 1999; Benvenuti et al., 2002; Menard et al., 2014	pumice overlying palaeosol, youngest tephra at Deka Wede
Pumice (Haroresa)	7.67408	38.81026	tephra	Qup?	^{14}C (melanoides shells)	11252–11068 to 7338–7173 Cal BP	Benvenuti et al., 2013	pumice bracketed by gravels, youngest tephra at Haroresa

Table 4.1: *Compilation of new and existing age constraints on volcanism at Aluto. $^{40}Ar/^{39}Ar$ ages shown are the weighted mean ± standard error of the mean (1σ), and in brackets the arithmetic mean ± one standard deviation (we quote the latter throughout the manuscript). Errors on other ages are quoted as originally published. Radiocarbon dates were calibrated with IntCal13 (Reimer et al., 2013) and OxCal v.4.2. Calibrated radiocarbon ages (2σ confidence interval) represent the age range of the deposits below and above the tephra layer, respectively.*

Unit		Nqui[1]	Nqub[1]	Qdt[2]	Qgyi[1]	Qgei[2]	Qcr[2]	Qao[2]	Qpo[2]	Qwai[2]	Qup[2]	Qpby[2]	Qpoy[2]
TAS subdivision		Rhyolite (C)	Basalt	Trachyte (C)	Rhyolite (P)	Rhyolite (C)	Rhyolite (C)	Rhyolite (P)	Rhyolite (P)	BTA	Rhyolite (P)	Rhyolite (P)	Rhyolite (P)
Type sample		S-1	S-2	15 02 08	18 11 07b/S-3	13 05 04	18 02 04	02 02 12	18 01 08	15 01 07B	03 02 23	30 01 06B	31 01 LE
Type location	**Lat (°N)**	Rift escarpment near Munesa	Eastern flank of Aluto complex	7.680784	7.69173	7.84068	7.74193	7.74960	7.83245	7.83979	7.81641	7.82314	7.78321
	Lon (°E)			38.806054	38.79719	38.73031	38.80486	38.80618	38.74576	38.72940	38.75248	38.78288	38.82680
Age (ka)		2300 ± 300 (†)	1600 ± 500 (†)	570–330 (+)	316 ± 19 (*)	306 ± 12 (*)	55 ± 19 (*)	n.d.	22 ± 14 (*)	n.d.	n.d.	n.d.	12 ± 7 (*)
SiO_2		70.21	49.76	65.18	69.92	71.13	70.02	72.68	73.15	59.85	70.86	72.41	73.56
TiO_2		0.50	2.86	0.89	0.44	0.34	0.43	0.30	0.22	1.64	0.17	0.23	0.32
Al_2O_3		12.23	16.79	15.46	10.37	11.46	12.08	10.03	8.88	15.13	7.78	9.05	9.78
FeO_t		5.85	11.56	5.72	6.74	5.21	5.57	5.25	5.82	7.32	6.48	5.37	5.03
MnO		0.17	0.17	0.22	0.27	0.22	0.19	0.22	0.25	0.14	0.32	0.22	0.22
MgO		0.30	4.15	0.59	0.21	0.10	0.10	0.00	0.00	2.53	0.00	0.00	0.00
CaO		0.13	7.83	2.14	0.54	0.39	0.18	0.24	0.20	4.83	0.14	0.20	0.22
Na_2O		4.06	3.28	5.46	5.98	5.79	5.32	6.15	6.31	4.64	6.69	5.22	5.80
K_2O		4.09	1.10	3.38	4.38	4.51	4.72	4.39	4.27	2.70	4.15	4.41	4.35
P_2O_5		0.03	0.62	0.21	0.02	0.02	0.01	0.01	0.01	0.27	0.01	0.01	0.01
SO_3		-	-	0.01	-	0.00	0.00	0.00	0.00	0.06	0.00	0.00	0.00
LOI		1.91	1.49	0.31	0.68	0.22	0.82	-0.22	-0.04	0.57	2.14	2.19	-0.40
Total		99.48	99.61	99.57	99.55	99.42	99.43	99.06	99.08	99.70	98.74	99.32	98.89
NK/A		0.91	0.39	0.82	1.41	1.26	1.15	1.48	1.69	0.70	1.99	1.48	1.46
Y		74	33	76	73	68	64	100	116	32	190	121	88
Zr		1156	285	627	992	838	787	942	1102	359	1655	1059	771
Nb		147	38	84	166	142	120	151	166	46	264	170	122
Rb		62	15	82	110	112	69	106	124	63	156	110	83
Sr		7	484	300	12	11	7	4	2	361	8	5	5
Ba		105	539	955	287	234	370	213	347	776	397	367	470
La		196	50	75	125	102	58	124	147	50	230	145	106
Ce		191	97	152	252	227	103	255	302	96	475	299	216
Cr		3	21	0	3	0	0	2	1	12	0	0	2
Co		10	41	4	12	4	4	10	9	21	0	0	13
Ni		5	17	0	3	0	0	0	1	7	1	0	1
V		4	281	9	5	6	2	0	0	180	0	0	0

Table 4.2: *Geochemical overview of the main eruptive units. Major element concentrations are in wt. %, trace element concentrations are in ppm. Major elements were measured by XRF, trace elements were measured by either XRF or ICP-MS, as indicated by 1, 2 in the unit row, respectively. For the TAS subdivision row, P and C correspond to pantellerite and comendite respectively. TA stands for trachyandesite. The symbols represent ages from Teklemariam, 1996 (†), Le Turdu et al., 1999 (+) and this study (*). n.d. stands for no data. For SO_3 dash (-) indicates below detection limits. LOI: loss on ignition. NK/A: is an indication of peralkalinity and was calculated as molar $(Na_2O + K_2O)/Al_2O_3$ (e.g., Macdonald, 1974)*

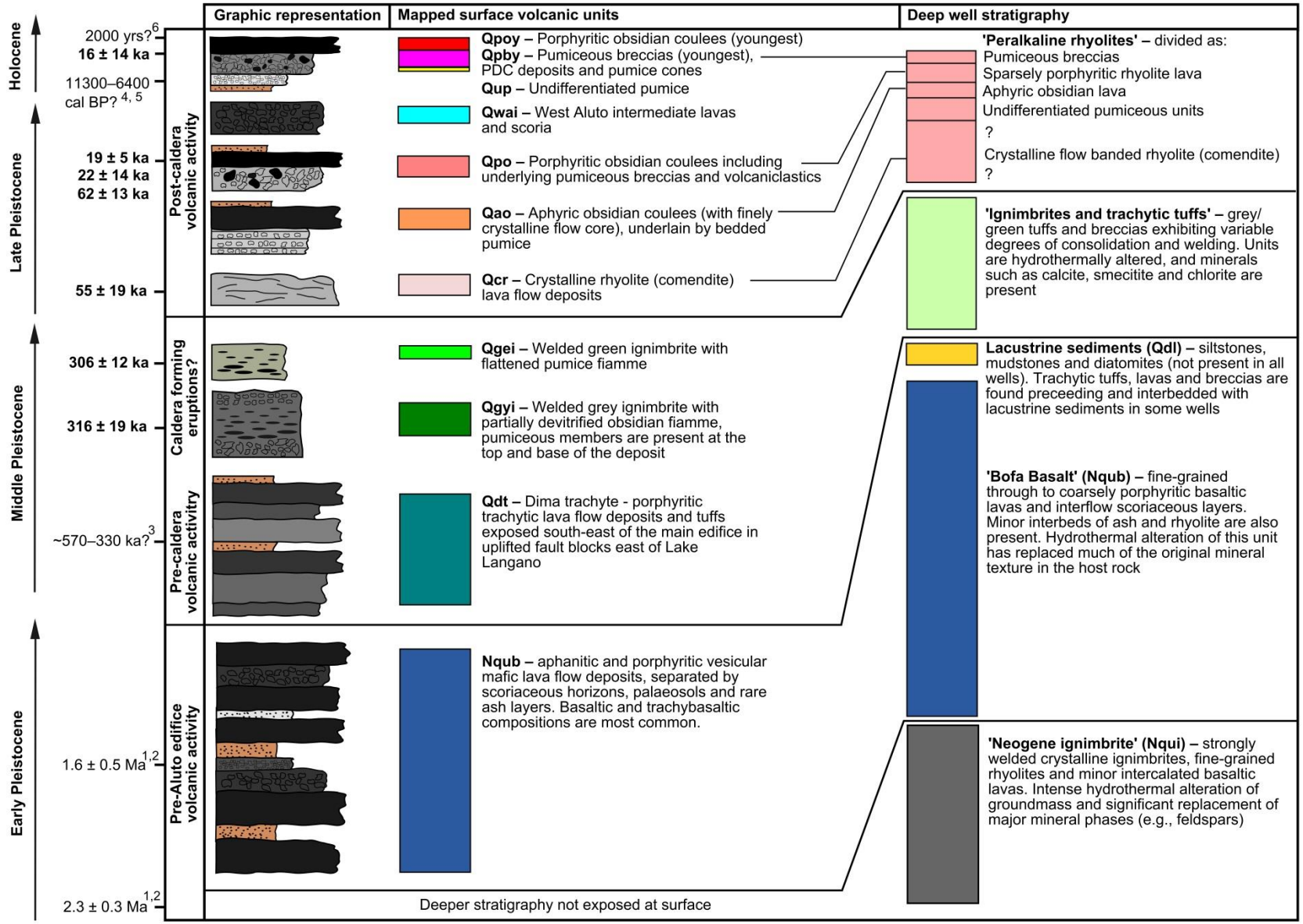

Figure 4.3: *Stratigraphic summary correlating the volcanic units mapped at the surface (Fig. 4.4) with the lithological sequence reconstructed from deep well cores and cuttings (Yimer, 1984; Mamo, 1985; Electroconsult, 1986; Gizaw, 1993; Gianelli and Teklemariam, 1993; Teklemariam, 1996; Teklemariam et al., 1996). Colours of the mapped surface volcanic units correspond with the shading in the geological map in Figure 4.4. The relative thickness of each unit corresponds to the height of the coloured rectangle. Ages marked to the left of the stratigraphy are from $^{40}Ar/^{39}Ar$ determinations (Table 1) unless indicated otherwise by numerical superscripts. Literature ages are from: [1]: Teklemariam, 1996; [2]: Teklemariam et al., 1996; [3]: Le Turdu et al., 1999; [4]: Gasse and Street, 1978; [5]: Benvenuti et al., 2013; [6]: Gianelli and Teklemariam, 1993.*

4.5.1.1 Neogene Ignimbrites (Neogene-Quaternary undifferentiated ignimbrites, Nqui)

The base of all deep wells is represented by a sequence of rhyolitic ignimbrites and lavas at least 400–500 m thick (Gizaw, 1993; Gianelli and Teklemariam, 1993; Teklemariam et al., 1996; Figs. 4.2, 4.3). Welded crystal-rich ignimbrites and fine-grained rhyolites dominate the sequence but volumetrically subordinate basaltic lava layers are also observed (Yimer, 1984; Mamo, 1985). The ignimbrite horizons are generally reported to be vesicular and crystal-rich, with a mineral assemblage of sanidine, quartz, magnetite and amphibole (Teklemariam et al., 1996). The ignimbrites represent the main reservoir for the geothermal field (Fig. 4.2) and have undergone extensive hydrothermal alteration (Teklemariam et al., 1996). Note that previous authors commonly refer to this unit as 'Tertiary Ignimbrite'.

4.5.1.2 Bofa Basalts (Neogene-Quaternary undifferentiated basaltic lavas, Nqub)

Ignimbrite units are overlain by a sequence of coarsely porphyritic and aphanitic basaltic lavas with intervening scoria horizons, palaeosols and minor ash beds (the Bofa Basalts, Figs. 4.2, 4.3). Basaltic rock horizons are found in all deep wells and have a maximum thickness of ~1000 m in LA-3 (Teklemariam, 1996; Teklemariam et al., 1996). The Bofa Basalts represent sub-aerial eruptive sequences (lavas and scoria) rather than intrusive bodies (Teklemariam et al., 1996).

4.5.1.3 Lacustrine sediments (Quaternary deep well lacustrine sediments, Qdl)

Stratigraphically above the Bofa Basalts (Nqub) is a sequence of lacustrine sediments, predominantly mudstones and siltstones, that have been identified in all wells except LA-4 and LA-5 (Fig. 4.3, Teklemariam et al., 1996). The lacustrine sediments show spatial variations in thickness, becoming progressively thinner to the east of the Aluto complex (Gizaw, 1993; Ginaelli and Teklemariam, 1993; Teklemariam et al., 1996; Hutchison et al., 2015). The maximum thickness of the lacustrine sediments is ~400 m in well LA-2 (Teklemariam et al., 1996). In the centre of the complex they have a thickness of ~80 m in well LA-8 (Mamo,1985, Table A2.2) and 2 km east of this (traversing a major fault zone at Artu Jawe, Fig. 4.4), lacustrine

sediments are absent in deep well LA-4 (Yimer, 1984, Table A2.1) and LA-5 (Ginaelli and Teklemariam, 1993; Teklemariam, 1996). This pattern suggests considerable topographic offsets existed during lacustrine sediment deposition. Given the rift setting, it is assumed that deposition of the lacustrine sequences took place in a faulted environment and that the greatest thicknesses of sediments were established in the most down-thrown blocks on the west side of the complex (Hutchison et al., 2015).

A number of wells on Aluto show trachytic units preceding and interbedded with the lacustrine sediments (Figs. 4.2, 4.3). Core and cutting samples reveal that these units are composed of grey, variably consolidated trachytes (including tuffs, lavas and breccias) with phenocrysts of alkali feldspar (Mamo, 1985). Intense hydrothermal alteration has led to calcite, chlorite and smectite precipitation in these units (e.g., Teklemariam et al., 1996) greatly complicating interpretation of the original rock texture and their relation to the lacustrine sequences.

The lacustrine sediments and overlying ignimbrites (Section 4.5.1.4, below) are highly altered and rich in clay minerals (e.g., chlorite, illite and smectite) (Teklemariam et al., 1996). It is likely that these units provide a low porosity and low permeability clay cap layer that seals the Aluto-Langano geothermal reservoir (Fig. 4.2; Teklemariam, 1996).

4.5.1.4 Ignimbrites and trachytic tuffs (Qdt–Qgei)

Overlying the lacustrine sediments and Bofa Basalts are grey-green welded ignimbrites, variably consolidated tuffs and lithic breccias (Fig. 4.2, Teklemariam et al., 1996). The tuffs have a fine, devitrified groundmass, and contain sanidine phenocrysts as well as rhyolitic and trachyitic lithic fragments (Yimer, 1984; Mamo, 1985). The ignimbrite sequences are thickest in the centre of the complex where they are in excess of 300 m in well LA-8 (Mamo, 1985, Table A2.1).

4.5.1.5 Peralkaline rhyolites (Qcr–Qpoy)

The uppermost units found in the Aluto wells are peralkaline rhyolites (Figs. 4.2, 4.3), and include obsidian lavas, finely crystalline lavas and pumice breccias (Tables A2.1 and A2.2). There are no detailed descriptions of the sub-units within the peralkaline rhyolite sequence, and at present it is not possible to correlate sub-units (e.g., individual lava flow deposits) between the wells and assess lithological or thickness variations. Descriptions of well LA-4 by Yimer (1984) provide the most comprehensive account of the lithological sub-units within the peralkaline rhyolite sequence (Fig. 4.3, Table A2.1), but future work to systematically log these horizons is essential. Above the ignimbrite and trachytic tuff sequences (Section 4.5.1.4), Yimer (1984) identified flow banded comenditic rhyolites in a core cut at 256–266 m. Unfortunately, no cores were taken across the ~30 m transition from the major ignimbrites to the comendites, Table A2.1, leaving considerable uncertainty as to the nature of the contact between these units (Fig. 4.3, discussed in Section 4.8.2). Cuttings suggest that superposed on the comenditic rhyolites are ~50 m of pumiceous deposits and then ~30 m of aphyric obsidian lava (Yimer, 1984). The aphyric obsidian is then succeeded by ~40 m of sparsely porphyritic rhyolite lavas and finally, the upper most section comprises ~30 m of pumiceous breccias (Fig. 4.3).

Figure 4.4: *Geological map of Aluto volcano produced through interpretation of remote sensing imagery with field validation. Projection is UTM (Universal Transverse Mercator) Zone 37N, with the WGS84 (World Geodetic System 1984) datum. Coordinates are in meters. The new map builds on previous geological mapping of Aluto by Kebede et al. (1985) as well as maps of Quaternary lacustrine sediments presented by Benvenuti et al. (2002, 2013). Note the apparent lack of outcrop of units Qgei and Qcr is due to their limited exposure at the base of deep gorges, which are invariably covered by thick sequences of younger units. Outcrops labelled with a '?' were not visited during our field campaign and have been categorized on the basis of surface geological descriptions by Kebede et al. (1985); future mapping should aim to verify the relationship between these outcrops and the new stratigraphy. Local names that are referred to in text and subsequent figures are italicised. Faults have been mapped previously by Agostini et al. (2011) and Hutchison et al. (2015). Fumarole vents and hot spring locations are from Kebede et al. (1985). The deep geothermal wells are identified by blue circles and labels. White stars link to the key stratigraphic sections in Figure 4.5A–M.*

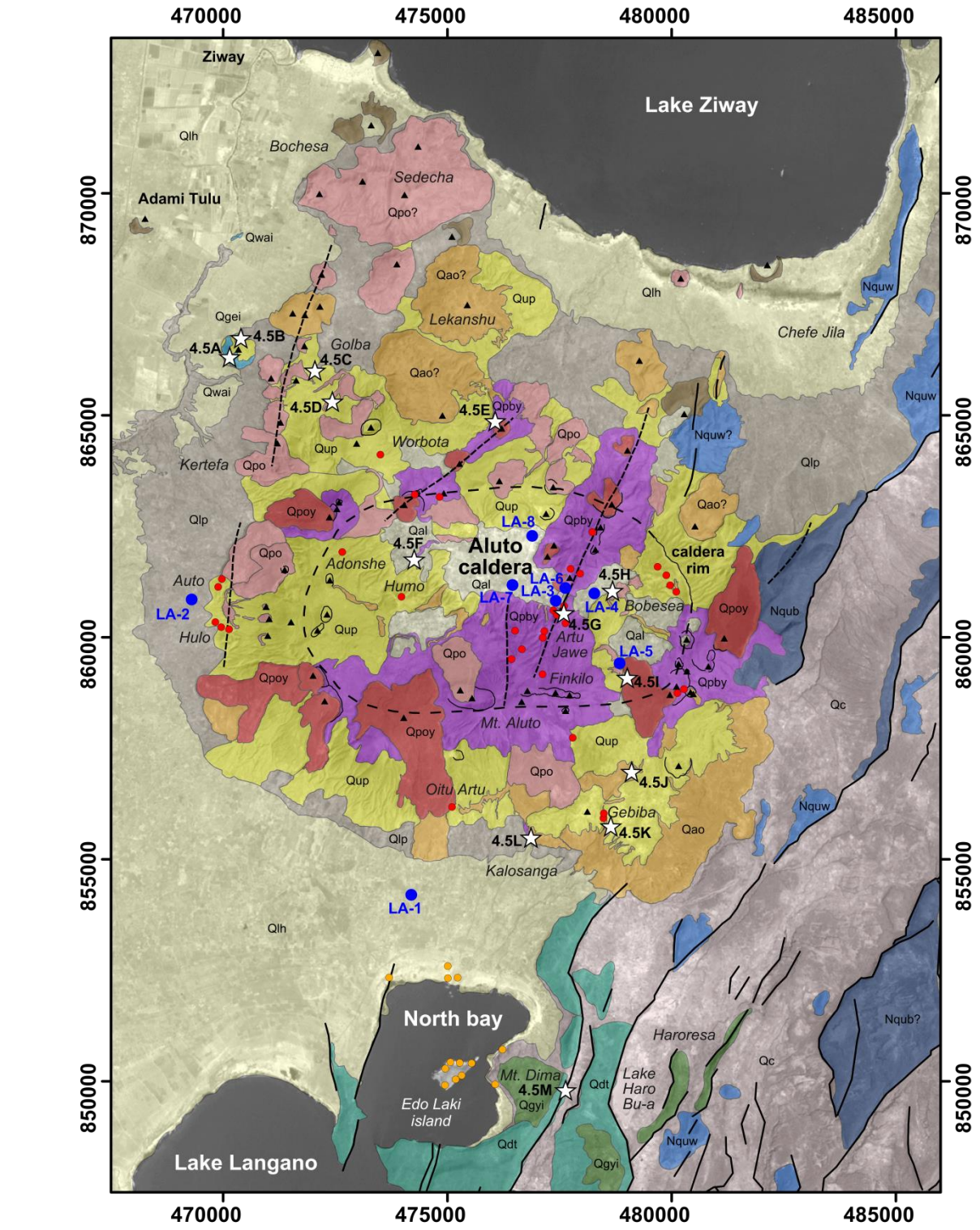

Peralkaline rhyolites (post-caldera)

- Qpoy: Porphyritic obsidian coulees (youngest)
- Qpby: Pumiceous breccias, PDCs and pumice cones (youngest)
- Qup: Undifferentiated pumice
- Qwai: West Aluto intermediate lavas and scoria cones
- Qpo: Porphyritic obsidian coulees
- Qao: Aphyric obsidian coulees (including underlying bedded pumice)
- Qcr: Comenditic rhyolite

Welded ignimbrites (caldera-forming eruptions?)

- Qgei: Welded green ignimbrite
- Qgyi: Welded grey ignimbrites and associated pyroclastics

Trachytes (pre-caldera?)

- Qdt: Trachytic tuffs and lavas

Pre-Aluto mafic activity

- Nqub: Undifferentiated mafic lavas

Undifferentiated volcanics

- Nquw: Undifferentiated Wonji scoria cones
- Qutc: Undifferentiated tuff cone

Sedimentary rocks

- Qal: Alluvium and reworked volcaniclastics
- Qlh: Holocene lacustrine sediments
- Qlp: Pleistocene lacustrine sediments
- Qc: Colluvial and fluvial deposits (gravels, sands and muds)

Symbols

- Fault
- Crater
- Fault (inferred)
- Volcanic vent
- Fumarole vents
- Hot springs
- Deep geothermal well
- Stratigraphic section (Fig. 4.5)

4.5.2 Field stratigraphy

In the following sections we establish the field relations between the volcanic units exposed at the surface. Section 4.5.2.1 describes units that were identified off the main volcanic edifice in faulted sections around the margins of the Aluto complex; representative of the deepest accessible stratigraphy in the study region. Section 4.5.2.2 describes the succession of units identified on the main volcanic edifice, providing a complete sequence from the base to the top of the edifice. Finally, Section 4.5.2.3 describes the main sedimentary units as well as undifferentiated volcanic deposits. The key accompanying figures are: the synthetic stratigraphy of the surface volcanic units (Fig. 4.3, left-hand columns); the new geological map of Aluto (Fig. 4.4); graphic logs of key stratigraphic sections (Fig. 4.5) and annotated field photographs (Figs. 4.6 and 4.7). In addition, representative geochemical data for each of the main units are given in Table 2.

4.5.2.1 Off-edifice and uplifted volcanic units

Neogene-Quaternary undifferentiated basaltic lavas (Nqub)

On the uplifted eastern flank of Aluto (Fig. 4.4) ~200 m of aphanitic and porphyritic vesicular basalt lavas were identified. The sequence comprises weathered basaltic lavas and breccias separated by minor palaeosols and scoriaceous horizons. East of Haroresa, south-east of the main edifice (Fig. 4.4) several large fault scarps ~100 m in height also reveal thick sequences of basaltic lava flow deposits comparable to those on the uplifted eastern flank of Aluto (Kebede et al., 1985). Blocks of basalt are identified as rare lithic clasts within PDC deposits on the main edifice suggesting that these units underlie the Aluto complex.

Quaternary trachytic tuffs and lavas (Qdt)

Comenditic trachyte tuffs and lavas (Qdt), ~100 m thick, are exposed in fault scarps east of Lake Langano (at Mt. Dima, Fig. 4.4 and Fig. 4.5M). The trachytes are composed of both porphyritic and aphanitic types, and display varying degrees of vesiculation. Bright red blocky breccias are found between the layers of trachyte lava (Figs. 4.5M, 4.7A), suggesting that there were

considerable hiatuses and periods of reworking between emplacement of the major lava flow units.

Quaternary grey welded ignimbrites (Qgyi)

The next unit in the stratigraphic sequence is a package of strongly welded grey ignimbrites (Qgyi) that contain abundant lithic fragments and elongate fiamme (composed of partially devitrified obsidian). The welded ignimbrites (Qgyi) overly the trachytic lavas (Qdt) at Mt. Dima (Fig. 4.4), although the contact was not clearly exposed (Fig. 4.5M). For the majority of Qgyi exposures only the grey densely welded zone of the ignimbrite is visible at the surface. Kebede et al. (1985) reported that in more complete sections the ignimbrites have a moderately compacted and poorly welded pumiceous base that grades upward into the densely welded zone before transitioning back into a non-welded pumiceous top. The thickness of this unit in well-exposed sections near Haroresa (Fig. 4.4) is ~50 m (Kebede et al., 1985).

Quaternary green welded ignimbrites (Qgei)

Deposits of a welded green ignimbrite (map unit Qgei) are found in an uplifted fault block on the west of Aluto (Figs. 4.4, 4.5B). Qgei is composed of fine-grained pistachio-green matrix with flattened pumice fiamme and accessory lithic rock fragments (Fig. 4.7B). The stratigraphic context of Qgei is difficult to resolve owing to limited exposure; however at the type locality west of the edifice (Fig. 4.5B) it is immediately overlain by lacustrine sediments (siltstones, diatomite and reworked tephra) suggesting that it was emplaced in a lake basin. We frequently identified Qgei (and also Qgyi) as accidental lithic clasts within younger PDC deposits on the central edifice, suggesting that these two major ignimbrite units underlie the complex, and are considerably older than the volcanic units identified on the main edifice (Qcr–Qpoy, following section).

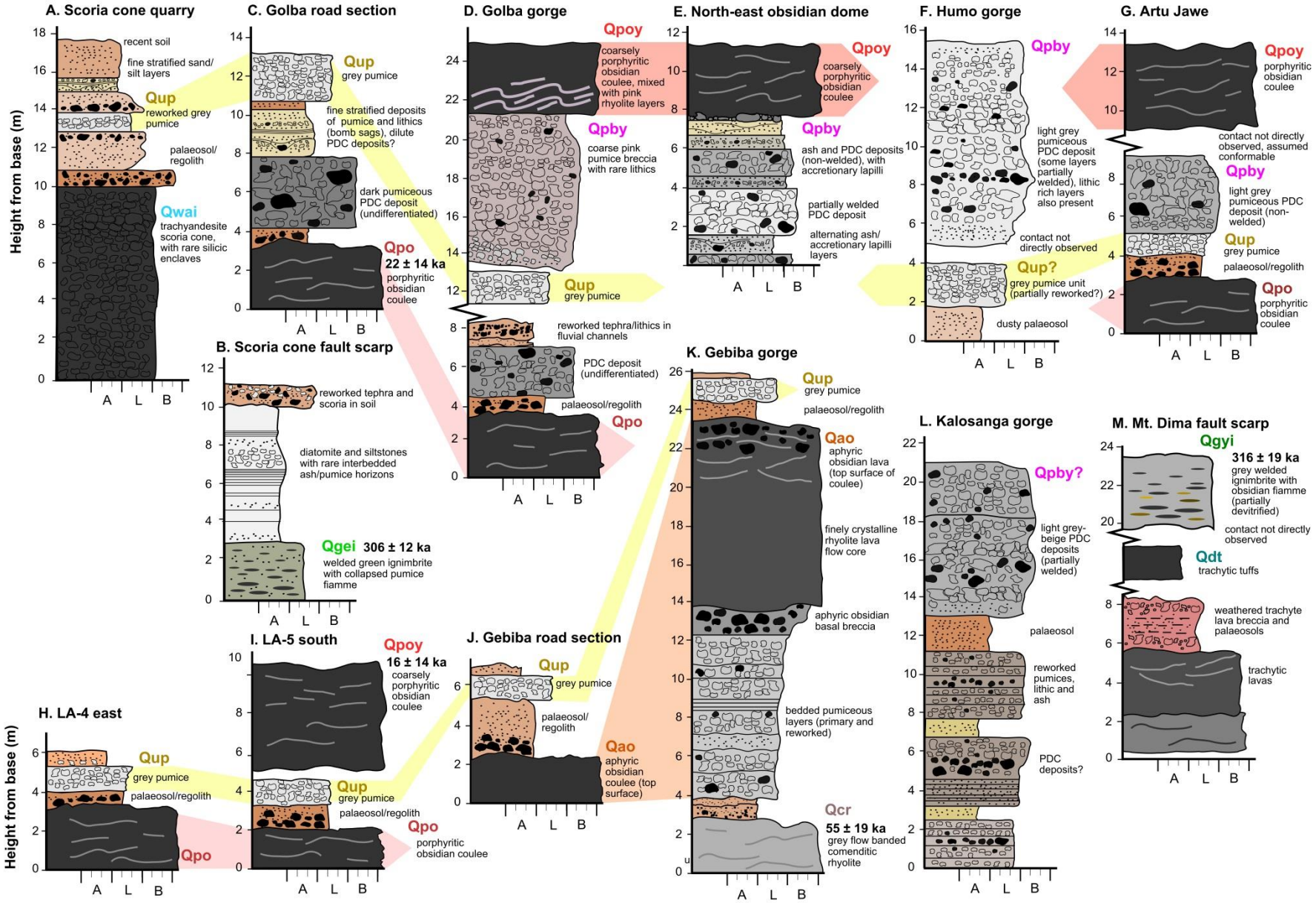

Figure 4.5: *Key stratigraphic sections used to constrain the eruptive stratigraphy (Fig. 4.3). Correlations are shown by the shaded colours that connect the sections. The location of each section is shown by the stars on the geological map (Fig. 4.4). Ages shown alongside the stratigraphy were determined by $^{40}Ar/^{39}Ar$ methods (Table 1 and Section 4.5.3). The bulk grain size of the volcaniclastic fragments in the deposit is given by the scale at the base of each section: A corresponds to ash, L to lapilli and B to blocks and bombs.*

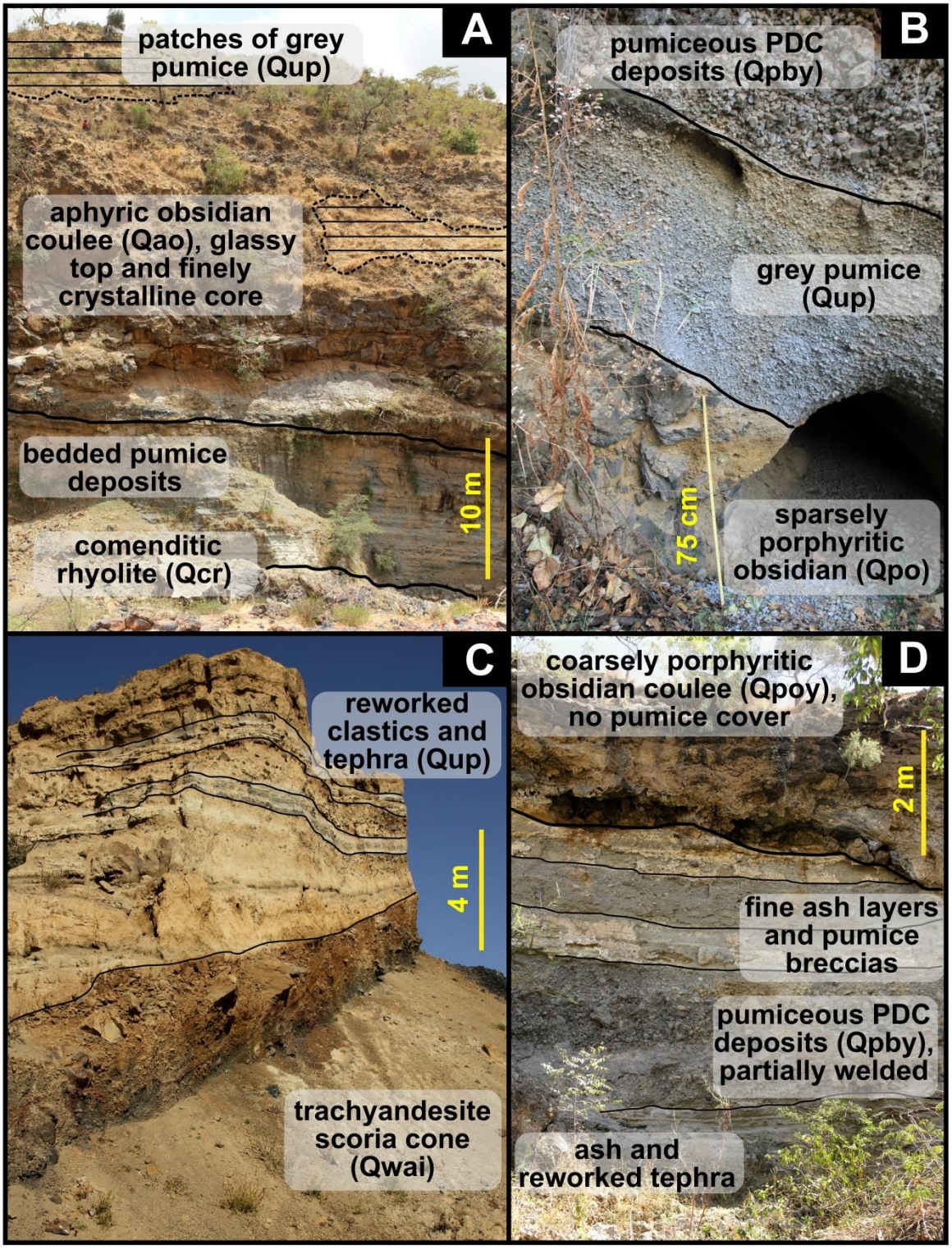

Figure 4.6: *Photographs of key stratigraphic sections. The photographs correspond with stratigraphic logs in Fig. 4.5 (A: Fig. 4.5K; B: Fig. 4.5G; C: Fig. 4.5A and D: Fig. 4.5E). The locations of the stratigraphic logs (which are tied to the photographs) are shown on the geological map in Figure 4.4.*

4.5.2.2 On-edifice volcanic units

Quaternary comenditic rhyolite (Qcr)

The deepest deposits accessible on the main Aluto edifice are found at the base of Gebiba gorge on the south-east slope (Figs. 4.4, 4.5K, 4.6A). On the floor of the gorge the upper 5 m of a grey aphanitic lava (Qcr) is exposed. Qcr is a flow-banded comeditic rhyolite lava with large sanidine phenocrysts (1–3 mm diameter).

Quaternary aphyric obsidian (Qao)

Overlying Qcr in Gebiba gorge is a ~10 m thick sequence of pumice, ash and breccia units (Fig. 4.6A). The contact between Qcr and the overlying volcaniclastic sequence is poorly exposed but taken to be unconformable (Fig. 4.5K). The volcaniclastic beds are themselves overlain by an obsidian lava flow deposit (Figs. 4.5K, 4.6A), which has a blocky aphyric obsidian surface and basal breccia (each ~2 m thick), and a ~7 m thick flow core comprised of finely crystalline rhyolite (Fig. 4.5K). The aphyric obsidian lavas and underlying bedded pumice are classified together as Qao. Qao lavas are dominantly exposed on the south-east slopes of the Aluto edifice where they cover an area of ~15 km^2 and extend for >7 km away from the centre of the edifice (Fig. 4.4).

Quaternary porphyritic obsidian (Qpo)

The next phase of activity is represented by sparsely porphyritic obsidian lavas (Qpo), identified in Figure 4.5 (sections C, D, G, H and I) and Figure 4.6B. These lava flow deposits are ubiquitously covered by thin soil horizons (30 cm – 1 m) and tephra (Fig. 4.6B). A major dome of the Qpo unit is developed on the northern rim of the complex, where lavas extend ~2.5 km north of the volcanic vents (Fig. 4.4). Many of the Qpo lavas extend from breached craters suggesting that explosive phases preceded the lavas (although no underlying volcaniclastic units were exposed).

Quaternary west Aluto intermediate lavas (Qwai)

Eruption of intermediate lavas is restricted to the west of the edifice (Qwai, Fig. 4.4). The main occurrence of Qwai is a small trachyandesite scoria cone, ~65 m high and ~600 m diameter, south of the main access road to Aluto from Adami Tullo (Figs. 4.4, 4.5A and 4.6C). The scoria cone is covered by a thin layer of pumice (Figs. 4.5A, 4.6C) suggesting it developed prior to the most recent explosive eruptive phases (Qup, next section).

Quaternary undifferentiated pumice (Qup)

Covering all previously mentioned deposits of Aluto is an undifferentiated pale grey pumice deposit, Qup (Fig. 4.4, numerous sections in Fig. 4.5, and Fig. 4.6A–C). The thickness of the tephra varies across the complex from a few centimetres up to several meters where it has experienced reworking on steep slopes. The tephra comprises lapilli-pumice, and has rare chips of obsidian and hydrothermally altered material (less than 1 cm in size). Qup ubiquitously overlies palaeosols (e.g., Figs. 4.5, 4.7C) indicating that this unit marks the initiation of a major explosive eruption sequence. Field exposures (Figs. 4.6B, 4.7C) suggest that this unit is a single pumice fallout deposit, and likely to be the product of a (sub) Plinian eruption, but further work needs to be done to verify this.

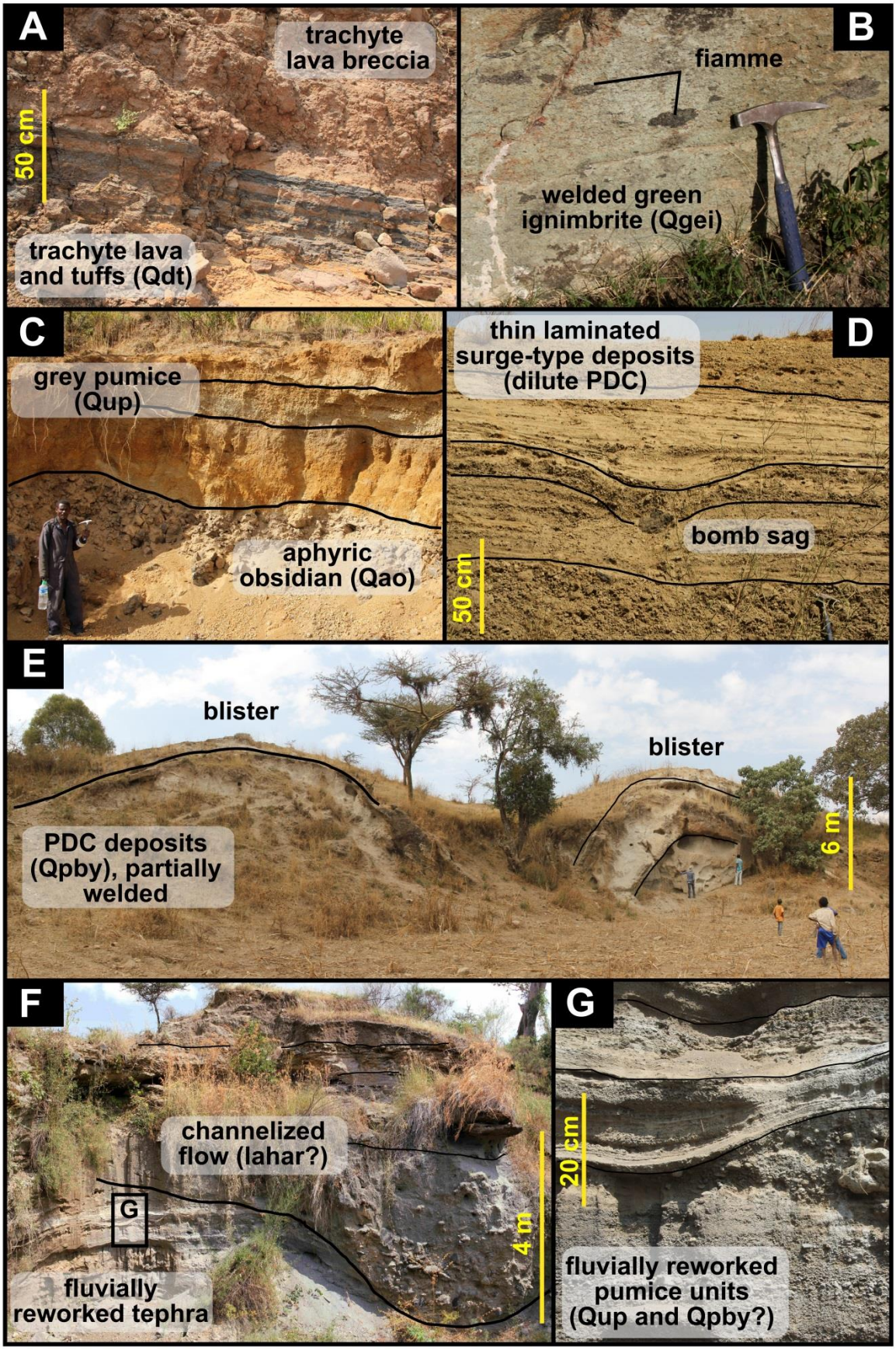
A
trachyte lava breccia
50 cm
trachyte lava and tuffs (Qdt)
B
fiamme
welded green ignimbrite (Qgei)
C
grey pumice (Qup)
aphyric obsidian (Qao)
D
thin laminated surge-type deposits (dilute PDC)
bomb sag
50 cm
E
blister
blister
PDC deposits (Qpby), partially welded
6 m
F
channelized flow (lahar?)
G
4 m
fluvially reworked tephra
G
20 cm
fluvially reworked pumice units (Qup and Qpby?)

Figure 4.7: *Photographs showing field relations of key units.* ***A)*** *Trachytic lava and breccias (Qdt) exposed in uplifted fault blocks south-east of the Aluto edifice (Fig. 4.5M).* ***B)*** *Green welded ignimbrite (Qgei, from section Fig. 4.5B) with collapsed pumiceous fiamme, hammer for scale 30 cm in length.* ***C)*** *Contact between aphyric obsidian lava (regolith) and light grey pumice unit (Qup) with ~1 m thick bright orange palaeosol developed (Fig. 4.5J).* ***D)*** *Section 4.of explosive eruptions units, indicative of phreatomagmatic processes (Fig. 4.5C).* ***E)*** *Hummocky 'blister' structures developed within a welded PDC deposit (Qpby, near Fig. 4.5F).* ***F)*** *Fluvially reworked tephras and volcaniclastic material deposited on the southern slope of the edifice, the large channel cutting down through the stratigraphy is typical of a lahar unit with a coarse lithic base load of obsidian cobbles.* ***G)*** *Detail inset from F), showing thin channels of reworked tephra (likely derived from units Qup and Qpby). Photographs F and G were taken ~1 km south-west of stratigraphic section 5K (see Fig. 4.4).*

Quaternary pumiceous breccias youngest (Qpby)

Pumiceous breccias (Qpby) are encountered above the Qup tephra at Humo gorge and Artu Jawe (Fig. 4.5F, G and Fig. 4.6B, D). Qpby units were erupted from discrete vents across the complex and were not erupted in a single event (although some ignimbrites appear to have closely followed Qup with little evidence for any substantial hiatus, e.g., Fig. 4.6B). Qpby units have been emplaced as both PDCs (Fig. 4.6B, D) with run outs of several kilometres and localized pumice cones (Fig. 4.5D). The pumice cones comprise coarse (up to 30 cm diameter), clast-supported pumice exposures that have a mantle-bedded morphology (e.g., Golba gorge, Fig. 4.5D). Pumice cones are typically between 10–100 m in height, and may extend to ~1 km from the erupting vent; effusive obsidian coulees (e.g., Qpoy, next section) commonly follow, breaching the walls of the pumice cone.

Qpby PDC units, such as those identified at Humo gorge (Fig. 4.5F), show characteristic peralkaline ignimbrite textures with large pumice clasts (5–30 cm diameter) and lithic-rich horizons set in a variably welded ashy matrix. North-east of Humo gorge, PDC deposits display hummocky ('blister') structures, 6–8 m in height, and 15–20 m in diameter (Fig. 4.7E). Ignimbrite blisters have been described at a number of other peralkaline systems (Gibson, 1967, 1970; Williams et al., 2004; Mundula et al., 2013) and are linked to gas coalescence and deformation of the ignimbrite upon emplacement and prior to cooling and solidification. Qpby deposits often contain accretionary lapilli (Fig. 4.5E), bomb sag structures and thinly stratified ash horizons (Fig. 4.5C, Fig. 4.7D) indicative of surge-type (dilute PDC) deposits, as have been

reported at many other silicic volcanoes (e.g., Santorini, Sparks and Wilson, 1990), and identify phreatomagmatic eruptive processes at Aluto.

Overall the Qpby units represent a mixture of volcaniclastic deposits that were either built up around erupting vents (pumice cones), or formed density currents during particularly explosive phases. Their general evolution and morphology is comparable to the silicic lava cones and shields described by Mahood and Hildreth (1986) at Pantelleria.

Quaternary porphyritic obsidian youngest (Qpoy)

The youngest volcanic deposits of Aluto are coarsely porphyritic obsidian lavas (Qpoy, e.g., Fig. 4.5D, E, G, I; Fig. 4.6D). Qpoy lavas range from ~200 m to ~2.5 km in length, and show marked differences in surface weathering, suggesting that they were not emplaced in a single eruptive event. Qpoy vents commonly coincide with volcanic or tectonic structures, such as the caldera ring fault or the Artu Jawe fault zone that runs NNE-SSW east of the caldera floor (Fig. 4.4, Hutchison et al., 2015).

4.5.2.3 Undifferentiated volcanic or sedimentary units

Undifferentiated volcanic units (Qutc and Nquw)

North of the Aluto edifice we identify numerous tuff cones (map unit Qutc), around the shore of Lake Ziway (Fig. 4.4), and to the east of Aluto, we have mapped scoria cones and basaltic fissure lavas occurring in the Wonji fault belt (Nquw, Fig. 4.4). Given their proximity and comparable surface weathering to the volcanic deposits of Aluto we assume that these formed contemporaneously to the Aluto edifice; however, their precise relations to the proximal volcanic stratigraphy have yet to be constrained.

Pleistocene and Holocene lacustrine units (Qlp and Qlh)

Lacustrine sediments (predominantly siltstone, sandstone and diatomite) deposited in the Ziway-Shala basin are found north, south and west of the main edifice (Fig. 4.4, Gasse and Street, 1978; Street, 1979; Le Turdu et al., 1999; Benvenuti et al., 2002, 2013). While previous authors (e.g., Benvenuti et al., 2002) have defined several unconformity-bounded units that record major stages in the lake evolution, we simply delineate the main boundary between Pleistocene and Holocene sediments (Qlp and Qlh, respectively) in our geological map (Fig. 4.4). The Holocene high-stand of the Ziway-Shala basin (between 10–5 ka) was 1670 m above sea level (Benvenuti et al., 2002), and therefore sediments in the plains around Aluto that are below this height level are assumed to be Holocene in age. Conversely, sediments above 1670 m height are correlated to the Late Pleistocene Megalake phase deposited during the last glacial period, ~100–22 ka (Benvenuti et al., 2002, 2013). The deep gullies west of Aluto that drain into the Bulbulla river are an exception to this, where ~50 m thick sequences of Pleistocene lacustrine sediments have been described by Gasse and Street, (1978), Street (1979), Benvenuti et al. (2002) and Ménard et al. (2014).

Reworked volcaniclastic sediments and colluvial-fluvial sediments (Qal and Qc)

There is abundant evidence for fluvial reworking of volcaniclastic material on Aluto (map unit Qal). On the flanks of the main edifice, drainage networks are well developed and have reworked volcaniclastic material in both narrow streams (Fig. 4.6G) and large channels (potentially episodic lahars, Fig. 4.6F). The caldera floor of Aluto is a self-contained basin that has been infilled by reworked volcanic deposits derived from the rim of the complex (mostly rounded pumice lapilli as well as sand-silt size lithic fragments). It is possible that Aluto hosted a caldera lake during periods of humid climate, and this feature may explain the phreatomagmatic characteristics of PDC deposits reported in unit Qpby (Section 4.5.2.2).

East of Aluto undifferentiated terrigenous clastic sediments (gravel, sandstone, siltstone and mudstone) were identified (map unit Qc). These units are representative of colluvial and fluvial sedimentary facies deposited on the margins of the Ziway-Shala lake basin.

4.5.3 Age constraints and correlations between the surface and deep stratigraphy

New and existing age constraints on volcanism are given in Table 4.1, and shown alongside our stratigraphic interpretations in Fig. 4.3. These units are discussed from the base to the top of the pile. The ignimbrite units (Nqui) found at the base of the deep wells lack robust age constraints, as K/Ar analysis of altered feldspars yielded a minimum age of 1.4 Ma (WoldeGabriel et al., 1990). Nevertheless, previous authors (e.g., WoldeGabriel et al., 1990, 1992; Teklemariam, 1996) have correlated the Aluto deep well ignimbrites (Nqui) with petrologically and geochemically analogous ignimbrites found near Munesa (Fig. 4.1B), which yielded ages of 3.51 ± 0.03 Ma (Munesa Crystal Tuff), 2.9 ± 0.3 Ma (Munesa Vitrophyre) and 2.30 ± 0.03 Ma (Neogene Ignimbrite). These correlations should be viewed with caution until further evaluation and age analysis is undertaken.

The next unit is Nqub, and on the on the basis of their comparable geochemistry, thicknesses and emplacement style, we correlate the surface exposures of basaltic lava (Nqub) with the Bofa Basalt unit described in the deep wells (Fig. 4.3, Table A2.1,2 and Gianelli and Teklemariam, 1993). The age of Nqub is constrained at 1.6 Ma ± 0.5 Ma by a K/Ar determination from a porphyritic basalt lava on the eastern flank of Aluto (Table 4.1, Teklemariam, 1996).

No direct ages are available for lacustrine sequences encountered in the deep wells (Qdl). These sequences appear to represent the oldest lacustrine sediments deposited in the Ziway-Shala basin (Fig. 4.1B), and probably have an age of ~570–330 ka (i.e., the maximum age range for the basin, Le Turdu et al., 1999).

Trachytic tuffs and lavas found at Mt. Dima (Qdt) are tentatively correlated with the trachytes identified in the deep wells (Fig. 4.3), on the basis of their similar deep position in the stratigraphy and their broad compositional similarity. Direct ages for trachyte lavas are still to be established, however their close association with lacustrine sediments (Section 4.5.1.3) would suggest that their ages are roughly equivalent (around ~570–330 ka), and indeed they must have erupted before ~310 ka, the age of the overlying ignimbrites.

The welded ignimbrite sequences, Qgyi and Qgei, yield overlapping $^{40}Ar/^{39}Ar$ ages of 316 ± 13 ka and 306 ± 12 ka (Table 4.1) and we correlate these units with the thick ignimbrite and tuff sequences described in the deep wells (Section 4.5.1.4, Fig. 4.3).

For the units on the main edifice of Aluto our $^{40}Ar/^{39}Ar$ results support ages of the comenditic rhyolites (Qcr) at 54 ± 13 ka, the sparsely porphyritic obsidian coulees (Qpo) at 62 ± 13, 22 ± 14 and 19 ± 5 ka, and the youngest obsidian coulees (Qpoy) at 16 ± 14 ka. West of Aluto, in the deep gorges of the Bulbula plain, Gasse and Street (1978) and Street (1979) identified numerous volcaniclastic horizons interbedded with lacustrine sediments and dated these using radiocarbon methods. The largest volcaniclastic sequence, informally known as the Abernosa pumice, was deposited between ~28–25,000 and ~15–13,000 Cal BP, and preserves ~13 distinct tephra layers (Gasse and Street, 1978). The youngest tephra layer identified by Gasse and Street (1978) as well as Benvenuti et al. (2013), shows a broad age overlap between ~11,300 and ~6,400 Cal BP (Table 4.1). This correlation, combined with the radiocarbon ages, would suggest that the youngest eruptive products (Qpoy and Qpby) are younger than ~10 ka (Section 4.8.3), which is consistent within error of the $^{40}Ar/^{39}Ar$ for Qpoy. Overall the radiocarbon ages from the Bulbula sections are in agreement with our chronology and support the interpretation that there have been frequent explosive eruptions at Aluto over the last 30 ka.

The ages also constrain Qao lavas between 74–49 ka and the Qwai scoria cone to >10 ka (i.e., older than overlying Qup, Figs. 4.3, 4.6C). In Figure 4.3 probable links between the surface volcanic deposits on the main edifice and the peralkaline rhyolites in deep wells are shown, and were made on the basis of comparable lithological descriptions.

4.6. Petrography and geochemistry

4.6.1 Petrography

Basaltic lavas from Aluto (Nqub) are vesicular and variably porphyritic (0–40 vol. % phenocrysts) with holocrystalline matrix textures. The phenocryst assemblage is dominated by plagioclase, with subordinate clinopyroxene, olivine and Fe-Ti oxides. The minerals found in the matrix are equivalent to the phenocryst assemblage. Trachyandesite lavas (sampled from the scoria cone, Qwai, Fig. 4.6C) are highly vesicular, and aphyric to scarcely phyric, with microphenocrysts predominantly represented by plagioclase feldspar. Within the trachyandesite scoria cone (Qwai, Section 4.5.2.2) small (<1 cm) fragments of silicic rocks (possessing a granular texture) as well as xenocrysts of sanidine-anorthoclase (partially resorbed) and aenigmatite are found mantled by the trachyandesite groundmass. The bulk geochemical composition of these silicic enclaves is comparable to the peralkaline rhyolites of Aluto (see Figs. 4.8–4.10, red star). The enclaves likely represent partially disaggregated xenoliths of intrusive silicic rocks that were entrapped by the trachyandesite melt prior to eruption.

Trachyte lavas (Qdt) are moderately porphyritic with phenocrysts of plagioclase feldspar, as well as subordinate clinopyroxene and olivine, set in a glassy groundmass with plagioclase microphenocrysts showing a sub-parallel alignment. Welded ignimbrites contain large phenocrysts of sanidine (10 vol. % in Qgyi and 30 vol. % in Qgei) as well as less common alkali pyroxene, aenigmatite and Fe-Ti oxides set in a devitrified groundmass. Rhyolite and trachyte lava xenoliths (1–3 cm in size) are common, as are glassy fiamme and collapsed vesicles.

Samples from obsidian coulees are either aphyric (e.g., Qao) or porphyritic (e.g., Qpo and Qpoy). Porphyritic obsidian samples contain phenocrysts of sanidine-anorthoclase, aenigmatite, alkali pyroxene (aegirine-augite), quartz, Fe–Ti oxides and rare amphibole. The porphyritic obsidians are typically glomeroporphyritic, and the matrix contains aligned microlites of sanidine-anorthoclase, alkali pyroxene and aenigmatite. Quartz-feldspar granophyric textured intergrowths (1–3 mm) were also identified in several porphyritic obsidian deposits and likely represent cognate xenocrysts. Flow banding is common and defined by variable concentrations of aligned microlites and/or vesicles. Phenocryst content varies from 0–40% between the different obsidian lavas, and appears to be greatest in the youngest least weathered obsidian coulee (the eastern most Qpoy deposit, Fig. 4.4). Pumice deposits have similar crystal assemblages to their associated obsidian lavas although are generally lower in total phenocryst content (i.e., closer to aphyric).

4.6.2 Major elements

Rocks were classified using the total alkalis-silica (TAS) diagram (Fig. 4.8A, after Le Maitre, 2002). Note that in all geochemical plots (Figs. 4.8–4.11) we have adopted a colour scheme that differentiates the main eruptive units following the interpretations that were made in Section 4.5, and which we expand on further in Section 4.7. The major element data shows that the majority of volcanic rocks sampled at the surface of Aluto are of rhyolitic composition (Fig. 4.8A). Overall, there is a large range in silica content across the sample suite (SiO_2 43–76 wt. %) and there are representatives of each major compositional division, although rocks of intermediate composition are least abundant.

The silicic rocks of Aluto are represented by trachytes (Qdt), and rhyolites (all units on the main volcanic edifice, Qcr–Qpoy, as well as the welded ignimbrite units, Qgyi and Qgei). Silicic rocks were further classified as pantellerites and comendites according to the FeO_t – Al_2O_3 diagram

(Fig. 4.8B) after Macdonald et al. (1974). Trachytes (Qdt) are comenditic, welded ignimbrite units, Qgyi and Qgei, show panterlleritic and comenditic compositions respectively, and the bulk of post-caldera samples are pantelleritic rhyolites (the only exception is the comenditic rhyolite Qcr, found at the base of the main edifice, Section 4.5.2.2).

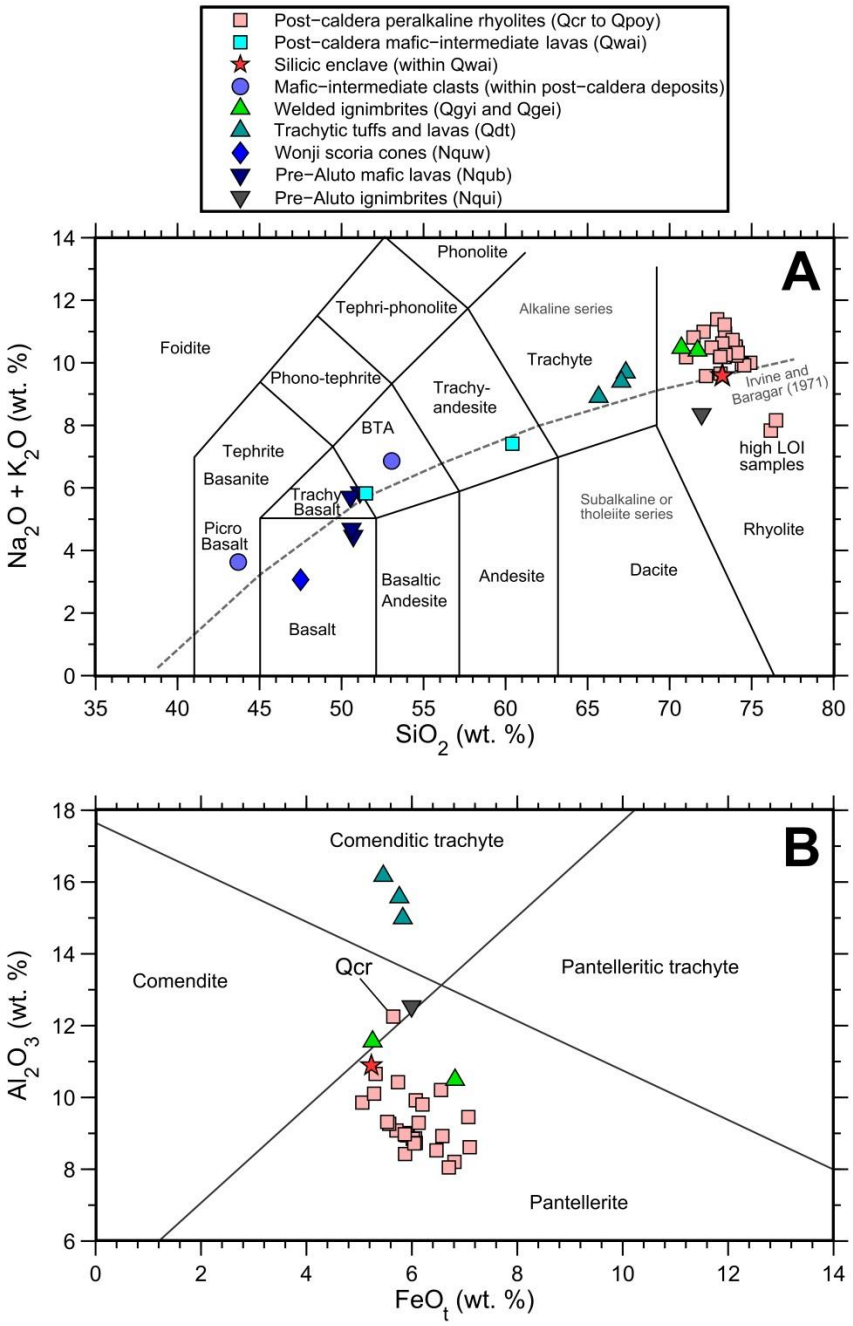

Figure 4.8: *Geochemical overview of Aluto volcanic rocks.* ***(A)*** *Total alkalis versus silica (TAS) diagram (Le Maitre, 2002). The grey dashed line shows the alkaline-sub-alkaline divide of Irvine and Baragar (1971). Two rhyolite pumice samples, discussed in text, show high loss on ignition (LOI) values and low Na_2O values suggestive of post-emplacement alteration. These samples have been removed from subsequent plots.* ***(B)*** *Classification diagram of peralkaline rhyolites and trachytes (Macdonald et al., 1974). Qcr corresponds to the comenditic rhyolite sampled from the base of the Aluto stratigraphy (the earliest post-caldera phase, Sections 4.5.2.2 and 4.5.3).*

Two rhyolite pumice samples (17-01-01K and 17-01-01G, Table A2.3) showed anomalously low Na_2O values (2.8 wt. %) and high loss on ignition (>5 wt. %) compared to other pumice samples (Table A2.3a); these samples are distinct outliers on the TAS diagram (Fig. 4.8A). Previous studies also identified anomalous low Na_2O values in seemingly pristine pumice samples (e.g., Peccerillo et al. 2003; Fontijin et al., 2013). These authors suggest that post-emplacement alteration processes (e.g., leaching through surface water interaction) may be the causal factor. Aluto samples that showed Na_2O loss were sampled from isolated pumice cones on the north-western periphery of the complex; these would have been located at the edge of the lake during lacustrine high stands (Gasse and Street, 1978; Le Turdu et al., 1999; Benvenuti et al., 2002, Fig. 4.4) and this may explain the alteration through interaction with surface waters. In all geochemical plots subsequent to Fig. 4.8A these altered samples have been excluded.

Analyses of mafic samples are limited to four Pre-Aluto (Nqub) units (Fig. 4.3), and a single Wonji lava (Nquw) sampled from a scoria cone ~10 km north-east of Aluto. The mafic units have a transitional composition and straddle the alkaline-subalkaline divide of Irvine and Baragar (1971) (Fig. 4.8A). A scoriaceous boulder of alkali picro-basalt composition was also sampled from a tuff cone (Qutc, at Adami Tullo, Fig. 4.4) by Di Paola (1972).

Intermediate products (SiO_2 52–65 wt. %) are restricted to the post-caldera intermediate units (Qwai, Section 4.5.2.7) and a lithic clast of basaltic trachyandesite composition (Fig. 4.8A) sampled from within a young PDC deposit (Qpby).

Major elements (Fig. 4.9) have trends characteristic of protracted fractional crystallization processes controlled by removal of olivine, clinopyroxene, plagioclase, Fe-Ti oxide, quartz, anorthoclase and aenigmatite (in approximate order of appearance). TiO_2, FeO_t, MgO and CaO all decrease with increasing SiO_2 (i.e., they behave compatibly with increasing fractionation).

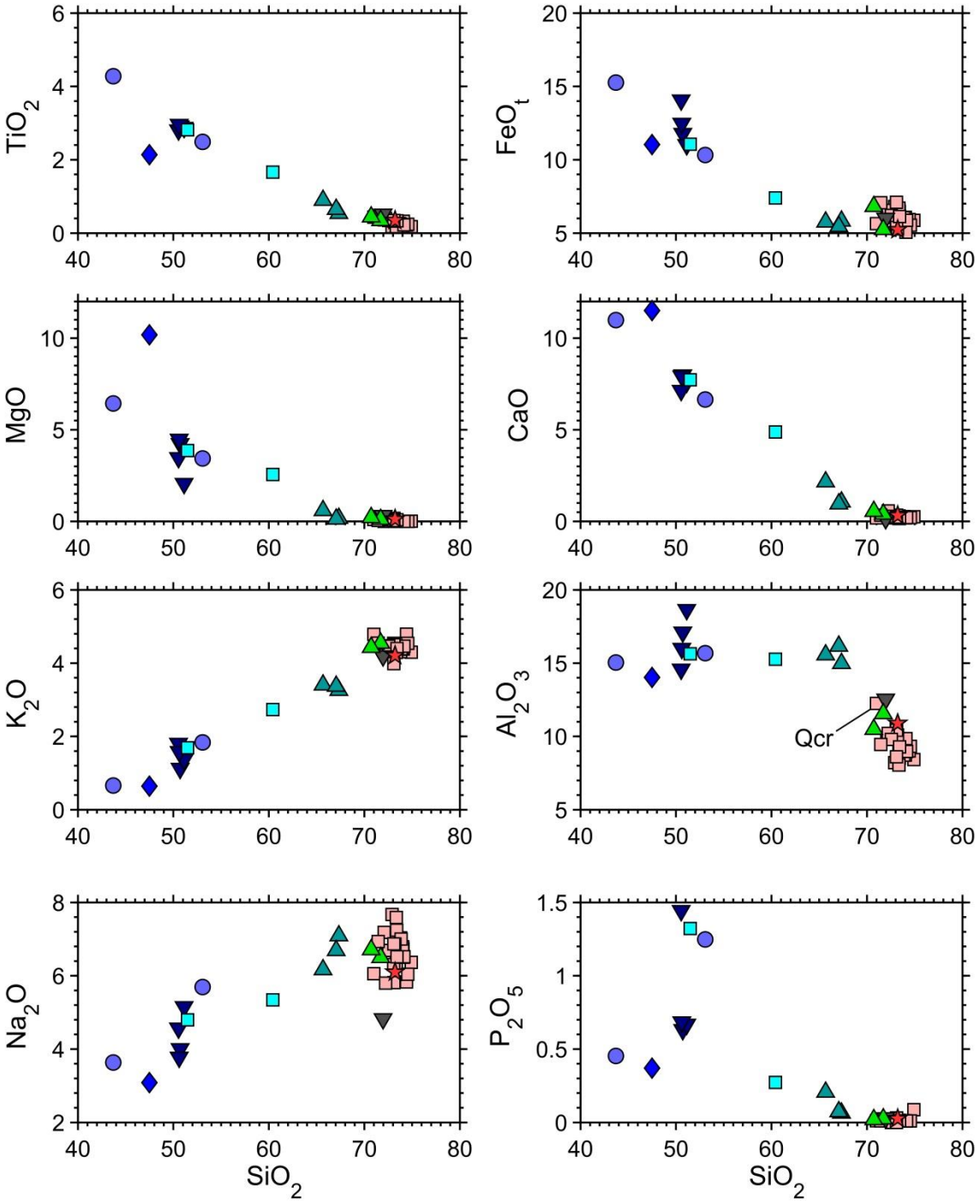

Figure 4.9: *Harker variation diagrams of whole-rock compositions determined by XRF. All concentrations are shown in wt. %. Key as for Figure 4.8. Qcr corresponds to the comenditic rhyolite sampled from the base of the Aluto stratigraphy (the earliest post-caldera phase, Sections 4.5.2.2 and 4.5.3).*

K_2O has a smooth linear increase. Al_2O_3 has values of ~15 wt. % in the mafic to trachytic units but decreases to 8–12 wt. % in the rhyolite units, highlighting the onset of plagioclase feldspar as the major fractionating phase after ~67 wt. % SiO_2. Na_2O shows a generally increasing trend from mafic through to trachytic samples, and then considerable variation (5–7 wt. %) in the rhyolites. The variation in Na_2O after ~72 wt. % SiO_2 reflects the dominance of alkali feldspar as a fractionating phenocryst phase (Section 4.6.1). P_2O_5 shows a general decrease with increasing SiO_2 but with a significant inflexion at ~55 wt.% SiO_2 (P_2O_5 behaviour likely reflects late fractionation of apatite; although rare it is likely to be an accessory phase throughout the crystallizing sequence, e.g., Field et al., 2013).

4.6.3 Trace elements

Selected trace elements and incompatible element ratios are presented in Fig. 4.10. The bulk of our new trace element data were determined by ICP-MS, although for two samples (13-05-04: unit Qgei, 15-02-09: unit Qdt) certain incompatible element values were above the analytical range at the time of measurement (Table A2.2c). In these cases we have plotted the equivalent trace element concentration determined by XRF (Table A2.3b). For elements analysed by both methods results compared well (<10% deviation between ICP-MS and XRF values for identical samples) and are within the uncertainty of measurements (Section 4.3). We have also included trace element data for three samples from Teklemariam (1996) in Figure 4.10. Trace element concentrations of these samples (S1: unit Nqui, S2: unit Nqub and S3: unit Qgyi, Table A2.2d) were determined by XRF methods and because identical samples and standards were not run between our and their analysis we have been cautious not to interpret anything beyond the broad geochemical trends.

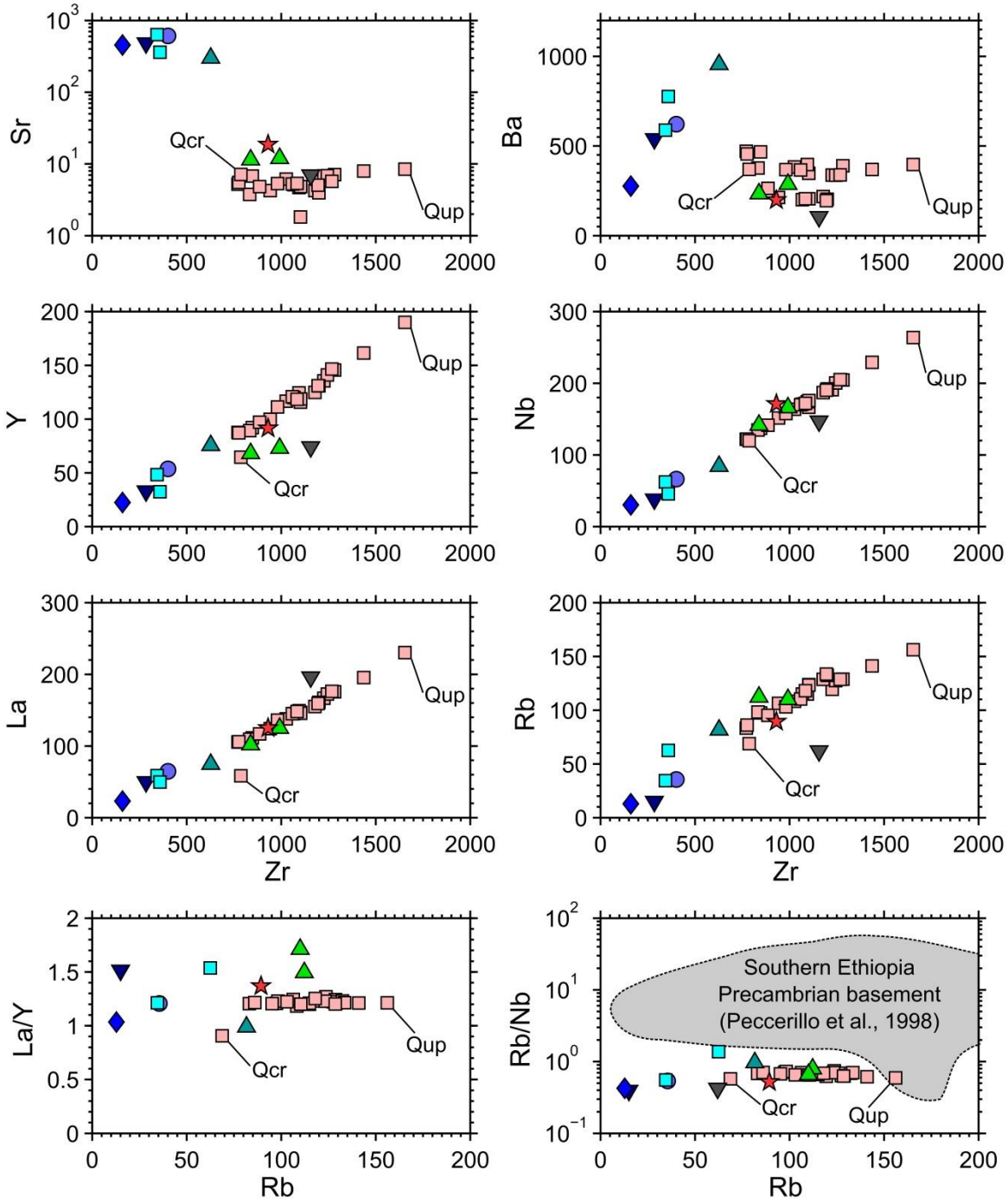

Figure 4.10: *Whole-rock trace element variation diagrams plotted against Zr. All concentrations are shown in ppm. These represent whole-rock values determined by both XRF and ICP-MS methods (see text for discussion of compatibility). Key as for Figure 4.8. Qcr corresponds to the comenditic rhyolite sampled from the base of the Aluto stratigraphy (the earliest post-caldera phase, Sections 4.5.2.2 and 4.5.3).*

Sr does not change significantly from basaltic through to the intermediate and trachytic lavas but shows a marked depletion in rhyolites (Fig. 4.10); indicative of high degrees of feldspar removal. Ba shows an increase from basalts to trachytes before showing a marked inflexion at ~700 ppm Zr due to the appearance of alkali feldspar as a major fractionating phase in the rhyolites.

Incompatible elements (Y, Nb, La, Rb and Zr) reveal a near continuous fractionation sequence of Aluto lavas, the only significant gap occurs between Zr values of 450–700 ppm where only one representative trachyte sample exists. Incompatible-incompatible element diagrams (Fig. 4.10, Y, Nb, La and Rb against Zr) show smooth linear positive trends that pass through the origin, and are consistent with Aluto's evolved pantellerites being derived from a mafic parent with similar chemistry to the pre-Aluto (Nqub) or Wonji lavas (Nquw). The post-caldera rhyolites cover a considerable range in incompatible element values and the most evolved samples are from the grey pumice unit Qup (Section 4.5.2.2) which has 1650 ppm Zr. Notably, the comenditic rhyolite unit (Qcr), the earliest recognizable phase of post-caldera volcanism, is offset from the main fractionation trend for certain incompatible trace-elements (e.g., Y and La against Zr, Fig. 4.9). An ignimbrite sampled from a fault scarp near Munesa (Fig. 4.1B) by Teklemariam, (1996) that we classify as a Pre-Aluto ignimbrite (Nqui) also falls off the main linear array evidencing a different fractionation trend from the Aluto sample suite.

Ratios of incompatible elements such as La/Y and Rb/Nb (Fig. 4.10) do not show significant variations within the sample suite, and indeed the post-caldera rhyolites (excluding Qcr) show an extremely constant ratio. The Rb/Nb ratio of Precambrian crustal rocks, which represent a likely component of the basement rock, are much higher than any samples from Aluto (Fig. 4.10). We follow previous arguments of Peccerillo et al., (2003) and suggest that partial melting of these crustal rocks would tend to increase the large ion lithophile element and high field strength element ratios (LILE/HFSE, e.g. Rb/Nb in Fig. 4.10) in the melt, making it extremely unlikely

that the peralkaline magmas were derived from crustal anatexis alone (discussed further in Section 4.8.1).

4.6.4 Examining fractional crystallization processes

Major and trace element trends are indicative of fractional crystallization (Section 4.6.2 and 6.3). To assess the viability of this process in generating the Aluto sample suite we adopt the simple approach of Blundy and Wood (1991), and model evolving Sr concentrations in a melt governed by feldspar fractionation. From our petrographic observations (Section 4.6.1) it is clear that feldspar is the main phenocryst phase found throughout the sequence, and assuming that the system is dominated by feldspar fractionation then the progressive change in composition from anorthite to albite to anorthoclase (and the corresponding increase in the feldspar-melt partition coefficient, D_{Sr}) should explain the Sr whole-rock trends (e.g., Blundy & Wood, 1991).

In the model Zr is taken to be completely incompatible (in line with trace element observations in Section 4.6.3 and the lack of zirconium-bearing minerals observed petrographically) and is used as a proxy for melt fraction (F). The Wonji basalt sample (Nquw) which is poorly evolved and least enriched in incompatible trace elements (161 ppm Zr) is our best estimate of a parental magma, and we use Zr_{parent} / Zr_{sample} as an indicator of the fraction of liquid remaining. In the model we also assume that the partitioning of Sr between plagioclase feldspar and silicate melt (D_{Sr}) as a function of anorthite (An) content and temperature, as described by Blundy and Wood (1991), is the only process controlling Sr evolution in the melt. For each calculation we crystallize 10 % of the residual liquid, and the temperature and An content of plagioclase are adjusted at each step (as shown in Figures 12 A and B). The temperature changes linearly from 1150°C to 650°C with fraction of liquid remaining (Fig. 4.11A), while the An content of plagioclase varies from An_{90} to An_{20} (Fig. 4.11B). These assumptions are based on petrological constraints of magma temperatures and mineralogy variations from Dabbahu volcano (Ethiopia)

after Field et al. (2013); the only peralkaline volcano in the region where these detailed constraints exist. Four different fractionation trends are considered (Fig. 4.11 C–E) each representing a constant percentage of plagioclase in the crystallizing assemblage (30%, 50%, 70% and 90% are shown). The resultant change of the bulk partition coefficient (D_{Sr}) is shown in Figure 4.11C, and modelled melt Sr evolution is compared to the Aluto whole-rock data in Figure 4.11D, E.

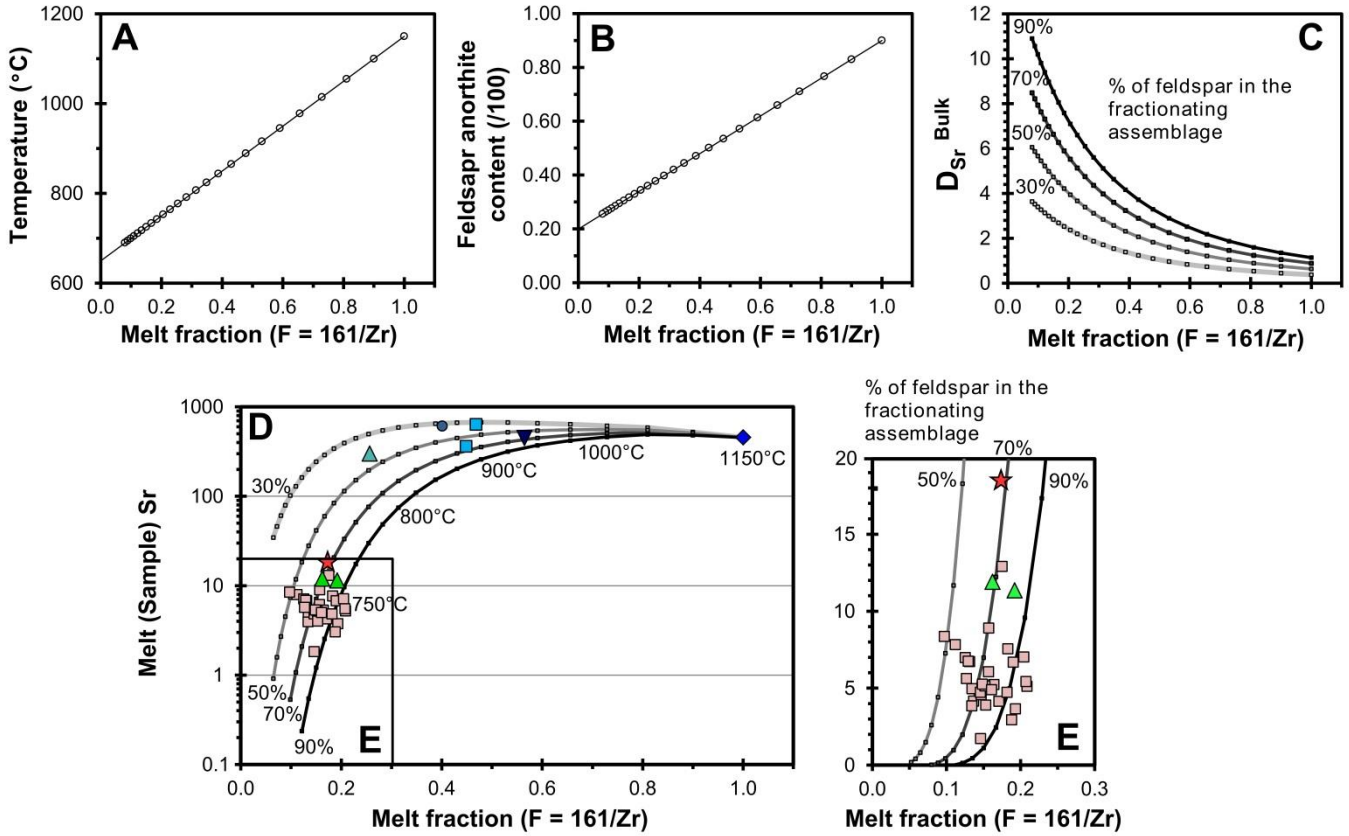

Figure 4.11: *Melt models to predict Sr concentration in a feldspar-dominated crystallizing assemblage using Zr as a proxy for melt fraction. We assume that the poorly evolved Wonji basalt (Nquw), which is least enriched in incompatible trace elements, is representative of a parental magma. The modelled temperatures, anorthite-content and the calculated bulk partition coefficient (D_{Sr}), are plotted in* ***A–C****, respectively. For each increment we crystallize 10 % of the residual melt relative to the previous step. We consider four models where proportion of plagioclase as a percentage of total phenocrysts is held constant at 30, 50, 70 and 90 %.* ***D)*** *Variation in Sr content of Aluto samples during fractionation (coloured points), compared to the modelled melt evolution trends (shown as lines where each point represents 10 % crystallization of residual melt relative to the previous step). Data are plotted using the coloured symbols (see Figure 4.8 for legend).* ***E)*** *Shows inset from D with a linear vertical scale.*

The Aluto whole-rock Sr values broadly match the melt evolution predicted by the models (Fig. 4.11D, E), although there is an obvious gap in samples between the trachytes and the least evolved rhyolite (i.e., the silicic enclave sampled from the scoria cone sequence, shown as the red star). The key observation from Fig. 4.11D is that it is possible to link back the peralkaline rhyolite Sr concentrations to the least evolved basaltic lavas via feldspar fractionation and this lends support to fractional crystallization being the dominant process in controlling melt evolution at Aluto. The models suggest that the total amount of fractional crystallization required to generate the peralkaline rhyolites from parental basaltic lavas is > 80%, and that feldspar must be the dominant phase in the crystallizing assemblage (≥ 50%) in order to generate the rhyolites (in agreement with petrological observations made in Section 4.6.1). A key implication of this model, and the trace element diagrams in Figure 4.10, is that degree of differentiation has changed through time. The welded ignimbrites are more chemically evolved than the trachytes, while the post-caldera magmas have undergone even more extreme fractionation. In Section 4.8.1 we consider petrogenesis and melt evolution processes at Aluto further, as well future work that will be necessary to test our hypotheses.

4.7. Evolution of the Aluto volcanic complex

Using our new stratigraphic and age constraints we present a conceptual model outlining the development of the Aluto complex within the context of the evolving rift (Fig. 4.12).

4.7.1 Pre-Aluto ignimbrite units (4–2 Ma)

Rifting of the CMER in the Pliocene and into the earliest Pleistocene (before 2 Ma) was characterized by displacement along ~50 km long, widely spaced, NE-SW border faults (Bonini et al., 2005; Corti, 2009; Agositini et al., 2011). Volcanic activity was diffuse and silicic complexes were developed across a wide footprint of the rift (e.g., Mohr and Potter, 1976; WoldeGabriel et al., 1990). The oldest deposits identified in the Aluto deep wells are thick

sequences of silicic ignimbrites (Nqui, Fig. 4.3). Hydrothermal alteration of these deep well units is extensive and greatly complicates thorough geochemical correlations and geochronological analyses (WoldeGabriel et al., 1990). The Nqui ignimbrites are presently constrained to be greater than 1.4 Ma in age (Table 4.1), and in line with field correlations made by WoldeGabriel et al. (1990) and Teklemariam et al. (1996) we speculate that they derive from voluminous explosive eruptions at large axial volcanic complexes of Munesa (WoldeGabriel, 1990, 1992) and Gademotta (Laury and Albritton, 1975; Vogel et al., 2006), as well as the off-axis complexes (Mohr and Potter, 1976) which were all active within this time frame (Fig. 4.12A).

4.7.2 Rift localization and associated basaltic fissure eruptions (2–0.5 Ma)

A major shift in the style of rifting took place in the CMER after ~2 Ma (Boccaletti et al., 1998; Ebinger and Casey, 2001; Bonini et al., 2005), when deformation localized into axial volcanic segments (Corti, 2009; Agositini et al., 2011; Keir et al., 2015). Large volumes of mafic magma have been intruded into the roots of these segments (up to depths of ~10 km, Keranen et al., 2004) and above these intense faulting and dyking facilitate extension of the brittle upper-crust (Keir et al., 2006, 2015). Short (<20 km long), NNE-SSW trending, closely spaced Wonji faults (Fig. 4.12B) characterize tectonic deformation in these segments (Ebinger and Casey, 2001; Keir et al., 2015).

The >500 m thick sequences of sub-aerial basalt and trachybasalt units (Nqub, Fig. 4.3, 8), dated at ~1.5 Ma (Table 4.1), coincide with this major shift of deformation within the rift valley. Our interpretation is that these mafic lavas and scoria deposits relate to fissure eruptions occurring along the rift axis in tandem with Wonji fault development (Fig. 4.12B, analogous to present day rift-related volcanism in Afar, Ferguson et al., 2010). The great thickness of the mafic units as well as the occurrence of intervening palaeosol layers, suggests that Nqub sequences were generated from numerous eruptive events over a timescale ranging between 100 ka – 1 Ma.

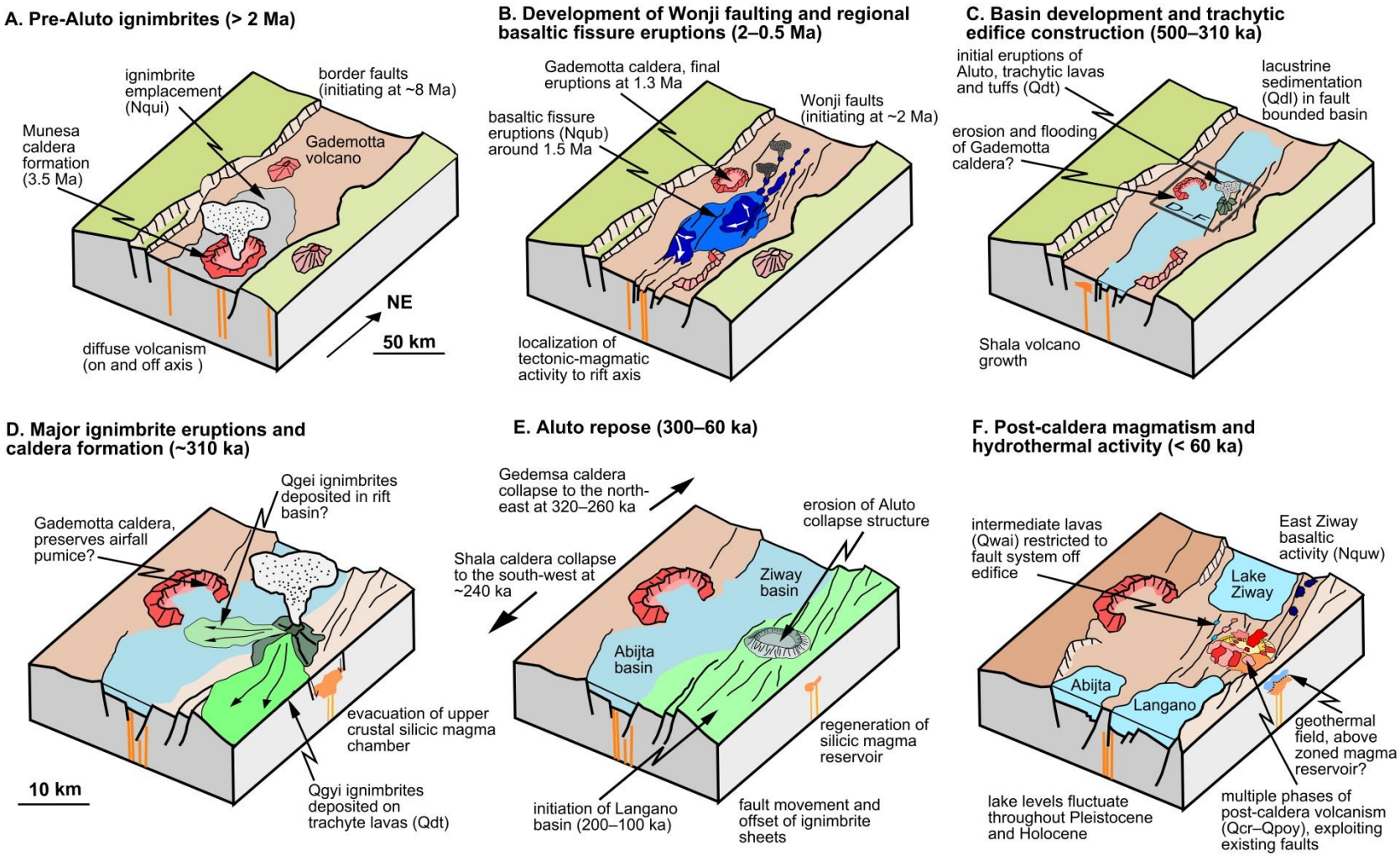

Figure 4.12: *Schematic diagrams depicting the evolution of the Aluto volcanic complex within the context of the evolving Ziway-Shala rift basin.*

4.7.3 Basin development and growth of the trachytic edifice (500–310 ka)

Following the mafic fissure eruptions, deep wells on the west of Aluto record lacustrine sediments accumulating within the fault controlled Ziway-Shala basin (which formed between 570–330 ka, Le Turdu et al., 1999, Fig. 4.12C). A number of the deep wells also show trachytic tuffs and lavas interbedded with the lacustrine sediments (Section 4.5.1.3, Fig. 4.3). The deep well trachytes are correlated with the trachytic units found at Mt Dima (Fig. 4.4, Fig. 4.5M), and mark the onset of silicic volcanism in the region (i.e., they represent the earliest eruptive products of the Aluto volcanic complex). Our interpretation is that trachyte lava flows and tuffs built up a low relief silicic complex (or lava shield) upon the faulted rift terrain. Trachytic lava piles, as envisaged here (Fig. 4.12C), appear to commonly form the earliest growth stages of peralkaline volcanic edifices in both the Ethiopian and Kenyan rift systems (e.g., Shala: Mohr et al., 1980, Kone: Rampey et al., 2010, Emuruangogolak: Weaver, 1977; Macdonald 2012, Menegai: Leat et al., 1984; Macdonald et al., 1994, Olkaria: Clarke et al., 1990; Macdonald et al., 2008 and Longonot: Scott, 1980; Clarke et al., 1990; Scott and Skilling, 1999; Macdonald et al., 2014).

4.7.4 Climactic caldera-forming eruptions (~310 ka)

Caldera formation at peralkaline volcanoes is typically linked to explosive eruptions that generate widespread tuff sheets (e.g., Green Tuff, Pantelleria, Mahood, 1984; Hildreth and Mahood, 1986; Williams et al., 2013). At Aluto, the remnant caldera wall structure (Fig. 4.4), as well as constraints from soil-CO_2 degassing and vent alignments (Hutchison et al., 2015) all suggest that the complex has undergone at least one caldera-forming eruption. The welded ignimbrite units Qgei and Qgyi have overlapping $^{40}Ar/^{39}Ar$ ages of 316 ± 13 ka and 306 ± 12 ka (Table 4.1), and represent the best candidates for widely dispersed, explosive ignimbrite sheets associated with a classic peralkaline caldera collapse (Fig. 4.12D). While there is insufficient field evidence to assess how these deposits physically relate (e.g., whether the ignimbrites represent one or multiple eruptive events), their componentry (large obsidian and pumice fiamme, of diameter >10

cm), thicknesses (>10 m) and dense welding suggest that they are the proximal deposits of large-scale ignimbrite-forming eruption(s).

4.7.5 Volcanic hiatus at Aluto (300–60 ka)

Following the major ignimbrite eruptions at Aluto there appears to have been a significant hiatus (~250 kyr) in volcanic activity (Fig. 4.12E). During this period major ignimbrite eruptions and caldera collapse took place at neighbouring volcanoes of Gedemsa: 320–260 ka; Shala: 240 ± 30 ka and Corbetti: 175 ± 20 ka (Mohr et al., 1980; Peccerillo et al., 2003; Hutchison et al., in review). At ~100 ka the Langano basin developed south of Aluto (Fig. 4.12E, Le Turdu et al., 1999) establishing a single deep freshwater lake in the region (Benvenuti et al., 2002).

4.7.6 Post-caldera activity (< 60 ka)

Volcanic activity resumed at Aluto after ~60 ka, and has been marked by the eruption of rhyolite lavas flows, pumice fallout and PDCs from vents largely confined to the main edifice (Fig. 4.12F). Our mapping allowed us to classify four distinct eruptive sequences, each bounded by palaeosols that mark a hiatus in volcanic activity (Fig. 4.3). The earliest phase consists of the comenditic rhyolite lavas (Qcr) which erupted at 55 ± 19 ka. The next phase is represented by bedded pumice deposits and aphyric obsidian lavas (Qao). No ages have been determined for Qao, but this unit is stratigraphically bracketed between 74 and 49 ka using the ages of the underlying and overlying units of Qcr and Qpo, respectively (Fig. 4.3). Subsequent eruptions comprise a series of sparsely porphyritic obsidian lava flows (Qpo) with ages of 62 ± 13 ka, 22 ± 14 ka and 19 ± 5 ka. Finally, the youngest eruptive phase at Aluto, likely occurring after 10 ka (Section 4.5.3), relates to volcanic units Qup–Qpoy.

Silicic eruption cycles for the post-caldera phases appear to initiate with an explosive eruption building small pumice cones and/or emplacing PDC deposits; these are then followed by effusive

eruptions comprising obsidian or finely crystalline rhyolite lavas (e.g., Fig. 4.5E, K and Fig. 4.6 A, D). This cyclic activity is consistent with a scenario where volatile rich magmas accumulate in the roof of the magmatic reservoir, overpressure triggers eruption of a gas-rich pumice units which are then followed by degassed obsidian coulees (in line with typical models of rhyolite lava dome emplacement from elsewhere, e.g., Mono Craters, California, Fink et al., 1980, and Pantelleria, Mahood and Hildreth, 1986).

While we have classified four post-caldera eruptive phases, the field evidence from the youngest pumice breccias and obsidian lavas (Qpby and Qpoy), as well as the $^{40}Ar/^{39}Ar$ ages for Qpo units (Fig. 4.3, Table 4.1), demonstrate that individual lavas are erupted from discrete vents across the complex over a prolonged period of time. Therefore the mapped eruptive phases represent a sequence of rhyolite lava dome events, rather than a single eruption from a single vent. Volcanic vent locations, particularly for the youngest obsidian coulees (Qpo and Qpoy) are commonly linked to a structural control imposed by the underlying caldera ring fault or tectonic faults (Hutchison et al., 2015). Small volume intermediate eruptions (<0.01 km^3) have occurred on Aluto but are restricted to the faulted zones on the western flank (Fig. 4.4; 12F). Phreatomagmatic eruptions are also a common feature of volcanism in the last 60 ka (Fig. 4.7D), these would have occurred around the flanks of the volcano at the shoreline of the Ziway-Shala lake, but also potentially within the caldera when rising magma interacted with water stored in a caldera lake or geothermal reservoir.

4.8. Insights into silicic peralkaline volcanism in Ethiopia

4.8.1 Geochemistry and magmatic evolution

The geochemical results and trace element modelling for the Aluto whole-rock suite (Section 4.6) are consistent with fractional crystallization as the fundamental process generating the evolved peralkaline melts erupted from the complex. This agrees well with geochemical and petrological

arguments, modelling and experiments reported by several authors for the MER (e.g., Caricchi et al., 2006; Peccerillo et al., 2003, 2007; Ronga et al., 2009; Rooney et al., 2012; Giordano et al., 2014), as well as for other basalt–trachyte–pantellerite suites in comparable geodynamical contexts (e.g., Dabbahu, Barberi et al., 1975; Field et al., 2012, 2013 and Pantelleria, Civetta et al., 1998; White et al., 2009; Neave et al., 2012) which all identify fractional crystallization as the key petrogenetic process.

It has been argued that crustal assimilation may play a significant role at a number of other peralkaline centres (Davies and Macdonald, 1987; Black et al., 1997; Bohrson and Reid, 1997; Tura et al., 1999), however, based on characteristic trace element signatures (e.g., Rb/Nb Fig. 4.10) we suggest there is no requirement for any significant contribution from crustal melting to form the post-caldera rhyolites at Aluto. A more stringent test for crustal assimilation at Aluto will require additional radiogenic isotope analysis (Sr-Nd-Pb) and would be greatly complemented by a better understanding of lithospheric structure and composition in the CMER (e.g., Cromwell et al., 2010). Indeed at Fentale and Gedemsa volcanoes (also located in the MER), Giordano et al. (2014) found isotopic evidence for minor (~ 2%) crustal assimilation in mafic magmas as well as low temperature contamination of rhyolites by hydrothermal/meteoric fluids. It is important to recognize that while our results suggest fractional crystallization processes dominate at Aluto (Figs. 4.8–4.12), minor assimilation and contamination cannot presently be ruled out.

Understanding how the silicic melt reservoirs of the MER were assembled and the timescales over which this occurred is a major challenge, but nonetheless essential if we wish to achieve a complete synthesis of the magmatic processes that have operated during rift evolution. At Aluto, a great thickness (>500 m) of mafic lavas (Nqub) were erupted regionally prior to the formation of the silicic complex (Fig. 4.12B), and our trace element geochemistry (Section 4.6.3) and

modelling (Section 4.6.4, Fig. 4.11) leads us to hypothesize that the mafic lavas are part of the same magmatic lineage as the peralkaline rhyolites. At present geochemical analyses of primitive mafic lavas from Aluto are extremely limited (Figs. 4.8–4.10) and further sampling, ideally complemented by melt inclusion studies, will be necessary to verify how representative our choice of parental melt composition is (Section 4.6.4).

Linking the Nqub basaltic lavas and the peralkaline rhyolites of Aluto as a single lineage, would suggest they were both generated from the same mantle-derived basaltic melt. We envisage a scenario where basaltic parental melt flux out of the MER mantle reservoir was focused into the axial volcanic segments of the rift zone (Section 4.7.2). Mantle-derived basaltic melt intruded within the volcanic segments could be tapped into the Wonji fault plumbing systems (Rooney et al., 2007) and erupt regionally (e.g., Nqub or Nquw), or alternatively could stall and fractionate, ultimately allowing evolved melts to accumulate in the upper crust. The silicic volcanoes of the MER are located at the ends of the volcanic segments (e.g., Mohr et al., 1980; Casey et al., 2006) and it is commonly assumed that reduced extensional stresses (Keranen et al., 2004; Beutel et al., 2010) and/or the cooled crust abutting the segment tip (Ebinger et al., 2008) hindered magma ascent at these sites. An alternative view is that once the upper crustal reservoir and the volcanic edifice began to establish then the stress regime could have acted to focus magma ascent in the crust, essentially capturing later melts beneath the volcanic edifice (Karlstrom et al., 2009). In any case we suggest that the evolved silicic melts of Aluto represent the stalled, structurally focused component of mantle-derived basaltic melts.

The earliest silicic eruptions from Aluto were trachytic (Qdt, Fig. 4.12C), and it is plausible that the peralkaline melts that would later form the major ignimbrites (Qgyi and Qgei) were extracted from the trachytes (e.g., Rooney et al., 2012). Incompatible trace elements and modelling (Figs. 4.10 and 4.11) indicate that trachytic lava can be produced via ~70 % fractional crystallization

from the least evolved (parental) basaltic lavas found in the study area, while welded ignimbrites require >80 % fractionation.

The large silicic melt reservoir (pre-requisite for units Qgei and Qgyi) was likely to have been assembled during an episode of high heat and mass input (e.g., Tappa et al., 2011; Frazer et al., 2014; Macdonald et al., 2014). The elevated rates of magma and heat supply may have limited the degree of differentiation, and hence incompatible element concentrations in the pre- and syn-caldera samples (e.g., Y, Nb, La, Rb and Zr, Fig. 4.10) do no approach the high values seen in many of the recent post-caldera products. A similar temporal trend is observed at Longonot (Macdonald et al., 2014) where periods of strong convection in the magma reservoir in the build up to caldera formation limit any extreme compositional variations. By ~310 ka a large volume of melt- and volatile-rich magma had formed at shallow crustal levels beneath Aluto and the major caldera-forming eruptions could be initiated (Fig. 4.12D). The substantial time gap of ~250 kyr between the welded ignimbrites and post-caldera phases (Fig. 4.12 E, Section 4.7.5) suggests that there was a near total withdrawal of eruptible magma from the upper crustal chamber.

The first post-caldera phase of Aluto (comenditic rhyolites, Qcr) are less evolved than the major welded ignimbrite units and fall off the fractionation trend for certain trace elements (e.g., La and Y in Fig. 4.10). It is has been demonstrated at a number of other peralkaline systems that the first post-caldera phases consist of mixed rhyolites and trachytes with mafic material from lower in the reservoir (e.g., at Menegai, Leat et al., 1984 and Longonot, Macdonald et al., 2014). While the data presented here do not allow us to thoroughly address this issue we suggest that dedicated microanalytical and isotopic studies of the comenditic rhyolites (Qcr) will be key to identifying evidence for melt mixing and contamination.

The post-caldera rhyolites show a large range of incompatible element concentrations and the pumice unit Qup, which likely represents a Plinian eruption, has the most chemically evolved composition (Fig. 4.10). The extreme enrichments in incompatible element concentrations after ~60 ka may be explained by formation of a stratified shallow magmatic reservoir with a compositionally zoned cap (e.g., Mahood et al., 1981; Leat et al., 1984; Hildreth and Mahood, 1986; Civetta et al., 1988; Macdonald and Scaillet, 2006; Neave et al., 2012; Macdonald et al., 2014). In this case the most evolved compositions (e.g., Qup) would be generated following periods of extensive crystal fractionation and/or decreasing melt supply to the shallow magmatic reservoir, which would have driven the magma in the cap to more evolved compositions. A comprehensive analysis of melt compositions (e.g., Neave et al., 2012), as well as additional age constraints on the post-caldera phases will be critical to further assessing temporal variations in geochemistry; and will provide important information on the current trajectory of melt evolution.

Intermediate lavas (Qwai) are demonstrably scarce (Fig. 4.4) but yield valuable insights into current state of magmatic system. At Aluto intermediate eruptions are restricted to low-lying vents in faulted regions west of the edifice (Section 4.5.2.2) and the presence of silicic enclaves within the scoria cone sequences (Section 4.6.1) suggest that mafic and silicic compositions must be present within the same magma plumbing system. On the main edifice of Aluto there is no evidence for mafic-intermediate magmas having erupted, nor do we find any mixing-mingling between mafic-intermediate and silicic magmas. Peralkaline melt zones are commonly assumed to form a density barrier that prohibits mafic melts from reaching the surface (Mahood et al. 1984; Neave et al., 2012). The fact that no mafic-intermediate lavas are found on the centre of the Aluto edifice suggests that peralkaline melts beneath the complex are sufficiently aggregated to prohibit ascent of dense mafic melts. Hence mafic-intermediate magma rise to the surface can only be accomplished via fault networks beyond the edge of the silicic melt cap. This contrasts markedly with Gedemsa (a peralkaline complex 75 km north-east of Aluto) where basaltic lavas

have erupted within the caldera and have entrained silicic liquids as well as partially crystalline silicic rock fragments (Peccerillo et al., 2003). Aluto has undergone much greater volumes of post-caldera volcanism than Gedemsa (Hutchison et al., in review); it also hosts a much larger geothermal field and shows evidence for ground deformation (Biggs et al., 2011), these lines of evidence as well as the absence of mafic lavas on the centre of the Aluto complex are consistent with a more consolidated melt zone here.

4.8.2 The pace of silicic volcanism in the MER

Our stratigraphy shows that Aluto underwent an early phase of edifice building (duration not yet constrained but likely on order of 150–400 kyr, based on similar peralkaline complexes in the Kenyan rift, e.g., Menegai, Leat, 1984 and Longonot, Clarke et al., 1990), major ignimbrite eruptions at ~310 ka, a period of repose lasting 250 kyr and then episodic post-caldera volcanism after ~60 ka. The apparent lack of volcanic activity at Aluto between 300 and 60 ka could be explained by a real hiatus in volcanism, or potentially a gap in sampling. Our updated stratigraphy (Fig. 4.3) represents the most complete coverage of the volcanic eruptive events to date, and on the basis of our lithological correlations between the surface and deep stratigraphy (Section 4.5.3) we consider that this hiatus in volcanism is real. However, until unambiguous geochronological measurements are made across a complete field or core section that covers the transition from major ignimbrite eruptions to the post-caldera eruptions some uncertainty remains.

Overall, our geological interpretations and new ages suggest that silicic volcanism at Aluto can be considered episodic on a variety of timescales. Large volume caldera-forming events take place on long-timescales >100 kyr, linked to substantial deliveries of mantle-derived melt to the mid-crust. Stalling of magmas and melt capture processes (e.g., Keranen et al., 2004; Beutel et al., 2010; Ebinger et al., 2008; Karlstrom et al., 2009) help to assemble large volume upper-crustal

magma reservoirs (>10 km^3), and crystal fractionation is key to driving melt evolution to silicic compositions (Peccerillo et al., 2003; Rooney et al., 2012). We also see evidence for shorter timescale (ca. 10 kyr) eruptive cycles, represented at Aluto by unconformity-bounded post-caldera phases (Fig. 4.3, Section 4.7.5). These cycles may link to the recharge and replenishment of small volumes (<10 km^3) of melt and volatiles in the cap of established upper crustal reservoirs (e.g., Civetta et al., 1988). Silicic eruptive fluxes at the rift segment scale (Hutchison et al., in review) are also consistent with a 'pulsed model' of magma supply and eruption, typified by short episodes of major ignimbrite activity as well as long hiatuses in eruptive activity.

4.8.3 Future volcanic hazards

Volcanic phenomena that have occurred at Aluto in the last 10 ka include obsidian coulees (Qpoy), pumice cones and PDCs (Qpby), and pumice fallout (Qup). Lahars (Qal) have also occurred, although may only have been facilitated during episodes of humid climate prior to ~5 ka (e.g., Le Turdu et al., 1999; Benvenuti et al., 2002). In Table 3 we evaluate potential volcanic hazards and population exposure at Aluto.

Based on the record of past volcanism, a future eruption of Aluto will begin with a moderate explosive eruption to form a pumice cone (potentially with localized PDCs), followed by emplacement of an obsidian coulee (Table 3). The recent obsidian coulees (Qpoy) have volumes of 1–100 x 10^6 m^3 (e.g., Fig. A2.1). Pumice cones (Qpby) built up prior to the obsidian coulees are difficult to trace laterally, but we estimate that small cones have volumes of ~10 x 10^6 m^3 while the largest pumice cones (e.g., the large Qpby dome mapped north of well LA-6, Fig. 4.4) have volumes of ~250 x 10^6 m^3. Our geological mapping (Fig. 4.4) shows that there have been thirteen obsidian coulees (map unit Qpoy) emplaced over the last ~10,000 years. Of the thirteen Qpoy coulees that have erupted a few of these appear to have erupted synchronously, and for simplicity, if we assume there have been 10 distinct eruptions, this would support an average

Potential hazard	Eruption of tephra	Phreatomagmatic/ Phreatic eruptions	Pyroclastic density current (PDC)	Lava flow (basaltic)	Lava dome (rhyolitic)	Changes in diffuse degassing	Debris avalanche
Origin and characteristics	Explosive vertical eruption of pumice and lithic fragments into the air; distribution controlled by column height and wind field	Magma water interaction, explosion due to rapid release of steam; vent will be located within geothermal field	Eruption of molten/hot fragments of pumice entraining lithic clasts; distribution is topographically controlled	Largely effusive eruption of molten lava, slow moving, controlled by topography	Initiate with explosive eruption building up pumice dome near vent; rhyolite lava breaches dome and is emplaced slowly and will be topographically controlled	Areas of diffuse degassing migrate with time; potential for dense volcanic gases (e.g., CO_2) to concentrate in depressions	Result from slope failure of volcanic edifice
Typical length scale (relative to vent)	10–30 km	5 km	10 km	500 m to 1 km	500 m to 2.5 km	1 km	< 5km
Effect on land and objects	Blanketing of land and loading of property near vent	Burning, burial and impact damage to land and property	Burning, burial and impact damage to land and property	Burning, burial and destruction of land and property	Burning, burial and destruction of land and property	Destruction and damage to vegetation; danger for people living in properties nearby where gases (e.g., CO_2) can accumulate	Burial and destruction of land and property
Degree of risk and population exposure	Moderate for people living within 10 km of volcano (25,000); low to people beyond this (315,000)	High for people living within 5km of volcano (6,000), low for people within 10 km (25,000)	High for people living within 10 km of volcano (25,000), particularly those closest to volcano and living in valleys	Low for people living within 10 km of volcano (25,000), typically associated with fault zones on flanks of complex	Low to moderate for people living within 10 km of volcano (25,000), explosive phases and dome collapse represent greatest risk	Low for people living with 5 km of volcano (6,000)	High for people living with 5 km of volcano (6,000), especially for those living adjacent to steep slopes at the base of complex
Number of deposits recognized in last 10,000 years	At least one eruption in last 10,000 years emplaced tephra to >10 km from vent, pumice fall on main edifice is 2–3 m thick	unknown	At least one PDC deposit within caldera following Qup unit (Fig. 4.5E, F), deposits are 5–10 m thick on main edifice	At least one basaltic eruption. Qwai lava flow deposit 2.5 km west of Adami Tullo (Qwai, Fig. 4.4) appears fresh, no cover by Qup	Approximately thirteen silicic domes within the last 10,000 years, some may have erupted synchronously, suggest eruption rate of around 1 per 1000 years. Volume typically between 1–100 km^3, with maximum of ~250km^3	unknown	unknown

Table 4.3: *Potential volcanic hazards at Aluto. Population data was provided by the Smithsonian Global Volcanism Program (Siebert and Simkin, 2002).*

silicic lava dome eruption at a rate of 1 per 1000 years. This value is broadly in line with observations of tephra layers preserved in lacustrine sections west of the Aluto that showed ~13 tephra horizons within the Abernosa pumice deposit, which spans a period of ~15,000 years (Section 4.5.3, Gasse and Street, 1978).

A salient feature of volcanism over the last 10,000 years is that lavas have erupted from discrete vents associated with volcanic and tectonic faults (Hutchison et al., 2015) but they show no obvious spatial progression with time. Real-time monitoring networks (e.g., Sparks, 2003) will be vital to constraining magma movement within the subsurface prior to future eruptions. More generally, a thorough understanding of the recurrence interval of post-caldera phases (e.g., Pyle and Elliott, 2006; Nomikou et al., 2014), detailed mapping of tephra fall (e.g., Fontijin et al., 2010, 2011) and PDC deposits (e.g., Wiart and Oppenheimer, 2000, 2004; Rampey et al., 2010, 2014), and forward modelling of a spectrum of eruption scenarios (e.g. Aspinall and Woo, 2014; Jenkins et al., 2015) will be critical for developing probabilistic models of volcanic hazard at Aluto.

4.9. Conclusions

Field mapping, remote sensing, geochronology and geochemistry provide new insights into the eruptive history and magmatic evolution of the Aluto volcanic complex in Ethiopia. The first eruptions followed a period of mafic fissure volcanism and rift basin development. The complex was initially built up as a trachytic edifice, via both explosive and effusive activity. At ~310 ka the complex underwent a phase of major explosive activity (represented in the field by extensive welded ignimbrite sheets) which we propose developed a caldera rim structure and ring fault. After a substantial hiatus in activity, post-caldera volcanism began at ~60 ka. We identify four distinct post-caldera rhyolitic sequences that include pumice fall, PDC and lava flow units. Rhyolitic lavas have progressively in-filled the caldera, and their eruptions have exploited

structural weaknesses created by the volcanic ring fault and through going tectonic faults. Whole-rock geochemical data suggests that crustal melting did not play a significant role in generating the evolved rocks of Aluto, and without isotopic constraints the simplest interpretation of our data is that silicic magmas of Aluto were mainly generated through protracted fractional crystallization processes. Recent silicic eruptions appear to occur at an average rate of 1 per 1000 years, and we expect that future eruptions of Aluto will involve explosive emplacement of localised pumice cones and effusive obsidian coulees of volumes between 1–100 x 10^6 m^3. Given that >300,000 people live within 30 km of Aluto, as well as the targeted geothermal investment, permanent volcanic monitoring is a critical next step to enable effective management and mitigation of future risk at this volcano.

Chapter 5

Silicic eruptive fluxes in the Main Ethiopian Rift

A version of this chapter is currently undergoing revisions for publication as an article in Nature Geoscience: Hutchison et al. *in review*. A pulse of rift volcanism in Ethiopia at the dawn of modern humans. Authors as follows:

William Hutchison*[1], Raffaella Fusillo[2], David M. Pyle[1], Tamsin A. Mather[1], Jon Blundy[2], Juliet Biggs[2], Gezahegn Yirgu[3], Benjamin E. Cohen[4], Richard Brooker[2], Dan N. Barfod[4] and Andrew T. Calvert[5]

1. Department of Earth Sciences, University of Oxford, South Parks Road, Oxford OX1 3AN, UK
2. School of Earth Sciences, University of Bristol, Wills Memorial Building, Queens Road, Bristol BS8 1RJ, UK
3. School of Earth Sciences, University of Addis Ababa, P.O. Box 1176, Addis Ababa, Ethiopia
4. NERC Argon Isotope Facility, Scottish Universities Environmental Research Centre, Rankine Avenue, East Kilbride, Scotland G75 0QF, UK
5. U.S. Geological Survey, 345 Middlefield Road, MS-937, Menlo Park, California 94025, USA

Abstract

The Main Ethiopian Rift is the most extensive active continental volcanic field in the world, and is the location of the longest records of human co-existence with volcanoes. Over 10 million people live within the Ethiopian rift valley, but current understanding of the magnitude and timing of large explosive eruptions is poor. New precise $^{40}Ar/^{39}Ar$ age determinations of seven volcanic units suggest that the rift experienced a major pulse of explosive volcanic activity between 320–170 ka. During this period, at least four distinct volcanic centers underwent large volume (> 10 km^3) caldera-forming eruptions, with eruptive fluxes elevated five times above the average eruption rate for the past 700 kyr. The temporal clustering of the ignimbrite eruptions suggests that development of large volume silicic magma reservoirs was closely synchronous. We suggest that a pulse of mantle-derived basalt was delivered to the crust, after c.a. 2 Ma, and that stalling of magma at favorable structural loci was critical in generating the flare-up ignimbrites. Explosive silicic volcanism in the Ethiopian rift valley appears to be episodic, creating geologically brief intervals of environmental change that would have remodeled landscapes and ecosystems occupied by early hominin populations.

5.1 Introduction

Continental rift zones often undergo episodes of intense silicic volcanism, or ‘flare-ups’ where eruption rates are elevated 3–10 times above the steady-state (e.g., Wilson et al., 2009). Intracrustal magma reservoirs storing large volumes of evolved, eruptible magma are an essential prerequisite, and it is commonly assumed that these can only be assembled when the mantle-to-crust magma flux is elevated significantly above the steady-state Burns et al. (2015). Establishing whether a continental rift is in steady-state or flare-up mode has clear implications for volcanic hazard assessment and allows valuable long-term predictions of eruptive fluxes to be made.

The Main Ethiopian Rift (Fig. 5.1a), located at the northern tip of the East African Rift system (Corti, 2009), is a 600 km long active continental rift that hosts a current population in excess of 10 million. Forty years ago, based on their regional field studies, Mohr et al. (1980) speculated that a paroxysm of crustal extension and silicic volcanism (i.e., a flare-up) took place in the MER during the Middle Pleistocene (between 300–200 ka). However at that time, there were few constraints on ages and erupted volumes from the individual silicic volcanic centers (Fig. 5.1b), and this important hypothesis for the evolution of the MER environment and future hazards here has not yet been tested.

The Middle Pleistocene (781–126 ka) of Ethiopia spans a key juncture in hominin evolution, represented by the arrival of anatomically modern humans (AMH) at around 200 ka (McDougall et al., 2005). There is a consensus that the major events in hominin evolution occurred in East Africa (Maslin et al., 2014); and that key evolutionary steps link to periods of environmental change (Potts, 2012). A current theme of this research is that episodes of extreme environmental fluctuation, wet-dry variations, and their knock-on effects in terms of resource availability drove hominin speciation and the emergence of AMH (Maslin et al., 2014). While attempts to understand the links between past environmental change and human evolution have stimulated

considerable research into African palaeoclimate (Trauth et al., 2007), comparatively little attention has been paid to the role that explosive volcanism may have played in influencing habitability and regional environmental change (Basell, 2008). The fundamental – and unanswered question – is whether explosive volcanic activity in the MER has been steady or pulsed through the Quaternary; and whether eruptions were of sufficient size to have caused profound environmental change.

We present new age data for caldera-forming eruptions at Aluto and Corbetti volcanoes (A and C in Fig. 5.1b) as well as an analysis of eruption scales, and use these to evaluate the Middle Pleistocene (300–200 ka) flare-up hypothesis (Mohr et al., 1980). Our results suggest that the onset of the Middle Stone Age in Ethiopia (c.a. 300 ka; Morgan and Renne, 2008) was indeed a period of elevated magmatic flux and caldera-forming volcanism. We consider the causes for the flare-up, the broader implications of this mode of activity, and the potential impacts both for early hominin populations living in the MER, and for current volcanic hazards in the region.

Figure 5.1. *Topographic maps of the East Africa (a) and the Main Ethiopian Rift (b).* ***a:*** *Red lines indicate major plate boundaries, grey triangles show Quaternary volcanoes, black stars identify key archaeological sites dated as Middle Stone Age (MSA), after Basell, (2008), and black arrows show current extension vectors (relative to a fixed Nubian plate, Stamps et al., 2008).* ***b:*** *Hillshade digital elevation model showing the study region. Quaternary silicic volcanic complexes are outlined by the red dashed lines, and include: Corbetti (C); Shala (S); Aluto (A); Bora-Bericcio (B) and Gedemsa (G), solid red lines indicate calderas. Beige shaded area identifies the maximum extent of the Ziway-Shala lake system in the Late Pleistocene (Benvenuti et al., 2002). The major present-day lakes are identified as: KO: Lake Koka; ZI: Lake Ziway; LA: Lake Langano; AB: Lake Abijta, SH: Lake Shala and AW: Awasa. Faults, after Agostini et al. (2011), are shown as blue lines. Major structural features include: East Abijta fault (EAF); Katlo Horst (KH); West Langano fault (WLF); West Ziway fault (WZF) and the Wonji fault belt (WFB), summarized in Figure 5.4 and by Le Turdu et al. (1999). Approximate extent of the volcanic segments are shown by black shaded areas (Le Turdu et al., 1999; Casey et al., 2006). Black stars show Middle Stone Age sites at Gademotta Ridge (GAD), grey stars show Late Stone Age sites adjacent to the Bulbula River (BUL). Illustrative isopachs (thickness of tephra fall deposits) predicted for an eruption of 5 km^3 silicic magma (equivalent to 12 km^3 of tephra), were calculated using the exponential thinning relationship (Pyle, 1989) and are shown as rose circles with white outlines (the vent location is arbitrary, for simplicity no external wind field was considered, and we have assumed a conservative tephra thickness of 1 m proximal to the vent).*

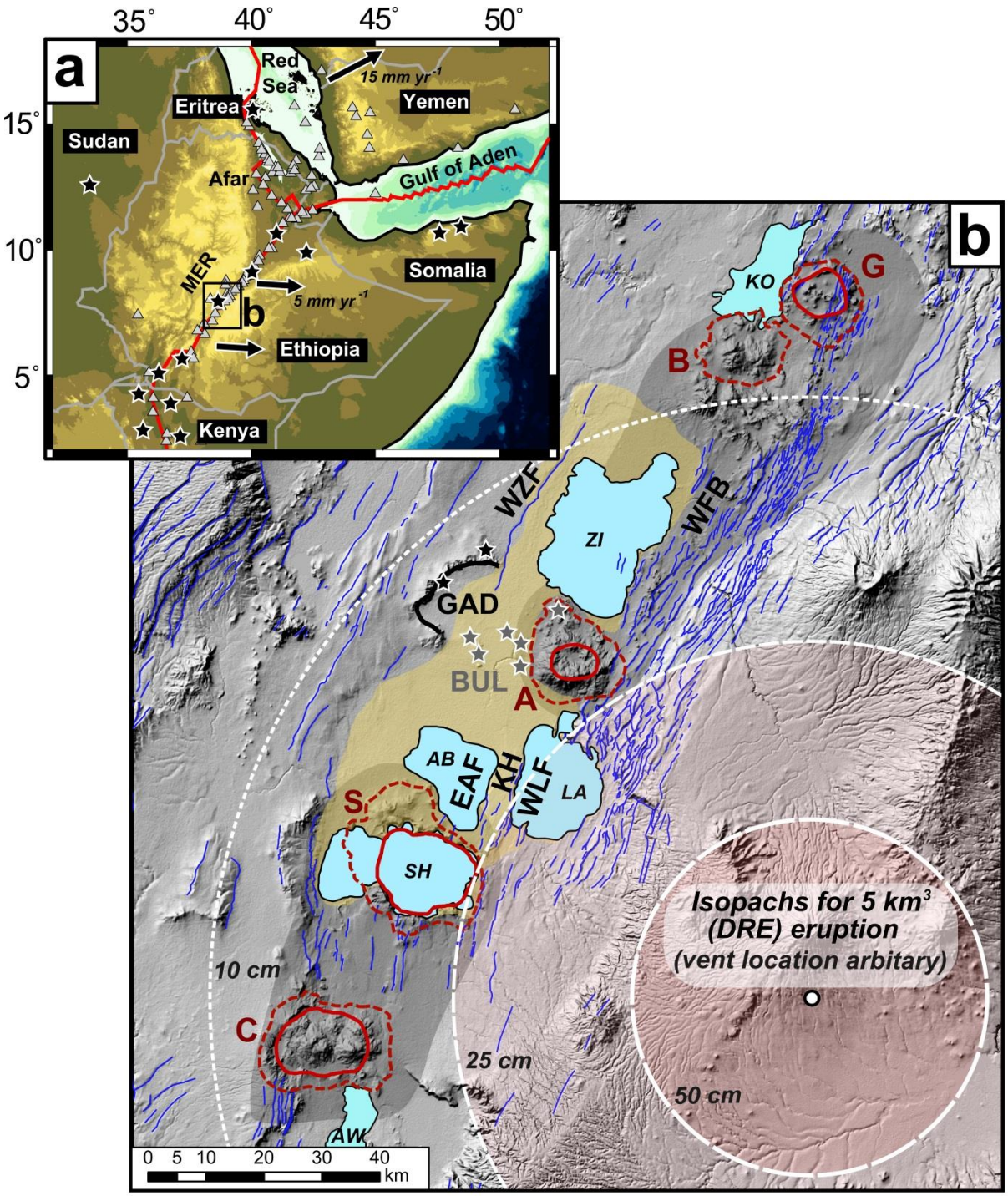

5.2 Methods

Full methods are provided in Appendix 3. Section A3.1 provides all $^{40}Ar/^{39}Ar$ geochronology methods, diagrams and data for the Aluto and Corbetti samples (Appendix A3.1.1 and A3.1.2, respectively). For consistency throughout the article $^{40}Ar/^{39}Ar$ ages represent the arithmetic mean, the error quoted is one standard deviation of the data and includes the error in J. All $^{40}Ar/^{39}Ar$ and

K/Ar ages were calculated (or recalculated) according to the decay constants of Renne et al. (2011) and an atmospheric $^{40}Ar/^{36}Ar$ ratio of 298.56 (Lee et al., 2006). Recalculation of the K/Ar ages for Gedemsa (Peccerillo et al., 2003) and Shala (Mohr et al., 1980) yielded only negligible changes (i.e., only appearing in the non-significant digits, and much smaller than the analytical errors) so we quote the ages as originally published. Appendix 3.2 provides an overview of how we used digital elevation models and field measurements to estimate eruptive volumes. In sections A3.2.1–A3.2.4 we summarize the known eruptive history for each complex and present the volume calculations in detail.

5.3 Eruptive history of Aluto and Corbetti

Aluto and Corbetti are two major silicic volcanoes located in the central section of the MER (CMER, Corti, 2009; Agostini et al., 2011; Keir et al., 2015. The volcanoes are adjacent to the Ziway-Shala basin, which formed a single connected lake in the Late Pleistocene (~100 ka) (Le Turdu et al., 1999; Benvenuti et al., 2002) Both complexes have caldera structures (Fig. 5.1b), thought to have formed in response to large explosive eruptions that deposited extensive ignimbrite sheets (Di Paola, 1971; Hutchison et al., 2015). The volcanic stratigraphy of Aluto and Corbetti volcanoes, verified by new $^{40}Ar/^{39}Ar$ ages, is presented in Figure 5.2.

The deep stratigraphy of Aluto is exposed along faults on the margins of the complex. South-east of the main edifice (Fig. A3.1a), a sequence of massive, dull-grey, strongly welded ignimbrites, rich in lithic fragments and with abundant obsidian fiamme, are exposed (Fig. 5.2). Ignimbrite sequences are typically 20–50 m thick and are underlain by trachytic lavas, breccias and minor tuff horizons that comprise the earliest silicic eruptions of Aluto (Fig. 5.2). Massive, pistachio green, welded ignimbrites are also exposed east of Aluto (Fig. A3.1a), here containing abundant pumice fiamme. The deposit is immediately overlain by lacustrine sediments (Fig. 5.2) suggesting that it was emplaced in a lake basin. The Aluto welded ignimbrites have overlapping

ages of 316 ± 19 and 306 ± 12 ka (Fig. 5.2). While there is insufficient field evidence to assess how they physically relate (e.g., whether the ignimbrites represent one or multiple eruptions) their componentry (large obsidian and pumice fiamme, of >10 cm diameter), thicknesses (>10 m) and dense welding indicate that they are the proximal deposits of large-scale ignimbrite-forming eruptions.

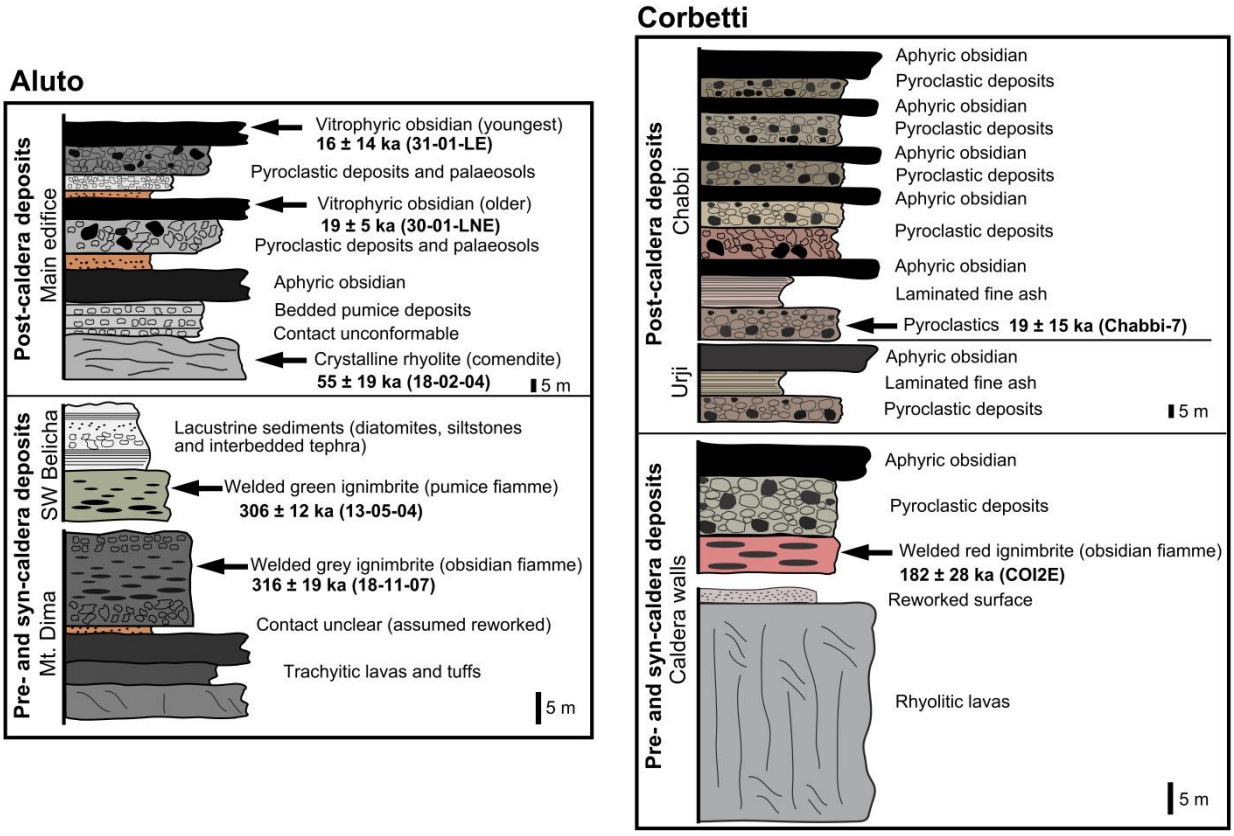

Figure 5.2. *Simplified eruptive stratigraphy for Aluto and Corbetti volcanoes. Arrows indicate units with new $^{40}Ar/^{39}Ar$ ages (mean ± one standard deviation).*

The main edifice of Aluto (Fig. A3.1a) comprises a pile of coalescing obsidian coulees and pumiceous pyroclastic deposits. Comenditic rhyolites dating from ~60 ka were identified at the base of the edifice; while the youngest obsidian coulees have ages of 10–20 ka (Fig. 5.2). All of the units that comprise the main edifice (Fig. 5.2) are products of small-volume post-caldera eruptions that would have largely affected local (<10 km) rather than regional scales.

At Corbetti, the earliest activity is represented by a sequence of rhyolitic lava flows (>50 m thick) exposed in the caldera walls (Fig. A3.1b). The pre-caldera lavas are covered by massive, red, welded ignimbrites that have an age of 182 ± 28 ka. Unwelded pyroclastic deposits and aphyric obsidian coulees overlie the welded ignimbrite; together this sequence represents a single major eruptive unit and is the largest explosive eruption to have occurred at the Corbetti complex. Following the major ignimbrite eruption, two eruptive centers (Chabbi and Urji, Fig. A3.1b) developed within the collapsed caldera (Di Paola, 1971). Post-caldera activity at these centers is characterized by a succession of explosive and effusive rhyolites, predominantly pyroclastic flows and aphyric obsidian coulees (Fig. 5.2). The oldest deposits of these cones have an age of ~20 ka.

The new chronostratigraphic results support a simple staged eruptive history for both Aluto and Corbetti volcanoes. Each underwent an early phase of silicic activity, building a low relief shield, as observed at other peralkaline volcanoes in East Africa (e.g., Kone: Rampey et al., 2015, Menegai: Leat et al., 1984; Macdonald et al., 1994, Olkaria and Longonot: Clarke et al. 1990). The pre-caldera activity was followed by a major phase of caldera collapse, and ignimbrite emplacement, and later post-caldera volcanism progressively in-filled the calderas (Hutchison et al., 2015).

5.4 Wider evidence for a flare-up

Shala and Gedemsa volcanoes (S and G in Fig. 5.1b, Mohr et al., 1980; Peccerillo et al., 2003), show similar patterns of edifice growth, collapse and post-caldera resurgence to Aluto and Corbetti. At Shala, caldera collapse at 240 ± 30 ka (K/Ar dating, errors quoted at 1σ, after Mohr et al., 1980) followed a period of rhyolitic-trachytic edifice growth, and eruption of pumiceous and welded ignimbrites (Mohr et al., 1980). At Gedemsa, north-east of the Ziway-Shala basin (Fig. 5.1b), the largest ignimbrite eruptions and resultant caldera collapse also followed a phase

of silicic edifice building (Peccerillo et al., 2003). K/Ar dating showed that pre- and post- caldera rocks bracket an age of 320–260 ka for collapse events at Gedemsa (Peccerillo et al., 2003).

Evidence from Gedemsa, Aluto, Shala and Corbetti volcanoes points to a common eruptive history in three stages: early edifice growth; caldera collapse, and a post-caldera phase. In Figure 5.3a, we show erupted magma volumes (dense rock equivalent, DRE) calculated for each stage using digital elevation models (DEMs) and thickness estimates (A3.2). The cumulative erupted volume is dominated by Shala caldera, although caldera-forming eruptions at the other silicic volcanoes also contributed significant pulses of silicic magma (Fig. 5.3a). From these data we estimate the CMER Mid-Pleistocene (781–126 ka) average eruption rate as 0.5 $km^3 ka^{-1}$. From 320–170 ka the eruption rate is 2.5 $km^3 ka^{-1}$, five times the Mid-Pleistocene average, and comparable to the long-term magmatic output from Taupo Volcanic Zone and Yellowstone (~3 km^3 ka^{-1}, Houghton et al., 1995), the largest active silicic magmatic systems on Earth.

Further evidence for the flare-up is found at Gademotta Ridge, ~20 km north-west of Aluto (GAD in Fig. 5.1b), where colluvial-alluvial sediments and tephra preserve hominin occupation sites from the Middle and Late Pleistocene(Laury and Albritton, 1975; Morgan and Renne, 2008; Sahle et al., 2013, 2014). The sediments and tephra deposited at Gademotta Ridge rest unconformably on an extinct collapsed caldera dated to c.a. 1.3 Ma (Vogel et al., 2006). Three major distal tephra layers have been identified at Gademotta Ridge, they are 0.5–1 m thick and of fallout origin (Laury and Albritton, 1975). $^{40}Ar/^{39}Ar$ ages for the tephra units range from 302 ± 22 to 195 ± 15 ka (Fig. 5.3b, overlapping the flare-up period). The Gademotta stratigraphy clearly demonstrates that several major explosive eruptions occurred during the flare-up period, and that significant volumes of tephra were dispersed across and along the rift, although future geochemical investigations should be undertaken to unambiguously link the distal tephras with the proximal ignimbrites and confirm geochronological correlations (Fig. 5.3).

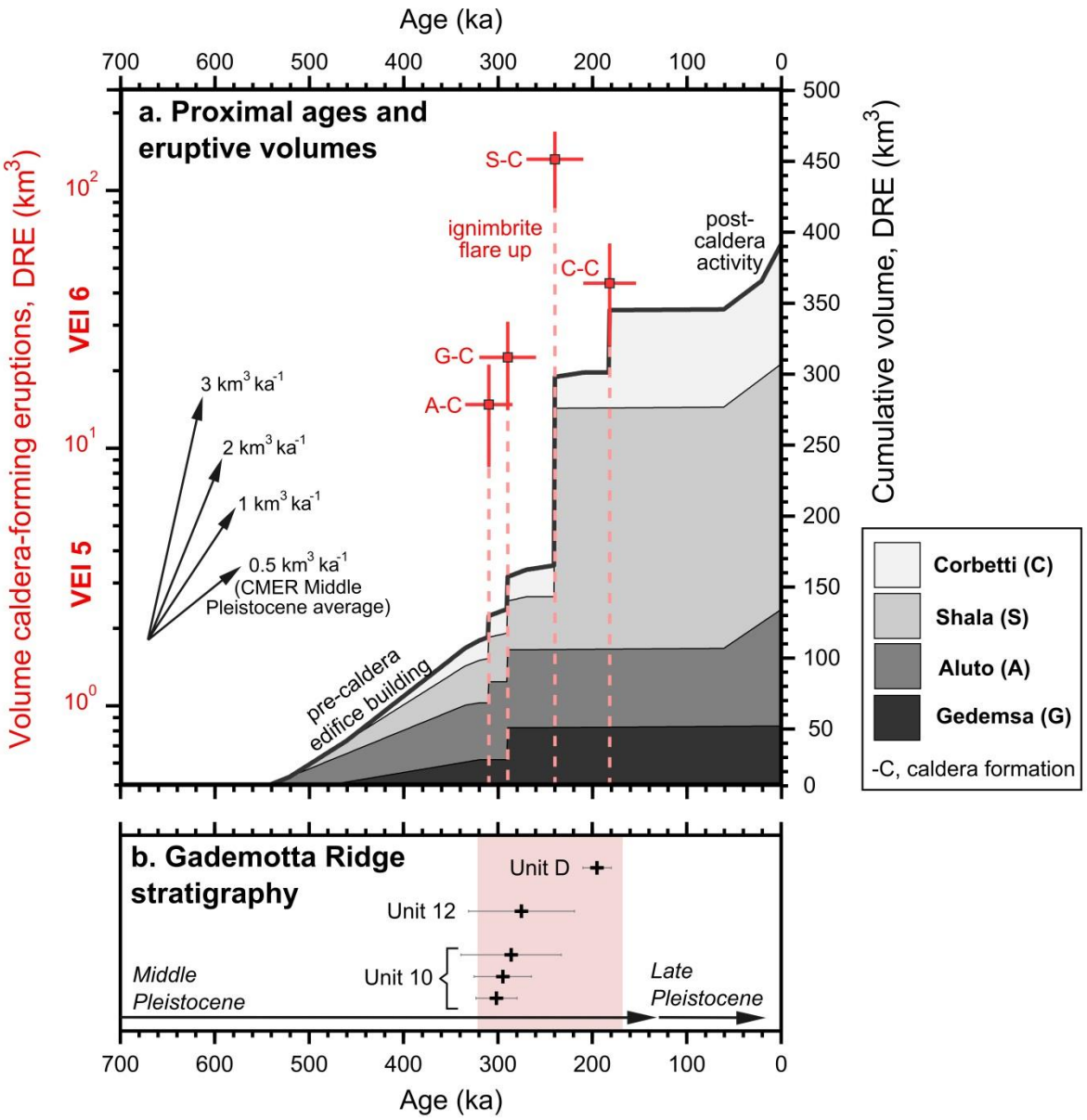

Figure 5.3. ***a:*** *Age-volume plot for Gedemsa (G), Aluto (A), Shala (S) and Corbetti (C) volcanoes. The left hand axis shows the volume of individual caldera-forming eruptions (log scale) and corresponds to the dashed red bars (labeled for each volcano). Red data points show the mean age and medium caldera eruption volume estimate (see Appendix 3.2 for full details), horizontal error bars show the standard deviation of the age data (except in the case of Gedemsa when caldera formation is bracketed by dates), vertical error bars show the low and high estimates for caldera eruption volume (Appendix 3.2). The right hand axis shows the cumulative volume for the complexes (individual volcano records are stacked). For the pre- and post- caldera phases we have assumed linear magma supply rates. For the pre-caldera edifice we assume that onset of caldera growth occurred 250 ka prior to the caldera-forming eruption (in line with observations from other peralkaline volcanoes in East Africa, Leat et al., 1984; Clarke et al., 1990). Arrows show eruptive fluxes of 0.5, 1, 2 and 3 km^3 ka^{-1}. Peak eruptive flux occurs between 320–170 ka when the major caldera-forming events occurred at all four volcanoes. Between 320 and 170 ka the silicic eruptive flux was 2.5 km^3 ka^{-1}; five times greater than the time-averaged Middle Pleistocene (781–126 ka) eruption flux of 0.5 km^3 ka^{-1}, and approaching long-term magmatic output from Taupo Volcanic Zone and Yellowstone (~3 km^3 ka^{-1}, Houghton et al., 1995).* ***b:*** *^{40}Ar/^{39}Ar ages for tephras from Gademotta Ridge (after Morgan and Renne, 2008; Sahle et al., 2013, 2014, ages recalculated to decay constants of Renne et al., (2011) where necessary). Black horizontal bars give typical 1σ standard error on the mean for each tephra as originally quoted by Sahle et al. (2013, 2014). Grey horizontal bars show one standard deviation of the data (i.e., equivalent to the error quoted on our new ^{40}Ar/^{39}Ar ages throughout the chapter).*

We have shown that four silicic volcanic complexes in a ~200 km segment of the MER all underwent their largest explosive eruptions in a geologically short time-span between 320 and 170 ka (Fig. 5.3a). It is unlikely that the magmatic reservoirs of the flare-up ignimbrites were connected. The ~40 km distance separation between the complexes, lack of overlap and nesting of collapse structures (Fig. 5.1b), as well as geophysical imaging (Whaler and Hautot, 2006), all suggest that the MER silicic complexes host discrete shallow magmatic reservoirs, and therefore we view these as independent collapse events. Assuming the caldera-forming eruptions were independent, and each major eruption could have occurred randomly at some point during the c.a. 500 kyr 'life-time' of these volcanoes then the cumulative Poisson probability that more than 3 eruptions occurred in a 150 ka window (pink shaded area in Figure 5.3b) would be 0.03. This demonstrates that a chance clustering is highly unlikely.

5.5 Igniting a flare-up

Flare-ups are often linked to periods of increased mantle magma productivity which elevate mantle-to-crust magmatic fluxes significantly above the steady-state (Burns et al., 2015). During these episodes of increased magmatic and thermal input to the crust, large volumes of chemically evolved, eruptible silicic magma are generated (Tappa et al., 2011; Frazer et al., 2014). Once assembled, eruption of spatially-separated, melt- and volatile-rich reservoirs are triggered internally by magmatic overpressure, or through external processes such as regional stress changes and faulting (Aguirre-Diaz et al., 2003; Cooper et al., 2012). We briefly outline the spatial and temporal constraints on the flare-up and develop a hypothesis surrounding its origins.

The long-term record of volcanism in the CMER (Fig. 5.3a) is consistent with a 'pulsed model' of silicic magma productivity; characterized by episodes of major ignimbrite eruptions (320–170 ka), but also by significant hiatuses (e.g., the post-caldera phase, where >150 kyr elapsed before volcanism resumed at Aluto and Corbetti, and only very small volumes, <5 km^3 DRE, have been

erupted at Gedmesa and Shala). Temporal clustering of the ignimbrite eruptions (Fig. 5.3a) also suggests that development of the silicic magma reservoirs was closely synchronous. Thermal and density considerations require that large upper-crustal magma bodies (i.e., flare-up magmas) are geologically short-lived (Lipman, 2007), and therefore the clustering of eruptions implies that assembly of the separate silicic magma reservoirs was approximately coeval. To initiate simultaneous silicic magma reservoir development along the rift zone we suggest that a period of elevated mantle-to-crust magma flux is necessary (Fig. 5.4), potentially driven by rapid localized thinning of the plate followed by extensive decompression melting (Keir et al., 2015).

Melt flux out of the MER mantle reservoir would be focused into axial volcanic segments; ~15 km wide, ~50 km long, en-echelon features located along the axis of the rift (Corti, 2009; Keir et al., 2015). The volcanic segments have been active since ~2 Ma (Fig. 5.4), and there is evidence that large volumes of mafic magma are intruded into the roots of the segments (up to depths of ~10 km, Keranen et al., 2004). The silicic volcanoes are located at the ends of the volcanic segments (Fig. 5.1b, Mohr et al., 1980; Keranen et al., 2004; Casey et al., 2006), presumably where magma ascent was hindered due to reduced extensional stresses (Keranen et al., 2004; Beutel et al., 2010) and/or the cooled crust abutting the segment tip (Ebinger et al., 2008). This emphasizes a further fundamental concept: silicic magma reservoirs had to develop in regions where magma stalled and ponded, allowing fractionation and accumulation of silicic melts in the upper crust.

Synthesizing these concepts, we propose that an increased melt flux out of the mantle reservoir, delivered to the axial volcanic segments of the MER initiated growth of the flare-up magmas, and that melt focusing, by capture (Karlstrom et al., 2009) and/or stalling at the segment tips (Keranen et al., 2004; Beutel et al., 2010; Ebinger et al., 2008) provided an important structural trap. Geological constraints on the pre-flare up period are limited due to poor exposure of the

deep stratigraphic sequences. However, evidence from geothermal wells on Aluto reveals that prior to the first silicic eruptions, voluminous basaltic fissure eruptions occurred (generating ~1 km thick sequences, Teklemariam et al., 1996); we suggest that the magma bodies for the flare-up ignimbrites could represent the stalled, structurally focused, component of this large mantle-derived melt flux (Fig. 5.4).

Once large melt- and volatile-rich silicic reservoirs were assembled ignimbrite eruptions could be initiated. The precise trigger of the flare-up between 320–170 ka remains open to debate, and we offer two scenarios to explain this. Either, the major eruptions were driven by processes internal to the silicic magma bodies (i.e., the separate reservoirs each reached critical overpressure within this time-frame), or alternatively, eruptions were triggered by external processes such fault growth in the Ziway-Shala basin (Fig. 5.4, Mohr et al., 1980; Le Turdu et al., 1999), static stress changes in response to neighboring caldera collapses, or dyke intrusions (Sparks et al., 1977). Although the data presented in this study do not allow a thorough examination of these hypotheses, we suggest that detailed reconstruction of the flare-up magma reservoirs, in terms of crystallization, thermal and storage histories (e.g., Cooper et al., 2012; Burns et al., 2015), will be central to testing these hypotheses.

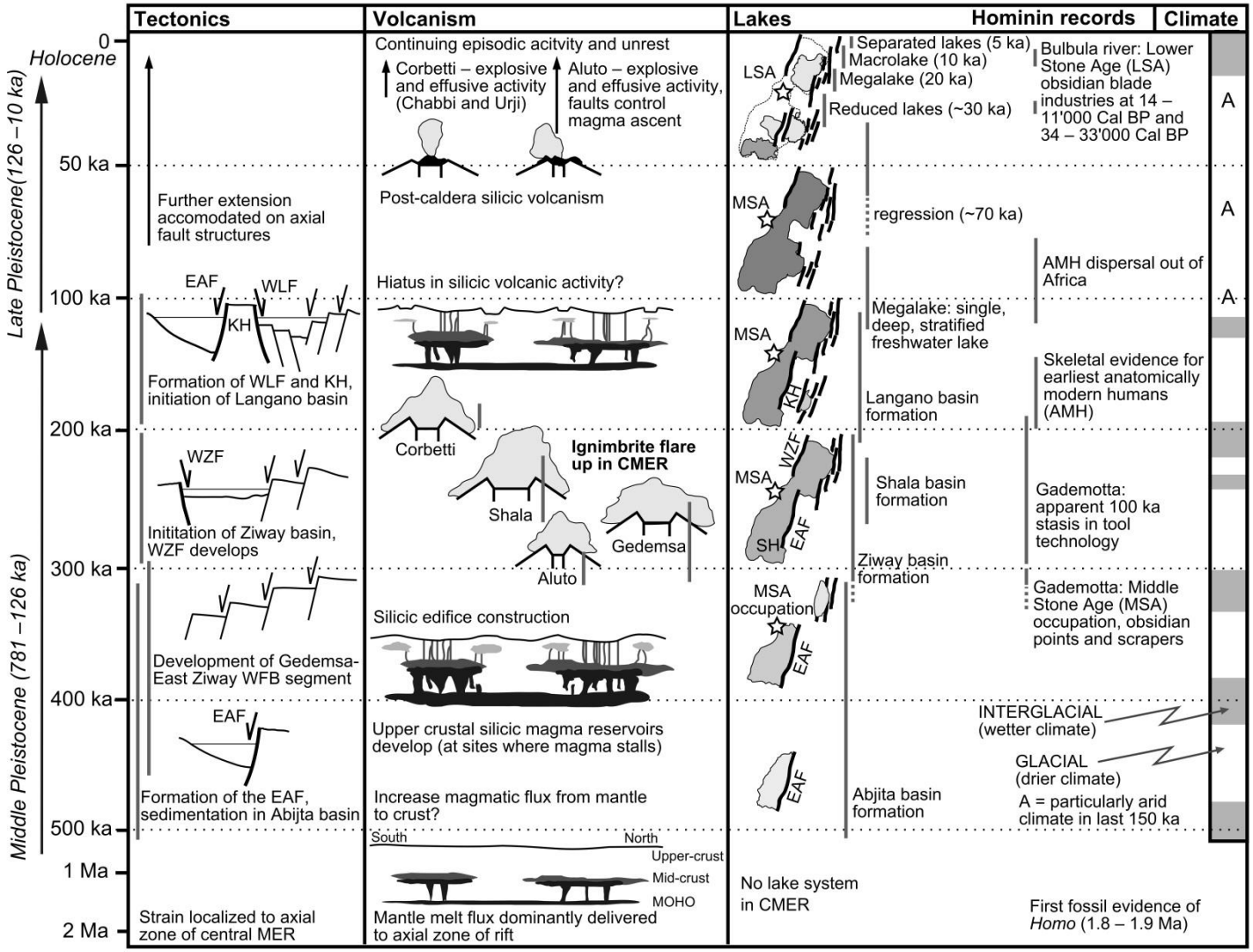

Figure 5.4. *Synthesis of the tectonic, volcanic, lake, climate and hominin records for the Ziway–Shala rift basin (after Le Turdu et al., 1999; Benvenuti et al., 2002; Sahle et al., 2014; Menard et al., 2014, and references therein). Grey vertical bars for tectonic, volcanic, lacustrine and hominin records represent the existing age uncertainties. Major structural (tectonic) features include: East Abijta fault (EAF); Katlo Horst (KH); West Langano fault (WLF); West Ziway fault (WZF) and the Wonji fault belt (WFB), are shown on Figure 5.1b, and summarized after Le Turdu et al., 1999. Shading of the lakes gives a qualitative representation of their depth. Stars identify hominin occupations such as the Middle Stone Age (MSA) sites of Gademotta Ridge (GAD, Fig. 5.1b) and Late Stone Age (LSA) sites adjacent to the Bulbula River (BUL, Fig. 5.1b). Pleistocene glacial-interglacial cycles, shaded white and grey respectively, are summarized from stacked benthic foram $\delta^{18}O$ time-series (Lisiecki and Raymo, 2005).*

5.6 Impacts of a mid-Pleistocene flare-up

Environmental change and variability have been proposed as drivers for the major events in East African hominin evolution (Maslin et al., 2014). Recent studies have tended to focus on glacial-interglacial climate fluctuations, leading to short alternating periods of arid-humid environmental variations in East Africa, as the main control on human evolutionary and cultural development (Potts, 2012; deMenocal, 2004). A fuller understanding of the drivers of environmental change and its consequences in an active rift setting requires a broader perspective. In Figure 5.4, we synthesize the Quaternary history of the Ziway-Shala rift basin. This demonstrates that tectonic, volcanic, climatic and human evolutionary processes not only operate on comparable time-scales, but that they are also coupled. For example: faulting and strain localization controls magma ascent and ponding in the continental crust, which establishes silicic reservoirs; tectonic faulting and caldera collapse generate basins which develop large deep lakes in periods of humidity; lakes dictate site selection and resource availability for hominin populations, and the establishment of lakes and deep groundwater circulation may in turn affect the style of volcanism. Thus to fully understand the links between environmental changes and human evolution, volcanic and tectonic processes (Bailey et al., 2011) must be considered alongside palaeoclimate evidence.

The major explosive volcanic eruptions discussed here (DRE volumes of 10–150 km^3) would have caused rapid and profound environmental disruption in the region. Close to their source vents ignimbrites reach 100–300 m thickness, and mapping (Mohr et al., 1980) suggests that major collapse ignimbrites had run out distances of 15 km to 40 km. Maps illustrating the scale of tephra fallout for a conservative eruption volume of 5 km^3 of silicic magma are shown in Figure 5.1b. Tephra fall deposits at least 50 cm thick would extend to distances of at least 30 km from the vent, whereas finer fractions greater than 10 cm would be dispersed to distances of ~100 km. A key implication is that tephra would be dispersed over distances greater than both the width of the rift and the lake basin. Ash and acid sulfate release from such events would have affected rift

lakes and vegetation causing a cascade of environmental disruption, remodeling the landscapes and resources on which hominins and other organisms depended. How this sequence of major explosive volcanic eruptions directly impacted hominin populations in the MER is not known, and high resolution archeological reconstructions (e.g., Riede, 2014) will be critical to evaluating the response of the human landscape to major geological events. Comparable volcanic eruptions in the Palaeolithic (e.g., Laacher See volcano in Northern Europe, ~13,000 BP, DRE volume of 6.3 km^3) have been linked to significant demographic upheaval (population declines and relocations) as well as marked reductions in technological complexity (Riede, 2014).

Pulses of explosive volcanism may typify the East Africa Rift; each of these would cause significant environmental change, and as such, should not be overlooked as a driver of the population bottlenecks seen in early hominin populations in East Africa (Basell, 2008), as well as a major 'push' factor that dispersed humans within and out of Africa, along with climate ameliorations in the Late Pleistocene (Parton et al., 2015). Geological processes in East Africa (i.e., volcanism and tectonics) occur at rates comparable to Quaternary climatic change (Fig. 5.4), and the magnitude, timings and feedbacks of these processes must be resolved before we can draw firm links between environmental change and human evolution.

Finally, our hypothesis suggests that the major silicic volcanoes of the MER are currently in a post-caldera stage of evolution. This would suggest that the likelihood of large caldera-forming eruptions from these volcanoes in the near future is low. Our new ages and stratigraphies (Fig. 5.2) reveal that small explosive and effusive eruptions have occurred frequently over the last 20 ka and we emphasize that all of the volcanoes pose a continuing hazard to the region (Yirgu et al., 2014).

Chapter 6

Summary and conclusions

6.1 Overview

This thesis explores Quaternary silicic volcanism in the Main Ethiopian Rift (MER) with a central focus on the Aluto volcano complex. Like many other volcanoes in the MER there have been limited prior geochemical or geochronological studies on erupted products from Aluto; and few attempts to place the volcanism here in any regional context. We have addressed these issues by bringing together a range of geological, geophysical and geochemical techniques to investigate active volcanic processes at Aluto, and to understand more about its overall development and magmatic evolution. Owing to the absence of previous studies, the approach in this thesis has been deliberately broad and has been undertaken in order to begin to characterize various magmatic and volcanic processes that might be prevalent throughout the rift system by using a range of techniques. It was hoped that, in uniting these diverse techniques, our reserach might understand more about the volcanic system as a whole.

The Introduction of the thesis (Section 1.5) sets out three main challenges to understanding past, present and future volcanic processes in this rift segment; the following sections summarize how our new work links to these challenges. In each section I first consider the relevance to Aluto (local scale), then take a more regional (rift-scale) view of the conclusions, and finally I point to future research opportunities.

6.2 Past – *How have the MER silicic volcanic complexes evolved? Have the rates of silicic volcanism been steady or pulsed over geological timescales?*

Relevance to Aluto

In Chapter 4 we showed that the first eruptions at Aluto followed a period of mafic fissure volcanism, faulting and rift basin development. The volcanic complex was initially built up as a trachytic edifice, via both explosive and effusive activity, and at ~310 ka Aluto underwent a

phase of major explosive activity (represented in the field by extensive welded ignimbrite sheets). We propose that a caldera rim structure and ring fault were developed at this stage (Chapters 2 and 4). After a substantial hiatus in activity, post-caldera volcanism began at ~60 ka. We identify four distinct post-caldera rhyolitic sequences that include pumice fall, pyroclastic density current and lava flow units. Rhyolitic lavas have progressively in-filled the caldera, and their eruptions have exploited structural weaknesses created by a volcanic ring fault and through going tectonic faults.

The study supports fractional crystallization as the key petrogenetic process generating the evolved peralkaline rocks of Aluto (Chapter 4). Our modelling determined that >80% fractionation was required to obtain the evolved pantellerite compositions from basalts that are of similar geochemistry to nearby rift-related Wonji basalts. Overall this is consistent with other studies and geochemical modelling which have suggested that fractional crystallisation is the key driver of silicic melt evolution throughout the East African Rift System (e.g., Peccerillo et al., 2003; Macdonald et al., 2008). Crustal contamination may play a subtle role at Aluto, although we found no petrographic evidence for assimilated crust, nor did we see any clear geochemical signatures (i.e., Rb/Nb, Zr/Th and other incompatible element ratios were constant throughout much of the rock sequence).

Regional outlook

In Chapter 5 we suggested that Gedemsa, Aluto, Shala and Corbetti volcanoes showed similar patterns of edifice growth, caldera collapse, and post-caldera resurgence. By estimating the volumes and timescales of silicic eruptions, we propose that there was major pulse of explosive volcanic activity in the MER between 320–170 ka; a time period that covers a key juncture in hominin evolution, represented by the arrival of anatomically modern humans (AMH) at around 200 ka (McDougall et al., 2005). During this period, these four volcanic centres each underwent

large volume (> 10 km^3) caldera-forming eruptions, and eruptive fluxes were elevated significantly above the average eruption rate for the past 700 kyr. The notion that continental rifts undergo episodic outbursts of intensive silicic volcanism (or 'flare-up' events) has been suggested previously in other rifts such as the Taupo Volcanic Zone (New Zealand, Wilson et al., 2009), Tepic-Zacoalco rift (Mexico, Frey et al., 2007) and Sierra Madre Occidental (Mexico, Aguirre-Diaz and Labarthe-Hernandez, 2003). However, the role that episodic silicic volcanism played in East Africa on human evolutionary timescales has been little studied; this work reiterates the need for multi-disciplinary approaches to document the complex interactions of volcanism, tectonics, and paleoclimate, as well as their impact on paleobiological records, including hominins.

Further work

Our hypothesis that there was a period of elevated silicic volcanism in the Middle Pleistocene should be a major focus for future interdisciplinary research. Further stratigraphic and geochronological constraints are needed from other silicic centres along the rift valley to test whether this event was localized to the complexes we have studies here, or if it was more widespread (i.e. was the whole rift-segment affected). Further work also needs to be undertaken to link the proximal volcanic stratigraphies (Chapter 5) with the distal sections (e.g., Gademotta ridge, Morgan and Renne, 2008; Sahle et al., 2013, 2014). Tephrochonology and geochemical fingerprinting of these different deposits should make this possible (e.g., Smith et al., 2011). It will also be useful to reconstruct the magma bodies, in terms of their crystallization, thermal and storage histories (e.g., Burns et al., 2015). Multiscale geochemical and isotopic investigations, coupled with geothermobarometry, should shed light on how these large melt reservoirs were assembled and whether fundamental changes in the upper crustal magmatic dynamics took place during the Middle Pleistocene of Ethiopia. We suggested that these eruptions would have had a dramatic effect on the local environment, but major questions remain about how the human

landscape responded to these changes. High resolution archaeological reconstructions (e.g., Riede, 2014) will be critical to evaluating the response of hominin populations in terms of dispersals and technological stasis.

From a petrogenetic viewpoint, major questions remain about how the Aluto silicic rocks have evolved. While our results point towards fractional crystallization being the dominant process at Aluto, future isotopic studies (e.g., O, Sr, Nd and Pb) should be undertaken to understand partial melting, and coupled assimilation and fractional crystallisation (AFC) processes (e.g., Peccerillo et al., 2003). Studies conducted in Iceland over the last two decades strongly support the notion that these petrogenetic processes are linked to the thermal state of the crust (Martin and Sigmarsson, 2010). When the crust is hot, and the geothermal gradient is high, this will lead to a greater degree of partial crustal melting. When the geothermal gradient is lower, less partial melting will take place, and magma will reside longer in the crust prior to eruption. Ultimately, the latter will act to amplify fractional crystallisation processes. In Ethiopia, recent geophysical constraints, principally seismic and magnetotelluric data (Hammond et al., 2011; Dessisa et al., 2013), demonstrate that there are large variations in crustal thickness and geothermal gradient across the rift zone. A major research challenge would be to investigate whether these variations in the thermal and mechanical state of the Ethiopian crust influence the petrogenetic processes in a way that is analogous to geochemical variations seen in the Icelandic rift zone (Martin and Sigmarsson, 2010).

6.3 Present – *What volcanic processes are taking place today? What can we learn about MER geothermal systems, and how can we best exploit these resources?*

Relevance to Aluto

Diffuse volcanic degassing takes place at a number of sites across the Aluto volcanic complex and in Chapter 2 we established that faults provide the main conduits not only for gas, but also for

hydrothermal fluid and magma pathways. These observations, as well as characteristic CO_2–$\delta^{13}C$ (Chapter 3), lead us to suggest that the Aluto magmatic and hydrothermal systems are physically connected by faults and fractures. We envisage a scenario in which deep (> 2km), hot (>250°C) geothermal fluids receive a continuous input of heat and volatiles from a deeper magma reservoir. Fluids migrate along major tectonic faults that dissect the complex and ascend to the surface, the fluids degas and high-concentrations of magmatic CO_2 are released.

Episodic uplift-subsidence events also typify the Aluto volcanic system (Chapter 3). A joint inversion of new and existing InSAR data suggests that the source is located at ~5 km and requires an inflationary volume change of $+12–16 \times 10^6$ m^3 (Chapter 3). These volumes are well below those associated with geothermal production and are more typical of recent eruptive volumes (Chapter 4). Deformation events play out in a style characteristic of a coupled magmatic-hydrothermal system. On this basis we propose that uplift is caused by a deep magmatic intrusion or magmatic fluid injection and that faults provide key pathways for gas and fluid leakage into the geothermal reservoir. This hypothesis can be tested by monitoring changes in gas flux and composition along Aluto's main fault zone, which provides an important conduit for fluid upflow and for sampling the deep reservoirs.

Regional outlook

From a geothermal perspective, it is clear that understanding fluid movement along fault structures is paramount to drilling success (i.e., only two of the eight wells drilled on Aluto, those located along the Artu Jawe fault zone, are productive). This underscores the importance of undertaking detailed geophysical surveys and structural mapping to constrain hydrothermal flow along the major structures prior to drilling. For similar, structurally complex, rift volcanoes which are also targets of future geothermal exploration (e.g., Corbetti, Fentale, and Dofen in the MER), it is critical to understand the key structures and their impact on subsurface fluid flow in order to

maximize productivity of the field. Although these structures introduce significant complexities, fractured geothermal fields may also present new opportunities for exploitation; for example, Curewitz and Karson (1997) showed that the intersection of faults may provide efficient conduits to concentrate hydrothermal fluids in upward flow.

Our study also indicates that the magmatic and geothermal systems hosted by the MER volcanoes could provide a significant flux of deep carbon and volatiles to the atmosphere (Burton et al., 2013). The estimated CO_2 flux for Aluto (250-500t d^{-1}, Chapter 2) is comparable to volcanic plume CO_2 fluxes measured at active volcanoes such as Merapi (Indonesia), Vulcano (Italy), Sierra Negra (Ecuador), and Villarrica (Chile) (see Burton et al., 2013). Aluto is the first silicic caldera-forming volcano of the EARS to be studied for diffuse CO_2 degassing budget (Chapter 2) and so further work is needed to understand whether these fluxes are representative of a 'typical' rift peralkaline system.

Further work

A major challenge is to constrain how hydrothermal and magmatic fluids are distributed and stored in the subsurface of Aluto and how they upwell along the mapped fault zones. Further geochemical-geophysical measurements of volcanic gases (e.g., CO_2, Rn and Th) as well as electrical resistivity and self-potential across fault planes (e.g., Giammanco et al., 2009; Siniscalchi et al., 2010) may provide vital insights into fluid circulation and the connections to the deeper reservoirs. In addition, uplift-subsidence pulses could be investigated in much more detail by deploying dense GPS networks and undertaking time-lapse gravity measurements. Together these techniques could be used to infer the density of the intrusive fluids and their relation to the deformation source (e.g., Gottsmann and Battaglia, 2008).

6.4 Future – *What are the recent rates of volcanism at Aluto and in the MER? What hazards can we foresee?*

Relevance to Aluto

From our geological mapping we were able to identify a number of volcanic hazards that have occurred at Aluto in the last 10,000 years (Chapter 4), and on this basis we believe that the most likely future eruption of Aluto will involve explosive emplacement of localised pumice cones and effusive obsidian coulees of volumes between 1–100 x 10^6 m^3. While our age constraints remain fairly tentative it appears that recent silicic eruptions have occurred at an average rate of 1 per 1000 years. Larger explosive eruptions from Aluto, which would generate more widespread pumice airfall or pyroclastic density currents (PDCs), are also expected and there is abundant evidence from the Bulbulla gorge (10 km west of Aluto) that 10–15 primary tephra layers have been emplaced in last 30,000 years (Gasse and Street, 1978).

Regional outlook

Our regional investigation of silicic eruptive fluxes (Chapter 5) suggests that the major silicic volcanoes of the MER are currently in a post-caldera stage of evolution. Therefore the likelihood of large caldera-forming eruptions from these volcanoes in the near future is low. However, the new ages and stratigraphies (Chapters 4 and 5) clearly reveal that small explosive and effusive eruptions have occurred frequently over the last 60 ka at both Aluto and Corbetti and we emphasize that all of the MER volcanoes pose a continuing hazard to the region. This is supported by evidence from InSAR (Biggs et al., 2011) and seismicity (Keir et al., 2006) which has identified volcanic unrest at these complexes.

Further work

The major questions to be addressed are how much eruptible melt is stored beneath the MER volcanoes, and how well aggregated are these peralkaline melts. At a number of large caldera

complexes in the MER (e.g., Kone and Gedemsa) it has been recognized that basalts have erupted through caldera floor during the waning stages of silicic magmatic activity (Peccerillo et al., 2003 and Rampey et al., 2010). In Chapter 4 we suggested that, since no mafic-intermediate lavas are found on the centre of the Aluto edifice, this could be taken as evidence that peralkaline melts beneath this complex are sufficiently aggregated to prohibit ascent of denser mafic melts. Simple geological observations such as this might provide a means for qualitatively establishing where aggregated silicic melt zones exist beneath the MER. These observations, together with regional InSAR and seismicity surveys, may provide a rapid means of targeting the "high-risk" complexes.

Once "high-risk" complexes are established then real-time monitoring networks (e.g., Sparks, 2003) will be vital in constraining magma movement within the subsurface prior to future eruptions. More generally, a thorough understanding of the recurrence interval of post-caldera phases (e.g., Pyle and Elliott, 2006; Nomikou et al., 2014), detailed mapping of tephra fall (e.g., Fontijin et al., 2010, 2011) and PDC deposits (e.g., Wiart and Oppenheimer, 2000, 2004; Rampey et al., 2010, 2014), and forward modelling of a spectrum of eruption scenarios (e.g. Aspinall and Woo, 2014; Jenkins et al., 2015) will be critical for developing probabilistic models of volcanic hazard at the MER complexes.

References

Abebe, B., Acocella, V., Korme, T., and Ayalew, D., 2007, Quaternary faulting and volcanism in the Main Ethiopian Rift: Journal of African Earth Sciences, v. 48, p. 115–124, doi: 10.1016/j.jafrearsci.2006.10.005.

Acocella, V., Korme, T., Salvini, F., and Funiciello, R., 2003, Elliptic calderas in the Ethiopian Rift: control of pre-existing structures: Journal of Volcanology and Geothermal Research, v. 119, p. 189–203.

Acocella, V., Di Lorenzo, R., Newhall, C., and Scandone, R., 2015, An overview of recent (1988 to 2014) caldera unrest: knowledge and perspectives: Reviews of Geophysics, in press.

Agostini, A., Bonini, M., Corti, G., Sani, F., and Mazzarini, F., 2011, Fault architecture in the Main Ethiopian Rift and comparison with experimental models: Implications for rift evolution and Nubia–Somalia kinematics: Earth and Planetary Science Letters, v. 301, p. 479–492, doi: 10.1016/j.epsl.2010.11.024.

Aguirre-Díaz, G.J., and Labarthe-Hernández, G., 2003, Fissure ignimbrites: Fissure-source origin for voluminous ignimbrites of the Sierra Madre Occidental and its relationship with Basin and Range faulting: Geology, v. 31, p. 773–776, doi: 10.1130/G19665.1.

Aiuppa, A., Caleca, A., Federico, C., Gurrieri, S., and Valenza, M., 2004, Diffuse degassing of carbon dioxide at Somma–Vesuvius volcanic complex (Southern Italy) and its relation with regional tectonics: Journal of Volcanology and Geothermal Research, v. 133, p. 55–79, doi: 10.1016/S0377-0273(03)00391-3.

Allis, R., Bromley, C., and Currie, S., 2009, Update on subsidence at the Wairakei–Tauhara geothermal system, New Zealand: Geothermics, v. 38, p. 169–180.

Amelung, F., Galloway, D.L., Bell, J.W., Zebker, H.A., and Laczniak, R.J., 1999, Sensing the ups and downs of Las Vegas: InSAR reveals structural control of land subsidence and aquifer-system deformation: Geology, v. 27, p. 483–486.

Anderson, E., Crosby, D., and Ussher, G., 2000, Bulls-Eye!—simple resistivity imaging to reliably locate the geothermal reservoir, in Proceedings of the 2000 World Geothermal Congress, Kyushu–Tohoku, Japan, May, p. 909–914.

Árnason, K., Karlsdóttir, R., Eysteinsson, H., Flóvenz, Ó.G., and Gudlaugsson, S.T., 2000, The resistivity structure of high-temperature geothermal systems in Iceland, in Proceedings of the World Geothermal Congress 2000, Kyushu-Tohoku, Japan, p. 923–928.

Arnórsson, S., 1995, Geothermal systems in Iceland: structure and conceptual models – I. High-temperature areas: Geothermics, v. 24, p. 564–602.

Aspinall, W., Auker, M., Hincks, T., Mahony, S., Nadim, F., Pooley, J., Sparks, R.S.J., and Syre, E., 2011, Volcano hazard and exposure in GFDRR priority countries and risk mitigation measures, in Volcano Risk Study 0100806-00-1-R, Global Facil. for Disaster Reduct. and Recovery, Global Facil. for Disaster Reduct. and Recovery, Washington, D. C.

Aspinall, W.P., and Woo, G., 2014, Santorini unrest 2011–2012: an immediate Bayesian belief network analysis of eruption scenario probabilities for urgent decision support under uncertainty: Journal of Applied Volcanology, v. 3, p. 1–12.

Bailey, G.N., and King, G.C.P., 2011, Dynamic landscapes and human dispersal patterns: Tectonics, coastlines, and the reconstruction of human habitats: Quaternary Science Reviews, v. 30, p. 1533–1553, doi: 10.1016/j.quascirev.2010.06.019.

Barberi, F., Ferrara, G., Santacroce, R., Treuil, M., and Varet, J., 1975, A transitional basalt-pantellerite sequence of fractional crystallization, the Boina Centre (Afar Rift, Ethiopia): Journal of Petrology, v. 16, p. 22–56, doi: 10.1093/petrology/16.1.22.

Barry, P.H., Hilton, D.R., Fischer, T.P., de Moor, J.M., Mangasini, F., and Ramirez, C., 2013, Helium and carbon isotope systematics of cold "mazuku" CO_2 vents and hydrothermal gases and fluids from Rungwe Volcanic Province, southern Tanzania: Chemical Geology, v. 339, p. 141–156, doi: 10.1016/j.chemgeo.2012.07.003.

Barry, P.H., Hilton, D.R., Füri, E., Halldórsson, S.A., and Grönvold, K., 2014, Carbon isotope and abundance systematics of Icelandic geothermal gases, fluids and subglacial basalts with implications for mantle plume-related CO_2 fluxes: Geochimica et Cosmochimica Acta, v. 134, p. 74–99.

Basell, L.S., 2008, Middle Stone Age (MSA) site distributions in eastern Africa and their relationship to Quaternary environmental change, refugia and the evolution of Homo sapiens: Quaternary Science Reviews, v. 27, p. 2484–2498, doi: 10.1016/j.quascirev.2008.09.010.

Bastow, I.D., Nyblade, A.A., Stuart, G.W., Rooney, T.O., and Benoit, M.H., 2008, Upper mantle seismic structure beneath the Ethiopian hot spot: Rifting at the edge of the African low-velocity anomaly: Geochemistry, Geophysics, Geosystems, v. 9.

Battaglia, M., Segall, P., and Roberts, C., 2003, The mechanics of unrest at Long Valley caldera, California. 2. Constraining the nature of the source using geodetic and micro-gravity data: Journal of Volcanology and Geothermal Research, v. 127, p. 219–245.

Battaglia, M., Troise, C., Obrizzo, F., Pingue, F., and De Natale, G., 2006, Evidence for fluid migration as the source of deformation at Campi Flegrei caldera (Italy): Geophysical Research Letters, v. 33.

Baubron, J., Rigo, A., and Toutain, J., 2002, Soil gas profiles as a tool to characterise active tectonic areas: the Jaut Pass example (Pyrenees, France): Earth and Planetary Science Letters, v. 196, p. 69–81.

Bendick, R., Bilham, R., Asfaw, L., and Klemperer, S., 2006, Distributed Nubia–Somalia relative motion and dyke intrusion in the main Ethiopian rift: Geophysical Journal International, v. 165, p. 303–310.

Benito-Calvo, A., Barfod, D.N., McHenry, L.J., and de la Torre, I., 2014, The geology and chronology of the Acheulean deposits in the Mieso area (East-Central Ethiopia): Journal of human evolution, v. 76, p. 26–38.

Benvenuti, M., Carnicelli, S., Belluomini, G., Dainelli, N., Di Grazia, S., Ferrari, G.., Iasio, C., Sagri, M., Ventra, D., Atnafu, B., and Kebede, S., 2002, The Ziway–Shala lake basin (Main Ethiopian rift, Ethiopia): a revision of basin evolution with special reference to the Late Quaternary: Journal of African Earth Sciences, v. 35, p. 247–269, doi: 10.1016/S0899-5362(02)00036-2.

Benvenuti, M., Bonini, M., Tassi, F., Corti, G., Sani, F., Agostini, A., Manetti, P., and Vaselli, O., 2013, Holocene lacustrine fluctuations and deep CO_2 degassing in the northeastern Lake Langano Basin (Main Ethiopian Rift): Journal of African Earth Sciences, v. 77, p. 1–10, doi: 10.1016/j.jafrearsci.2012.09.001.

Berardino, P., Fornaro, G., Lanari, R., and Sansosti, E., 2002, A new algorithm for surface deformation monitoring based on small baseline differential SAR interferograms: Geoscience and Remote Sensing, IEEE Transactions on, v. 40, p. 2375–2383.

Beutel, E., van Wijk, J., Ebinger, C., Keir, D., and Agostini, A., 2010, Formation and stability of magmatic segments in the Main Ethiopian and Afar rifts: Earth and Planetary Science Letters, v. 293, p. 225–235, doi: 10.1016/j.epsl.2010.02.006.

Biggs, J., Anthony, E.Y., and Ebinger, C.J., 2009, Multiple inflation and deflation events at Kenyan volcanoes, East African Rift: Geology, v. 37, p. 979–982.

Biggs, J., Lu, Z., Fournier, T., and Freymueller, J.T., 2010, Magma flux at Okmok Volcano, Alaska, from a joint inversion of continuous GPS, campaign GPS, and interferometric synthetic aperture radar: Journal of Geophysical Research, v. 115, p. 1–11, doi: 10.1029/2010JB007577.

Biggs, J., Bastow, I.D., Keir, D., and Lewi, E., 2011, Pulses of deformation reveal frequently recurring shallow magmatic activity beneath the Main Ethiopian Rift: Geochemistry Geophysics Geosystems, v. 12, p. 1–11, doi: 10.1029/2011GC003662.

Biggs, J., Ebmeier, S.K., Aspinall, W.P., Lu, Z., Pritchard, M.E., Sparks, R.S.J., and Mather, T.A., 2014, Global link between deformation and volcanic eruption quantified by satellite imagery: Nature communications, v. 5.

Black, S., Macdonald, R., and Kelly, M.R., 1997, Crustal origin for peralkaline rhyolites from Kenya: evidence from U-series disequilibria and Th-isotopes: Journal of Petrology, v. 38, p. 277–297.

Blundy, J.D., and Wood, B.J., 1991, Crystal-chemical controls on the partitioning of Sr and Ba between plagioclase feldspar, silicate melts, and hydrothermal solutions: Geochimica et Cosmochimica Acta, v. 55, p. 193–209, doi: 10.1016/0016-7037(91)90411-W.

Boccaletti, M., Bonini, M., Mazzuoli, R., and Abebe, B., 1998, Quaternary oblique extensional tectonics in the Ethiopian Rift (Horn of Africa): Tectonophysics, v. 287, p. 97–116.

Bohrson, W.A., and Reid, M.R., 1997, Genesis of silicic peralkaline volcanic rocks in an ocean island setting by crustal melting and open-system processes: Socorro Island, Mexico: Journal of Petrology, v. 38, p. 1137–1166.

Bonini, M., Souriot, T., Boccaletti, M., and Brun, J.P., 1997, Successive orthogonal and oblique extension episodes in a rift zone: laboratory experiments with application to the Ethiopian Rift: Tectonics, v. 16, p. 347–362.

Bonini, M., Corti, G., Fabrizio, I., Manetti, P., Mazzarini, F., Abebe, T., and Pecskay, Z., 2005, Evolution of the Main Ethiopian Rift in the frame of Afar and Kenya rifts propagation: Tectonics, v. 24, doi: 10.1029/2004TC001680.

Bosworth, W., Burke, K., & Strecker, M., 2003, Effect of stress fields on magma chamber stability and the formation of collapse calderas: Tectonics, v. 22, p. 1042.

Bottinga, Y., 1969, Calculated fractionation factors for carbon and hydrogen isotope exchange in the system calcite-carbon dioxide-graphite-methane-hydrogen-water vapor: Geochimica et Cosmochimica Acta, v. 33, p. 49–64.

Buck, W.R., 2004, Consequences of asthenospheric variability on continental rifting: Rheology and deformation of the lithosphere at continental margins, v. 62, p. 1–30.

Buck, W.R., 2006, The role of magma in the development of the Afro-Arabian Rift System: Geological Society, London, Special Publications, v. 259, p. 43–54.

Burns, D.H., de Silva, S.L., Tepley, F., Schmitt, A.K., and Loewen, M.W., 2015, Recording the transition from flare-up to steady-state arc magmatism at the Purico–Chascon volcanic complex, northern Chile: Earth and Planetary Science Letters, v. 422, p. 75–86, doi: 10.1016/j.epsl.2015.04.002.

Burton, M.R., Sawyer, G.M., and Granieri, D., 2013, Deep Carbon Emissions from Volcanoes: Reviews in Mineralogy and Geochemistry, v. 75, p. 323–354, doi: 10.2138/rmg.2013.75.11.

Caliro, S., Chiodini, G., Galluzzo, D., Granieri, D., La Rocca, M., Saccorotti, G., and Ventura, G., 2004, Recent activity of Nisyros volcano (Greece) inferred from structural, geochemical and seismological data: Bulletin of Volcanology, v. 67, p. 358–369, doi: 10.1007/s00445-004-0381-7.

Caliro, S., Chiodini, G., Moretti, R., Avino, R., Granieri, D., Russo, M., and Fiebig, J., 2007, The origin of the fumaroles of La Solfatara (Campi Flegrei, south Italy): Geochimica et Cosmochimica Acta, v. 71, p. 3040–3055.

Carapezza, M.L., and Granieri, D., 2004, CO_2 soil flux at Vulcano (Italy): comparison between active and passive methods: Applied Geochemistry, v. 19, p. 73–88, doi: 10.1016/S0883-2927(03)00111-2.

Cardellini, C., Chiodini, G., and Frondini, F., 2003, Application of stochastic simulation to CO_2 flux from soil: Mapping and quantification of gas release: Journal of Geophysical Research, v. 108, p. 2425–2437, doi: 10.1029/2002JB002165.

Caricchi, L., Ulmer, P., and Peccerillo, A, 2006, A high-pressure experimental study on the evolution of the silicic magmatism of the Main Ethiopian Rift: Lithos, v. 91, p. 46–58, doi: 10.1016/j.lithos.2006.03.008.

Caricchi, L., Biggs, J., Annen, C., and Ebmeier, S., 2014, The influence of cooling, crystallisation and re-melting on the interpretation of geodetic signals in volcanic systems: Earth and Planetary Science Letters, v. 388, p. 166–174.

Carnec, C., and Fabriol, H., 1999, Monitoring and modeling land subsidence at the Cerro Prieto geothermal field, Baja California, Mexico, using SAR interferometry: Geophysical Research Letters, v. 26, p. 1211–1214.

Casey, M., Ebinger, C., Keir, D., Gloaguen, R., and Mohamed, F., 2006, Strain accommodation in transitional rifts : extension by magma intrusion and faulting in Ethiopian rift magmatic segments, in Yirgu, G., Ebinger, C.J., and Maguire, P.K.H. eds., The Afar Volcanic Province within the East African Rift System, Geological Society, London, Special Publications, p. 143–163.

Cashman, K. V., Soule, S.A., Mackey, B.H., Deligne, N.I., Deardorff, N.D., and Dietterich, H.R., 2013, How lava flows: New insights from applications of lidar technologies to lava flow studies: Geosphere, v. 9, p. 1664–1680, doi: 10.1130/GES00706.1.

Cebriá, J.M., Martín-Escorza, C., López-Ruiz, J., Morán-Zenteno, D.J., and Martiny, B.M., 2011, Numerical recognition of alignments in monogenetic volcanic areas: Examples from the Michoacán-Guanajuato Volcanic Field in Mexico and Calatrava in Spain: Journal of Volcanology and Geothermal Research, v. 201, p. 73–82, doi: 10.1016/j.jvolgeores.2010.07.016.

Chaussard, E., and Amelung, F., 2012, Precursory inflation of shallow magma reservoirs at west Sunda volcanoes detected by InSAR: Geophysical Research Letters, v. 39.

Chiodini, G., Avino, R., Brombach, T., Caliro, S., Cardellini, C., De Vita, S., Frondini, F., Granirei, D., Marotta, E., and Ventura, G., 2004, Fumarolic and diffuse soil degassing west of Mount Epomeo, Ischia, Italy: Journal of Volcanology and Geothermal Research, v. 133, p. 291–309, doi: 10.1016/S0377-0273(03)00403-7.

Chiodini, G., Cioni, R., Guidi, M., and Raco, B., 1998, Soil CO_2 flux measurements in volcanic and geothermal areas: Applied Geochemistry, v. 13, p. 543–552.

Chiodini, G., Frondini, F., Cardellini, C., Granieri, D., Marini, L., and Ventura, G., 2001, CO_2 degassing and energy release at Solfatra volcano, Campi Flegrei, Italy: Journal of Geophy, v. 106, p. 213–221.

Chiodini, G., Todesco, M., Caliro, S., Del Gaudio, C., Macedonio, G., and Russo, M., 2003, Magma degassing as a trigger of bradyseismic events: The case of Phlegrean Fields (Italy): Geophysical Research Letters, v. 30.

Chiodini, G., Caliro, S., Cardellini, C., Avino, R., Granieri, D., and Schmidt, a., 2008, Carbon isotopic composition of soil CO_2 efflux, a powerful method to discriminate different sources feeding soil CO_2 degassing in volcanic-hydrothermal areas: Earth and Planetary Science Letters, v. 274, p. 372–379, doi: 10.1016/j.epsl.2008.07.051.

Chiodini, G., Caliro, S., Cardellini, C., Granieri, D., Avino, R., Baldini, a., Donnini, M., and Minopoli, C., 2010, Long-term variations of the Campi Flegrei, Italy, volcanic system as revealed by the monitoring of hydrothermal activity: Journal of Geophysical Research: Solid Earth, v. 115, p. 1982–1984, doi: 10.1029/2008JB006258.

Chiodini, G., Caliro, S., De Martino, P., Avino, R., and Gherardi, F., 2012, Early signals of new volcanic unrest at Campi Flegrei caldera? Insights from geochemical data and physical simulations: Geology, v. 40, p. 943–946, doi: 10.1130/G33251.1.

Chiodini, G., Vandemeulebrouck, J., Caliro, S., D'Auria, L., De Martino, P., Mangiacapra, A., and Petrillo, Z., 2015, Evidence of thermal-driven processes triggering the 2005–2014 unrest at Campi Flegrei caldera: Earth and Planetary Science Letters, v. 414, p. 58–67.

Chorowicz, J., 2005, The East African rift system: Journal of African Earth Sciences, v. 43, p. 379–410, doi: 10.1016/j.jafrearsci.2005.07.019.

Chorowicz, J., Collet, B., Bonavia, F.F., and Korme, T., 1994, Northwest to north-northwest extension direction in the Ethiopian rift deduced from the orientation of extension structures and fault-slip analysis: Geological Society of America Bulletin, v. 106, p. 1560–1570, doi: 10.1130/0016-7606(1994)105<1560:NTNNED>2.3.CO;2.

Civetta, L., Cornette, Y., Gillot, P.Y., and Orsi, G., 1988, The eruptive history of Pantelleria (Sicily Channel) in the last 50 ka: Bulletin of Volcanology, v. 50, p. 47–57.

Civetta, L., D'Antonio, M., Orsi, G., and Tilton, G.R., 1998, The Geochemistry of Volcanic Rocks from Pantelleria Island, Sicily Channel: Petrogenesis and Characteristics of the Mantle Source Region: Journal of Petrology, v. 39, p. 1453–1491, doi: 10.1093/petroj/39.8.1453.

Clarke, M.G.C., Woodhall, D., Allen, G., and Darling, W.G., 1990, Geological, Volcanological and Hydrogeological Controls on the Occurrence of Geothermal Activity in the Area Surrounding Lake Naivasha, Kenya.: Nottingham, Derry and Sons Ltd, 138 p.

Cole, J., Milner, D., and Spinks, K., 2005, Calderas and caldera structures: a review: Earth-Science Reviews, v. 69, p. 1–26, doi: 10.1016/j.earscirev.2004.06.004.

Cole, J.W., 1969, Gariboldi Volcanic Complex, Ethiopia: Bulletin Volcanologique, v. 33,p. 566–578.

Cooper, G.F., Wilson, C.J.N., Millet, M.A., Baker, J. a., and Smith, E.G.C., 2012, Systematic tapping of independent magma chambers during the 1Ma Kidnappers supereruption: Earth and Planetary Science Letters, v. 313-314, p. 23–33, doi: 10.1016/j.epsl.2011.11.006.

Cornwell, D.G., Maguire, P.K.H., England, R.W., and Stuart, G.W., 2010, Imaging detailed crustal structure and magmatic intrusion across the Ethiopian Rift using a dense linear broadband array: Geochemistry, Geophysics, Geosystems, v. 11.

Corti, G., 2008, Control of rift obliquity on the evolution and segmentation of the main Ethiopian rift: Nature Geoscience, v. 1, p. 258–262, doi: 10.1038/ngeo160.

Corti, G., 2009, Continental rift evolution: From rift initiation to incipient break-up in the Main Ethiopian Rift, East Africa: Earth-Science Reviews, v. 96, p. 1–53, doi: 10.1016/j.earscirev.2009.06.005.

Corti, G., Philippon, M., Sani, F., Keir, D., and Kidane, T., 2013, Re-orientation of the extension direction and pure extensional faulting at oblique rift margins: Comparison between the Main Ethiopian Rift and laboratory experiments: Terra Nova, v. 25, p. 396–404, doi: 10.1111/ter.12049.

Corti, G., Sani, F., Philippon, M., Sokoutis, D., Willingshofer, E., and Molin, P., 2013, Quaternary volcano-tectonic activity in the Soddo region, western margin of the Southern Main Ethiopian Rift: Tectonics, v. 32, p. 1–19, doi: 10.1002/tect.20052.

Crowley, J., and Zimbelman, D., 1997, Mapping hydrothermally altered rocks on Mount Rainier, Washington, with airborne visible/infrared imaging spectrometer (AVIRIS) data: Geology, v. 25, p. 559–562.

Cumming, W., 2009, A conceptual model approach to the geophysical exploration of permeable geothermal reservoirs that considers context and uncertainty, in 2009 SEG Annual Meeting, Society of Exploration Geophysicists.

Curewitz, D., and Karson, J. A, 1997, Structural settings of hydrothermal outflow: Fracture permeability maintained by fault propagation and interaction: Journal of Volcanology and Geothermal Research, v. 79, p. 149–168, doi: 10.1016/S0377-0273(97)00027-9.

d'Acremont, E., Leroy, S., Beslier, M.-O., Bellahsen, N., Fournier, M., Robin, C., Maia, M., and Gente, P., 2005, Structure and evolution of the eastern Gulf of Aden conjugate margins from seismic reflection data: Geophysical Journal International, v. 160, p. 869–890.

D'Alessandro, W., Brusca, L., Kyriakopoulos, K., Michas, G., and Papadakis, G., 2008, Methana, the westernmost active volcanic system of the south Aegean arc (Greece): Insight from fluids geochemistry: Journal of Volcanology and Geothermal Research, v. 178, p. 818–828, doi: 10.1016/j.jvolgeores.2008.09.014.

D'Auria, L., Giudicepietro, F., Aquino, I., Borriello, G., Del Gaudio, C., Lo Bascio, D., Martini, M., Ricciardi, G.P., Ricciolino, P., and Ricco, C., 2011, Repeated fluid-transfer episodes as a mechanism for the recent dynamics of Campi Flegrei caldera (1989–2010): Journal of Geophysical Research: Solid Earth (1978–2012), v. 116.

Dakin, G., and Gibson, I.L., 1971, A Preliminary Account of Alutu, a Pantelleritic Volcano in the Main Ethiopian Rift: Bull. Geophys. Obs. Addis Ababa, v. 13, p. 110–114.

Darling, W.G., Griesshaber, E., Andrews, J.N., Armannsson, H., and O'Nions, R.K., 1995, The origin of hydrothermal and other gases in the Kenya Rift Valley: Geochimica et cosmochimica acta, v. 59, p. 2501–2512.

Darling, W., Gizaw, B., and Arusei, M., 1996, Lake-groundwater relationships and fluid-rock interaction in the East African Rift Valley: isotopic evidence: Journal of African Earth Sciences, v. 22, p. 423–431.

Darling, W.G., 1998, Hydrothermal hydrocarbon gases: 2, Application in the East African Rift system: Applied geochemistry, v. 13, p. 825–840.

Darrah, T.H., Tedesco, D., Tassi, F., Vaselli, O., Cuoco, E., and Poreda, R.J., 2013, Gas chemistry of the Dallol region of the Danakil Depression in the Afar region of the northern-most East African Rift: Chemical Geology, v. 339, p. 16–29.

Davies, G.R., and Macdonald, R., 1987, Crustal Influences in the Petrogenesis of the Naivasha Basalt—Comendite Complex: Combined Trace Element and Sr-Nd-Pb Isotope Constraints: Journal of Petrology, v. 28, p. 1009–1031.

de Moor, J.M., Fischer, T.P., Sharp, Z.D., Hilton, D.R., Barry, P.H., Mangasini, F., and Ramirez, C., 2013, Gas chemistry and nitrogen isotope compositions of cold mantle gases from Rungwe Volcanic Province, southern Tanzania: Chemical Geology, v. 339, p. 30–42.

deMenocal, P.B., 2004, African climate change and faunal evolution during the Pliocene-Pleistocene: Earth and Planetary Science Letters, v. 220, p. 3–24, doi: 10.1016/S0012-821X(04)00003-2.

Deutsch, C. V, and Journel, A.G., 1998, GSLIB, Geostatistical Software Library and Users Guide: New York, Oxford University Press.

Di Paola, G.M., 1971, Geology of the Corbetti Caldera area (Main Ethiopian Rift Valley): Bulletin Volcanologique, v. 35, p. 497–506, doi: 10.1007/BF02596970.

Di Paola, G.M., 1972, The Ethiopian Rift Valley (between 7° 00′ and 8° 40′ lat. North): Bulletin Volcanologique, v. 36, p. 517–560, doi: 10.1007/BF02599823.

Dzurisin, D., Yamashita, K.M., and Kleinman, J.W., 1994, Mechanisms of crustal uplift and subsidence at the Yellowstone caldera, Wyoming: Bulletin of Volcanology, v. 56, p. 261–270.

Eberhard, A., Foster, V., Briceño-Garmendia, C., Ouedraogo, F., Camos, D., and Shkaratan, M., 2008, Underpowered: the state of the power sector in Sub-Saharan Africa. World Bank, Washington, DC.

Eberhard, A., and Shkaratan, M., 2012, Powering Africa: Meeting the financing and reform challenges: Energy Policy, v. 42, p. 9–18.

Ebinger, C., and Casey, M., 2001, Continental breakup in magmatic provinces: An Ethiopian example: Geology, v. 29, p. 527–530, doi: 10.1130/0091-7613(2001)029<0527:CBIMPA>2.0.CO;2.

Ebinger, C., 2005, Continental break-up: the East African perspective: Astronomy & Geophysics, v. 46, p. 16–21.

Ebinger, C.J., Keir, D., Ayele, a., Calais, E., Wright, T.J., Belachew, M., Hammond, J.O.S., Campbell, E., and Buck, W.R., 2008, Capturing magma intrusion and faulting processes during continental rupture: seismicity of the Dabbahu (Afar) rift: Geophysical Journal International, v. 174, p. 1138–1152, doi: 10.1111/j.1365-246X.2008.03877.x.

Ebinger, C., Ayele, A., Keir, D., Rowland, J., Yirgu, G., Wright, T., Belachew, M., and Hamling, I., 2010, Length and Timescales of Rift Faulting and Magma Intrusion: The Afar Rifting Cycle from 2005 to Present: Annual Review of Earth and Planetary Sciences, v. 38, p. 439–466, doi: 10.1146/annurev-earth-040809-152333.

Ebmeier, S.K., Biggs, J., Mather, T.A., Wadge, G., and Amelung, F., 2010, Steady downslope movement on the western flank of Arenal volcano, Costa Rica: Geochemistry, Geophysics, Geosystems, v. 11.

Ebmeier, S.K., Biggs, J., Mather, T.A., Elliott, J.R., Wadge, G., and Amelung, F., 2012, Measuring large topographic change with InSAR: lava thicknesses, extrusion rate and subsidence rate at Santiaguito volcano, Guatemala: Earth and Planetary Science Letters, v. 335, p. 216–225.

Ebmeier, S.K., Biggs, J., Mather, T.A., and Amelung, F., 2013, On the lack of InSAR observations of magmatic deformation at Central American volcanoes: Journal of Geophysical Research: Solid Earth, v. 118, p. 2571–2585.

Egger, A.E., Glen, J.M.G., and McPhee, D.K., 2014, Structural controls on geothermal circulation in Surprise Valley, California: A re-evaluation of the Lake City fault zone: Geological Society of America Bulletin, v. 126, p. 523–531.

ELC Electroconsult, 1986, Exploitation of Langano-Aluto geothermal resources feasibility report. Geothermal Exploration Project, Ethiopian Lake District Rift.

Ellis, A.J., and Golding, R.M., 1963, The solubility of carbon dioxide above 100 degrees C in water and in sodium chloride solutions: American Journal of Science, v. 261, p. 47–60.

Farrar, C., Sorey, M., Evans, W., and Howle, J., 1995, Forest-killing diffuse CO_2 emission at Mammoth Mountain as a sign of magmatic unrest: Nature, v. 376, p. 675–678.

Favara, R., Giammanco, S., Inguaggiato, S., and Pecoraino, G., 2001, Preliminary estimate of CO_2 output from Pantelleria Island volcano (Sicily, Italy): evidence of active mantle degassing: Applied Geochemistry, v. 16, p. 883–894, doi: 10.1016/S0883-2927(00)00055-X.

Ferguson, D.J., Barnie, T.D., Pyle, D.M., Oppenheimer, C., Yirgu, G., Lewi, E., Kidane, T., Carn, S., and Hamling, I., 2010, Recent rift-related volcanism in Afar, Ethiopia: Earth and Planetary Science Letters, v. 292, p. 409–418, doi: 10.1016/j.epsl.2010.02.010.

Ferguson, D.J., Maclennan, J., Bastow, I.D., Pyle, D.M., Jones, S.M., Keir, D., Blundy, J.D., Plank, T., and Yirgu, G., 2013, Melting during late-stage rifting in Afar is hot and deep: Nature, v. 499, p. 70–73.

Fialko, Y., and Simons, M., 2000, Deformation and seismicity in the Coso geothermal area, Inyo County, California: Observations and modeling using satellite radar interferometry: Journal of Geophysical Research: Solid Earth (1978–2012), v. 105, p. 21781–21793.

Field, L., Blundy, J., Calvert, A., and Yirgu, G., 2013, Magmatic history of Dabbahu, a composite volcano in the Afar Rift, Ethiopia: Geological Society of America Bulletin, v. 125, p. 128–147.

Fink, J., 1980, Surface folding and viscosity of rhyolite flows: Geology, v. 8, p. 250–254.

Fontijn, K., Ernst, G.G.J., Elburg, M. a., Williamson, D., Abdallah, E., Kwelwa, S., Mbede, E., and Jacobs, P., 2010, Holocene explosive eruptions in the Rungwe Volcanic Province, Tanzania: Journal of Volcanology and Geothermal Research, v. 196, p. 91–110, doi: 10.1016/j.jvolgeores.2010.07.021.

Fontijn, K., Ernst, G.G.J., Bonadonna, C., Elburg, M. a., Mbede, E., and Jacobs, P., 2011, The ~4-ka Rungwe Pumice (South-Western Tanzania): A wind-still Plinian eruption: Bulletin of Volcanology, v. 73, p. 1353–1368, doi: 10.1007/s00445-011-0486-8.

Fontijn, K., Elburg, M. a., Nikogosian, I.K., van Bergen, M.J., and Ernst, G.G.J., 2013, Petrology and geochemistry of Late Holocene felsic magmas from Rungwe volcano (Tanzania), with implications for trachytic Rungwe Pumice eruption dynamics: Lithos, v. 177, p. 34–53, doi: 10.1016/j.lithos.2013.05.012.

Frazer, R.E., Coleman, D.S., and Mills, R.D., 2014, Zircon U-Pb geochronology of the Mount Givens Granodiorite: Implications for the genesis of large volumes of eruptible magma: Journal of Geophysical Research : Solid Earth, p. 2907–2924, doi: 10.1002/2013JB010716.

Fridriksson, T., Kristjánsson, B.R., Ármannsson, H., Margrétardóttir, E., Ólafsdóttir, S., and Chiodini, G., 2006, CO_2 emissions and heat flow through soil, fumaroles, and steam heated mud pools at the Reykjanes geothermal area, SW Iceland: Applied Geochemistry, v. 21, p. 1551–1569, doi: 10.1016/j.apgeochem.2006.04.006.

Fridriksson, T., 2009, Diffuse CO_2 degassing through soil and geothermal exploration: Short Course on Surface Exploration for Geothermal Resources-UNU-GTP and LaGeo, El Salvador.

Frondini, F., Chiodini, G., Caliro, S., Cardellini, C., Granieri, D., and Ventura, G., 2004, Diffuse CO_2 degassing at Vesuvio, Italy: Bulletin of Volcanology, v. 66, p. 642–651, doi: 10.1007/s00445-004-0346-x.

Furman, T., 2006, Tertiary Mafic Lavas of Turkana, Kenya: Constraints on East African Plume Structure and the Occurrence of High-μ Volcanism in Africa: Journal of Petrology, v. 47, p. 1221–1244, doi: 10.1093/petrology/egl009.

Gasse, E., and Street, F., 1978, Late Quaternary lake-level fluctuations and environments of the northern Rift Valley and Afar region (Ethiopia and Djibouti): Palaeogeography, Palaeoclimatology, Palaeoecology, v. 24.

Gebregzabher, Z., 1986, Hydrothermal alteration minerals in Aluto Langano geothermal wells, Ethiopia: Geothermics, v. 15, p. 735–740.

George, R., Rogers, N., and Kelley, S., 1998, Earliest magmatism in Ethiopia: evidence for two mantle plumes in one flood basalt province: Geology, v. 26, p. 923–926.

Gerlach, T.M., and Taylor, B.E., 1990, Carbon isotope constraints on degassing of carbon dioxide from Kilauea Volcano: Geochimica et Cosmochimica Acta, v. 54, p. 2051–2058.

Geyer, A., and Marti, J., 2008, The new worldwide collapse caldera database (CCDB): A tool for studying and understanding caldera processes: Journal of Volcanology and Geothermal Research, v. 175, p. 334–354, doi: 10.1016/j.jvolgeores.2008.03.017.

Giammanco, S., Parello, F., Gambardella, B., Schifano, R., Pizzullo, S., and Galante, G., 2007, Focused and diffuse effluxes of CO_2 from mud volcanoes and mofettes south of Mt. Etna (Italy): Journal of Volcanology and Geothermal Research, v. 165, p. 46–63, doi: 10.1016/j.jvolgeores.2007.04.010.

Giammanco, S., Immè, G., Mangano, G., Morelli, D., and Neri, M., 2009, Comparison between different methodologies for detecting radon in soil along an active fault: The case of the Pernicana fault system, Mt. Etna (Italy), Applied Radiation and Isotopes, v. 67, p. 178–185. doi:10.1016/j.apradiso.2008.09.007

Gianelli, G., and Teklemariam, M., 1993, Water-rock interaction processes in the Aluto-Langano geothermal field (Ethiopia): Journal of Volcanology and Geothermal Research, v. 56, p. 429–445.

Gibert, E., Travi, Y., Massault, M., Tiercelin, J.-J., and Chernet, T., 2002, AMS-14C chronology of a lacustrine sequence from Lake Langano (Main Ethiopian Rift); correction and validation steps in relation with volcanism, lake water and carbon: Radiocarbon, v. 44, p. 75–92.

Gibson, I.L., 1969, The structure and volcanic geology of an axial portion of the Main Ethiopian Rift: Tectonophysics, v. 8, p. 561–565.

Gibson, I., 1970, A pantelleritic welded ash-flow tuff from the Ethiopian Rift Valley: Contributions to Mineralogy and Petrology, v. 28, p. 89–111.

Gillespie, R., Street-Perrott, F., and Switsur, R., 1983, Post-glacial arid episodes in Ethiopia have implications for climate prediction: Nature, v. 306, p. 680–683.

Giordano, F., D'Antonio, M., Civetta, L., Tonarini, S., Orsi, G., Ayalew, D., Yirgu, G., Dell'Erba, F., Di Vito, M. a., and Isaia, R., 2014, Genesis and evolution of mafic and felsic magmas at Quaternary volcanoes within the Main Ethiopian Rift: Insights from Gedemsa and Fanta 'Ale complexes: Lithos, v. 188, p. 130–144, doi: 10.1016/j.lithos.2013.08.008.

Giordano, G., Pinton, A., Cianfarra, P., Baez, W., Chiodi, A., Viramonte, J., Norini, G., and Groppelli, G., 2013, Structural control on geothermal circulation in the Cerro Tuzgle–Tocomar geothermal volcanic area (Puna plateau, Argentina): Journal of Volcanology and Geothermal Research, v. 249, p. 77–94.

Girona, T., Costa, F., Newhall, C., and Taisne, B., 2014, On depressurization of volcanic magma reservoirs by passive degassing: Journal of Geophysical Research: Solid Earth, v. 119, p. 8667–8687.

Gizaw, B., 1993, Aluto-Langano geothermal field, Ethiopian Rift Valley: physical characteristics and the effects of gas on well performance: Geothermics, v. 22, p. 101–116.

Gottsmann, J., and Battaglia, M., 2008, Deciphering causes of unrest at explosive collapse calderas: recent advances and future challenges of joint time-lapse gravimetric and ground deformation studies: Developments in Volcanology, v. 10, p. 417–446.

Gregg, T.K.P., Fink, J.H., and Griffiths, R.W., 1998, Formation of multiple fold generations on lava flow surfaces: Influence of strain rate, cooling rate, and lava composition: Journal of Volcanology and Geothermal Research, v. 80, p. 281–292, doi: 10.1016/S0377-0273(97)00048-6.

Grove, A.T., and Goudie, S., 1971, Late quaternary lake levels in the rift valley of southern Ethiopia and elsewhere in tropical Africa: Nature, v. 234, p. 403–405.

Grove, A.T., Street, F.A., and Goudie, S., 1975, Former Lake Levels and Climatic Change in the Rift Valley of Southern Ethiopia: The Geographical Journal, v. 141, p. 177–194.

Guarnieri, A.M., and Prati, C., 1996, ScanSAR focusing and interferometry: Geoscience and Remote Sensing, IEEE Transactions on, v. 34, p. 1029–1038.

Guarnieri, A.M., Cafforio, C., Guccione, P., Pasquali, P., and Desnos, Y.L., 2003, ENVISAT ASAR ScanSAR interferometry. IEEE International Geoscience and Remote Sensing Symposium Proceedings. Piscataway: Institute of Electrical and Electronics Engineers:.

Halldórsson, S.A., Hilton, D.R., Scarsi, P., Abebe, T., and Hopp, J., 2014, A common mantle plume source beneath the entire East African Rift System revealed by coupled helium-neon systematics: Geophysical Research Letters, v. 41, p. 2304–2311.

Hamlyn, J.E., Keir, D., Wright, T.J., Neuberg, J.W., Goitom, B., Hammond, J.O.S., Pagli, C., Oppenheimer, C., Kendall, J., and Grandin, R., 2014, Seismicity and subsidence following the 2011 Nabro eruption, Eritrea: Insights into the plumbing system of an off-rift volcano: Journal of Geophysical Research: Solid Earth, v. 119, p. 8267–8282.

Hayward, N., and Ebinger, C., 1996, Variations in the along-axis segmentation of the Afar Rift system: Tectonics, v. 15, p. 244–257.

Hendrie, D.B., Kusznir, N.J., Morley, C.K., and Ebinger, C.J., 1994, Cenozoic extension in northern Kenya: a quantitative model of rift basin development in the Turkana region: Tectonophysics, v. 236, p. 409–438.

Hernández, P., Pérez, N., Salazar, J., Nakai, S., Notsu, K., and Wakita, H., 1998, Diffuse emission of carbon dioxide, methane, and helium-3 from Teide Volcano, Tenerife, Canary Islands: Geophysical Research Letters, v. 25, p. 3311–3314.

Hernández, P., Salazar, J., Shimoike, Y., Mori, T., Notsu, K., and Perez, N., 2001, Diffuse emission of CO_2 from Miyakejima volcano, Japan: Chemical Geology, v. 177, p. 175–185.

Hernández Perez, P., Notsu, K., Tsurumi, M., Mori, T., Ohno, M., Shimoike, Y., Salazar, J., and Perez, N., 2003, Carbon dioxide emissions from soils at Hakkoda, north Japan: Journal of Geophysical Research, v. 108, 2210, doi: 10.1029/2002JB001847.

Hilton, D.R., Ramirez, C.J., Mora-Amador, R., Fischer, T.P., Fueri, E., Barry, P.H., and Shaw, A.M., 2010, Monitoring of temporal and spatial variations in fumarole helium and carbon dioxide characteristics at Poás and Turrialba volcanoes, Costa Rica (2001-2009): Geochemical Journal, v. 44, p. 431–440.

Hilton, D.R., Halldórsson, S. a., Barry, P.H., Fischer, T.P., de Moor, J.M., Ramirez, C.J., Mangasini, F., and Scarsi, P., 2011, Helium isotopes at Rungwe Volcanic Province, Tanzania, and the origin of East African Plateaux: Geophysical Research Letters, v. 38, p. n/a–n/a, doi: 10.1029/2011GL049589.

Holohan, E., Troll, V. R., Walter, T. R., Munn, S., McDonnell, S., and Shipton, Z, 2005, Elliptical calderas in active tectonic settings: an experimental approach: Journal of Volcanology and Geothermal Research, v. 144, 119–136.

Houghton, B.F., Wilson, C.J.N., O, M.M., Lanphere, M. a., Weaver, S.D., Briggs, R.M., and Pringle M S, 1995, Chronology and dynamics of a large silicic magmatic system : Central Taupo Volcanic Zone , New Zealand: Geology, v. 23, p. 13–16, doi: 10.1130/0091-7613(1995)023<0013.

Hurwitz, S., Christiansen, L.B., and Hsieh, P.A., 2007, Hydrothermal fluid flow and deformation in large calderas: Inferences from numerical simulations: Journal of Geophysical Research: Solid Earth (1978–2012), v. 112.

Hutchison, W., Mather, T.A., Pyle, D.M., Biggs, J., and Yirgu, G., 2015, Structural controls on fluid pathways in an active rift system: A case study of the Aluto volcanic complex: Geosphere, p. 1–21, doi: 10.1130/GES01119.1.

Hutnak, M., Hurwitz, S., Ingebritsen, S.E., and Hsieh, P.A., 2009, Numerical models of caldera deformation: Effects of multiphase and multicomponent hydrothermal fluid flow: Journal of Geophysical Research: Solid Earth (1978–2012), v. 114.

Irvine, T.N., and Baragar, W.R.A., 1971, A guide to the chemical classification of the common volcanic rocks: Canadian journal of earth sciences, v. 8, p. 523–548.

Javoy, M., and Pineau, F., 1991, The volatiles record of a “popping” rock from the Mid-Atlantic Ridge at 14 N: chemical and isotopic composition of gas trapped in the vesicles: Earth and Planetary Science Letters, v. 107, p. 598–611.

Jenkins, S.F., Barsotti, S., Hincks, T.K., Neri, A., Phillips, J.C., Sparks, R.S.J., Sheldrake, T., and Vougioukalakis, G., 2015, Rapid emergency assessment of ash and gas hazard for future eruptions at Santorini Volcano, Greece: Journal of Applied Volcanology, v. 4, p. 16.

Johnston, J.M., Pellerin, L., and Hohmann, G.W., 1992, Evaluation of electromagnetic methods for geothermal reservoir detection.: Transactions- Geothermal Resources Council,.

Karlstrom, L., Dufek, J., and Manga, M., 2009, Organization of volcanic plumbing through magmatic lensing by magma chambers and volcanic loads: Journal of Geophysical Research: Solid Earth, v. 114, p. 1–16, doi: 10.1029/2009JB006339.

Kebede, S., 2012, Geothermal exploration and development in Ethiopia: status and future plan: Short Course VII on Exploration for Geothermal Resources.

Kebede, S., Mamo, T., and Abebe, T., 1985, Geological report and explanation to the geological map of Aluto-Langano geothermal area: Ethiopian Institute of Geological Surveys, 60 p.

Keiding, M., Árnadóttir, T., Jónsson, S., Decriem, J., and Hooper, A., 2010, Plate boundary deformation and man-made subsidence around geothermal fields on the Reykjanes Peninsula, Iceland: Journal of Volcanology and Geothermal Research, v. 194, p. 139–149.

Keir, D., Kendall, J.-M., Ebinger, C.J., and Stuart, G.W., 2005, Variations in late syn-rift melt alignment inferred from shear-wave splitting in crustal earthquakes beneath the Ethiopian rift: Geophysical Research Letters, v. 32, p. L23308, doi: 10.1029/2005GL024150.

Keir, D., Ebinger, C.J., Stuart, G.W., Daly, E., and Ayele, a., 2006, Strain accommodation by magmatism and faulting as rifting proceeds to breakup: Seismicity of the northern Ethiopian rift: Journal of Geophysical Research, v. 111, p. 1–17, doi: 10.1029/2005JB003748.

Keir, D., Bastow, I.D., Corti, G., Mazzarini, F., and Rooney, T.O., 2015, The origin of along-rift variations in faulting and magmatism in the Ethiopian Rift: Tectonics, v. 34, p. 464–477, doi: 10.1002/2014TC003698.

Kendall, J., Stuart, G., Ebinger, C., Bastow, I., and Keir, D., 2005, Magma-assisted rifting in Ethiopia: Nature, v. 433, p. 146–148, doi:10.1038/nature03161.

Keranen, K., and Klemperer, S.L., 2008, Discontinuous and diachronous evolution of the Main Ethiopian Rift: Implications for development of continental rifts: Earth and Planetary Science Letters, v. 265, p. 96–111, doi: 10.1016/j.epsl.2007.09.038.

Keranen, K., Klemperer, S.L., and Gloaguen, R., 2004, Three-dimensional seismic imaging of a protoridge axis in the Main Ethiopian rift: Geology, v. 32, p. 949, doi: 10.1130/G20737.1.

Keranen, K.M., Klemperer, S.L., Julia, J., Lawrence, J.F., and Nyblade, A.A., 2009, Low lower crustal velocity across Ethiopia: Is the Main Ethiopian Rift a narrow rift in a hot craton? Geochemistry, Geophysics, Geosystems, v. 10.

Koepenick, K., Brantley, S., Thompson, J., Rowe, G., Nyblade, A., and Moshy, C., 1996, Volatile emissions from the crater and flank of Oldoinyo Lengai volcano, Tanzania: Journal of Geophysical Research, v. 101, p. 819–830.

Lahitte, P., Gillot, P.-Y., and Courtillot, V., 2003, Silicic central volcanoes as precursors to rift propagation: the Afar case: Earth and Planetary Science Letters, v. 207, p. 103–116, doi: 10.1016/S0012-821X(02)01130-5.

Lan, T.F., Yang, T.F., Lee, H.-F., Chen, Y.-G., Chen, C.-H., Song, S.-R., and Tsao, S., 2007, Compositions and flux of soil gas in Liu-Huang-Ku hydrothermal area, northern Taiwan: Journal of Volcanology and Geothermal Research, v. 165, p. 32–45, doi: 10.1016/j.jvolgeores.2007.04.015.

Laury, R.L., and Albritton, C.C., 1975, Geology of Middle Stone Age archaeological sites in the main Ethiopian rift valley: Geological Society of America Bu, v. 86, p. 999–1011, doi: 10.1130/0016-7606(1975)86<999.

Le Maitre, R.W., Streckeisen, A., Zanettin, B., Le Bas, M.J., Bonin, B., and Bateman, P., 2002, Igneous rocks: a classification and glossary of terms: recommendations of the International Union of Geological Sciences Subcommission on the Systematics of Igneous Rocks: Cambridge University Press.

Le Turdu, C., Tiercelin, J.-J., Gibert, E., Travi, Y., Lezzar, K.-E., Richert, J.-P., Massault, M., Gasse, F., Bonnefille, R., Decobert, M., Gensous, B., Jeudy, V., Tamrat, E., Mohammed, M.U., et al., 1999, The Ziway–Shala lake basin system, Main Ethiopian Rift: Influence of volcanism, tectonics, and climatic forcing on basin formation and sedimentation: Palaeogeography, Palaeoclimatology, Palaeoecology, v. 150, p. 135–177, doi: 10.1016/S0031-0182(98)00220-X.

Leat, P.T., MacDonald, R., and Smith, R.L., 1984, Geochemical evolution of the Menengai Caldera Volcano, Kenya: Journal of Geophysical Research: Solid Earth, v. 89, p. 8571–8592, doi: 10.1029/JB089iB10p08571.

Lee, J.-Y., Marti, K., Severinghaus, J.P., Kawamura, K., Yoo, H.-S., Lee, J.B., and Kim, J.S., 2006, A redetermination of the isotopic abundances of atmospheric Ar: Geochimica et Cosmochimica Acta, v. 70, p. 4507–4512.

Li, Z., Muller, J., Cross, P., and Fielding, E.J., 2005, Interferometric synthetic aperture radar (InSAR) atmospheric correction: GPS, Moderate Resolution Imaging Spectroradiometer (MODIS), and InSAR integration: Journal of Geophysical Research: Solid Earth (1978–2012), v. 110.

Lipman, P.W., 1997, Subsidence of ash-flow calderas: relation to caldera size and magma-chamber geometry: Bulletin of Volcanology, v. 59, p. 198–218, doi: 10.1007/s004450050186.

Lipman, P.W., 2007, Incremental assembly and prolonged consolidation of Cordilleran magma chambers: Evidence from the Southern Rocky Mountain volcanic field: Geosphere, v. 3, p. 42–70, doi: 10.1130/GES00061.1.

Lisiecki, L.E., and Raymo, M.E., 2005, A Pliocene-Pleistocene stack of 57 globally distributed benthic $\delta^{18}O$ records: Paleoceanography, v. 20, p. 1–17, doi: 10.1029/2004PA001071.

Lollar, B.S., Ballentine, C.J., and Onions, R.K., 1997, The fate of mantle-derived carbon in a continental sedimentary basin: integration of C He relationships and stable isotope signatures: Geochimica et Cosmochimica Acta, v. 61, p. 2295–2307.

Lowenstern, J.B., Smith, R.B., and Hill, D.P., 2006, Monitoring super-volcanoes: geophysical and geochemical signals at Yellowstone and other large caldera systems: Philosophical Transactions of the Royal Society of London A: Mathematical, Physical and Engineering Sciences, v. 364, p. 2055–2072.

Lundgren, P., Usai, S., Sansosti, E., Lanari, R., Tesauro, M., Fornaro, G., and Berardino, P., 2001, Modeling surface deformation observed with synthetic aperture radar interferometry at Campi Flegrei caldera: Journal of Geophysical Research, 106 (B9), 2001.

Lutz, T., 1986, An analysis of the orientations of large-scale crustal structures: A statistical approach based on areal distributions of pointlike features: Journal of Geophysical Research: Solid Earth, v. 91, p. 421–434.

Lutz, T., and Gutmann, J., 1995, An improved method for determining and characterizing alignments of pointlike features and its implications for the Pinacate volcanic field, Sonora, Mexico: Journal of Geophysical Research: Solid Earth, v. 100, p. 17659–17670.

Macdonald, R., 1974, Nomenclature and petrochemistry of the peralkaline oversaturated extrusive rocks: Bulletin volcanologique, v. 38, p. 498–516.

Macdonald, R., Navarro, J.M., Upton, B.G.J., and Davies, G.R., 1994, Strong compositional zonation in peralkaline magma: Menengai, Kenya Rift Valley: Journal of Volcanology and Geothermal Research, v. 60, p. 301–325, doi: http://dx.doi.org/10.1016/0377-0273(94)90057-4.

Macdonald, R., and Scaillet, B., 2006, The central Kenya peralkaline province: Insights into the evolution of peralkaline salic magmas: Lithos, v. 91, p. 59–73, doi: 10.1016/j.lithos.2006.03.009.

Macdonald, R., Belkin, H.E., Fitton, J.G., Rogers, N.W., Nejbert, K., Tindle, a. G., and Marshall, a. S., 2008, The Roles of Fractional Crystallization, Magma Mixing, Crystal Mush Remobilization and Volatile-Melt Interactions in the Genesis of a Young Basalt-Peralkaline Rhyolite Suite, the Greater Olkaria Volcanic Complex, Kenya Rift Valley: Journal of Petrology, v. 49, p. 1515–1547, doi: 10.1093/petrology/egn036.

Macdonald, R., 2012, Evolution of peralkaline silicic complexes: Lessons from the extrusive rocks: Lithos, v. 152, p. 11–22.

Macdonald, R., Bagiński, B., and Upton, B.G.J., 2014, The volcano–pluton interface; The Longonot (Kenya) and Kûngnât (Greenland) peralkaline complexes: Lithos, v. 196, p. 232–241.

Mackenzie, G.D., Thybo, H., and Maguire, P.K.H., 2005, Crustal velocity structure across the Main Ethiopian Rift: results from two-dimensional wide-angle seismic modelling: Geophysical Journal International, v. 162, p. 994–1006, doi: 10.1111/j.1365-246X.2005.02710.x.

Macpherson, C., and Mattey, D., 1994, Carbon isotope variations of CO_2 in Central Lau Basin basalts and ferrobasalts: Earth and planetary science letters, v. 121, p. 263–276.

Mahood, G.A., 1984, Pyroclastic rocks and calderas associated with strongly peralkaline magmatism: Journal of Geophysical Research, v. 89, p. 8540, doi: 10.1029/JB089iB10p08540.

Mahood, G. A. and Hildreth, W., 1983, Nested calderas and trapdoor uplift at Pantelleria, Strait of Sicily: Geology, v. 11, p. 722–726.

Mahood, G. A. & Hildreth,W., 1986, Geology of the peralkaline volcano at Pantelleria, Strait of Sicily: Bulletin of Volcanology, v. 48, p. 143–172.

Mamo, T., 1985, Petrography and rock chemistry of well LA-8 Aluto-Langano geothermal system, Ethiopia, Unpublished report, Geothermal Institute, University of Auckland, 48 pp.: 48 p.

Mann, D., and Freymueller, J., 2003, Volcanic and tectonic deformation on Unimak Island in the Aleutian Arc, Alaska: Journal of Geophysical Research: Solid Earth (1978–2012), v. 108.

Marty, B., and Zimmermann, L., 1999, Volatiles (He, C, N, Ar) in mid-ocean ridge basalts: Assesment of shallow-level fractionation and characterization of source composition: Geochimica et Cosmochimica Acta, v. 63, p. 3619–3633.

Maslin, M.A., and Christensen, B., 2007, Tectonics, orbital forcing, global climate change, and human evolution in Africa: introduction to the African paleoclimate special volume: Journal of human evolution, v. 53, p. 443–464.

Maslin, M. a., Brierley, C.M., Milner, A.M., Shultz, S., Trauth, M.H., and Wilson, K.E., 2014, East african climate pulses and early human evolution: Quaternary Science Reviews, v. 101, p. 1–17, doi: 10.1016/j.quascirev.2014.06.012.

Maslin, M.A., Shultz, S., Trauth, M.H., and Maslin, M.A., 2015, A synthesis of the theories and concepts of early human evolution: Philosophical Transactions of the Royal Society of London B: Biological Sciences 370.1663 (2015): 20140064.

Massonnet, D., and Feigl, K.L., 1998, Radar interferometry and its application to changes in the Earth's surface: Reviews of Geophysics, v. 36, p. 441–500.

Massonnet, D., Holzer, T., and Vadon, H., 1997, Land subsidence caused by the East Mesa geothermal field, California, observed using SAR interferometry: Geophysical Research Letters, v. 24, p. 901–904.

Mattia, M., Bonaccorso, A., and Guglielmino, F., 2007, Ground deformations in the Island of Pantelleria (Italy): Insights into the dynamic of the current intereruptive period: Journal of Geophysical Research: Solid Earth (1978–2012), v. 112.

McDougall, I., Brown, F.H., and Fleagle, J.G., 2005, Stratigraphic placement and age of modern humans from Kibish, Ethiopia.: Nature, v. 433, p. 733–736, doi: 10.1038/nature03258.

Ménard, C., Bon, F., Dessie, A., Bruxelles, L., and Mensan, R., 2014, Late Stone Age variability in the Main Ethiopian Rift : New data from the Bulbula River, Ziway–Shala basin: Quaternary International, v. 343, p. 53–68, doi: 10.1016/j.quaint.2014.07.019.

Mielnick, P., and Dugas, W., 2000, Soil CO_2 flux in a tallgrass prairie: Soil Biology and Biochemistry, v. 32, p. 221–228.

Mohr, P., 1966, Chabbi volcano (Ethiopia): Bulletin of Volcanology, v. 29, p. 797–815.

Mohr, P. A., 1971, Ethiopian rift and plateaus - Some volcanic petrochemical differences: v. 76, p. 1967–1984, doi: 10.1029/JB076i008p01967.

Mohr, P.A., and Potter, E.C., 1976, The Sagatu Ridge dike swarm, Ethiopian rift margin: Journal of Volcanology and Geothermal Research, p. 55–71, doi: 10.1016/0377-0273(76)90018-4.

Mohr, P., Mitchell, J.G., and Raynolds, R.G.H., 1980, Quaternary volcanism and faulting at O'A caldera, Central Ethiopian Rift: Bulletin of Volcanology, v. 43, p. 173–189, doi: 10.1007/BF02597619.

Mook, W.G., Bommerson, J.C., and Staverman, W.H., 1974, Carbon isotope fractionation between dissolved bicarbonate and gaseous carbon dioxide: Earth and Planetary Science Letters, v. 22, p. 169–176.

Moore, R.K., Claassen, J.P., and Lin, Y.H., 1981, Scanning spaceborne synthetic aperture radar with integrated radiometer: Aerospace and Electronic Systems, IEEE Transactions on, p. 410–421.

Morgan, L.E., and Renne, P.R., 2008, Diachronous dawn of Africa's Middle Stone Age: New $^{40}Ar/^{39}Ar$ ages from the Ethiopian Rift: Geology, v. 36, p. 967, doi: 10.1130/G25213A.1.

Morley, C.K., Wescott, W.A., Stone, D.M., Harper, R.M., Wigger, S.T., and Karanja, F.M., 1992, Tectonic evolution of the northern Kenyan Rift: Journal of the Geological Society, v. 149, p. 333–348.

Mundula, F., Cioni, R., and Mulas, M., 2013, Rheomorphic diapirs in densely welded ignimbrites: The Serra di Paringianu ignimbrite of Sardinia, Italy: Journal of Volcanology and Geothermal Research, v. 258, p. 12–23, doi: 10.1016/j.jvolgeores.2013.03.025.

Nakamura, K., 1977, Volcanoes as possible indicators of tectonic stress orientation–principle and proposal: Journal of Volcanology and Geothermal Research, v. 2, p. 1–16.

Neave, D.A., Fabbro, G., Herd, R.A., Petrone, C.M., and Edmonds, M., 2012, Melting, differentiation and degassing at the Pantelleria volcano, Italy: Journal of Petrology, v. 53, p. 637–663.

Nomikou, P., Parks, M.M., Papanikolaou, D., Pyle, D.M., Mather, T. a., Carey, S., Watts, a. B., Paulatto, M., Kalnins, M.L., Livanos, I., Bejelou, K., Simou, E., and Perros, I., 2014, The emergence and growth of a submarine volcano: The Kameni islands, Santorini (Greece): GeoResJ, v. 1-2, p. 8–18, doi: 10.1016/j.grj.2014.02.002.

Notsu, K., Sugiyama, K., Hosoe, M., Uemura, a., Shimoike, Y., Tsunomori, F., Sumino, H., Yamamoto, J., Mori, T., and Hernández, P., 2005, Diffuse CO_2 efflux from Iwojima volcano, Izu-Ogasawara arc, Japan: Journal of Volcanology and Geothermal Research, v. 139, p. 147–161, doi: 10.1016/j.jvolgeores.2004.08.003.

Nyblade, A.A., and Brazier, R.A., 2002, Precambrian lithospheric controls on the development of the East African rift system: Geology, v. 30, p. 755–758.

Nyblade, A.A., Owens, T.J., Gurrola, H., Ritsema, J., and Langston, C.A., 2000, Seismic evidence for a deep upper mantle thermal anomaly beneath east Africa: Geology, v. 28, p. 599–602.

Oppenheimer, C., Pyle, D.M., and Barclay, J., 2003, Volcanic degassing: Geological Society of London, 410 p.

Orsi, G., Civetta, L., Del Gaudio, C., De Vita, S., Di Vito, M.A., Isaia, R., Petrazzuoli, S.M., Ricciardi, G.P., and Ricco, C., 1999, Short-term ground deformations and seismicity in the resurgent Campi Flegrei caldera (Italy): an example of active block-resurgence in a densely populated area: Journal of Volcanology and Geothermal Research, v. 91, p. 415–451.

Padrón, E., Hernández, P., Toulkeridis, T., Pérez, N.M., Marrero, R., Melián, G., Virgili, G., and Notsu, K., 2008, Diffuse CO_2 emission rate from Pululahua and the lake-filled Cuicocha calderas, Ecuador: Journal of Volcanology and Geothermal Research, v. 176, p. 163–169, doi: 10.1016/j.jvolgeores.2007.11.023.

Pagli, C., Wright, T.J., Ebinger, C.J., Yun, S.-H., Cann, J.R., Barnie, T., and Ayele, A., 2012, Shallow axial magma chamber at the slow-spreading Erta Ale Ridge: Nature Geoscience, v. 5, p. 284–288.

Pantaleo, M., and Walter, T.R., 2013, The ring-shaped thermal field of Stefanos crater, Nisyros Island: a conceptual model: Solid Earth Discussions, v. 5, p. 2005–2042, doi: 10.5194/sed-5-2005-2013.

Parker, A.L., Biggs, J., and Lu, Z., 2014, Investigating long-term subsidence at Medicine Lake Volcano, CA, using multitemporal InSAR: Geophysical Journal International, v. 199, p. 844–859.

Parkinson, K., 1981, An improved method for measuring soil respiration in the field: Journal of Applied Ecology, v. 18, p. 221–228.

Parks, M.M., Biggs, J., England, P., Mather, T. a., Nomikou, P., Palamartchouk, K., Papanikolaou, X., Paradissis, D., Parsons, B., Pyle, D.M., Raptakis, C., and Zacharis, V., 2012, Evolution of Santorini Volcano dominated by episodic and rapid fluxes of melt from depth: Nature Geoscience, v. 5, p. 749–754, doi: 10.1038/ngeo1562.

Parks, M.M., Caliro, S., Chiodini, G., Pyle, D.M., Mather, T.A., Berlo, K., Edmonds, M., Biggs, J., Nomikou, P., Raptakis, C. 2013, Distinguishing contributions to diffuse CO_2 emissions in volcanic areas from magma degassing and thermal decarbonation using soil gas $^{222}Rn - \delta^{13}C$ systematic: application to Santorini volcano. Earth and Planetary Science Letters, v. 377-378, p. 180-190.

Parks, M.M., Moore, J.D.P., Papanikolaou, X., Biggs, J., Mather, T.A., Pyle, D.M., Raptakis, C., Paradissis, D., Hooper, A., and Parsons, B., 2015, From quiescence to unrest: 20 years of satellite geodetic measurements at Santorini volcano, Greece: Journal of Geophysical Research: Solid Earth, v. 120, p. 1309–1328.

Parton, A., Farrant, A.R., Leng, M.J., Telfer, M.W., Groucutt, H.S., Petraglia, M.D., and Parker, a. G., 2015, Alluvial fan records from southeast Arabia reveal multiple windows for human dispersal: Geology, v. 43, p. 1–4, doi: 10.1130/G36401.1.

Paulsen, T.S., and Wilson, T.J., 2010, New criteria for systematic mapping and reliability assessment of monogenetic volcanic vent alignments and elongate volcanic vents for crustal stress analyses, Tectonophysics, v. 482, p.16–28.

Peccerillo, A., Mandefro, B., Solomon, G., Bedru, H., and Tesfaye, K., 1998, The Precambrian rocks from Southern Ethiopia: petrology, geochemistry and their interaction with the recent volcanism from the Ethiopian Rift Valley: Neues Jahrbuch für Mineralogie-Abhandlungen, p. 237–262.

Peccerillo, A., Barberio, M.R., Yirgu, G., Ayalew, D., Barbieri, M., and Wu, T.W., 2003, Relationships between Mafic and Peralkaline Silicic Magmatism in Continental Rift Settings: a Petrological, Geochemical and Isotopic Study of the Gedemsa Volcano, Central Ethiopian Rift: Journal of Petrology, v. 44, p. 2003–2032, doi: 10.1093/petrology/egg068.

Peccerillo, A., Donati, C., Santo, A., and Orlando, A., 2007, Petrogenesis of silicic peralkaline rocks in the Ethiopian rift: geochemical evidence and volcanological implications: Journal of African Earth, v. 48, p. 161–173, doi: 10.1016/j.jafrearsci.2006.06.010.

Pellerin, L., Johnston, J.M., and Hohmann, G.W., 1996, A numerical evaluation of electromagnetic methods in geothermal exploration: Geophysics, v. 61, p. 121–130.

Peltier, A., Finizola, A., Douillet, G.A., Brothelande, E., and Garaebiti, E., 2012, Structure of an active volcano associated with a resurgent block inferred from thermal mapping: The Yasur–Yenkahe volcanic complex (Vanuatu): Journal of Volcanology and Geothermal Research, v. 243-244, p. 59–68, doi: 10.1016/j.jvolgeores.2012.06.022.

Petit, C., and Ebinger, C., 2000, Flexure and mechanical behavior of cratonic lithosphere: Gravity models of the East African and Baikal rifts: Journal of Geophysical Research: Solid Earth (1978–2012), v. 105, p. 19151–19162.

Pik, R., Deniel, C., Coulon, C., Yirgu, G., and Marty, B., 1999, Isotopic and trace element signatures of Ethiopian flood basalts: evidence for plume–lithosphere interactions: Geochimica et Cosmochimica Acta, v. 63, p. 2263–2279.

Pik, R., Marty, B., Carignan, J., Yirgu, G., and Ayalew, T., 2008, Timing of East African Rift development in southern Ethiopia: Implication for mantle plume activity and evolution of topography: Geology, v. 36, p. 167–170.

Pinel, V., Poland, M.P., and Hooper, A., 2014, Volcanology: Lessons learned from synthetic aperture radar imagery: Journal of Volcanology and Geothermal Research, v. 289, p. 81–113.

Piperno, M., Collina, C., Gallotti, R., Raynal, J.-P., Kieffer, G., Bourdonnec, F.-X. le, Poupeau, G., and Geraads, D., 2009, Introduction: Current Issues in Oldowan Research, in Braun, D.R. and Hovers, E. eds., Interdisciplinary Approaches to the Oldowan, Springer Netherlands, p. 111–128.

Pizzi, A., Coltorti, M., Abebe, B., Disperati, L., Sacchi, G., and Salvini, R., 2006, The Wonji fault belt (Main Ethiopian Rift): structural and geomorphological constraints and GPS monitoring, in Yirgu, G., Ebinger, C.J., and Maguire, P.K.H. eds., The Afar Volcanic Province within the East African Rift System, Geological Society, London, Special Publications, v. 259, p. 191–207, doi: 10.1144/GSL.SP.2006.259.01.16.

Poland, M., Hamburger, M., and Newman, A., 2006, The changing shapes of active volcanoes: History, evolution, and future challenges for volcano geodesy: Journal of Volcanology and Geothermal Research, v. 150, p. 1–13.

Potts, R., 2012, Evolution and environmental change in early human prehistory: Annual Review of Anthropology, v. 41, p. 151–167, doi: 10.1146/annurev-anthro-092611-145754.

Pritchard, M.E., and Simons, M., 2002, A satellite geodetic survey of large-scale deformation of volcanic centres in the central Andes: Nature, v. 418, p. 167–171, doi: 10.1038/nature00872.

Pritchard, M.E., and Simons, M., 2004, An InSAR-based survey of volcanic deformation in the central Andes: Geochemistry Geophysics Geosystems, v. 5, p. 1–42, doi: 10.1029/2003GC000610.

Pyle, D.M., 1989, The thickness, volume and grainsize of tephra fall deposits: Bulletin of Volcanology, v. 51, p. 1–15, doi: 10.1007/BF01086757.

Pyle, D.M., 2012, Small volcanic eruptions and the stratospheric sulfate aerosol burden: Environmental Research Letters, v. 7, p. 31001.

Pyle, D.M., and Elliott, J.R., 2006, Quantitative morphology, recent evolution, and future activity of the Kameni Islands volcano, Santorini, Greece: Geosphere, v. 2, p. 253, doi: 10.1130/GES00028.1.

Rampey, M.L., Oppenheimer, C., Pyle, D.M., and Yirgu, G., 2010, Caldera-forming eruptions of the Quaternary Kone Volcanic Complex, Ethiopia: Journal of African Earth Sciences, v. 58, p. 51–66, doi: 10.1016/j.jafrearsci.2010.01.008.

Rampey, M.L., Oppenheimer, C., Pyle, D.M., and Yirgu, G., 2014, Journal of African Earth Sciences Physical volcanology of the Gubisa Formation , Kone Volcanic Complex , Ethiopia: Journal of African Earth Sciences, v. 96, p. 212–219, doi: 10.1016/j.jafrearsci.2014.04.009.

Reimer, P., 2013, IntCal13 and Marine13 Radiocarbon Age Calibration Curves 0–50,000 Years cal BP: Radiocarbon, v. 55, p. 1869–1887, doi: 10.2458/azu_js_rc.55.16947.

Remy, N., Boucher, A., and Wu, J., 2009, Applied Geostatistics with SGeMS, A User's Guide: Cambridge, United Kingdom, Cambridge University Press.

Renne, P.R., Balco, G., Ludwig, K.R., Mundil, R., and Min, K., 2011, Response to the comment by WH Schwarz et al. on "Joint determination of 40 K decay constants and 40 Ar*/40 K for the Fish Canyon sanidine standard, and improved accuracy for 40 Ar/39 Ar geochronology" by PR Renne et al.(2010): Geochimica et Cosmochimica Acta, v. 75, p. 5097–5100.

Rey, A., Pegoraro, E., Tedeschi, V., De Parri, I., Jarvis, P.G., and Valentini, R., 2002, Annual variation in soil respiration and its components in a coppice oak forest in Central Italy: Global Change Biology, v. 8, p. 851–866.

Riede, F., 2014, Changes in mid- and far-field human landscape use following the Laacher See eruption (c. 13,000 BP): Quaternary International, doi: 10.1016/j.quaint.2014.07.008.

Ritsema, J., van Heijst, H.J., and Woodhouse, J.H., 1999, Complex shear wave velocity structure imaged beneath Africa and Iceland: Science, v. 286, p. 1925–1928.

Rizzo, A.L., Barberi, F., Carapezza, M.L., Di Piazza, A., Francalanci, L., Sortino, F., and D'Alessandro, W., 2015, New mafic magma refilling a quiescent volcano: Evidence from He-Ne-Ar isotopes during the 2011–2012 unrest at Santorini, Greece: Geochemistry, Geophysics, Geosystems, v. 16, p. 798–814, doi: 10.1002/2014GC005653.Received.

Rooney, T., Furman, T., Bastow, I., Ayalew, D., and Yirgu, G., 2007, Lithospheric modification during crustal extension in the Main Ethiopian Rift: Journal of Geophysical Research, v. 112, doi: 10.1029/2006JB004916.

Rooney, T.O., Bastow, I.D., and Keir, D., 2011, Insights into extensional processes during magma assisted rifting: Evidence from aligned scoria cones: Journal of Volcanology and Geothermal Research, v. 201, p. 83–96, doi: 10.1016/j.jvolgeores.2010.07.019.

Rooney, T.O., Hanan, B.B., Graham, D.W., Furman, T., Blichert-toft, J., and Schilling, J.G., 2012, Upper mantle pollution during Afar plume-continental rift interaction: Journal of Petrology, v. 53, p. 365–389, doi: 10.1093/petrology/egr065.

Rooney, T.O., Hart, W.K., Hall, C.M., Ayalew, D., Ghiorso, M.S., Hidalgo, P., and Yirgu, G., 2012, Peralkaline magma evolution and the tephra record in the Ethiopian Rift: Contributions to Mineralogy and Petrology, v. 164, p. 407–426, doi: 10.1007/s00410-012-0744-6.

Rosen, P.A., Hensley, S., Peltzer, G., and Simons, M., 2004, Updated repeat orbit interferometry package released: Eos, Transactions American Geophysical Union, v. 85, p. 47.

Rowland, J.V., and Sibson, R.H., 2004, Structural controls on hydrothermal flow in a segmented rift system, Taupo Volcanic Zone, New Zealand: Geofluids, v. 4, p. 259–283, doi: 10.1111/j.1468-8123.2004.00091.x.

Rowland, J. V., Wilson, C.J.N., and Gravley, D.M., 2010, Spatial and temporal variations in magma-assisted rifting, Taupo Volcanic Zone, New Zealand: Journal of Volcanology and Geothermal Research, v. 190, p. 89–108, doi: 10.1016/j.jvolgeores.2009.05.004.

Ruch, J., and Walter, T.R., 2010, Relationship between the InSAR-measured uplift, the structural framework, and the present-day stress field at Lazufre volcanic area, central Andes: Tectonophysics, v. 492, p. 133–140. doi:10.1016/j.tecto.2010.06.003

Rychert, C.A., Hammond, J.O.S., Harmon, N., Kendall, J.M., Keir, D., Ebinger, C., Bastow, I.D., Ayele, A., Belachew, M., and Stuart, G., 2012, Volcanism in the Afar Rift sustained by decompression melting with minimal plume influence: Nature Geoscience, v. 5, p. 406–409.

Sahle, Y., Hutchings, W.K., Braun, D.R., Sealy, J.C., Morgan, L.E., Negash, A., and Atnafu, B., 2013, Earliest stone-tipped projectiles from the Ethiopian rift date to >279,000 years ago: PLoS ONE, v. 8, p. 1–9, doi: 10.1371/journal.pone.0078092.

Sahle, Y., Morgan, L.E., Braun, D.R., Atnafu, B., and Hutchings, W.K., 2014, Chronological and behavioral contexts of the earliest Middle Stone Age in the Gademotta Formation, Main Ethiopian Rift: Quaternary International, v. 331, p. 6–19, doi: 10.1016/j.quaint.2013.03.010.

Saibi, H., Aboud, E., and Ehara, S., 2011, Analysis and interpretation of gravity data from the Aluto-Langano geothermal field of Ethiopia: Acta Geophysica, v. 60, p. 318–336, doi: 10.2478/s11600-011-0061-x.

Salazar, J.M.L., Hernández, P. a., Pérez, N.M., Melián, G., Álvarez, J., Segura, F., and Notsu, K., 2001, Diffuse emission of carbon dioxide from Cerro Negro Volcano, Nicaragua, Central America: Geophysical Research Letters, v. 28, p. 4275–4278, doi: 10.1029/2001GL013709.

Samsonov, S., Beavan, J., González, P.J., Tiampo, K., and Fernández, J., 2011, Ground deformation in the Taupo Volcanic Zone, New Zealand, observed by ALOS PALSAR interferometry: Geophysical Journal International, v. 187, p. 147–160.

Sano, Y., and Marty, B., 1995, Origin of carbon in fumarolic gas from island arcs: Chemical Geology, v. 119, p. 265–274.

Sarychikhina, O., Glowacka, E., Mellors, R., and Vidal, F.S., 2011, Land subsidence in the Cerro Prieto Geothermal Field, Baja California, Mexico, from 1994 to 2005: An integrated analysis of DInSAR, leveling and geological data: Journal of Volcanology and Geothermal Research, v. 204, p. 76–90.

Schöpa, A., Pantaleo, M., and Walter, T.R., 2011, Scale-dependent location of hydrothermal vents: Stress field models and infrared field observations on the Fossa Cone, Vulcano Island, Italy: Journal of Volcanology and Geothermal Research, v. 203, p. 133–145, doi: 10.1016/j.jvolgeores.2011.03.008.

Scott, S.C., 1980, The Geology of Longonot Volcano, Central Kenya: A Question of Volumes: Philosophical Transactions of the Royal Society A: Mathematical, Physical and Engineering Sciences, v. 296, p. 437–465, doi: 10.1098/rsta.1980.0188.

Scott, S.C., and Skilling, I.P., 1999, The role of tephrachronology in recognizing synchronous caldera-forming events at the Quaternary volcanoes Longonot and Suswa, south Kenya Rift: Geological Society, London, Special Publications, v. 161, p. 47–67, doi: 10.1144/GSL.SP.1999.161.01.05.

Shimoike, Y., Kazahaya, K., and Shinohara, H., 2002, Soil gas emission of volcanic CO_2 at Satsuma-Iwojima volcano , Japan: Earth, Planets and Space, v. 54, p. 239–247.

Sigmundsson, F., Hreinsdóttir, S., Hooper, A., Árnadóttir, T., Pedersen, R., Roberts, M.J., Óskarsson, N., Auriac, A., Decriem, J., and Einarsson, P., 2010, Intrusion triggering of the 2010 Eyjafjallajokull explosive eruption: Nature, v. 468, p. 426–430.

Sigmundsson, F., Hooper, A., Hreinsdóttir, S., Vogfjörd, K.S., Ófeigsson, B.G., Heimisson, E.R., Dumont, S., Parks, M., Spaans, K., and Gudmundsson, G.B., 2014, Segmented lateral dyke growth in a rifting event at Bardarbunga volcanic system, Iceland: Nature, v. 517, p. 191–195.

Siniscalchi, A., Tripaldi, S., Neri, M., Giammanco, S., Piscitelli, S., Balasco, M., Behncke, B.,Magrì, C., Naudet, V., Rizzo, E., 2010, Insights into fluid circulation across the Pernicana Fault (Mt. Etna, Italy) and implications for flank instability, Journal of Volcanology and Geothermal Research, v. 193, p. 137–142, doi:10.1016/j.jvolgeores.2010.03.013

Sparks, R.S.J., 2003, Forecasting volcanic eruptions: Earth and Planetary Science Letters, v. 210, p. 1–15, doi: 10.1016/S0012-821X(03)00124-9.

Sparks, R.S.J., and Wilson, C.J.N., 1990, The Minoan deposits: a review of their characteristics and interpretation, in Hardy, D., Keller, J., Galanopoulos, V.P., Flemming, N.C., and Druitt, T.H. eds., Thera and the Aegean World III, London, Thera Foundation London, p. 89–99.

Sparks, S.R.J., Sigurdsson, H., and Wilson, L., 1977, Magma mixing: a mechanism for triggering acid explosive eruptions: Nature, v. 267, p. 315–318.

Sparks, R.S.J., Biggs, J., and Neuberg, J.W., 2012, Monitoring volcanoes: Science, v. 335, p. 1310–1311.

Stamps, D.S., Calais, E., Saria, E., Hartnady, C., Nocquet, J.M., Ebinger, C.J., and Fernandes, R.M., 2008, A kinematic model for the East African Rift: Geophysical Research Letters, v. 35, p. 1–6, doi: 10.1029/2007GL032781.

Street, F., 1979, Quaternary lakes in the Ziway–Shala Basin, Southern Ethiopia. Unpublished Ph.D thesis, University of Cambridge: 475 p.

Szaran, J., 1997, Achievement of carbon isotope equilibrium in the system HCO_3^-(solution)-CO_2 (gas): Chemical Geology, v. 142, p. 79–86.

Tappa, M.J., Coleman, D.S., Mills, R.D., and Samperton, K.M., 2011, The plutonic record of a silicic ignimbrite from the Latir volcanic field, New Mexico: Geochemistry, Geophysics, Geosystems, v. 12, p. 1–16, doi: 10.1029/2011GC003700.

Tassi, F., Aguilera, F., Darrah, T., Vaselli, O., Capaccioni, B., Poreda, R.J., and Huertas, A.D., 2010, Fluid geochemistry of hydrothermal systems in the Arica-Parinacota, Tarapacá and Antofagasta regions (northern Chile): Journal of Volcanology and Geothermal Research, v. 192, p. 1–15.

Tassi, F., Vaselli, O., Papazachos, C.B., Giannini, L., Chiodini, G., Vougioukalakis, G.E., Karagianni, E., Vamvakaris, D., and Panagiotopoulos, D., 2013, Geochemical and isotopic changes in the fumarolic and submerged gas discharges during the 2011-2012 unrest at Santorini caldera (Greece): Bulletin of Volcanology, v. 75, p. 1–15, doi: 10.1007/s00445-013-0711-8.

Tedesco, D., Tassi, F., Vaselli, O., Poreda, R.J., Darrah, T., Cuoco, E., and Yalire, M.M., 2010, Gas isotopic signatures (He, C, and Ar) in the Lake Kivu region (western branch of the East African rift system): Geodynamic and volcanological implications: Journal of Geophysical Research: Solid Earth (1978–2012), v. 115.

Teklemariam, M., 1996, Water-rock interaction processes in the Aluto-Langano geothermal field Ethiopia, Unpublished Ph.D Thesis, University of Pisa, 245 p.

Teklemariam, M., Battaglia, S., Gianelli, G., and Ruggieri, G., 1996, Hydrothermal alteration in the Aluto-Langano geothermal field, Ethiopia: Geothermics, v. 25, p. 679–702.

Tibaldi, A., 1995, Morphology of pyroclastic cones and tectonics: Journal of Geophysical Research, v. 100, p. 24521–24535. doi: 10.1029/95JB02250

Tizzani, P., Battaglia, M., Zeni, G., Atzori, S., Berardino, P., and Lanari, R., 2009, Uplift and magma intrusion at Long Valley caldera from InSAR and gravity measurements: Geology, v. 37, p. 63–66.

Todesco, M., Chiodini, G., and Macedonio, G., 2003, Monitoring and modelling hydrothermal fluid emission at La Solfatara (Phlegrean Fields, Italy). An interdisciplinary approach to the study of diffuse degassing: Journal of Volcanology and Geothermal Research, v. 125, p. 57–79.

Todesco, M., Rutqvist, J., Chiodini, G., Pruess, K., and Oldenburg, C.M., 2004, Modeling of recent volcanic episodes at Phlegrean Fields (Italy): geochemical variations and ground deformation: Geothermics, v. 33, p. 531–547.

Trauth, M.H., Maslin, M. a., Deino, A.L., Strecker, M.R., Bergner, A.G.N., and Dühnforth, M., 2007, High- and low-latitude forcing of Plio-Pleistocene East African climate and human evolution: Journal of Human Evolution, v. 53, p. 475–486, doi: 10.1016/j.jhevol.2006.12.009.

Trauth, M.H., Maslin, M. a., Deino, A.L., Strecker, M.R., Bergner, A.G.N., and Dühnforth, M., 2007, High- and low-latitude forcing of Plio-Pleistocene East African climate and human evolution: Journal of Human Evolution, v. 53, p. 475–486, doi: 10.1016/j.jhevol.2006.12.009.

Trippanera, D., Porreca, M., Ruch, J., Pimentel, A., Acocella, V., Pacheco J., and Salvatore M., 2014, Relationships between tectonics and magmatism in a transtensive/transform setting: An example from Faial Island (Azores, Portugal): Geological Society of America Bulletin, v. 126, p. 164–181. doi: 10.1130/B30758.1.

Troise, C., De Natale, G., Pingue, F., Obrizzo, F., De Martino, P., Tammaro, U., and Boschi, E., 2007, Renewed ground uplift at Campi Flegrei caldera (Italy): New insight on magmatic processes and forecast: Geophysical Research Letters, v. 34.

Trua, T., Deniel, C., and Mazzuoli, R., 1999, Crustal control in the genesis of Plio-Quaternary bimodal magmatism of the Main Ethiopian Rift (MER): Geochemical and isotopic (Sr, Nd, Pb) evidence: Chemical Geology, doi: 10.1016/S0009-2541(98)00174-0.

Tu, K.P., Brooks, P.D., and Dawson, T.E., 2001, Using septum-capped vials with continuous-flow isotope ratio mass spectrometric analysis of atmospheric CO_2 for Keeling plot applications: Rapid Communications in Mass Spectrometry, v. 15, p. 952–956.

Valori, A.M., Teklemariam, M., and Ginaelli G, 1992, Evidence of temperature increase of CO_2-bearing fluids from Aluto-Langano geothermal field (Ethiopia): A fluid inclusions study of deep wells LA-3 and LA-6: European Journal of Mineralogy, v. 4, p. 907–919.

Vasco, D.W., Wicks, C., Karasaki, K., and Marques, O., 2002, Geodetic imaging: reservoir monitoring using satellite interferometry: Geophysical Journal International, v. 149, p. 555–571.

Vasco, D. W., Puskas, C. M., Smith, R. B., and Meertens, C. M., 2007, Crustal deformation and source models of the Yellowstone volcanic field from geodetic data, Journal of. Geophysical Research, 112, B07402, doi:10.1029/2006JB004641.

Vasco, D.W., Rutqvist, J., Ferretti, A., Rucci, A., Bellotti, F., Dobson, P., Oldenburg, C., Garcia, J., Walters, M., and Hartline, C., 2013, Monitoring deformation at the Geysers Geothermal Field, California using C-band and X-band interferometric synthetic aperture radar: Geophysical Research Letters, v. 40, p. 2567–2572.

Viveiros, F., Cardellini, C., Ferreira, T., Caliro, S., Chiodini, G., and Silva, C., 2010, Soil CO_2 emissions at Furnas volcano, São Miguel Island, Azores archipelago: Volcano monitoring perspectives, geomorphologic studies, and land use planning application: Journal of Geophysical Research, v. 115, p. B12208, doi: 10.1029/2010JB007555.

Vogel, J.C., Grootes, P.M., and Mook, W.G., 1970, Isotopic fractionation between gaseous and dissolved carbon dioxide: Zeitschrift für Physik, v. 230, p. 225–238.

Vogel, N., Nomade, S., Negash, A., and Renne, P.R., 2006, Forensic $^{40}Ar/^{39}Ar$ dating: a provenance study of Middle Stone Age obsidian artifacts from Ethiopia: Journal of Archaeological Science, v. 33, p. 1749–1765, doi: 10.1016/j.jas.2006.03.008.

Wadge, G., and Cross, A., 1988, Quantitative methods for detecting aligned points: an application to the volcanic vents of the Michoacan-Guanajuato volcanic field, Mexico: Geology, v. 16, p. 815–818.

Wauthier, C., Cayol, V., Poland, M., Kervyn, F., d'Oreye, N., Hooper, A., Samsonov, S., Tiampo, K., and Smets, B., 2013, Nyamulagira's magma plumbing system inferred from 15 years of InSAR: Geological Society, London, Special Publications, v. 380, p. 39–65.

Weaver, S.D., 1977, The Quaternary caldera volcano Emuruangogolak, Kenya Rift, and the petrology of a bimodal ferrobasalt-pantelleritic trachyte association: Bulletin Volcanologique, v. 40, p. 209–230.

Wegmüller, U., and Werner, C., 1997, Gamma SAR processor and interferometry software: ESA SP, p. 1687–1692.

Weiss, R.F., 1971, Solubility of helium and neon in water and seawater: Journal of Chemical & Engineering Data, v. 16, p. 235–241.

Werner, C., and Cardellini, C., 2006, Comparison of carbon dioxide emissions with fluid upflow, chemistry, and geologic structures at the Rotorua geothermal system, New Zealand: Geothermics, v. 35, p. 221–238, doi: 10.1016/j.geothermics.2006.02.006.

Werner, C., Brantley, S.L., and Boomer, K., 2000, CO_2 emissions related to the Yellowstone volcanic system: 2. Statistical sampling, total degassing, and transport mechanisms: Journal of Geophysical Research, v. 105, p. 10831, doi: 10.1029/1999JB900331.

Werner, C., Hurwitz, S., Evans, W.C., Lowenstern, J.B., Bergfeld, D., Heasler, H., Jaworowski, C., and Hunt, a., 2008, Volatile emissions and gas geochemistry of Hot Spring Basin, Yellowstone National Park, USA: Journal of Volcanology and Geothermal Research, v. 178, p. 751–762, doi: 10.1016/j.jvolgeores.2008.09.016.

Whaler, K.A., and Hautot, S., 2006, The electrical resistivity structure of the crust beneath the northern Main Ethiopian Rift, in Yirgu, G., Ebinger, C.J., and Maguire, P.K.H. eds., The Afar Volcanic Province within the East African Rift System, Geological Society, London, Special Publications, p. 293–305.

White, J.C., Parker, D.F., and Ren, M., 2009, The origin of trachyte and pantellerite from Pantelleria, Italy: Insights from major element, trace element, and thermodynamic modelling: Journal of Volcanology and Geothermal Research, v. 179, p. 33–55, doi: 10.1016/j.jvolgeores.2008.10.007.

White, R., and McKenzie, D., 1989, Magmatism at rift zones: the generation of volcanic continental margins and flood basalts: Journal of Geophysical Research: Solid Earth (1978–2012), v. 94, p. 7685–7729.

Wiart, P., and Oppenheimer, C., 2000, Largest known historical eruption in Africa: Dubbi volcano, Eritrea, 1861: Geology, v. 28, p. 291–294.

Wiart, P., and Oppenheimer, C., 2005, Large magnitude silicic volcanism in north Afar: The Nabro Volcanic Range and Ma'alalta volcano: Bulletin of Volcanology, v. 67, p. 99–115, doi: 10.1007/s00445-004-0362-x.

Wicks, C.W., Thatcher, W., Dzurisin, D., and Svarc, J., 2006, Uplift, thermal unrest and magma intrusion at Yellowstone caldera: Nature, v. 440, p. 72–75.

Williams, F.M., Williams, M.A.J., and Aumento, F., 2004, Tensional fissures and crustal extension rates in the northern part of the Main Ethiopian Rift: Journal of African Earth Sciences, v. 38, p. 183–197, doi: 10.1016/j.jafrearsci.2003.10.007.

Williams, R., Branney, M.J., and Barry, T.L., 2013, Temporal and spatial evolution of a waxing then waning catastrophic density current revealed by chemical mapping: Geology, v. 42, p. 107–110, doi: 10.1130/G34830.1.

Wilson, C.J.N., Rogan, A.M., Smith, I.E.M. , Northey, D.J., Nairn, I.A., and Houghton, B.F., 1984, Caldera volcanoes of the Taupo Volcanic Zone, New Zealand: Journal of Geophysical Research, v. 89, p. 8463–8484, doi:10.1029/JB089iB10p08463.

Wilson, C.J.N., Gravley, D.M., Leonard, G.S., and Rowland, J. V, 2009, Volcanism in the central Taupo Volcanic Zone, New Zealand: tempo, styles and controls: Studies in Volcanology: The Legacy of George Walker. Special Publications of IAVCEI, v. 2, p. 225–247.

Wilson, G., Wilson, T.M., Deligne, N.I., and Cole, J.W., 2014, Volcanic hazard impacts to critical infrastructure: A review: Journal of Volcanology and Geothermal Research, v. 286, p. 148–182.

Wilson, T.M., Stewart, C., Sword-Daniels, V., Leonard, G.S., Johnston, D.M., Cole, J.W., Wardman, J., Wilson, G., and Barnard, S.T., 2012, Volcanic ash impacts on critical infrastructure: Physics and Chemistry of the Earth, Parts A/B/C, v. 45, p. 5–23.

Wohletz, K., and Heiken, G., 1992, Volcanology and geothermal energy: University of California Press Berkeley.

WoldeGabriel, G., Aronson, J.L., and Walter, R.C., 1990, Geology, geochronology, and rift basin development in the central sector of the Main Ethiopia Rift: Geological Society of America Bulletin, v. 102, p. 439–458, doi: 10.1130/0016-7606(1990)102<0439.

WoldeGabriel, G., Walter, R.C., Aronson, J.L., and Hart, W.K., 1992, Geochronology and distribution of silicic volcanic rocks of Plio-Pleistocene age from the central sector of the Main Ethiopian Rift: Quaternary International, v. 13-14, p. 69–76, doi: 10.1016/1040-6182(92)90011-P.

WoldeGabriel, G., Heiken, G., White, T.D., Asfaw, B., Hart, W.K., and Renne, P.R., 2000, Volcanism, tectonism, sedimentation, and the paleoanthropological record in the Ethiopian Rift System, in Volcanic Hazards and Disasters in Human Antiquity, p. 83–99.

WoldeGabriel, G., Hart, W.K., and Heiken, G., 2005, Innovative tephra studies in the East African Rift System: Eos, Transactions American Geophysical Union, v. 86, p. 255, doi: 10.1029/2005EO270003.

Wolfenden, E., Ebinger, C., Yirgu, G., Deino, A., and Ayalew, D., 2004, Evolution of the northern Main Ethiopian rift: birth of a triple junction: Earth and Planetary Science Letters, v. 224, p. 213–228, doi: 10.1016/j.epsl.2004.04.022.

Wolfenden, E., Ebinger, C., Yirgu, G., Renne, P.R., and Kelley, S.P., 2005, Evolution of a volcanic rifted margin: Southern Red Sea, Ethiopia: Geological Society of America Bulletin, v. 117, p. 846, doi: 10.1130/B25516.1.

Yimer, M., 1984, The petrogenesis, chemistry and hydrothermal mineralogy of rocks in the Langano-Aluto geothemal system, Ethiopia, Unpublished report, Geothermal Institute, University of Auckland, 75 pp.: 75 p.

Yirgu, G., Ferguson, D.J., Barnie, T.D., and Oppenheimer, C., 2014, Recent volcanic eruptions in the Afar rift, northeastern Africa, and implications for volcanic risk management in the region: Extreme Natural Hazards, Disaster Risks and Societal Implications, v. 1, p. 200.

Appendix 1

Supplementary information for Chapter 3:

New constraints on causes of episodic unrest

Sample ID (Site-time)	$\delta^{13}C$ (‰)	$\delta^{13}C$ STD (‰)	$[CO_2]$ (ppm)	CO_2 flux (g m^{-2} d^{-1})	Additional notes
01A3-0	-4.73	0.07	2766		
01A3-40	-4.41		23068	33903	Analysis at UNM
01A4-0	-5.45	0.16	2985		
01A4-40	-3.51	0.03	16714	34028	
01A5-0	-4.93	0.07	3584		
01A5-40	-3.56	0.00	18248	38844	
01A6-0	-4.96	0.03	3510		
01A6-40	-3.51	0.01	22185	48657	
01B1-0	-5.27	0.04	2113		
01B1-40	-3.44		22023	4562	Analysis at UNM
01B2-0	-4.47	0.05	2425		
01B2-40	-3.37	0.01	4528		
01B4-0	-8.02	0.08	1931		
01B4-40	-4.26		17879	4493	Analysis at UNM
01B5-0	-6.92	0.05	1723		
01B5-40	-2.60	0.02	18926	3557	
01B6-0	-8.52	0.03	2377		
01B6-40	-2.69	0.00	26635	4087	
01B7-0	-7.59	0.08	1609		
01B7-40s	-6.08		14461	6391	Analysis at UNM
01B8-40	-2.60	0.03	21586	7409	
01B9-0	-6.78	0.04	1561		
01B9-40	-2.83	0.01	20837	4243	
01C1-0	-6.33	0.13	1725		
01C1-40	-3.89		12307	4646	Analysis at UNM
01C2-0	-5.73	0.10	2035		
01C2-40	-2.48	0.01	14833	4642	
01C3-0	-6.70	0.07	2279		
01C3-40	-2.77	0.00	15984	4740	
01C4-0	-5.89	0.04	1936		
01C4-40	-4.40	0.16	2949	4740	
02A1-0	-12.51	0.16	812		
02A1-40	-13.38	0.06	671	23	
02A3-0	-12.54	0.04	584		
02A3-40	-13.55	0.08	693	14	
02A4-0	-13.97	0.03	679		
02A4-40	-13.78	0.16	697	8	
02A5-0	-21.17	0.06	951		
02A5-40	-14.03	0.04	709	10	
03A1-0	-7.95	0.13	1561		
03A1-40	-3.31	0.01	5421	1390	
03A2-0	-5.28	0.06	2831		
03A2-40	-3.18	0.00	6231	1334	
03A3-0	-4.46	0.00	3852		
03A3-40	-5.93		8058	634	Analysis at UNM
03A4-0	-6.15	0.03	3164		
03A4-40	-3.17	0.01	6531	660	
03A7-0	-4.03	0.03	8010		
04A1-0	-9.91	0.07	914		
04A1-40	-8.93	0.13	1046	146	
04A2-0	-12.96	0.09	662		
04A2-40	-10.96	0.04	1137	162	
04A3-0	-13.26	0.02	655		
04A3-40	-8.92	0.01	1062	161	
04A4-0	-13.80	0.01	701		
04A4-40	-8.16	0.13	1087	200	
04A5-0	-12.93	0.06	655		
04A5-40	-8.41	0.03	1149	194	
04A6-0	-14.55	0.15	725		
04A6-40	-9.53	0.05	1146	195	
05A1-0	-12.53	0.10	553		
05A1-40	-14.14	0.07	739	4	
05A2-0	-12.96	0.03	590		
05A3-0	-13.87	0.20	660		
05A3-40	-11.97	0.09	560	12	
05A4-0	-12.22	0.02	544		
05A4-40	-13.69	0.16	681	5	
06A1-0	-4.17	0.02	45994		
06A1-40	-4.26		100310	34897	Analysis at UNM
06A2-0	-4.35	0.04	26178		
06A2-40DIL	-4.39	0.06	160378	42164	diluted
06A3-0	-4.39	0.02	37607		
06A3-40DIL	-4.54	0.09	167363	40497	diluted
06A4-0	-4.32	0.00	33807		
06A4-40	-4.22		101200	29056	Analysis at UNM
06A5-0	-4.30	0.01	42265		
06A5-40			86944		out of range
06A6-0	-4.19	0.03	47203		
06A6-40DIL	-4.40	0.02	156985	25389	diluted
07A1-0	-5.82	0.01	2226		
07A1-40	-7.56	0.01	1515	334	
07A2-40	-6.62	0.04	1722	431	
07A4-0	-18.03	0.01	1031		
07A4-40	-5.78	0.01	1892	401	
08A1-0	-14.68	0.09	837		
08A1-40	-12.89	0.07	1005	106	
08A2-0	-13.35	0.08	666		
08A2-40	-14.90	0.04	1037	101	

Table A1.1: *CO_2 –$\delta^{13}C$ values (‰V-PDB) of the gas sampled from the Artu Jawe Fault zone (AJFZ). CO_2 concentration measurements were made by mass spectrometry (shown in ppm). The CO_2 flux was measured in the field using and infrared gas analyser (LICOR LI-8100) and represent the calculated flux after in a two minute measurement time (g m^{-2} d^{-1}). Note that for a few samples the CO_2 concentration was out of the analytical range and so these were diluted prior to measurement. The bulk of the samples were analysed at INGV (Naples), the remainder were analysed at the University of New Mexico (UNM), see text for further discussion.*

Appendix 2

Supplementary information for Chapter 4: The volcanic and magmatic evolution of Aluto

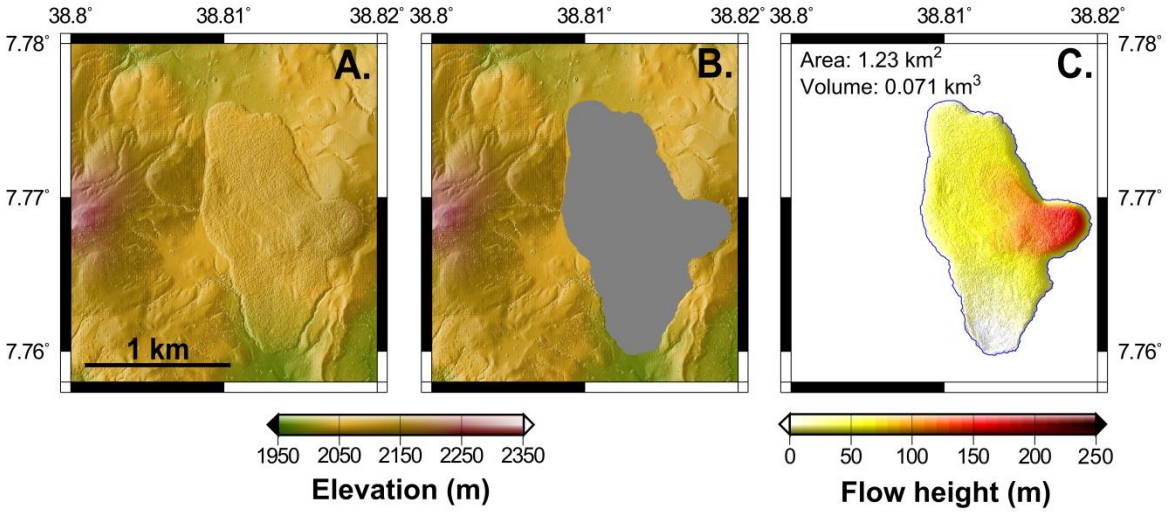

Figure A2.1: *Example of the DEM subtraction method of Nomikou et al., (2014) used here to mask out a typical obsidian coulee (map unit Qpoy) from the lidar DEM and estimate its volume. Note that the calculated volume of coulee has not been converted to a dense rock equivalent.*

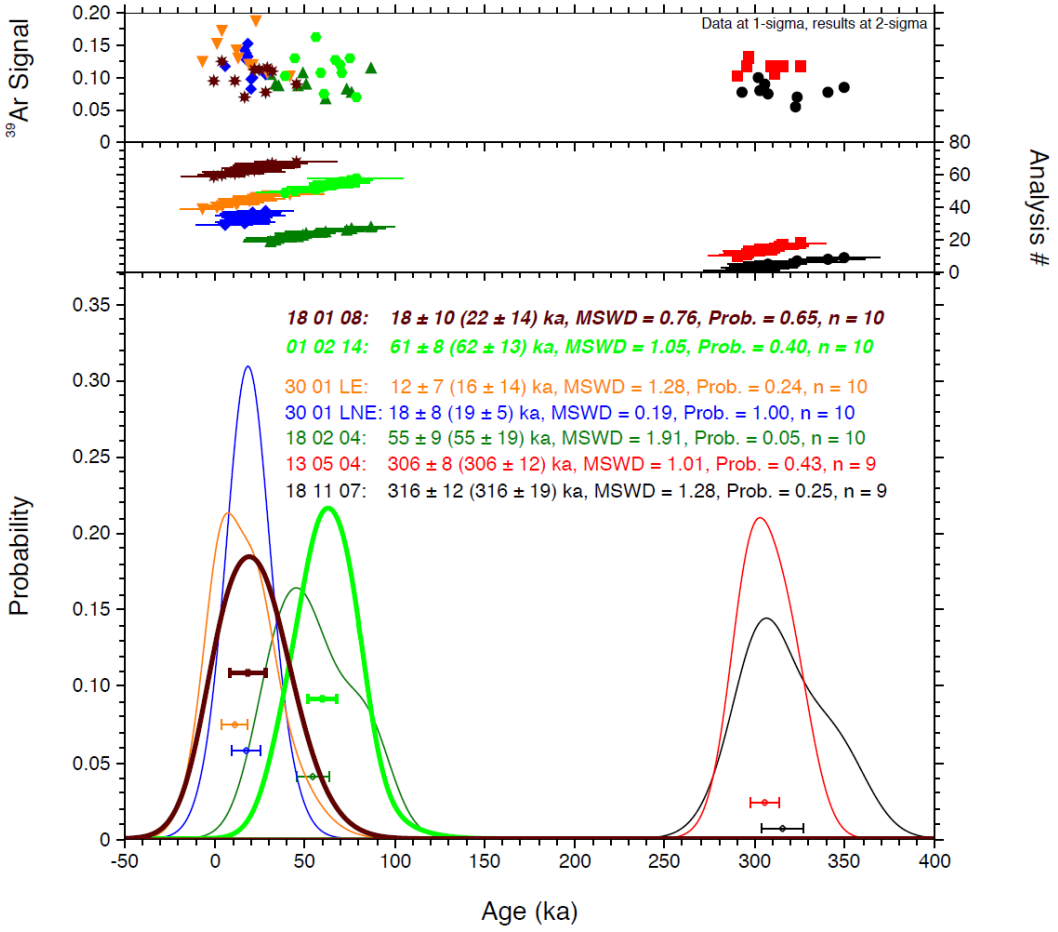

Figure A2.2: *Age probability spectra for SUERC $^{40}Ar/^{39}Ar$ sanidine analyses from Aluto. Ages shown are the weighted mean ± standard error of the mean (1σ), and in brackets the arithmetic mean ± one standard deviation. Ages from this study are shown in bold while those from Hutchison et al., (in review) are shown in regular font.*

[intentionally blank for geological map, Figure A2.3]

Table A2.1: *Descriptions of deep well stratigraphy for LA-4 and, after Yimer (1984)*

Major unit	Sub unit	Description	Minimum depth in well (m)	Maximum depth in well (m)	Thickness (m)
Aluto silicic volcanic products (Qdt - Qpby)	pumice and lithic breccias (post-caldera)	Pumiceous unit with fragments of vesicular obsidian, no hydrothermal alteration	0	32	32
	crystalline and glassy lavas (post-caldera)	~40 m of porphyritic, mildly vesicular pantellerite lava, with phenocrysts of amphibole and alkali feldspar. Succeeded by ~30 m of aphyric obsidian lava. Further underlain by 50 m of pumice, partially altered. Core cut at 256–266 m is a flow banded comendite (with fine groundmass of quartz and feldspar)	32	298	266
	tuffs (pre/syn caldera)	Ash flow tuffs and breccias, exhibiting variable degrees of consolidation. Core cut at 472.1–474.2 m reveals a porphyritic trachytic tuff consisting of alkali feldspars (now highly altered).	298	610	312
Bofa Basalt' (Nqub)	-	Hawaiite lavas, basaltic breccias and scoriaceous horizons, with minor ash and intermittent silicic lava. Hydrothermal alteration has resulted in replacement of plagioclase feldspars and phenocrysts, original groundmass texture heavily altered. A core at 1001–1002.8 m is typical of sequence revealing a fine-grained basalt with groundmass altered (chlorite/smectite), and exhibiting intense veining (haematite, pyrite and calcite).	610	1387	777
Neogene Ignimbrite' (Nqui)	-	Ignimbrite unit with minor intercalated layers of rhyolite lava. Ignimbrites described as hard (owing to silicified groundmass of quartz and alkali feldspar), red-brown colour and crystal rich (feldspar phenocrysts 3–4 mm in length). Intense alteration and recrystallization of ignimbrite layers occur throughout sequence.	1387	2026	639

Table A2.2: *Descriptions of deep well stratigraphy for LA-8 after Mamo (1985)*

Major unit	Sub unit	Description	Minimum depth in well (m)	Maximum depth in well (m)	Thickness (m)
Aluto silicic volcanic products (Qdt - Qpby)	Pumice breccia (post-caldera)	Peralkaline pumice with sparsely porphyritic obsidian and rhyolite	0	65	65
	Peralkaline crystalline rhyolite (post-caldera)	Pink-cream, hard crystalline rhyolite lava with phenocrysts of alkali feldspar. Minor intercalated ash/pumiceous layers. Limited alteration.	65	185	120
	Tuff (syn-caldera)	Grey-green, poorly to moderately compacted lithic and crystal-rich tuff. Samples from top of section are fine-grained with sanidine and clinopyroxene phenocrysts. Deeper in the section chlorite, calcite and hydrothermal quartz fill cavities in the ignimbrite.	185	545	360
Lacustrine sediments (Qdl)	-	Siltstones and minor ashes	545	613	68
Trachytic pyroclastics (Qdlt)	-	Light grey, dense trachytic tuff and lava units. The unit is highly fractured, with cavities filled by haematite and secondary quartz.	613	724	111
Bofa Basalt' (Nqub)	-	Fine to coarsely porphyritic basaltic lava flows and breccias with minor intercalated rhyolite lava flows.	724	1892	1168
Neogene Ignimbrite' (Nqui)	-	Coarsely porphyritic, strongly welded ignimbrite unit with minor rhyolite and basalt layers.	1892	2495	603

Table A2.3a–d: *Geochemical data tables. a: Sample locations and rock type. b: XRF, Department of Geology, University of Leicester. c: ICP-MS, Department of Earth Sciences, University of Oxford. d: Compilation of previously published and unpublished element data for Aluto.*

	Sample location		
Sample	**Lat (°N)**	**Lon (°E)**	**Deposit/rock type**
15-01-01B	7.83450	38.74411	Lithic clast from PDC
15-01-07A	7.83979	38.72940	Silicic enclave within scoria cone
15-01-07B	7.83979	38.72940	Scoria
16-01-05	7.73909	38.78976	Pumice from PDC
17-01-01K	7.85988	38.76332	Pumice from tuff cone
17-01-05	7.85265	38.85802	Scoria
17-01-01G	7.85988	38.76332	Pumice from tuff cone
18-01-04	7.83807	38.74357	Pumice from PDC
18-01-08	7.83245	38.74576	Porphyritic obsidian
18-01-11	7.82705	38.74850	Pumice from PDC
26-01-SMP	7.81605	38.77725	Porphyritic obsidian
26-01-21A	7.82045	38.78066	Pumice from PDC
27-01-03	7.78582	38.81331	Pumice airfall
30-01-LNE	7.81176	38.79360	Porphyritic obsidian
30-01-01B	7.80367	38.79438	Pumice from PDC
30-01-03B	7.80443	38.79433	Pumice from PDC
30-01-06B	7.82314	38.78288	Pumice from PDC
31-01-LE	7.78321	38.82680	Porphyritic obsidian
01-02-13	7.77226	38.77032	Porphyritic obsidian
01-02-14	7.77725	38.76988	Porphyritic obsidian
01-02-24	7.77725	38.76988	Porphyritic obsidian
02-02-01	7.74236	38.78922	Aphyric obsidian
02-02-02	7.74132	38.78875	Pumice from PDC
02-02-03	7.73988	38.78968	Pumice from PDC
02-02-12	7.74960	38.80618	Aphyric obsidian
03-02-23	7.81641	38.75248	Pumice airfall
03-02-28	7.82522	38.74909	Pumice cone
13-05-04	7.84068	38.73031	Welded ignimbrite
18-02-04	7.74193	38.80486	Aphanitic rhyolite lava
15-02-09	7.68078	38.80605	Trachyte lava
18-11-01	7.86210	38.73022	Basaltic lava
18-11-06	7.69705	38.79641	Trachyte lava
18-11-07b	7.69145	38.79720	Trachyte tuff

Major elements (XRF)

Bead	Sample	SiO2	TiO2	Al2O3	Fe2O3	MnO	MgO	CaO	Na2O	K2O	P2O5	SO3	LOI	Total
LF37276	15-01-01B	52.53	2.462	15.53	11.37	0.245	3.40	6.59	4.98	1.816	1.235	<0.002	0.28	100.44
LF37277	15-01-07A	72.85	0.341	10.84	5.79	0.213	0.12	0.32	5.41	4.187	0.026	<0.002	0.19	100.27
LF37278	15-01-07B	59.85	1.645	15.13	8.15	0.144	2.53	4.83	4.64	2.705	0.271	0.065	0.57	100.53
LF37279	16-01-05	72.43	0.168	8.14	6.31	0.261	0.01	0.24	5.51	4.155	0.084	<0.002	2.68	99.99
LF37280	17-01-01K	71.46	0.211	10.88	3.78	0.134	0.07	0.27	2.66	4.739	0.011	<0.002	5.68	99.90
LF37281	17-01-05	46.41	2.089	13.70	12.00	0.185	9.95	11.24	2.37	0.627	0.361	0.009	0.98	99.92
LF37282	17-01-01G	72.03	0.289	9.17	5.14	0.184	0.01	0.25	2.72	4.968	0.008	<0.002	5.15	99.91
LF37283	18-01-04	69.37	0.289	8.44	6.92	0.287	0.04	0.28	5.35	4.277	0.013	0.011	3.67	98.95
LF37284	18-01-08	73.15	0.222	8.88	6.48	0.246	<0.004	0.20	6.31	4.274	0.009	<0.002	-0.04	99.74
LF37285	18-01-11	71.04	0.214	8.60	6.29	0.238	<0.004	0.21	4.93	4.573	0.010	0.005	3.54	99.64
LF37286	26-01-SMP	71.77	0.279	8.69	6.38	0.254	<0.004	0.25	5.87	4.281	0.010	<0.002	1.94	99.72
LF37287	26-01-21A	71.79	0.273	8.72	6.37	0.254	<0.004	0.23	5.74	4.319	0.009	<0.002	2.22	99.92
LF37288	27-01-03	70.61	0.286	10.30	5.71	0.210	<0.004	0.25	5.45	4.387	0.009	<0.002	2.65	99.87
LF37292	30-01-LNE	73.36	0.245	8.99	6.29	0.236	<0.004	0.20	6.01	4.359	0.009	<0.002	-0.14	99.56
LF37289	30-01-01B	71.33	0.233	8.92	5.97	0.223	<0.004	0.20	5.70	4.364	0.011	0.004	2.83	99.80
LF37290	30-01-03B	70.74	0.241	8.49	6.46	0.262	<0.004	0.20	5.81	4.275	0.012	<0.002	3.21	99.69
LF37291	30-01-06B	72.41	0.233	9.05	5.98	0.223	<0.004	0.20	5.22	4.410	0.010	<0.002	2.19	99.92
LF37293	31-01-LE	73.56	0.318	9.78	5.59	0.216	<0.004	0.22	5.80	4.353	0.009	<0.002	-0.40	99.45
LF37294	01-02-13	73.30	0.243	8.79	6.65	0.268	<0.004	0.20	6.19	4.352	0.010	<0.002	-0.17	99.83
LF37295	01-02-14	71.30	0.171	8.02	7.41	0.318	<0.004	0.18	6.86	4.284	0.011	<0.002	-0.29	98.26
LF37296	01-02-24	72.70	0.180	8.44	7.13	0.296	<0.004	0.20	6.52	4.315	0.010	<0.002	-0.21	99.58
LF37297	02-02-01	70.71	0.352	9.73	6.63	0.275	<0.004	0.28	6.40	4.391	0.016	<0.002	-0.32	98.46
LF37298	02-02-02	72.25	0.164	8.52	6.60	0.275	<0.004	0.19	5.98	4.289	0.009	<0.002	2.04	100.31
LF37299	02-02-03	71.83	0.173	8.48	6.54	0.272	<0.004	0.19	6.17	4.268	0.010	0.007	1.91	99.84
LF37300	02-02-12	72.68	0.300	10.03	5.84	0.222	<0.004	0.24	6.15	4.389	0.011	<0.002	-0.22	99.65
LF37301	03-02-23	70.86	0.167	7.78	7.20	0.324	<0.004	0.14	6.69	4.147	0.014	<0.002	2.14	99.47
LF37302	03-02-28	71.34	0.215	8.63	6.28	0.239	<0.004	0.19	5.63	4.292	0.010	0.008	3.16	100.00

Bead	Sample	SiO2	TiO2	Al2O3	Fe2O3	MnO	MgO	CaO	Na2O	K2O	P2O5	SO3	LOI	Total
LF39203	13-05-04	71.13	0.34	11.46	5.80	0.219	0.10	0.39	5.79	4.514	0.025	-0.001	0.22	100.00
LF39204	18-02-04	70.02	0.43	12.08	6.20	0.190	0.10	0.18	5.32	4.719	0.011	-0.010	0.82	100.05
LF39205	15-02-09	65.18	0.89	15.46	6.36	0.222	0.59	2.14	5.46	3.380	0.206	0.005	0.31	100.21
LF39206R	18-11-01	50.24	2.75	15.25	12.00	0.262	3.77	7.54	4.03	1.649	1.290	0.024	0.49	99.29
LF39207	18-11-06	66.38	0.53	14.78	6.39	0.318	0.17	1.05	6.34	3.215	0.063	-0.007	0.76	99.98
LF39208	18-11-07b	65.92	0.64	15.90	5.97	0.100	0.12	0.94	5.92	3.315	0.072	-0.008	1.14	100.04

	Trace elements (XRF)																										
Pellet	**Sample**	**As**	**Ba**	**Ce**	**Co**	**Cr**	**Cs**	**Cu**	**Ga**	**La**	**Mo**	**Nb**	**Nd**	**Ni**	**Pb**	**Rb**	**Sb**	**Sc**	**Se**	**Sn**	**Sr**	**Th**	**U**	**V**	**W**	**Y**	**Zn**	**Zr**
L53619	**13-05-04**	10.1	234.4	226.7	3.9	<0.7	7.1	4.2	33.5	101.8	2.7	141.6	90.1	<0.6	12.6	112.2	<1.0	1.2	<0.6	6.7	11.5	16.6	4.1	6.5	2.4	68.1	187.8	838.4
L53620	**18-02-04**	4.6	369.7	102.8	3.6	<0.7	1.8	2.7	35.2	58.4	2.3	119.9	55.4	<0.6	10.9	68.8	<1.0	4.7	<0.6	4.8	7.1	13.1	1.7	1.8	<1.1	64.5	188.0	786.9
L53621	**15-02-09**	8.4	954.8	152.2	3.5	<0.7	2.0	4.6	26.6	74.7	4.2	84.3	74.5	<0.7	14.4	81.7	<1.0	13.0	<0.6	2.5	299.7	11.1	2.7	8.8	2.3	75.6	139.3	627.2

XRF Notes:

i) Major elements determined on fused glass beads prepared from ignited powders sample to flux ratio 1:5, 80% Li metaborate: 20% Li tetraborate flux results quoted as component oxide weight percent, re-calculated to include LOI

ii) Samples analysed on University of Leicester, Department of Geology PANalytical Axios Advanced XRF spectrometer

iii) Components with concentrations below the lower limit of detection reported as <LLD

Following pages: ICP-MS results. Analysis conducted at the Department of Earth Sciences, University of Oxford July 2013 (using Thermo Finnigan Element 2 Sector-Field ICP-MS)

Sample	Y89(LR) ug/g	Zr90(LR) ug/g	Nb93(LR) ug/g	Rb85(MR) ug/g	Sr86(MR) ug/g	Ba135(MR) ug/g	La139(MR) ug/g	Ce140(MR) ug/g	Nd146(MR) ug/g	Li7(LR) ug/g	Sc45(LR) ug/g	Mo95(LR) ug/g	Cd111(LR) ug/g	Sn117(LR) ug/g	Sn118(LR) ug/g
15_01_01B	53.6	401.6	66.1	35.5	610.0	621.3	64.7	130.0	72.4	14.5	17.5	1.6	0.5	2.2	2.2
17_01_05	22.4	160.9	30.2	12.9	455.5	276.4	23.2	48.7	26.4	10.5	31.8	0.8	0.2	1.3	1.3
18_11_01	48.3	343.7	62.1	34.5	634.8	588.4	58.6	127.0	68.1	10.1	19.4	2.3	0.5	2.3	2.3
15_01_07B	32.3	358.8	45.5	62.5	360.9	776.2	49.6	96.0	42.0	15.4	16.8	3.4	0.5	5.0	5.0
15_01_07A	91.5	931.0	171.1	89.4	18.6	198.6	125.2	248.5	108.7	28.7	1.7	2.6	1.1	8.5	8.8
16_01_05	135.4	1225.5	191.0	119.4	6.8	337.7	166.7	335.5	154.0	37.2	1.6	6.8	1.7	10.6	10.8
17_01_01K	89.3	880.4	132.8	120.0	7.6	69.3	106.1	213.8	91.6	11.1	2.5	6.3	1.1	10.7	10.8
18_01_04	92.1	846.8	137.2	97.5	6.8	467.2	111.2	230.0	104.2	25.9	2.7	6.0	1.2	10.2	10.4
18_01_08	115.8	1102.5	166.5	123.7	1.8	347.2	146.9	301.6	134.7	35.8	2.9	7.5	1.6	8.8	9.0
26_01_SMP	116.6	1026.8	163.7	108.2	6.2	383.5	137.9	286.0	133.7	30.5	2.1	7.5	1.5	7.8	8.0
30_01_LNE	124.8	1178.5	186.9	128.7	4.3	217.8	154.9	319.3	139.5	30.6	2.3	7.5	1.6	9.6	9.7
31_01_LE_1	87.6	771.5	121.7	83.2	5.2	470.2	105.6	216.4	100.1	23.6	1.3	5.8	1.1	6.2	6.3
01_02_13	124.4	1094.8	174.2	115.0	4.7	396.4	149.2	310.9	143.0	34.0	1.7	8.3	1.6	8.7	8.8
01_02_14	161.4	1436.7	229.1	141.1	7.9	369.3	195.5	403.1	185.0	44.2	1.9	10.6	2.0	11.1	11.2
01_02_24	145.6	1282.5	204.6	128.8	7.1	389.3	175.6	364.7	164.6	38.7	2.5	9.8	1.8	10.0	10.1
02_02_01	89.2	833.4	134.8	98.2	3.8	377.3	109.5	223.4	101.4	27.2	2.4	6.1	1.2	6.6	6.7
02_02_03	141.0	1244.7	200.4	127.5	6.8	337.2	172.4	348.4	160.1	40.9	3.1	7.6	1.7	16.2	16.4
02_02_12	99.7	942.3	151.5	106.4	4.2	213.1	124.1	254.5	111.7	29.8	1.8	6.8	1.3	7.5	7.7
03_02_23	190.0	1654.8	263.7	156.1	8.5	396.9	230.3	474.7	215.0	40.1	2.0	10.6	2.3	12.5	12.7
03_02_28	130.8	1199.9	192.1	132.4	4.0	203.1	160.9	328.3	145.5	35.2	1.9	11.0	1.7	12.9	13.1
17_01_01G	84.4	856.5	122.5	106.3	3.0	231.8	111.4	226.2	96.5	13.1	2.5	6.2	1.1	10.3	10.5
18_01_11	131.0	1195.5	190.4	133.5	5.1	195.1	159.2	325.9	142.8	24.5	1.9	8.2	1.7	14.0	14.2
26_01_21_A	111.3	980.6	157.7	103.1	5.3	368.3	136.0	277.2	125.2	28.7	1.5	7.2	1.5	7.6	7.7
27_01_03	97.0	885.8	141.5	95.2	4.8	263.3	117.0	248.9	108.8	24.8	1.6	6.2	1.3	10.0	10.1
30_01_01B_1	120.0	1068.6	170.9	114.9	5.1	200.1	145.2	286.3	130.9	33.1	1.8	7.3	1.5	11.1	11.3
30_01_03_B	118.7	1103.0	175.7	123.2	4.8	205.4	145.7	298.7	128.5	31.7	3.2	7.4	1.5	9.4	9.6
30_01_06_B	120.7	1058.9	169.9	110.4	5.2	366.7	145.0	299.0	132.9	31.0	1.6	7.9	1.5	12.3	12.4
31_01_LE_2	87.2	776.1	121.9	86.0	5.5	455.3	106.0	222.3	102.5	23.3	1.3	5.9	1.0	6.1	6.2
02_02_02	146.5	1268.1	205.1	128.6	5.7	338.4	176.2	357.8	162.9	34.3	1.9	6.9	1.7	15.2	15.6
18_11_06	69.5	96.2	83.3	68.9	218.9	1149.7	81.9	174.2	80.0	13.3	6.4	2.1	0.5	4.2	4.2
18_11_07b	108.0	542.4	94.5	75.7	235.7	896.5	233.3	136.8	266.2	9.3	9.4	2.3	0.6	4.9	5.0
30_01_01_B2	118.3	1083.9	171.9	118.0	5.4	205.4	148.2	293.4	132.9	33.0	2.5	7.4	1.5	11.5	11.7

Sample	Pb208(LR) ug/g	Th232(LR) ug/g	U238(LR) ug/g	V51(MR) ug/g	Cr52(MR) ug/g	Co59(MR) ug/g	Ni60(MR) ug/g	Cu63(MR) ug/g	Zn66(MR) ug/g	Ga69(MR) ug/g	Sb121(MR) ug/g	Te125(MR) ug/g	Cs133(MR) ug/g	Tl205(MR) ug/g	Ge72(HR) ug/g
15_01_01B	5.4	5.7	1.6	98.5	1.3	13.9	1.0	3.2	161.5	24.7	0.1	0.0	0.0	0.0	1.8
17_01_05	2.3	2.3	0.6	286.1	600.9	56.3	149.2	54.4	97.6	17.9	0.0	0.0	0.2	0.0	2.1
18_11_01	7.4	5.3	1.4	123.0	1.7	17.8	0.9	3.4	157.3	24.6	0.1	0.0	0.4	0.1	2.0
15_01_07B	9.5	10.0	2.5	179.6	12.3	21.3	7.2	32.5	102.0	24.2	0.1	0.0	0.5	0.1	1.4
15_01_07A	15.2	20.9	4.5	3.4	0.9	7.5	1.5	9.8	232.1	34.4	0.4	0.1	1.2	0.0	2.2
16_01_05	21.6	22.4	5.9	0.1	1.3	0.1	0.8	14.4	363.4	33.4	0.3	0.2	1.2	0.3	-0.4
17_01_01K	20.1	21.8	5.4	1.3	0.4	0.3	1.0	20.2	197.6	29.9	0.3	0.1	1.3	0.3	-0.2
18_01_04	15.8	16.3	4.4	0.4	0.3	0.1	0.5	25.8	271.6	33.1	0.2	0.2	0.8	0.2	-0.4
18_01_08	21.2	21.5	5.6	0.1	0.6	9.4	0.6	2.8	322.6	33.4	0.3	0.2	1.1	0.3	0.0
26_01_SMP	19.0	19.2	5.0	0.1	1.0	11.8	0.7	1.7	321.4	35.5	0.3	0.3	1.0	0.2	-0.1
30_01_LNE	22.5	23.1	5.9	0.2	1.2	7.2	0.5	1.6	343.9	35.8	0.3	0.2	1.1	0.3	0.4
31_01_LE_1	15.0	14.0	3.6	0.2	2.2	12.8	0.7	1.9	247.8	34.8	0.2	0.2	0.7	0.2	-0.1
01_02_13	20.4	20.3	5.3	0.0	0.9	4.4	0.3	5.0	346.5	35.7	0.3	0.1	1.1	0.2	0.1
01_02_14	26.4	27.4	7.3	0.0	0.8	5.8	0.5	0.7	446.2	36.1	0.4	0.3	1.4	0.3	2.7
01_02_24	23.6	24.2	6.5	0.1	0.8	11.7	0.6	1.6	400.6	35.5	0.3	0.2	1.2	0.3	2.3
02_02_01	15.5	16.7	4.4	0.1	0.6	8.5	0.7	0.9	268.0	35.2	0.2	0.1	0.7	0.2	2.3
02_02_03	22.6	23.5	6.3	0.0	0.8	1.1	1.6	35.8	380.0	35.4	0.3	0.2	1.1	0.2	2.7
02_02_12	17.8	18.6	4.9	0.1	2.4	9.7	0.4	0.7	277.5	35.2	0.2	0.2	0.8	0.2	2.1
03_02_23	29.9	30.7	8.2	0.1	0.5	0.0	0.5	1.1	475.1	34.8	0.4	0.2	1.5	0.4	2.8
03_02_28	23.1	23.9	6.3	0.2	1.7	0.1	3.2	23.8	353.0	34.4	0.3	0.3	1.0	0.3	2.5
17_01_01G	16.7	16.7	5.1	0.3	0.8	0.1	1.2	21.6	235.6	29.5	0.2	0.1	0.9	0.3	2.1
18_01_11	23.2	24.0	6.4	0.2	0.6	0.1	1.1	25.2	352.4	34.8	0.3	0.1	1.1	0.3	3.0
26_01_21_A	18.5	18.8	5.0	0.2	0.4	0.1	0.4	1.3	317.3	34.8	0.2	0.1	1.0	0.2	2.6
27_01_03	16.3	16.9	4.8	0.2	0.4	0.1	0.8	20.1	267.7	36.6	0.2	0.1	0.8	0.2	2.6
30_01_01B_1	20.9	22.0	5.7	0.4	1.2	0.2	0.9	14.3	314.9	33.7	0.3	0.1	1.0	0.2	2.3
30_01_03_B	21.3	22.0	5.8	0.2	0.3	0.1	0.3	5.5	320.8	34.2	0.2	0.1	1.0	0.3	2.3
30_01_06_B	19.7	20.0	5.4	0.1	0.4	0.1	0.3	20.6	331.6	34.3	0.3	0.2	1.0	0.2	2.6
31_01_LE_2	15.0	14.0	3.8	0.3	2.4	12.4	2.1	1.8	364.0	34.2	0.2	0.0	0.7	0.2	2.4
02_02_02	23.4	24.3	6.5	0.0	0.2	0.1	0.7	28.9	388.5	35.9	0.3	0.3	1.3	0.3	2.6
18_11_06	8.7	8.3	1.2	2.8	1.2	0.7	0.9	0.9	202.6	28.6	0.1	0.1	0.4	0.1	1.9
18_11_07b	6.2	10.4	2.5	2.2	1.2	0.5	0.5	0.4	188.9	30.2	0.1	0.1	0.4	0.1	1.9
30_01_01_B2	21.5	22.3	5.9	0.4	0.7	0.1	0.6	14.5	328.2	34.9	0.3	0.3	1.1	0.2	2.7

Sample	As75(HR) ug/g	Te125(HR) ug/g	Pr141(HR) ug/g	Sm149(HR) ug/g	Eu153(HR) ug/g	Gd157(HR) ug/g	Tb159(HR) ug/g	Dy163(HR) ug/g	Ho165(HR) ug/g	Er166(HR) ug/g	Tm169(HR) ug/g	Yb172(HR) ug/g	Lu175(HR) ug/g	Hf178(HR) ug/g	Ta181(HR) ug/g	W182(HR) ug/g	W183(HR) ug/g
15_01_01B	0.7	-0.1	18.2	14.3	4.2	13.4	1.9	10.6	2.0	5.5	0.7	4.4	0.6	8.5	3.9	0.6	0.6
17_01_05	0.9	0.4	6.3	4.9	1.5	4.8	0.8	4.2	0.8	2.4	0.3	2.1	0.3	3.3	1.6	16.1	17.0
18_11_01	1.2	0.0	17.3	14.0	4.5	13.5	1.9	10.5	2.0	5.5	0.7	4.2	0.7	8.4	3.8	0.6	0.6
15_01_07B	1.2	0.3	10.9	7.9	2.2	7.1	1.1	6.5	1.3	3.7	0.5	3.6	0.6	9.5	3.2	1.3	1.2
15_01_07A	2.1	0.1	29.6	20.6	3.4	19.0	3.1	18.0	3.7	10.8	1.5	10.7	1.5	23.4	10.4	56.7	57.4
16_01_05	2.3	0.1	37.8	30.6	6.1	28.6	4.6	27.7	5.4	16.1	2.2	15.4	2.1	30.3	12.0	2.5	2.7
17_01_01K	1.9	0.2	24.7	17.5	2.2	17.1	2.8	17.5	3.5	10.4	1.5	9.8	1.4	23.8	9.0	2.3	2.1
18_01_04	1.4	0.1	26.3	20.1	4.6	19.1	3.0	18.4	3.7	10.8	1.5	10.7	1.5	21.7	8.5	1.8	1.7
18_01_08	2.3	0.3	35.5	27.0	5.6	25.1	3.9	24.8	4.9	14.2	2.0	14.0	1.9	29.4	11.1	73.6	73.6
26_01_SMP	1.4	0.1	33.4	26.0	5.7	24.7	4.1	24.5	4.9	14.0	2.0	13.2	1.9	27.2	10.7	95.9	95.4
30_01_LNE	2.2	0.1	36.7	26.0	4.8	25.0	3.9	25.0	4.9	14.8	2.1	13.5	2.0	29.2	11.6	52.0	53.0
31_01_LE_1	1.8	0.1	26.3	20.3	4.1	18.4	2.9	17.7	3.7	10.6	1.5	9.8	1.4	20.2	8.0	108.2	106.0
01_02_13	2.1	0.0	38.1	27.2	5.7	26.2	4.4	26.0	5.2	14.7	2.1	13.4	2.0	28.6	11.4	42.6	41.7
01_02_14	2.9	0.2	45.2	37.7	7.4	34.1	5.5	33.3	6.3	19.3	2.8	18.1	2.6	36.7	14.2	46.4	46.7
01_02_24	2.3	0.4	41.9	34.4	7.0	31.4	5.0	31.4	6.0	17.8	2.5	16.8	2.4	34.9	13.3	93.6	95.4
02_02_01	1.5	0.0	24.6	20.5	4.1	18.7	3.0	18.3	3.7	10.3	1.5	10.7	1.5	21.7	8.6	64.3	63.7
02_02_03	2.7	0.2	41.9	32.7	6.4	30.3	4.8	30.4	5.9	16.7	2.4	16.2	2.3	32.6	12.8	2.7	2.7
02_02_12	1.8	0.4	28.7	22.0	3.6	20.5	3.2	20.0	3.9	11.5	1.7	11.3	1.6	24.5	9.5	73.4	76.1
03_02_23	3.1	0.2	52.3	42.1	8.5	39.8	6.5	38.4	7.6	21.9	3.1	20.2	2.9	42.3	16.4	3.6	3.5
03_02_28	2.8	0.1	37.1	29.5	5.3	25.8	4.3	26.3	5.2	15.3	2.3	15.0	2.0	31.1	12.4	2.5	2.4
17_01_01G	1.8	0.0	25.7	19.2	3.7	17.5	2.8	17.9	3.6	10.1	1.5	9.3	1.4	22.2	7.7	1.8	1.8
18_01_11	1.7	0.1	36.3	30.3	5.4	26.5	4.5	27.7	5.4	15.8	2.2	15.1	2.1	32.0	12.4	2.6	2.4
26_01_21_A	2.5	0.1	34.4	26.7	5.4	25.3	4.0	24.9	4.7	13.9	2.0	13.0	1.9	26.4	10.5	2.2	2.1
27_01_03	1.9	0.3	28.3	22.8	4.1	20.6	3.4	20.4	4.1	11.8	1.8	11.5	1.7	23.8	9.3	1.8	1.8
30_01_01B_1	2.1	-0.1	35.7	26.9	4.8	25.3	4.1	25.1	5.1	14.7	2.1	14.1	1.9	28.5	11.1	2.3	2.3
30_01_03_B	1.8	0.2	34.9	28.5	4.8	25.8	4.2	25.6	5.1	14.9	2.1	14.4	2.1	30.2	11.7	2.3	2.5
30_01_06_B	2.4	-0.1	34.2	28.9	5.7	25.4	4.1	25.1	5.1	14.4	2.1	13.6	1.9	27.8	10.6	2.0	2.0
31_01_LE_2	1.5	0.0	25.1	20.5	4.2	19.7	3.0	18.7	3.6	10.7	1.5	10.1	1.4	20.1	7.8	107.1	109.3
02_02_02	2.6	0.0	43.4	33.9	6.8	31.0	5.1	31.1	6.0	17.5	2.5	16.8	2.3	32.9	13.1	2.6	2.8
18_11_06	0.6	0.0	19.8	16.7	4.8	15.9	2.6	15.0	2.8	7.7	1.1	7.1	1.0	3.8	5.1	0.5	0.6
18_11_07b	0.9	0.1	64.8	55.4	9.1	43.7	5.9	31.3	5.2	13.2	1.7	10.7	1.4	14.8	5.7	0.6	0.5
30_01_01_B2	2.4	0.1	35.7	27.0	4.9	25.4	4.0	25.1	5.1	14.9	2.1	13.4	1.9	28.7	11.2	2.3	2.4

Sample		13_05_04	15_02_09	18_02_04
Y89(LR)	**ug/g**	67.2	70.2	63.7
Zr90(LR)	**ug/g**	Over range	604.2	818.9
Nb93(LR)	**ug/g**	151.4	87.6	127.4
Mo95(LR)	**ug/g**	2.3	3.8	1.0
Pb208(LR)	**ug/g**	13.6	16.2	12.3
Th232(LR)	**ug/g**	17.8	11.5	14.4
U238(LR)	**ug/g**	3.9	2.6	1.8
P31(MR)	**ug/g**	130.7	1108.3	60.5
Sc45(MR)	**ug/g**	1.9	14.3	4.8
V51(MR)	**ug/g**	5.9	8.1	0.2
Cr52(MR)	**ug/g**	2.3	4.0	0.9
Co59(MR)	**ug/g**	0.4	1.7	0.1
Ni60(MR)	**ug/g**	Below DL	Below DL	Below DL
Cu63(MR)	**ug/g**	4.1	2.9	0.7
Zn66(MR)	**ug/g**	246.6	188.2	241.4
Ga69(MR)	**ug/g**	37.7	29.6	38.8
Rb85(MR)	**ug/g**	118.2	85.4	71.6
Sr86(MR)	**ug/g**	10.7	326.0	6.0
Sr88(MR)	**ug/g**	11.1	333.1	5.9
Ba135(MR)	**ug/g**	258.5	Over range	403.7
Ce140(MR)	**ug/g**	232.4	164.5	105.3
Y89(LR)	**ug/g**	66.4	70.0	63.4
Nb93(LR)	**ug/g**	Over range	Over range	Over range
Mo95(LR)	**ug/g**	2.3	4.0	1.0
Pb208(LR)	**ug/g**	16.2	18.5	14.9
Th232(LR)	**ug/g**	18.0	11.5	14.5
U238(LR)	**ug/g**	4.0	2.7	1.8
Sc45(MR)	**ug/g**	1.8	14.2	4.7
Co59(MR)	**ug/g**	0.4	1.7	0.1
Ga69(MR)	**ug/g**	37.4	30.0	38.5
Cs133(MR)	**ug/g**	1.0	0.8	0.2
La139(HR)	**ug/g**	Over range	79.4	58.9
Pr141(HR)	**ug/g**	24.8	20.0	14.2
Nd146(HR)	**ug/g**	Over range	80.1	55.3
Sm149(HR)	**ug/g**	16.8	15.5	10.9
Eu153(HR)	**ug/g**	2.7	4.1	2.4
Gd157(HR)	**ug/g**	14.5	14.5	10.6
Tb159(HR)	**ug/g**	2.3	2.3	1.8
Dy163(HR)	**ug/g**	13.9	13.4	11.2
Ho165(HR)	**ug/g**	2.8	2.7	2.3
Er166(HR)	**ug/g**	8.3	7.7	7.2
Tm169(HR)	**ug/g**	1.2	1.1	1.1
Yb172(HR)	**ug/g**	8.6	7.4	7.6
Lu175(HR)	**ug/g**	1.3	1.1	1.2
Hf178(HR)	**ug/g**	21.1	14.6	19.7
Ta181(HR)	**ug/g**	8.9	5.0	7.2

Above ICP-MS results. Analysis conducted at the Department of Earth Sciences, University of Oxford December 2014 (Thermo Finnigan Element 2 Sector-Field ICP-MS)

		Major elements (wt. %)												Trace elements (ppm)										
Sample	**Rock type**	**SiO2**	**TiO2**	**Al2O3**	**FeOt**	**MnO**	**MgO**	**CaO**	**Na2O**	**K2O**	**P2O5**	**LOI**	**Total calc**	**Y**	**Zr**	**Nb**	**Rb**	**Sr**	**Ba**	**La**	**Ce**	**V**	**Cr**	**Co**	**Ni**
S-1 [a]	ignimbrite (Munesa escarpment)	70.21	0.5	12.23	5.85	0.17	0.3	0.13	4.06	4.09	0.03	1.91	99.48	74	1156	147	62	7	105	196	191	4	3	10	5
S-2 [a]	coarsely porphyritic basaltic lava	49.76	2.86	16.79	11.56	0.17	4.15	7.83	3.28	1.1	0.62	1.49	99.61	33	285	38	15	484	539	50	97	281	21	41	17
S-3 [a]	grey welded ignmbrite	69.92	0.44	10.37	6.74	0.27	0.21	0.54	5.98	4.38	0.02	0.68	99.55	73	992	166	110	12	287	125	252	5	3	12	3
DP4 [b]	scoriaceous boulder	42.38	4.15	14.59	14.80	0.21	6.24	10.65	2.88	0.64	0.44	2.24	99.22												
DP34 [b]	aphyric obsidian	70.45	0.44	9.32	6.97	0.36	0.05	0.33	6.18	4.48	0.01	3.74	102.33												
DP35 [b]	aphyric obsidian	72.23	0.34	8.51	7.01	0.38	0.04	0.23	6.13	3.94	0	0.91	99.72												
ETH-A12 [c]	coarsely porphyritic basaltic lava	50.45	2.84	18.40	10.87	0.17	2.03	7.48	4.43	1.35	0.66	0.56	99.24												
ETH-A13 [c]	aphyric basaltic lava	50.08	2.78	14.44	13.93	0.26	3.43	7.07	3.87	1.79	1.43	0.01	99.09												
Mamo-1494 [c]	porphyritic basaltic lava	48.04	2.81	15.18	11.84	0.2	4.24	7.52	2.95	1.5	0.65	3.43	98.36												

[a] Teklemariam, 1996 and Teklemariam et al., 1996; Major elements were determined by XRF, using lithium borate fusion technique. Trace elements were determined by XRF on powder rock pelets. Analyses were performed at the Department of Earth Sciences, University of Pisa.

[b] Di Paola, 1972; Major elements were determined by XRF (N.B. no trace elements for these samples)

[c] Yimer, 1984 and Mamo, 1985; Major elements were determined by XRF using lithium borate fusion technique. Analyses were performed at the Department of Geology, University of Auckland (N.B. no trace elements for these samples)

Appendix 3

Supplementary information for Chapter 5:

Silicic eruptive fluxes in the Main Ethiopian Rift

A3.1: $^{40}Ar/^{39}Ar$ geochronology

Unweathered rock samples were collected from sites shown on Figure A3.1 (coloured stars). Care was taken to avoid sampling lithic fragments in flow units. Rocks were pulverised in a jaw-crusher, and sanidine phenocrysts (250–500 μm in diameter) were separated from the crush using magnetic and LMT heavy liquid density separation techniques. Sanidine phenocrysts were leached ultrasonically in 5% Hydrofluoric acid for ~3 minutes to remove adhering glass and groundmass. Grains were thoroughly rinsed in distilled water and dried, followed by handpicking under a binocular microscope to remove any remaining contaminant phases (fluid/melt inclusions or quartz crystals).

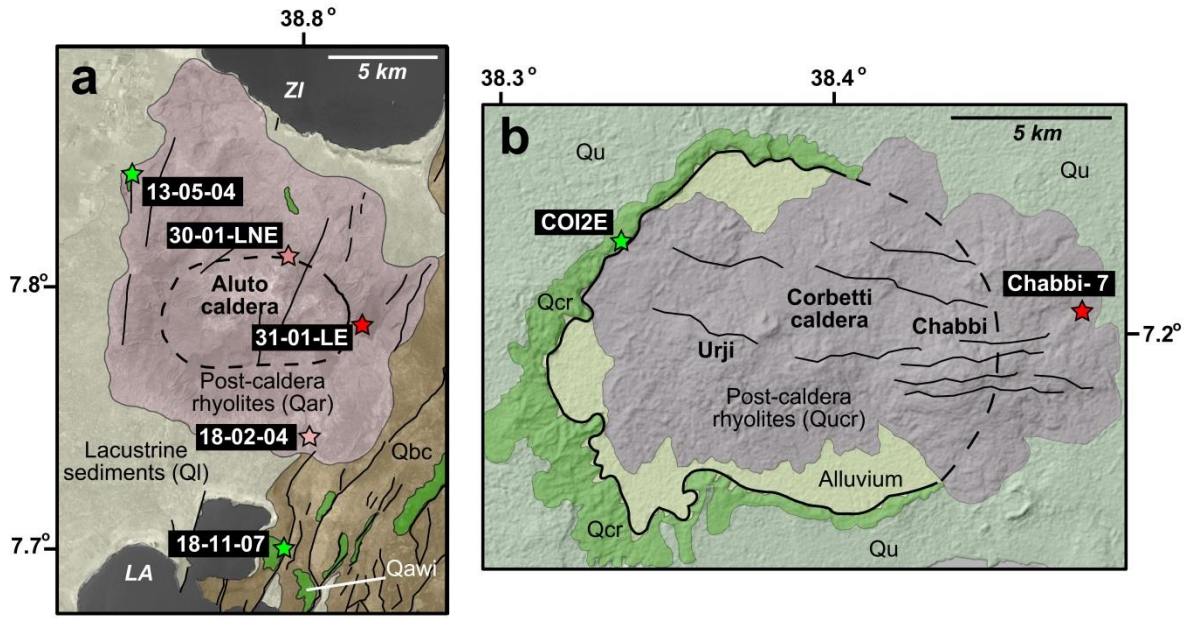

Figure A3.1. *Geological maps of Aluto (a) and Corbetti (b) showing the location of the sampled units (stars). The simplified units for Aluto (a) are: Ql, late Pleistocene-Holocene lacustrine sediments deposited in the Ziway-Shala basin (Benvenuti et al., 2002, 2013); Qbc, basaltic lavas and alluvial-colluvial sediments deposited on the rift margin; Qawi, Aluto welded ignimbrites (in the most uplifted fault sections these are underlain by pre-caldera lavas, see Figure 5.2) and Qar, Aluto post-caldera rhyolites (predominantly obsidian coulees and pyroclastic flows). The present-day lakes are identified as: ZI: Lake Ziway and LA: Lake Langano. The simplified geological map of Corbetti caldera (b) comprises the following units: Qcr, Corbetti rhyolitic lava, welded ignimbrite, pyroclastic deposits and obsidian coulees (pre- and syn- caldera); Qucr, Urji Chabbi pyroclastic flows and obsidian coulees (post-caldera units); Qu, Quaternary undifferentiated cover, rhyolitic and trachytic tuffs (mostly derived from Corbetti caldera collapse) as well as minor basalts flows, lacustrine sediments and alluvium. Faults, fissures and caldera ring faults mapped by Di Paola (1971), Agostini et al. (2011) and Hutchison et al. (2015) are shown as black lines.*

A3.1.1: Aluto samples

Aluto sanidine separates were loaded into aluminium disks and irradiated for 30 minutes in the Cd-lined facility at the TRIGA Reactor, Oregon State University. Grains of the neutron-flux standard Alder Creek sanidine (1.2056 ± 0.0019 Ma, Renne et al.,2011) were co-irradiated in the same aluminium disks, in separate wells. Following a ~2 month cooling period, the Aluto samples and Alder Creek sanidine crystals were analysed at the NERC Argon Isotope Facility, Scottish Universities Environmental Research Centre (SUERC) in a MAP-215 mass-spectrometer, with a measured sensitivity of 1.13×10^{-13} moles/Volt. All aliquots were totally fused using a focussed CO_2 laser, and the released gas purified using two SAES GP50 getters with ST101 Zr-Al cartridges (one at room temperature and the other at 450°C). Single crystals were analysed for Alder Creek sanidine, and 10–30 single crystals were analysed for each of the Aluto samples to screen for contaminant phases (Table A3.1). All of the single-crystal Aluto analyses yielded single-populations of crystals, indicating that no older contaminant phases were identified (Table A3.1). Therefore, in order to increase the amount of gas analysed for these young samples (and improve precision of the analyses), 10 crystals were fused together in each aliquot (Table A3.1) and these multi-crystal analyses were used to determine the ages of the Aluto samples (Fig. A3.2).

Isotope extraction, purification, extraction line operation and mass spectrometry were fully automated. Backgrounds were measured after every two analyses of unknowns. Average backgrounds and standard deviations from n = 133 blank analyses are as follows: ^{40}Ar (0.007448 ± 0.0001573 V), ^{39}Ar (0.000045 ± 0.0000140 V), ^{38}Ar (0.000042 ± 0.0000290 V), ^{37}Ar (0.000457 ± 0.0000322 V), and ^{36}Ar (0.000099 ± 0.0000150 V). Mass discrimination was monitored by analysis of air pipettes after every five analyses. The discrimination factor (D = 1.0066 ± 0.0024) was calculated using a power law (Mark et al., 2011) from the average $^{40}Ar/^{36}Ar$ ± standard deviation (290.8 ± 2.8, n = 71) of the air pipette data. Analyses of the Alder Creek sanidine

samples yielded a J factor of 0.0001427 ± 0.000000562. Data was corrected for mass discrimination, nucleogenic interferences, and atmospheric contamination using MassSpec software (version 8.058). Values used in the data regression are as follows:

$(^{40}Ar/^{36}Ar)_{Atm}$	298.56 ± 0.31	(Lee et al., 2006)
$^{40}K/K$	1.167 E-4 mol/mol	(Steiger and Jaeger, 1977)
$^{40}K\ \lambda\varepsilon$	(5.757 ± 0.016) E-11 a^{-1}	(Renne et al.,2011)
$^{40}K\ \lambda_{\beta}$	(4.9548 ± 0.0134) E-10 a^{-1}	(Renne et al.,2011)
$^{40}K\ \lambda$ total	(5.5305 ± 0.0135) E-10 a^{-1}	(Renne et al.,2011)
$^{37}Ar\ \lambda$	0.01983 ± .0000226 $days^{-1}$	(Renne and Norman, 2001)
$^{39}Ar\ \lambda$	(7.055 ± 0.039) E-6 $days^{-1}$	(Stoenner et al., 1965)
$^{36}Cl\ \lambda_{\beta}$	(6.1817 ± 0.040) E-9 $days^{-1}$	(Renne et al., 2008)

Reactor production ratios and interfering isotope production ratios are as follows:

$(^{36}Cl/^{38}Cl)_{Cl}$	263 ± 2	(Renne et al., 2008)
$(^{38}Ar/^{37}Ar)_{Ca}$	(1.96 ± 0.08) E-05	(Renne et al., 2005)
$(^{38}Ar/^{39}Ar)_{K}$	(1.22 ± 0.01) E-02	(Renne et al., 2005)
$(^{40}Ar/^{39}Ar)_{K}$	(7.30 ± 0.92) E-04	(Renne et al., 2005)
$(^{37}Ar/^{39}Ar)_{K}$	(2.24 ± 0.16) E-04	(Renne et al., 2005)
$(^{39}Ar/^{37}Ar)_{Ca}$	(6.95 ± 0.09) E-04	(Renne et al., 2005)
$(^{36}Ar/^{37}Ar)_{Ca}$	(2.65 ± 0.02) E-04	(Renne et al., 2005)

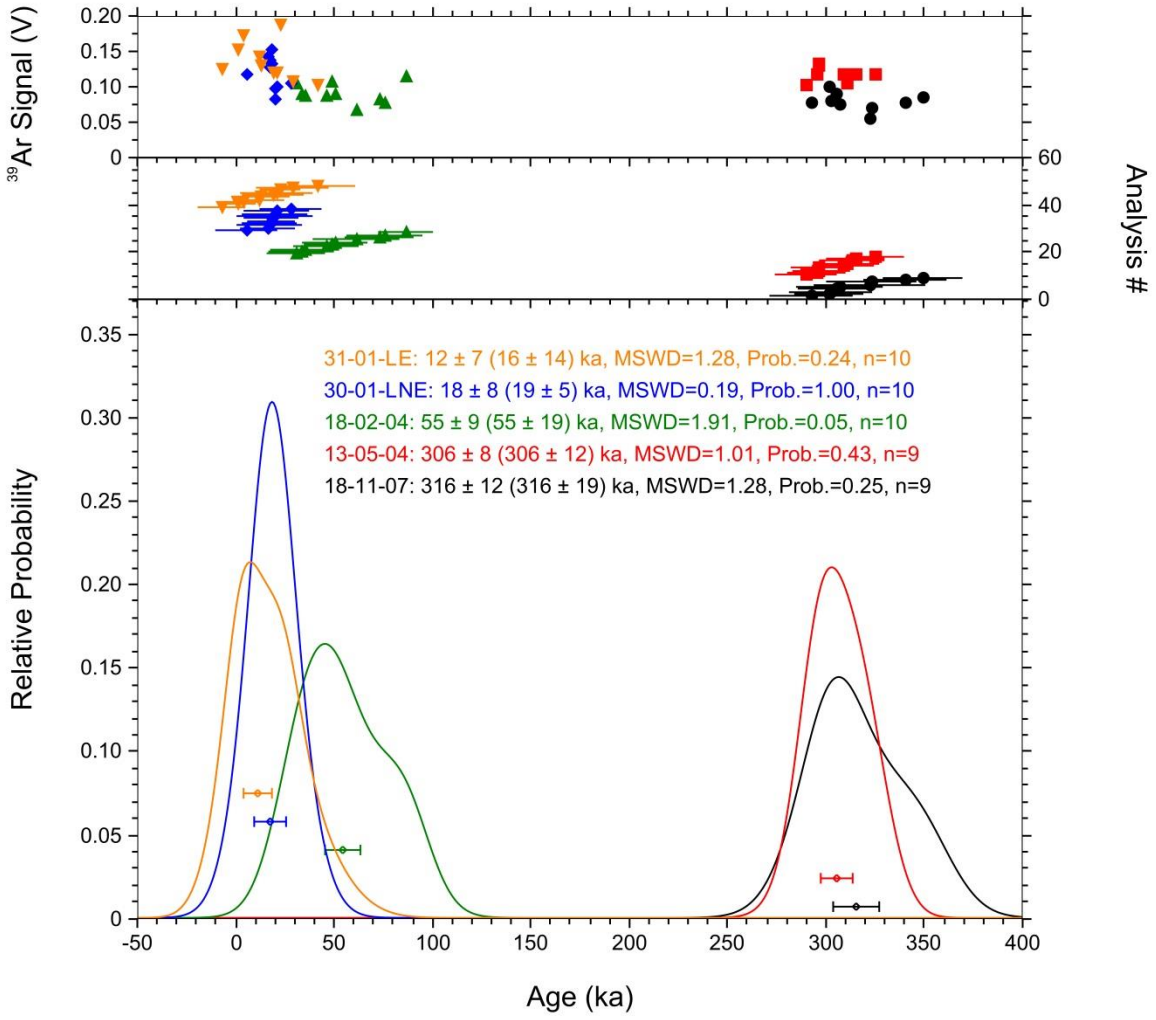

Figure A3.2. *Age probability spectra for SUERC $^{40}Ar/^{39}Ar$ sanidine analyses from Aluto. Ages shown are the weighted mean ± standard error of the mean (1σ), and in brackets the arithmetic mean ± one standard deviation.*

A3.1.2: Corbetti samples

For irradiation of the Corbetti samples 25 mg sanidine crystal separates were packaged in Al foil and placed in a cylindrical quartz vial, together with fluence monitors of known age and K-glass and fluorite to measure interfering isotopes from K and Ca. The quartz vials were wrapped in 0.5 mm-thick Cd foil to shield samples from thermal neutrons during irradiation. The samples were irradiated for one hour in the central thimble of the U.S. Geological Survey TRIGA reactor in Denver, Colorado (Dalrymple et al., 1981). The reactor vessel was rotated continuously during irradiation to avoid lateral neutron flux gradients and oscillated vertically to minimize vertical gradients. Reactor constants determined for these irradiations were indistinguishable from recent

irradiations, and a weighted mean of constants obtained over the past five years yields $^{40}Ar/^{39}Ar_K$ = 0.0010±0.0004, $^{39}Ar/^{37}Ar_{Ca}$ = 0.00071±0.00005, and $^{36}Ar/^{37}Ar_{Ca}$ = 0.000281±0.000006. TCR-2 sanidine from the Taylor Creek Rhyolite (Duffield and Dalrymple, 1990) was used as a fluence monitor with an age of 27.87 Ma. Results were recalculated to Fish Canyon sanidine (28.294 Ma, Renne et al., 2011) using $R_{TCs/FCs}$ = 1.00881±0.00046, determined in Menlo Park. TCR-2 is a secondary standard calibrated against the primary intralaboratory standard, SB-3, that has an age of 162.9 ± 0.9 Ma (Lanphere and Dalrymple, 2000). Fluence monitors and unknowns were analyzed using a continuous CO_2 laser system and mass spectrometer described by Dalrymple (1989). Gas was purified continuously during extraction using two SAES ST-172 getters operated at 4A and 0A.

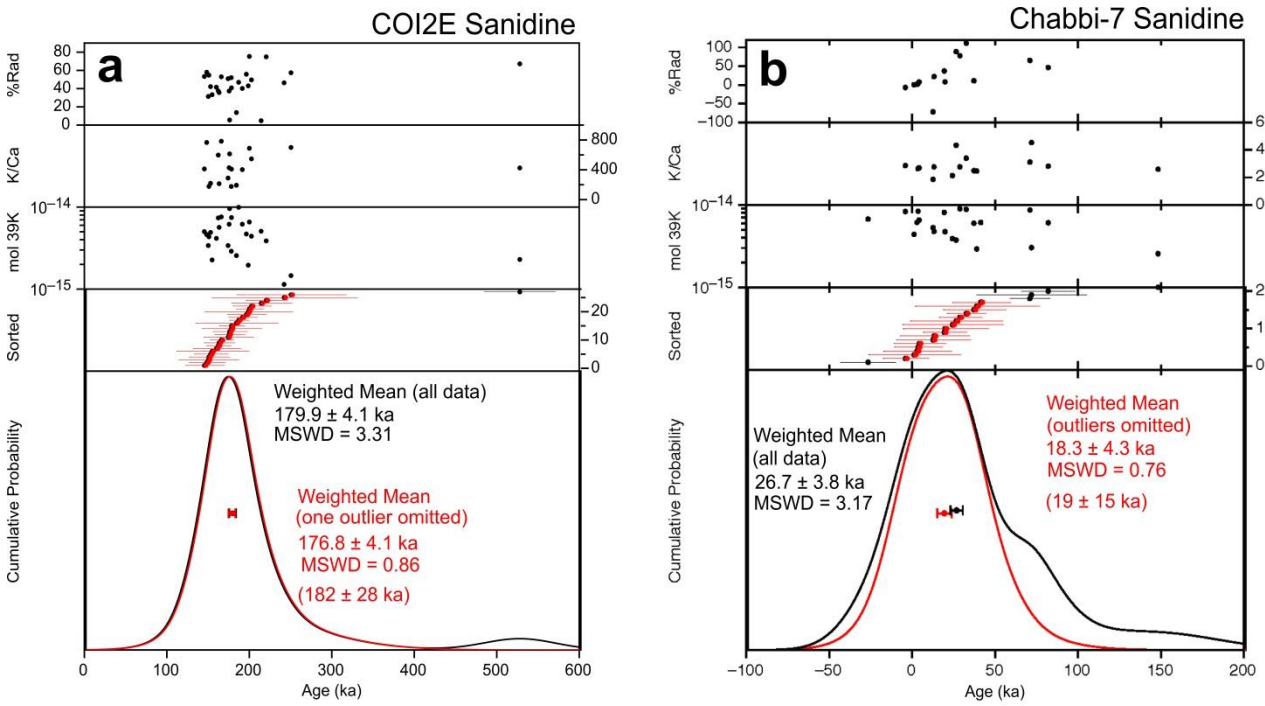

Figure A3.3. *Age probability spectrum for USGS $^{40}Ar/^{39}Ar$ sanidine analyses from Corbetti, (a) Sample COI2E and (b) Sample Chabbi-7. Ages shown are the weighted mean ± standard error of the mean (1σ), and in brackets the arithmetic mean ± one standard deviation..*

$^{40}Ar/^{39}Ar$ geochronology was performed at USGS Menlo Park. Discrimination was monitored by analyzing splits of atmospheric Ar from a reservoir attached to the extraction line and for these samples $D_{1amu} = 1.010795 \pm 0.000169$. Typical system blanks including mass spectrometer backgrounds were $1.5x10^{-18}$ mol of m/z 36, $9x10^{-17}$ mol of m/z 37, $3x10^{-18}$ mol of m/z 39 and $1.5x10^{-16}$ mol of m/z 40, where m/z is mass/charge ratio. Apparent ages were calculated from single crystal fusion data using atmospheric ratios and are plotted in Figure A3.3.

A3.2: Volume calculations

To obtain a first-order approximation of the volume of silicic magma produced at each volcano through time we consider their eruptive histories to be comprised of three main phases: a pre-collapse edifice; caldera collapse and post-caldera volcanism. These stages are a reasonable approximation of the long-term eruptive cycle of silicic peralkaline volcanoes (Mahood, 1984; Cole et al., 2005) and also agree with the existing constraints on the eruptive histories of the volcanic complexes considered in this study (Di Paola, 1971, 1972; Mohr et al., 1980; Kebede et al., 1985; Peccerillo et al., 2003).

For the pre-collapse edifice we characterize the volcano as a simple conical structure; the centre of the pre-collapse volcano is equivalent to the centre of the present-day caldera, and the slope of the pre-collapse volcano is calculated using the mean slope of the caldera walls away from the complex (e.g. Figure A3.4) using a present-day digital elevation model (DEM; we used SRTM 1 Arc-Second Global elevation data at a resolution of 30 m, the highest-resolution, freely-available topographic data available at this time). We then use thickness estimates of pre-caldera lavas, usually taken from caldera wall sequences, as the final variable to approximate the volume of the pre-collapse cone.

Calderas are volcanic collapse features related to withdrawal of magma from an underlying reservoir (Druitt and Sparks, 1984; Lipman, 1984; Cole et al., 2005). Since most calderas can be approximated by a subsiding block surrounded by a ring fault (Lipman, 1997; Roche et al., 2000), we assume that the calderas considered in this study consist of a cylindrical piston (caldera block) above a magma reservoir. Thus the net volume of the caldera can be used to estimate the volume of material ejected by the caldera-forming eruption. Kandlbauer and Sparks (2014) compared different methods for calculating eruptive volumes and found that estimates of caldera volumes compare well to those from ash fall and ignimbrite thickness extrapolations (Pyle, 1989; Bonadonna and Costa, 2012), supporting the method we have employed here. We assume that the cylindrical caldera collapse volume is defined by the long and short axis of the caldera structure and depth is defined by the present-day caldera wall height. Following observations of Lipman (1997) we assume that intra-caldera ignimbrite deposits partially infill the caldera floor. At Aluto volcano, deep well stratigraphy records confirm thick sequences (100–300 m) of caldera-filling ignimbrites (Teklemariam et al., 1996). Deep well records only exist for Aluto and therefore we have assumed that similar thicknesses of fill ignimbrites also exist at the other caldera complexes. The total volume of the caldera collapse is calculated by summing the present-day volume of the caldera and the volume of the intra-caldera fill (approximated as a cylinder with equivalent spatial dimensions to the caldera structure).

Following caldera collapse each volcano has undergone further (post-caldera) lava extrusion. The volume of the post-caldera deposits was calculated using DEMs following the method of Nomikou et al. (2014). For each volcano, polygons outlining the post-caldera deposits were created and used to mask out these volcanic landforms from the DEM. The removed region of the DEM was then interpolated using a variable tension parameter to derive a smoothed near-flat pre-eruption surface across the masked area. We then subtracted the present day DEM from the interpolated DEM (e.g., Fig. A3.5a minus Fig. A3.5c) and calculate the residual volume between

the surfaces, thus providing a volume estimate for the post-caldera eruptive products. DEM interpolations and volume calculations were carried out using GMT software (Wessel and Smith, 1998; Nomikou et al., 2014). This method calculates a minimum post-caldera volume, as it only accounts for proximal volcanic deposits rather than distal tephra dispersed far beyond the vent. Our mapping suggests that the bulk of post-caldera deposits are typified by localized pyroclastic flows and coulees (Fig. 5.2) rather than widely dispersed pumice fall units, and until detailed correlations of the post-caldera tephra sequences are completed the DEM differencing method (above) is the most appropriate method to use.

Eruptive volumes were then converted to a dense rock equivalent (DRE). For the pre- and post-caldera edifice we assume that the deposits comprise a 50:50 mix of silicic lava and volcaniclastic sequences (with bulk densities of 2200 kg m^{-3} and 1800 kg m^{-3} respectively, Fink (1980, 1983). DRE volumes are calculated assuming a (water-free) silicic magma density of 2380 kg m^{-3} (Ochs et al., 1999). The caldera volume is assumed to be equivalent to the volume of magma withdrawn from the reservoir and so no conversion is applied. For each volcanic complex the constraints on eruptive history and assumptions made in volume calculations are outlined explicitly below.

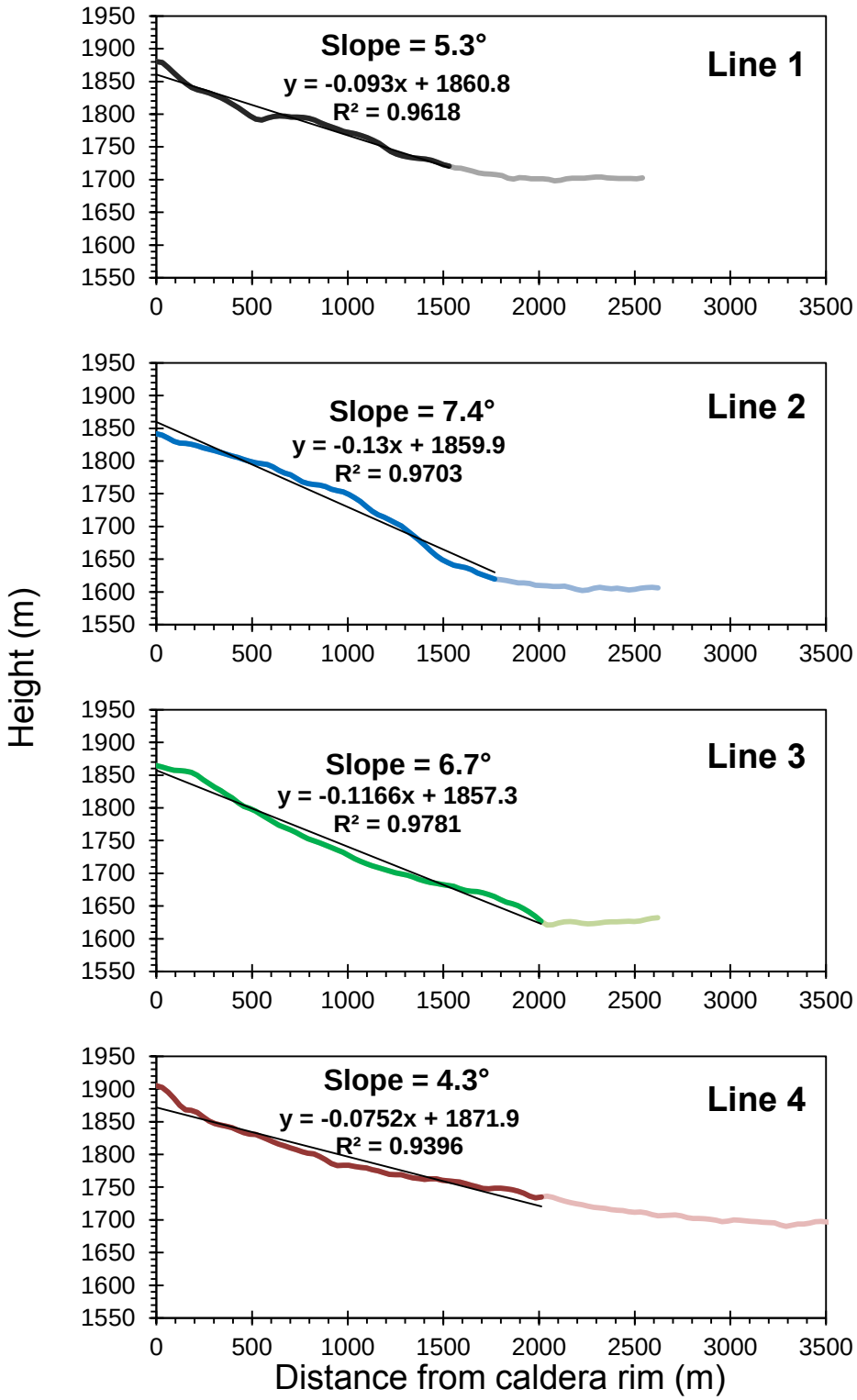

Figure A3.4. *Topographic profiles constructed away from the caldera walls of Gedemsa volcano (used to estimate the slope of the pre-collapse volcano, and combined with thickness estimates to calculate the volume of the pre-collapse edifice, see Appendix 3.2 for details). Profile lines are linked to Fig. A3.5.*

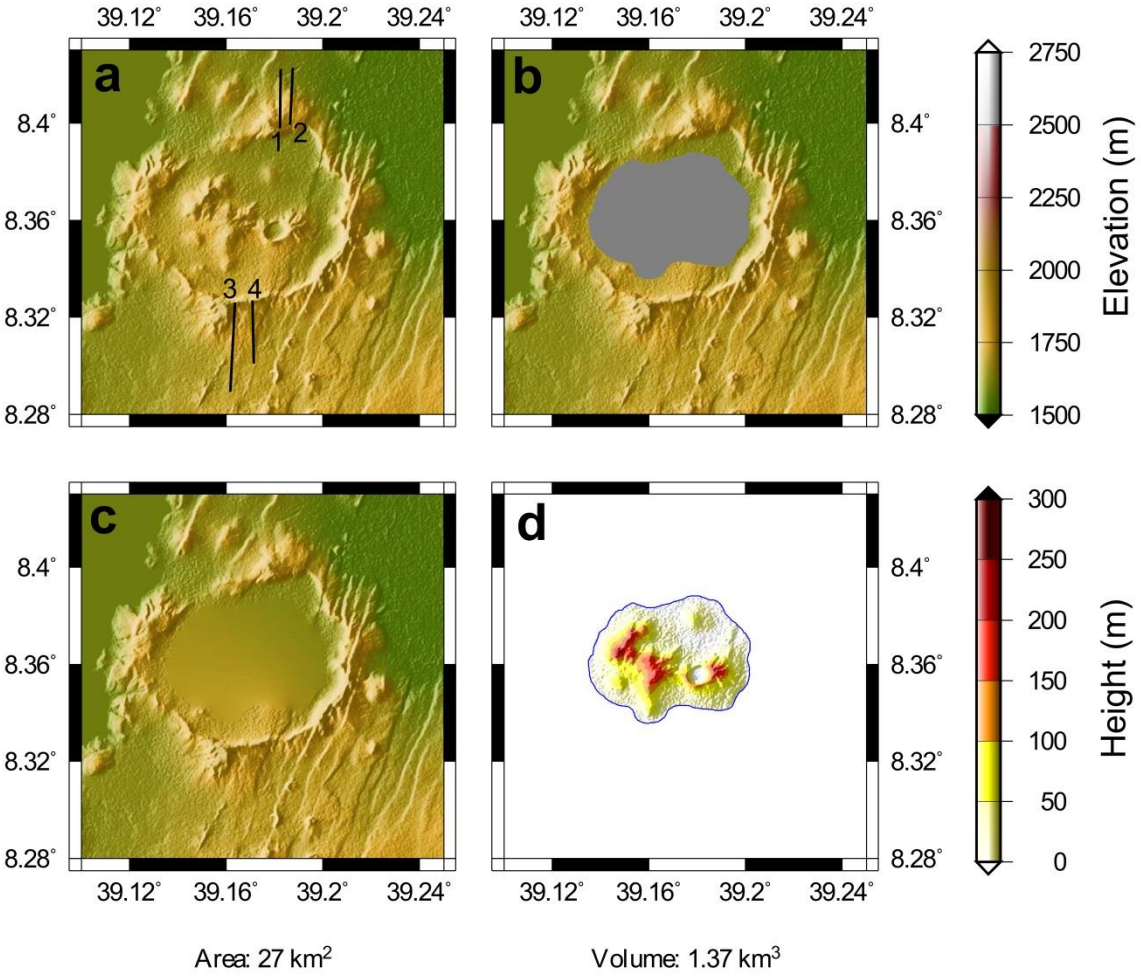

Figure A3.5. *DEM differencing method used to mask out post-caldera deposits at Gedemsa and calculate their volume. a, represents the present-day DEM, b, shows the masked area (grey), c shows the present-day DEM with interpolated masked surface and d, shows the difference between a and c, shown as residual height. The volume of masked area, i.e., the volume of post-caldera deposits, is given in the bottom right. Note that volume shown is not corrected to a dense rock equivalent (DRE).*

A3.2.1: Gedemsa

The pre-caldera volcanic sequences of Gedemsa are mostly comprised of rhyolitic lavas, although pumice fall and ignimbrite deposits are also present (Peccerillo et al., 2003; Giordano et al., 2014). Individual rhyolite lava flows are thick (20–30 m), 2–5 km long and show a clear flow folding (Giordano et al., 2014). Based on the geological map of Peccerillo et al. (2003) the minimum thickness of the pre-caldera deposits, identified in the northern caldera wall of Gedemsa, is 250 m. Slope measurements, made on the northern and southern back walls of the

caldera (i.e., the non-faulted sections) range between 4–7.5° (Fig. A3.4). The following estimates are made for the volume of the pre-collapse edifice:

Estimate	Caldera wall thicknesses (m)	Edifice slope (°)	Volume DRE (km^3)
High	300	7.5	35
Med	250	6	28
Low	150	4	18

The outline mapping of Gedemsa by Peccerillo et al. (2003) and Giordano et al. (2014) suggest that caldera collapse may not simply relate to a single event and that multiple explosive eruptions, occurring in different sectors of the volcano, over a 320–260 ka period generated the caldera. However, until detailed mapping of these individual eruptions takes place it is reasonable to assume that the bulk caldera subsidence over the collapse period is represented by the present-day (8 km × 9 km) caldera structure which has typical wall heights between 150–250 m. We estimate the collapse volume for Gedemsa as follows:

Estimate	Caldera wall height (m)	Intra-caldera fill (m)	Volume DRE (km^3)
High	250	300	31
Med	200	200	23
Low	150	100	14

Post-caldera volcanism at Gedemsa has generated a set of small coalescing edifices (200–250 m high) in the centre of the caldera (Fig. A3.5). The post-caldera eruptive units are composed of alternating rhyolitic lavas and pumice-fallout deposits (Peccerillo et al., 2003; Giordano et al., 2014), and the total volume of these vents and domes is calculated as ~1 km^3 DRE (Fig. A3.5).

A3.2.2: Aluto

Aluto contrasts from the other volcanoes of this study because it does not possess a well-defined caldera rim at the surface (Figs. A3.1a, A3.6). Our new eruptive stratigraphy (Fig. 5.2, and main text) does, however, demonstrate that Aluto has undergone major ignimbrite eruptions of

sufficient magnitude to be associated with caldera collapse. In addition, soil gas CO_2 surveys and vent alignments are strongly suggestive of a buried ring fault structure beneath the complex (Hutchison et al., 2015). Aluto has experienced much greater volumes of post-caldera volcanism compared to the other volcanoes considered in this study. These magmas have been concentrated up the ring fault and have erupted across the caldera rim; obscuring much of the original structure (Fig. A3.1a, Mohr et al., 1980; Hutchison et al., 2015).

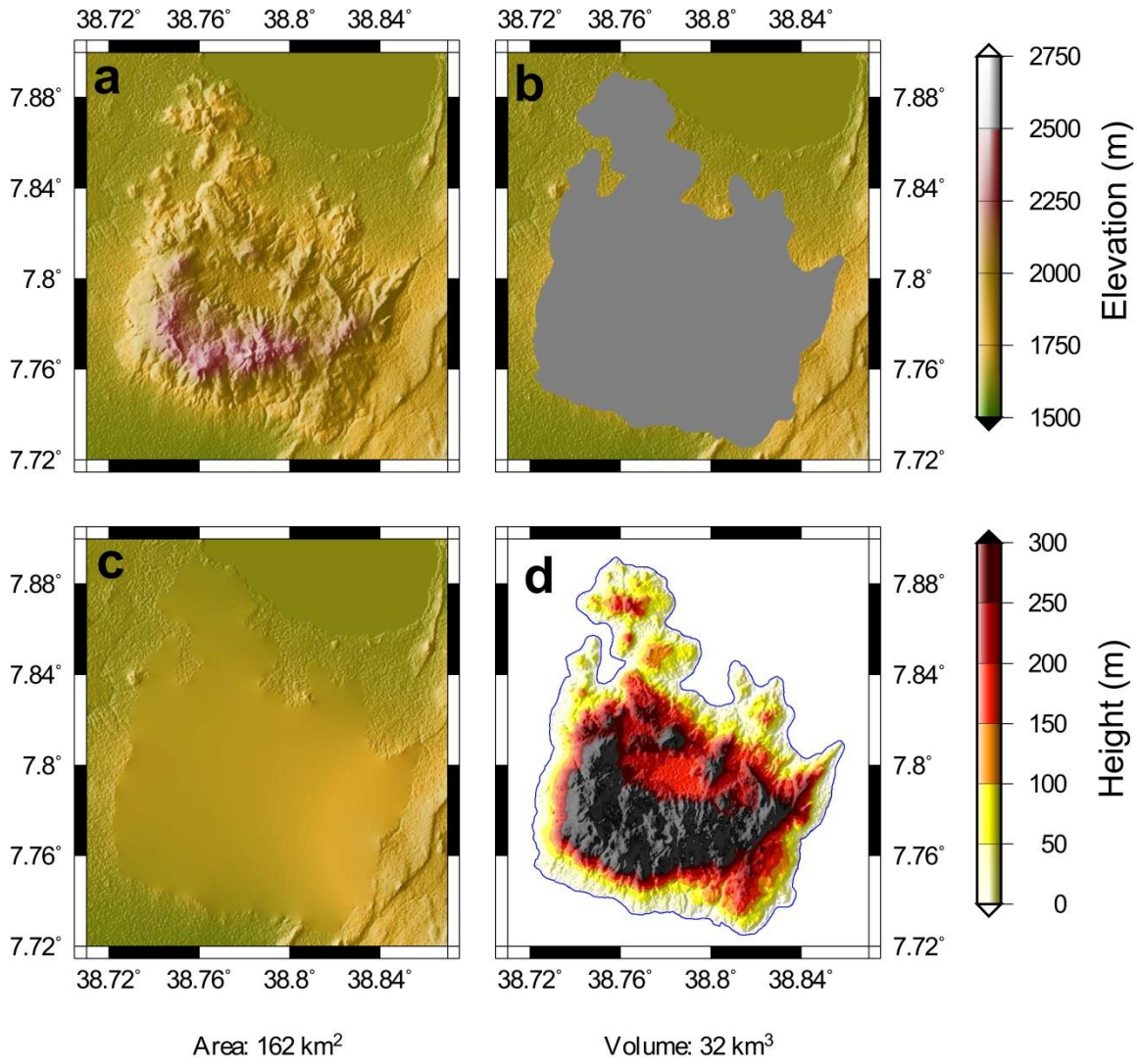

Figure A3.6. *DEM differencing method used to mask out and calculate the volume of the main edifice of Aluto, we approximate this as the volume of all post-caldera deposits (see Appendix 3.2.2 for details). Note that volume shown is not corrected to a dense rock equivalent (DRE).*

Evidence for a pre-collapse edifice at Aluto is found along faults on the margins of the complex (near Mt. Dima, Fig. A3.1a, Fig. 5.2) where a minimum thickness (~100 m) of trachyte lavas and tuffs ~8 km from the centre of the present edifice are found. The pre-caldera edifice of Aluto has been largely covered by recent volcanic deposits, and so we assume that the slope of the pre-caldera edifice is in line with that of neighbouring complexes (3–5°), and estimate the volume of the pre-collapse volcano as:

Estimate	Uplifted fault section thickness(m)	Edifice slope (°)	Volume DRE (km^3)
High	200	5	51
Med	150	4	40
Low	100	3	29

The ring structure of Aluto is hypothesized to be 9 km × 6 km and with a minimum height of ~100 m (Hutchison et al., 2015), allowing us to make the following estimates for the total volume of the Aluto collapse structure:

Estimate	Caldera wall height (m)	Intra-caldera fill (m)	Volume DRE (km^3)
High	300	300	21
Med	200	200	15
Low	100	100	8

Several phases of post-caldera silicic volcanism have occurred at Aluto over the last ~60 ka (Fig. 5.2), and deep wells sited in the centre of the complex reveal that post-caldera units (peralkaline rhyolite lavas and pyroclastic units) are ~300 m in thickness (Teklemariam et al., 1996; Teklemariam, 1996). Estimating the volume of these units using the DEM masking approach is complicated because the post-caldera deposits do not have a clearly defined morphology (i.e., they mantle the pre-existing volcanic collapse feature, rather than fill the caldera floor). The total volume of the present edifice is 32 km^3 (Fig. A3.6), this represents a relatively high estimate of the total volume of post-caldera products because the collapse topography, buried beneath the surface, may be included as part of the volume. A simplified approach to calculate the total

volume of the post-caldera units at Aluto, is to assume they have a constant thickness (250 m, after deep well observations, Teklemariam et al., 1996; Hutchison et al., 2015) proximal to the volcanic centre, equivalent to a cylinder of 6 km radius, and this yields a total volume of 28 km^3. This value is almost identical to the total volume of the current edifice (Fig. A3.6), and while the good agreement is probably partly fortuitous, it indicates that an estimate of ~30 km^3 is the correct order of magnitude and therefore we take the volume of post-caldera collapse products at Aluto as 27 km^3 DRE.

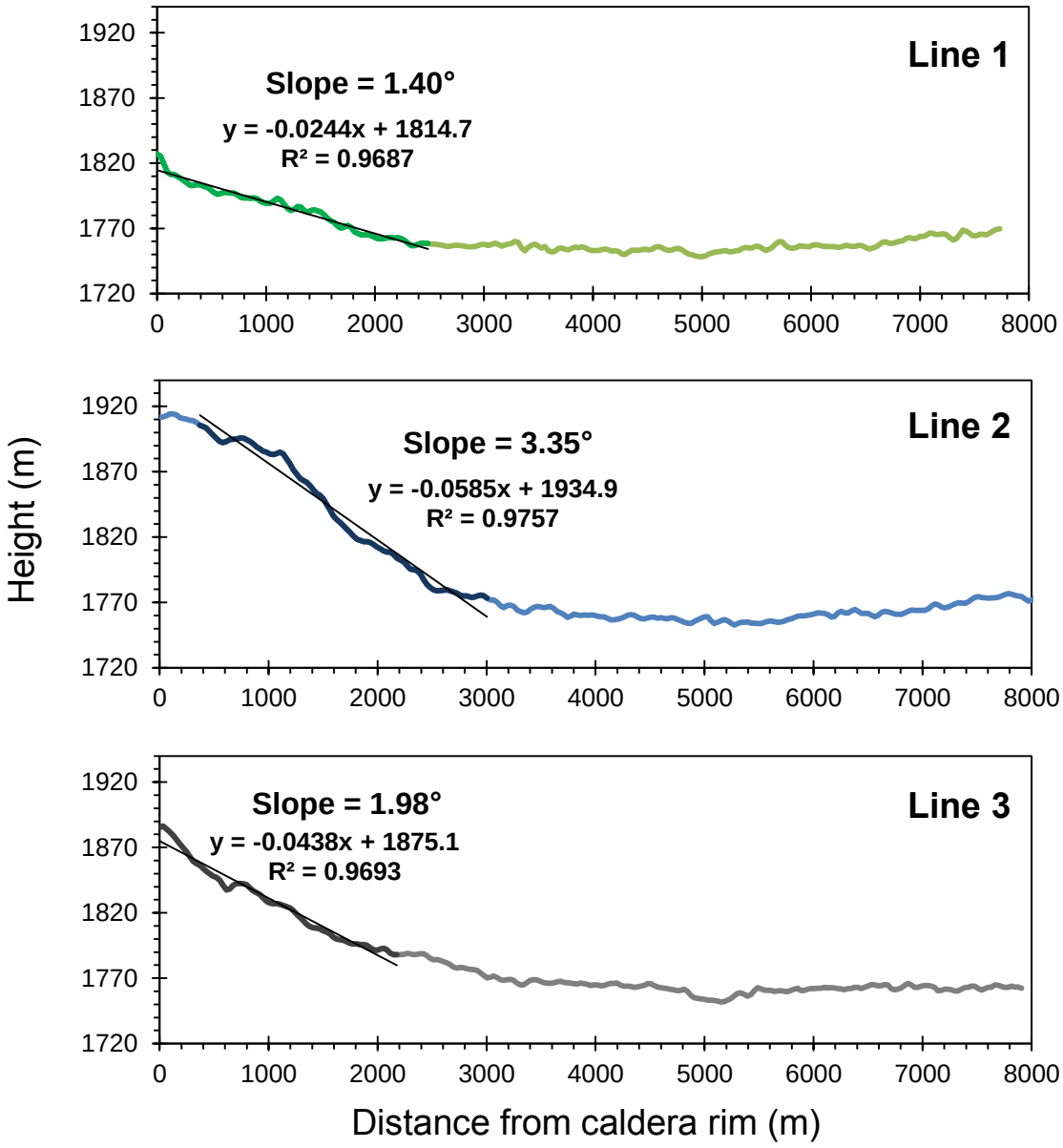

Figure A3.7. *Topographic profiles constructed away from the caldera walls of Shala volcano (used to estimate the slope of the pre-collapse volcano, and combined with thickness estimates to calculate the volume of the pre-collapse edifice, see Appendix 3.2.3 for details). Profile lines are linked to Fig. A3.8.*

A3.2.3 Shala

Mohr et al. (1980) consider pre-caldera topography of Shala volcano to have comprised a thick pile of flows and domes of rhyolite. Sites sampled at the caldera wall show minimum thicknesses of trachyte and rhyolite for the pre-collapse edifice of 50 –150 m (Mohr et al., 1980). Measurements of slope on the southern caldera wall (N.B. other wall sections are deeply eroded and/or faulted) show values of 2–4° (Fig. A3.7). Using these constraints the following estimates of the Shala pre-collapse edifice volume are:

Estimate	Caldera wall thicknesses (m)	Edifice slope (°)	Volume DRE (km^3)
High	200	5	51
Med	100	4	37
Low	50	3	26

Collapse at Shala is represented by the submerged caldera, 18 km east-west and 14 km north-south (Fig. A3.8). The maximum depth of Lake Shala, 260 m (Klemperer and Cash, 2007), is added to the height of the caldera wall above the lake surface (ranging from 100–350 m) and the following estimates are made:

Estimate	Caldera wall height (m)	Intra-caldera fill (m)	Volume DRE (km^3)
High	610	300	170
Med	510	200	133
Low	360	100	86

Post-caldera volcanism at Shala has been limited to the Tulu Fike pyroclastic cone on the northern shore of Shala lake (Mohr et al., 1980). DEM masking of the Tulu Fike deposits support a volume of 3 km^3 DRE for post-caldera volcanism at Shala (Fig. A3.8).

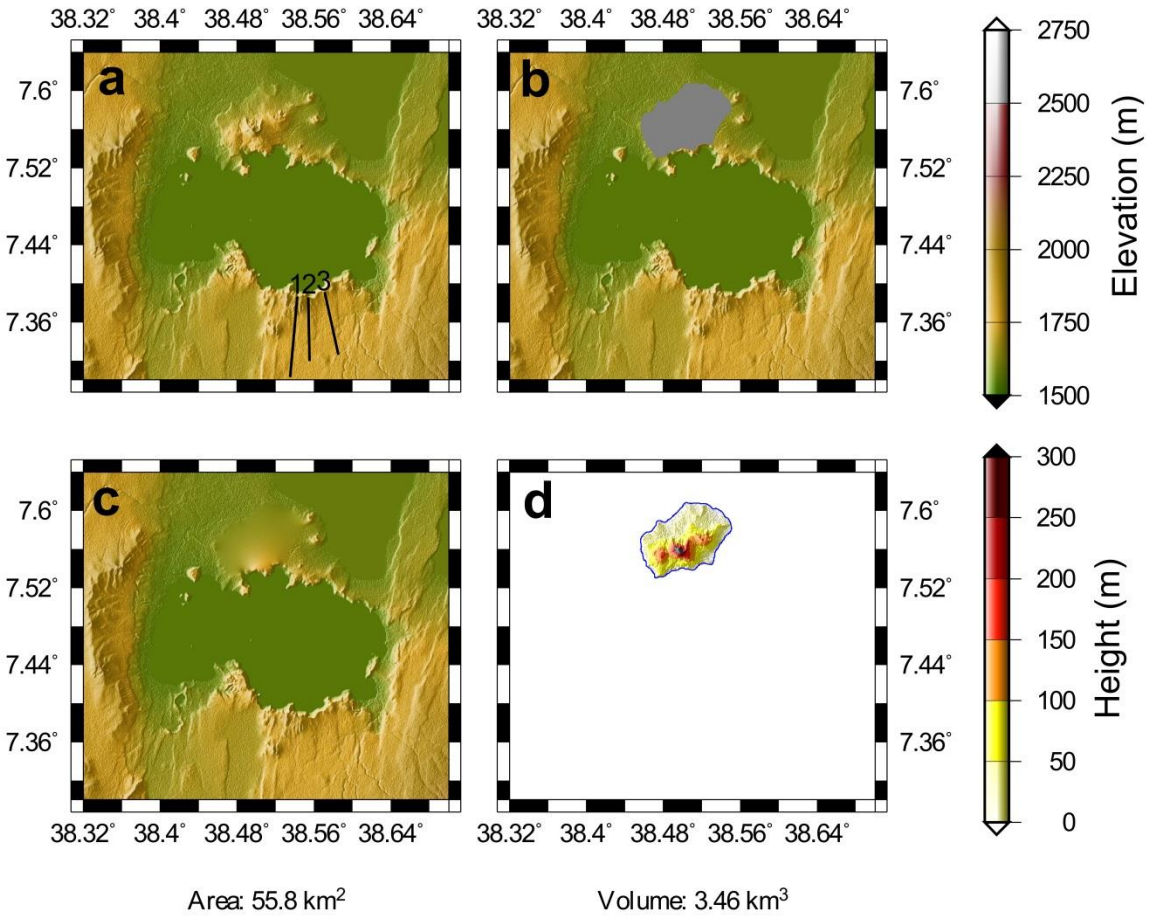

Figure A3.8. *DEM differencing method used to mask out post-caldera deposits at Shala and calculate their volume. The volume of masked area, i.e., the volume of post-caldera deposits, is given in the bottom right. Note that volume shown is not corrected to a dense rock equivalent (DRE).*

A3.2.4: Corbetti

Silicic lava domes and flows are reported in caldera wall sequences of Corbetti and pre-date the caldera-forming eruption (Fig. 5.2, Mohr, 1966; Di Paola, 1971, 1972). The pre-caldera lava exposures are well in excess of 50 m, and we consider a range of 100–200 m as a reasonable approximation of their true thickness. The range of slopes for the Corbetti caldera walls are shown in Figure A3.9 and allow the following volume estimates for the pre-collapse edifice to be made:

Estimate	Caldera wall thicknesses (m)	Edifice slope (°)	Volume DRE (km^3)
High	200	5	35
Med	150	3.5	25
Low	100	1.5	12

The Corbetti caldera (14 km × 11 km) has wall heights of 100–200 m and on the outskirts of the collapse deposits reach 200 m thickness (Di Paola, 1971). The following estimates of the caldera collapse volume are made:

Estimate	Caldera wall height (m)	Intra-caldera fill (m)	Volume DRE (km^3)
High	200	300	63
Med	150	200	44
Low	100	100	25

Post-caldera activity at Corbetti is represented by two very recent volcanic cones (Urji and Chabbi, Fig. A3.1b) formed of pumice flows, pumice fall and obsidian coulees. These cones have built up in the centre of the caldera and on the western rim (Fig. A3.10) and have a volume of 15 km^3 DRE.

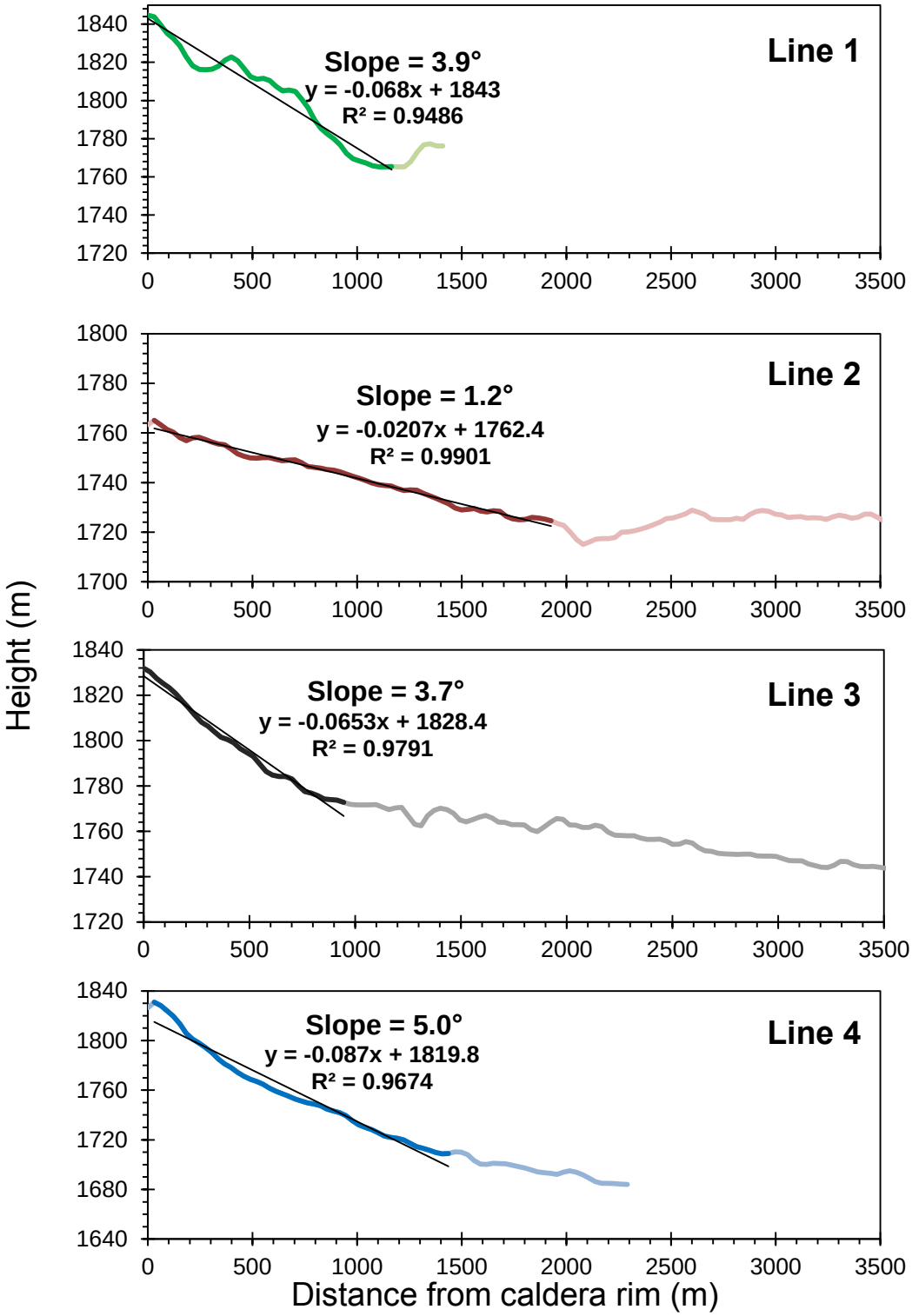

Figure A3.9. *Topographic profiles constructed away from the caldera walls of Corbetti volcano (used to estimate the slope of the pre-collapse volcano, and combined with thickness estimates to calculate the volume of the pre-collapse edifice, see Appendix 3.2.4 for details). Profile lines are linked to Fig. A3.10.*

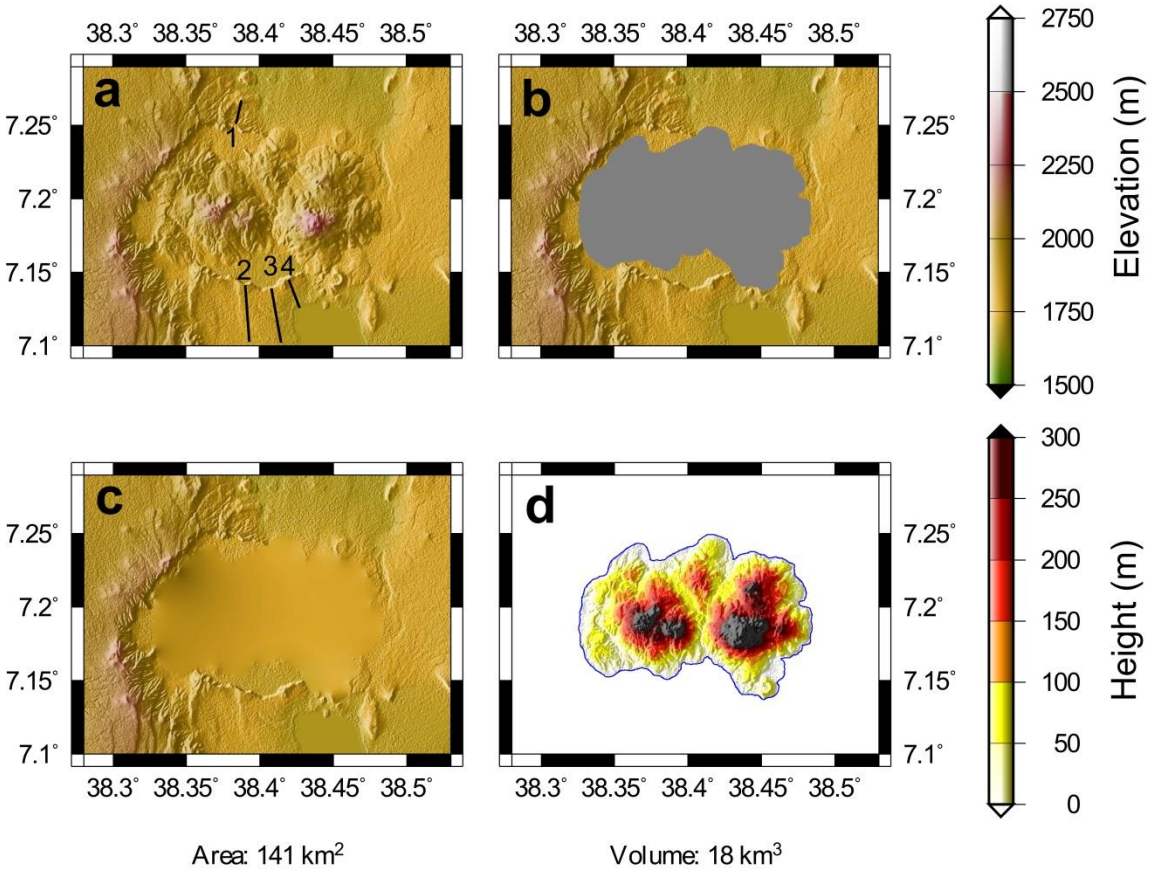

Figure A3.10. *DEM differencing method used to mask out post-caldera deposits at Corbetti and calculate their volume. The volume of masked area, i.e., the volume of post-caldera deposits, is given in the bottom right. Note that volume shown is not corrected to a dense rock equivalent (DRE).*

Run ID	Sample	36Ar / 39Ar	36Ar / 39Ar Er	37Ar / 39Ar	37Ar / 39Ar Er	Ca / K	Cl / K	38Ar / 39Ar	38Ar / 39Ar Er	40Ar / 39Ar	40Ar / 39Ar Er	Age (Ma)	Age Er (Ma)
91206-01A	01-02-14	0.0007756	0.0016201	0.0137732	0.0122411	0.0269958	0.0015605	0.0128837	0.0026804	0.3694264	0.0199175	0.0356669	0.1249116
91206-02A	01-02-14	0.0003401	0.0006597	0.0029615	0.0046149	0.0058045	-0.0049813	0.0105463	0.001412	0.2585328	0.0101024	0.0403632	0.0508838
91206-03A	01-02-14	0.0002254	0.0007437	0.00112	0.0050286	0.0021952	-0.0030072	0.0112055	0.0017781	0.2846771	0.0108233	0.0559172	0.0573621
91206-04A	01-02-14	0.0004641	0.00139	0.0148653	0.0096039	0.0291363	0.0016157	0.012844	0.003084	0.4552762	0.0214686	0.0818412	0.1072224
91206-05A	01-02-14	0.0010552	0.000936	0.0044747	0.0063195	0.0087704	0.0070816	0.0148406	0.0020281	0.3241916	0.013061	0.0022807	0.0721879
91206-06A	01-02-14	0.000133	0.0013033	0.0035056	0.0088055	0.0068711	-0.0007797	0.0119561	0.0028359	0.3370191	0.0190723	0.0765894	0.1005196
91206-07A	01-02-14	0.0005004	0.0011751	-0.0026234	0.0075101	-0.0051419	-0.0031648	0.0112031	0.0024566	0.443345	0.0190876	0.0755934	0.0906579
91206-08A	01-02-14	0.0002247	0.0014057	0.0144902	0.0136951	0.0284012	-0.0036754	0.0109744	0.0029819	0.2239789	0.0212067	0.0405791	0.1084291
91206-09A	01-02-14	0.0006058	0.0013174	-0.0024945	0.0087206	-0.0048893	-0.0029311	0.0113036	0.0033057	0.2352539	0.0193981	0.0137882	0.1016125
91206-10A	01-02-14	0.0002655	0.0015946	0.0005185	0.011656	0.0010163	-0.0176064	0.006179	0.0040124	0.362911	0.02513	0.0729586	0.1230127
91206-11A	01-02-14	0.000764	0.0002311	0.002665	0.0019551	0.0052234	-0.001232	0.0119191	0.0006902	0.4642777	0.0041323	0.0608022	0.0178468
91206-12A	01-02-14	0.000127	0.000165	0.0014537	0.0012654	0.0028492	0.0001108	0.0122621	0.0005451	0.3123834	0.0028469	0.0706561	0.0127315
91206-13A	01-02-14	0.000546	0.0001622	0.0092067	0.0018482	0.0180453	0.0001539	0.0123556	0.0006394	0.3149399	0.0032038	0.0391984	0.0125256
91206-14A	01-02-14	0.000045	0.0001324	0.0017546	0.0012052	0.003439	-0.0022182	0.0114435	0.0005157	0.3051314	0.0024301	0.0751019	0.0102185
91206-15A	01-02-14	0.0001613	0.0001936	0.0032543	0.0013345	0.0063785	-0.004388	0.0107172	0.0005455	0.2795673	0.0031972	0.0595699	0.0149379
91206-16A	01-02-14	0.0000187	0.0003049	0.0008417	0.0023906	0.0016497	-0.0063344	0.0100192	0.0006629	0.3119813	0.0040538	0.0788679	0.02351
91206-17A	01-02-14	0.000134	0.0001848	-0.0000346	0.001136	-0.0000678	-0.0015675	0.0116847	0.0006476	0.3111098	0.002826	0.0697583	0.0142551
91206-18A	01-02-14	0.0003587	0.0001352	0.0002873	0.0010302	0.000563	-0.0010996	0.0118884	0.0005345	0.2826617	0.0024951	0.0451116	0.0104379
91206-19A	01-02-14	0.0002786	0.0001393	-0.0005035	0.0010798	-0.0009868	-0.0010363	0.0118952	0.0005635	0.3461121	0.0029262	0.0676377	0.0107643
91206-20A	01-02-14	0.0002738	0.0001077	0.0019927	0.0008973	0.0039057	-0.0036056	0.0110083	0.0003882	0.3023173	0.0021853	0.0567538	0.0083213
91198-01A	13-05-04	0.0000254	0.0007835	0.0024022	0.0054807	0.0047083	-0.0028634	0.0112173	0.0017893	1.134494	0.0155651	0.2906044	0.0604859
91198-02A	13-05-04	0.0000885	0.0009913	0.0005939	0.0065951	0.0011641	-0.0013858	0.0117388	0.0027471	1.151667	0.017495	0.2901344	0.0764866
91198-03A	13-05-04	0.0006831	0.0007472	0.0000326	0.0044691	0.0000639	-0.0060419	0.0102454	0.0017944	1.286718	0.0131953	0.2791566	0.0576573
91198-04A	13-05-04	-0.0006484	0.0008766	0.0055869	0.0057266	0.0109504	-0.0011163	0.0116926	0.0022693	1.186348	0.0152105	0.3559461	0.067627
91198-05A	13-05-04	0.0000595	0.0010519	0.0045537	0.0052623	0.0089253	0.0104564	0.0158166	0.0021706	1.221025	0.0158991	0.3103737	0.0811274
91198-06A	13-05-04	0.0002133	0.0013309	0.0137717	0.0071835	0.0269927	-0.0095364	0.0089513	0.0026529	1.149191	0.0202162	0.280137	0.1026422
91198-07A	13-05-04	0.0000597	0.0011726	0.0094607	0.0070671	0.0185431	-0.0092273	0.0090291	0.0027703	1.260508	0.0180562	0.3205995	0.0904398
91198-08A	13-05-04	0.0002881	0.0011058	0.0004718	0.0075631	0.0009248	-0.0091758	0.0090903	0.002807	1.326503	0.018467	0.319847	0.0853051
91198-09A	13-05-04	-0.0002	0.0007247	0.001392	0.0043492	0.0027283	1.17E-06	0.0121627	0.0018179	1.17829	0.0130749	0.3192449	0.0559177
91198-10A	13-05-04	-0.0002558	0.0011258	0.0041355	0.0061064	0.0081056	-0.0039751	0.0107809	0.0023284	1.363783	0.0152327	0.3714417	0.0867966
91198-11A	13-05-04	0.0013698	0.0009664	0.0036015	0.0059522	0.0070591	-0.0082189	0.009624	0.0022638	1.442135	0.0192127	0.2664266	0.0746037
91198-12A	13-05-04	0.0010513	0.0012212	0.000863	0.0082933	0.0016914	-0.0031232	0.0113212	0.003004	1.344831	0.0216369	0.2658136	0.0942271
91198-13A	13-05-04	0.0000404	0.0008723	0.0001749	0.0057473	0.0003428	-0.0077853	0.0095231	0.001914	1.216801	0.016407	0.3106176	0.0673189
91198-14A	13-05-04	0.0002363	0.0013196	0.00074	0.0080698	0.0014505	0.0093956	0.0154843	0.0027484	1.13248	0.0238582	0.2738309	0.101831
91198-15A	13-05-04	0.001798	0.0011672	0.0067932	0.0079703	0.0133147	0.0070232	0.0149604	0.0025612	1.318248	0.0201597	0.2015865	0.0900607
91198-16A	13-05-04	0.0026906	0.0008043	0.004556	0.00551	0.0089298	0.0084452	0.015619	0.0019054	2.101595	0.0177361	0.3348846	0.0621225
91198-17A	13-05-04	7.31E-06	0.001067	0.0061084	0.0067357	0.0119725	-0.0021569	0.0114574	0.0024359	1.126438	0.0178016	0.2899935	0.0823176
91198-18A	13-05-04	0.0009543	0.0013137	0.0045888	0.007999	0.0089941	0.0078346	0.0150812	0.0031047	1.670794	0.0235079	0.3574786	0.1013669
91198-19A	13-05-04	0.0023194	0.0024384	0.0150668	0.0150279	0.0295312	-0.0231944	0.0046387	0.0051814	1.812182	0.0375436	0.2889529	0.1880671
91198-20A	13-05-04	0.0002165	0.001076	-0.0009942	0.0071261	-0.0019486	-0.0076789	0.009593	0.0023679	1.154733	0.0171099	0.2810207	0.0829969
91198-21A	13-05-04	0.0006088	0.000687	0.0000231	0.0044919	0.0000453	-0.0037614	0.0110177	0.0018929	1.226344	0.0132099	0.2693105	0.0530278
91198-22A	13-05-04	0.0010588	0.0007411	0.0032578	0.0046483	0.0063853	-0.0007019	0.0121574	0.0016914	1.150177	0.0138975	0.2150717	0.0572058
91198-23A	13-05-04	0.0001491	0.0017792	0.0097027	0.0095231	0.0190174	-0.0054816	0.0103376	0.0033184	1.315918	0.0209806	0.3280201	0.137149
91198-24A	13-05-04	0.0012504	0.0012132	-0.00115	0.0074728	-0.002254	0.0044513	0.0139706	0.0034061	1.385108	0.0218894	0.2608427	0.0936169
91198-25A	13-05-04	0.0000585	0.0009022	-0.001056	0.0057619	-0.0020698	-0.003309	0.01107	0.0026173	1.351984	0.0186591	0.3440883	0.0696553
91198-26A	13-05-04	0.0023525	0.0010331	-0.0062142	0.0066529	-0.0121799	-0.0047731	0.0109978	0.0024456	1.644675	0.0232582	0.2427981	0.0798026
91198-27A	13-05-04	0.0009177	0.0015082	0.0092225	0.0108187	0.0180762	-0.0029536	0.0113542	0.0041672	1.299314	0.024649	0.2645363	0.1163494

Table A3.1. $^{40}Ar/^{39}Ar$ age data table for Aluto (analysis conducted at SUERC).

Run ID	Sample	36Ar / 39Ar	36Ar / 39Ar Er	37Ar / 39Ar	37Ar / 39Ar Er	Ca / K	Cl / K	38Ar / 39Ar	38Ar / 39Ar Er	40Ar / 39Ar	40Ar / 39Ar Er	Age (Ma)	Age Er (Ma)
91198-28A	13-05-04	-0.0001624	0.0013195	0.0014117	0.0066778	0.0027669	0.0105008	0.0157902	0.0025452	1.215916	0.0172613	0.3260864	0.1017299
91198-29A	13-05-04	0.0002376	0.0009608	-0.0016189	0.0062931	-0.003173	-0.0087339	0.0092332	0.0027909	1.239934	0.0167661	0.3013635	0.0741282
91198-30A	13-05-04	0.0004139	0.0018582	-0.0185797	0.0114751	-0.0364157	0.017214	0.0182146	0.0043291	1.193159	0.032098	0.2754318	0.143361
91198-31A	13-05-04	0.0008874	0.0001533	0.0026098	0.0011034	0.0051152	0.0016653	0.0129414	0.0004565	1.46612	0.0088262	0.3097776	0.0120677
91198-32A	13-05-04	0.0003499	0.0001716	0.005225	0.0012375	0.010241	-0.0043991	0.0107488	0.0006032	1.31273	0.0068422	0.3116421	0.0133476
91198-33A	13-05-04	0.001966	0.0001588	0.0028884	0.0011167	0.0056612	-0.0049116	0.0108768	0.0004352	1.806446	0.0115991	0.3144872	0.0127245
91198-34A	13-05-04	0.0002176	0.000152	0.0058591	0.00118	0.0114839	-0.0039305	0.0108855	0.0004422	1.288094	0.0062643	0.3154918	0.011827
91198-35A	13-05-04	0.000255	0.0001321	0.0027394	0.0010505	0.0053692	-0.0042251	0.010791	0.000521	1.228112	0.0067052	0.2970687	0.0103306
91198-36A	13-05-04	0.0002761	0.0001482	0.0016361	0.0011424	0.0032068	-0.0034813	0.0110515	0.0005734	1.346792	0.0071245	0.3260409	0.0115681
91198-37A	13-05-04	0.0005643	0.0001449	0.0034821	0.0011899	0.0068249	-0.0053842	0.0104497	0.0006283	1.316747	0.006712	0.2961218	0.0113134
91198-38A	13-05-04	0.0007738	0.0001687	0.0001776	0.0013576	0.0003482	-0.0038121	0.0110313	0.0005909	1.357898	0.0065978	0.2905399	0.0131325
91198-40A	13-05-04	0.0003253	0.0001364	0.0036265	0.0009833	0.0071079	-0.0019883	0.0115756	0.0004825	1.246982	0.0068028	0.2965468	0.0106609
91204-01A	18-01-08	0.0016576	0.0007227	0.0009876	0.0052115	0.0019358	-0.0052777	0.0106925	0.002019	0.5666091	0.012697	0.0183251	0.0557849
91204-02A	18-01-08	0.0027515	0.0023229	0.0220339	0.014627	0.0431871	-0.0009366	0.0123948	0.0062989	0.5438048	0.0409062	-0.0713928	0.1792693
91204-03A	18-01-08	0.0058115	0.0014246	0.0040225	0.0070109	0.0078842	-0.0096381	0.0099718	0.0029448	1.837284	0.0200029	0.0262436	0.1099005
91204-04A	18-01-08	0.0006097	0.0008481	-0.0020554	0.0057382	-0.0040286	-0.0041492	0.0108843	0.0019702	0.2393297	0.0126603	0.0145422	0.0654193
91204-05A	18-01-08	0.0018917	0.0013215	0.0028278	0.0089903	0.0055425	0.0104	0.0161426	0.0029626	0.5859526	0.021368	0.0053581	0.101953
91204-06A	18-01-08	0.0040646	0.0014632	-0.0010566	0.0101077	-0.0020709	0.0012751	0.0134059	0.0037245	1.603668	0.0232021	0.1004527	0.1128985
91204-07A	18-01-08	0.0001363	0.0029572	-0.0201236	0.023759	-0.0394417	-0.000389	0.0120923	0.0072932	0.7355257	0.0415617	0.1786736	0.2280404
91204-08A	18-01-08	0.0027687	0.0012157	0.0004148	0.0083139	0.0008129	-0.0029997	0.0116875	0.0027594	0.9657807	0.0200078	0.0357187	0.093804
91204-09A	18-01-08	0.0001432	0.0010527	-0.0004735	0.0067579	-0.000928	0.015001	0.0173997	0.0027027	0.4187327	0.0172112	0.0968524	0.0812171
91204-10A	18-01-08	0.000789	0.0017989	-0.0016381	0.0122966	-0.0032106	0.0091945	0.0155192	0.004438	0.6078186	0.0290242	0.0958484	0.1387766
91204-11A	18-01-08	0.0029829	0.0002621	0.0017459	0.0015414	0.003422	0.0002993	0.0128654	0.0005079	1.069124	0.0063247	0.045917	0.0203574
91204-12A	18-01-08	0.0026081	0.0002671	0.0032852	0.0019307	0.0064389	-0.0064307	0.010474	0.0008414	0.8446604	0.0053136	0.0168886	0.020693
91204-13A	18-01-08	0.003359	0.0002316	0.0006207	0.0013139	0.0012165	-0.0033393	0.0116816	0.0006431	1.128398	0.0051247	0.0322027	0.0180378
91204-14A	18-01-08	0.0021966	0.0002313	0.0015313	0.0017816	0.0030014	-0.0089343	0.0095332	0.0007863	0.7663836	0.0049498	0.0283483	0.0179242
91204-15A	18-01-08	0.0019263	0.0001913	0.0020065	0.0016238	0.0039326	-0.0057572	0.0105778	0.0005672	0.6204307	0.0041051	0.0115299	0.0148355
91204-16A	18-01-08	0.0021124	0.000232	0.0029397	0.001185	0.0057619	-0.000819	0.0123156	0.0004968	0.7301023	0.0042944	0.02552	0.0179679
91204-17A	18-01-08	0.002614	0.0001435	-0.0004106	0.0011552	-0.0008047	-0.0034658	0.0114976	0.0005188	0.7968063	0.0042269	0.0040146	0.0112524
91204-18A	18-01-08	0.0020005	0.0001632	0.0007975	0.0011704	0.0015631	-0.0035501	0.0113529	0.0004844	0.68672	0.0040909	0.0228998	0.0126906
91204-19A	18-01-08	0.0031553	0.0001897	0.0036581	0.0013994	0.0071698	0.0011103	0.0131774	0.0005937	0.9431729	0.0057775	0.0001828	0.0148419
91204-20A	18-01-08	0.0024751	0.0002107	0.0015277	0.0011952	0.0029944	-0.0049732	0.0109516	0.0006124	0.8549766	0.0046141	0.0297613	0.0163618
91199-01A	18-02-04	-0.000076	0.0016119	0.0062573	0.0091612	0.0122644	-0.0053531	0.0103396	0.0034998	0.306664	0.0197226	0.0849046	0.1242735
91199-02A	18-02-04	0.0007936	0.0019991	0.0042548	0.0098194	0.0083395	-0.0052405	0.0105424	0.0041305	0.3201698	0.0226707	0.0213616	0.1541167
91199-03A	18-02-04	0.0008991	0.001565	0.0120446	0.009619	0.0236076	0.0007186	0.0126168	0.0041085	0.3236215	0.0242729	0.0142961	0.1207243
91199-04A	18-02-04	0.0038466	0.0019024	0.0012933	0.0128767	0.0025348	-0.0076225	0.0102966	0.004676	1.260065	0.0344291	0.0286204	0.1468055
91199-05A	18-02-04	0.0009664	0.002114	0.0040201	0.014468	0.0078794	-0.0018331	0.0117499	0.0052726	0.331119	0.039256	0.0108793	0.1631698
91199-06A	18-02-04	0.0008918	0.0009794	0.0016941	0.0063637	0.0033204	0.0080128	0.015131	0.0023476	0.3651517	0.0153644	0.0253831	0.0755578
91199-07A	18-02-04	0.00275	0.0018702	0.0124901	0.0123627	0.0244809	-0.0078064	0.010026	0.0038945	0.8593513	0.0293481	0.0099355	0.1442762
91199-08A	18-02-04	0	0.0030011	0.0153627	0.0256213	0.0301112	-0.006901	0.0098198	0.006949	0.5966231	0.049954	0.154046	0.2315349
91199-09A	18-02-04	0.0020637	0.0020578	0.0076487	0.0138277	0.0149915	0.0058093	0.0145918	0.004452	0.7964937	0.0329505	0.0465143	0.1587469
91199-10A	18-02-04	0.0010855	0.0007543	0.0030681	0.0049254	0.0060134	-0.0005723	0.0122071	0.0019875	0.4979937	0.0124445	0.0447477	0.0581994
91199-11A	18-02-04	0.0008102	0.0001661	0.005424	0.0012287	0.0106311	-0.0009304	0.0120317	0.0005705	0.3653186	0.003206	0.0317663	0.0128326
91199-12A	18-02-04	0.0007658	0.0001971	0.0042523	0.0017309	0.0083346	-0.0029511	0.0113266	0.0007024	0.4104232	0.0036829	0.0467966	0.015222
91199-13A	18-02-04	0.000827	0.0001932	0.0040183	0.0015321	0.0078758	-0.0077189	0.0096941	0.0004915	0.3797777	0.0034648	0.0341544	0.0149227
91199-14A	18-02-04	0.0005523	0.0001629	0.003412	0.0012228	0.0066874	-0.004751	0.0106657	0.0005512	0.3580472	0.003145	0.0497034	0.0125837
91199-15A	18-02-04	0.0009021	0.0001981	0.005038	0.0016037	0.0098745	-0.0044883	0.0108222	0.0006189	0.470011	0.004069	0.0516849	0.0153103

Table A3.1. $^{40}Ar/^{39}Ar$ age data table for Aluto (analysis conducted at SUERC).

Run ID	Sample	36Ar / 39Ar	36Ar / 39Ar Er	37Ar / 39Ar	37Ar / 39Ar Er	Ca / K	Cl / K	38Ar / 39Ar	38Ar / 39Ar Er	40Ar / 39Ar	40Ar / 39Ar Er	Age (Ma)	Age Er (Ma)
91199-16A	18-02-04	0.0003751	0.0002348	0.0047505	0.001999	0.0093109	-0.0004696	0.0121086	0.0007961	0.4070935	0.0043784	0.0760496	0.0181252
91199-17A	18-02-04	0.0007205	0.0002005	0.0064536	0.0016774	0.0126492	-0.0037052	0.0110579	0.0007821	0.3559665	0.003849	0.0362727	0.0154858
91199-18A	18-02-04	0.0009325	0.0002118	0.0039737	0.001676	0.0077885	-0.0055746	0.0104534	0.0007571	0.5647476	0.004628	0.0737613	0.0163772
91199-19A	18-02-04	0.000797	0.0002615	0.0028954	0.0021377	0.0056749	0.0009953	0.0126933	0.0009006	0.4800771	0.0048295	0.0623485	0.0201945
91199-20A	18-02-04	0.0010812	0.000157	0.0027726	0.0011791	0.0054342	-0.0015223	0.0118788	0.0006594	0.6627675	0.0040388	0.0875773	0.0121704
91197-01A	18-11-07	0.0018693	0.0009877	0.0032139	0.0065869	0.0062992	-0.0047797	0.0109041	0.0024149	1.837367	0.0202851	0.3299153	0.0762601
91197-02A	18-11-07	0.001143	0.0034149	0.0333681	0.017616	0.065403	0.0097864	0.0157886	0.0069253	1.524403	0.04421	0.3057814	0.2632758
91197-03A	18-11-07	0.000074	0.0014673	0.0237631	0.0093439	0.0465764	0.0045542	0.0137834	0.0036822	1.34963	0.0244583	0.3428139	0.1131961
91197-04A	18-11-07	0.0013498	0.0018498	0.0287298	0.0150546	0.0563116	0.0055152	0.014355	0.0036236	1.542908	0.0300448	0.2945193	0.1426936
91197-05A	18-11-07	0.0003158	0.0027705	0.0105393	0.0138603	0.0206571	0.013769	0.0170069	0.0046612	1.376753	0.0351602	0.3309377	0.2135865
91197-06A	18-11-07	0.002847	0.000958	0.0076025	0.0059319	0.0149011	-0.0081072	0.0099408	0.0023027	1.467313	0.0181706	0.1592265	0.0739529
91197-07A	18-11-07	0.0012651	0.0024821	0.01906	0.0150665	0.0373581	-0.0242397	0.0040794	0.005521	1.321934	0.0422839	0.2437601	0.1915033
91197-08A	18-11-07	0.0011026	0.0014188	0.0075602	0.0096416	0.014818	-0.0126174	0.0080568	0.003044	1.304757	0.027618	0.2516396	0.1095228
91197-09A	18-11-07	0.0002654	0.0041939	0.0238805	0.0280867	0.0468066	0.0054924	0.014143	0.0096242	1.653968	0.074994	0.4065889	0.3235955
91197-10A	18-11-07	0.0072345	0.0013034	0.0277056	0.0079717	0.0543041	-0.0173835	0.0075684	0.0036189	2.970094	0.0271785	0.2093676	0.1007501
91197-11A	18-11-07	0.0101055	0.0017742	0.0140457	0.0123677	0.0275298	-0.0126007	0.0097592	0.0038028	4.130182	0.0381555	0.2872523	0.1371048
91197-12A	18-11-07	0.0033588	0.002576	0.0110277	0.0174572	0.0216145	-0.0192162	0.0062066	0.0055227	1.624537	0.0392524	0.1604082	0.1986661
91197-13A	18-11-07	0.0019239	0.0015177	0.0011746	0.0092627	0.0023022	0.0162893	0.0181795	0.0035551	1.435808	0.0275152	0.2221249	0.1171256
91197-14A	18-11-07	0.0011018	0.0029731	0.0014833	0.0196986	0.0029073	0.0212085	0.0197207	0.0067797	1.523095	0.0494989	0.3079853	0.2293467
91197-15A	18-11-07	0.0232416	0.0017057	-0.0084613	0.0101791	-0.016584	-0.012206	0.0123721	0.0041266	8.399545	0.0658809	0.376423	0.1325143
91197-16A	18-11-07	0.0008792	0.0016735	0.0056108	0.0107013	0.0109972	-0.0117864	0.0083013	0.0041515	1.76391	0.0294375	0.3872586	0.129116
91197-17A	18-11-07	0.0004098	0.0018404	0.0015028	0.0121085	0.0029455	0.019851	0.0191222	0.0054658	1.245518	0.0326202	0.2896677	0.1420046
91197-18A	18-11-07	0.0006585	0.0014867	0.0012455	0.0092814	0.0024412	0.0016453	0.0128914	0.003503	1.300674	0.025637	0.2846989	0.1147018
91197-19A	18-11-07	0.0010255	0.002621	0.0063069	0.014743	0.0123615	-0.0011224	0.012006	0.0050469	1.405897	0.0324078	0.2836722	0.2020533
91197-20A	18-11-07	0.0029492	0.001642	0.0138605	0.0107144	0.0271669	-0.0090018	0.0096514	0.0033841	1.908123	0.0330456	0.2652074	0.1267525
91197-21A	18-11-07	0.001794	0.0028511	0.0157509	0.0141128	0.030872	0.0048469	0.0142088	0.0054973	1.431687	0.0401321	0.2313413	0.2198523
91197-22A	18-11-07	0.0007405	0.0020822	0.0104798	0.0111955	0.0205406	0.012651	0.0167015	0.0033373	1.432043	0.0283253	0.3124844	0.1605451
91197-23A	18-11-07	0.0019149	0.0033785	-0.0016944	0.0227211	-0.003321	-0.002323	0.01176	0.0072072	1.390907	0.0506107	0.2111306	0.2605673
91197-24A	18-11-07	0.0000116	0.0014308	0.0029064	0.0090967	0.0056966	-0.0148511	0.0070811	0.0032014	1.412604	0.0237412	0.3633949	0.1103722
91197-25A	18-11-07	0.0005105	0.0018746	0.0097581	0.0119478	0.019126	-0.003729	0.01101	0.0039149	1.414678	0.0309705	0.3256655	0.1446053
91197-26A	18-11-07	0.0001215	0.0018656	-0.014871	0.0116136	-0.0291469	0.0050853	0.013977	0.0042095	1.286587	0.0310279	0.3221022	0.143919
91197-27A	18-11-07	0.0020425	0.0027081	0.0263228	0.0143008	0.0515935	0.0023503	0.0133944	0.0051262	1.915546	0.0398682	0.3372396	0.2088291
91197-28A	18-11-07	0.001769	0.0013645	0.0057685	0.0095553	0.0113062	-0.0050552	0.0107901	0.0030878	1.389641	0.0227203	0.2221861	0.1052783
91197-29A	18-11-07	0.0018603	0.0022039	-0.0017796	0.0131053	-0.0034881	-0.0008269	0.0122656	0.0050882	1.87648	0.0334454	0.3406059	0.1699713
91197-30A	18-11-07	0.0021318	0.0033356	0.0103823	0.0215181	0.0203494	-0.0185523	0.0062042	0.0082699	1.563033	0.0541081	0.2390376	0.2573068
91197-31A	18-11-07	0.0019652	0.000201	0.0024373	0.0013352	0.0047772	0.0004902	0.0127394	0.0005414	1.774302	0.0112581	0.3062573	0.0158448
91197-32A	18-11-07	0.0010523	0.000175	0.0057291	0.00126	0.0112291	-0.0004203	0.0122532	0.0005746	1.487649	0.0085817	0.3026837	0.0136991
91197-33A	18-11-07	0.0023552	0.00023	0.0036699	0.0016026	0.0071931	-0.0017965	0.0120243	0.0006572	1.840926	0.0095603	0.2934305	0.0179842
91197-34A	18-11-07	0.0018251	0.000241	0.0007848	0.0017912	0.0015382	-0.0033053	0.0114042	0.0007861	1.737386	0.0090755	0.3074809	0.0187726
91197-35A	18-11-07	0.0010932	0.0002283	0.0012204	0.0016247	0.0023919	-0.0036685	0.011141	0.0005945	1.502929	0.0085084	0.3033738	0.0177483
91197-37A	18-11-07	0.0007783	0.0003225	0.0023614	0.0026639	0.0046283	-0.0047852	0.0106966	0.0011065	1.484865	0.0095495	0.3229941	0.0249664
91197-38A	18-11-07	0.0008803	0.000227	0.0025058	0.001748	0.0049113	-0.0026883	0.0114389	0.0005739	1.585247	0.0079768	0.3410372	0.0176363
91197-39A	18-11-07	0.0011553	0.0002517	0.0024893	0.001913	0.0048791	-0.0024419	0.0115757	0.0008637	1.600531	0.0083531	0.3237992	0.0195462
91197-40A	18-11-07	0.0011937	0.0002111	0.0026545	0.0017186	0.0052028	-0.0031	0.011356	0.0007546	1.715353	0.0089583	0.350471	0.0164667
91205-01A	30-01-LNE	0.0009679	0.0009721	0.0032769	0.0067531	0.0064227	-0.0109403	0.0086099	0.0021372	0.3638752	0.0144485	0.0191769	0.0749803
91205-02A	30-01-LNE	0.0011131	0.0010831	0.0059052	0.0076066	0.0115742	0.0053031	0.0142382	0.0027968	0.3377227	0.0178546	0.0013344	0.0835659

Table A3.1. $^{40}Ar/^{39}Ar$ age data table for Aluto (analysis conducted at SUERC).

Run ID	Sample	36Ar / 39Ar	36Ar / 39Ar Er	37Ar / 39Ar	37Ar / 39Ar Er	Ca / K	Cl / K	38Ar / 39Ar	38Ar / 39Ar Er	40Ar / 39Ar	40Ar / 39Ar Er	Age (Ma)	Age Er (Ma)
91205-03A	30-01-LNE	0.002401	0.0005624	-0.0003922	0.0063841	-0.0007686	-0.001992	0.0119657	0.0014489	0.7723962	0.0101261	0.0141357	0.0434287
91205-04A	30-01-LNE	0.0000581	0.0006303	-0.0000629	0.0046755	-0.0001232	0.0000112	0.0122148	0.0015587	0.0500985	0.0091388	0.0082609	0.0486171
91205-05A	30-01-LNE	0.0006951	0.0008426	0.0033405	0.004696	0.0065474	-0.0001526	0.0122783	0.0016517	0.5235793	0.0112232	0.081428	0.0649714
91205-06A	30-01-LNE	0.0006155	0.0006728	0.0002683	0.0046311	0.0005258	0.0040905	0.0137265	0.0019922	0.2056581	0.0101692	0.0054733	0.0518946
91205-08A	30-01-LNE	0.0014679	0.0009825	0.0003021	0.0065168	0.0005921	0.0019331	0.0131432	0.002697	0.2659424	0.0141878	-0.0446382	0.0757803
91205-09A	30-01-LNE	0.0003973	0.0016778	0.0013208	0.0095612	0.0025889	0.0052792	0.0140952	0.003225	0.1688856	0.020724	0.0128243	0.1293633
91205-10A	30-01-LNE	0.0005629	0.0033168	-0.0104904	0.0181073	-0.020561	-0.0000145	0.0123015	0.0068425	0.1563972	0.0391255	-0.0034105	0.255717
91205-11A	30-01-LNE	0.0011808	0.000177	0.0010023	0.0014265	0.0019646	0.0000163	0.0124281	0.000548	0.4375146	0.0034886	0.0217601	0.0136923
91205-12A	30-01-LNE	0.000258	0.0001789	0.0005188	0.0014159	0.0010169	-0.005665	0.0102952	0.0005247	0.1580482	0.0032034	0.0207139	0.0138115
91205-13A	30-01-LNE	0.0013363	0.000132	0.0010073	0.0009431	0.0019742	-0.0008732	0.0121508	0.0005001	0.4662697	0.0029735	0.0171922	0.0102432
91205-14A	30-01-LNE	0.0006689	0.0001772	0.0012423	0.0010662	0.0024349	-0.0029006	0.0113258	0.0003276	0.2683127	0.0024996	0.0175314	0.0136716
91205-15A	30-01-LNE	0.0005564	0.0001698	0.0010045	0.0013992	0.0019689	-0.0074875	0.009723	0.000667	0.2771289	0.0029765	0.0284552	0.0131102
91205-16A	30-01-LNE	0.0010784	0.0001336	0.0014624	0.0009946	0.0028663	-0.0013626	0.0119334	0.0005176	0.3960099	0.0031885	0.0189442	0.0103502
91205-17A	30-01-LNE	0.0008399	0.0001424	0.0003915	0.0010695	0.0007674	-0.0026763	0.0114355	0.0004584	0.3205374	0.0027607	0.0178157	0.0110075
91205-18A	30-01-LNE	0.0009044	0.0001562	0.0011156	0.0012889	0.0021866	0.0007721	0.0126367	0.0006598	0.2962113	0.0028601	0.0065916	0.0120706
91205-19A	30-01-LNE	0.0007648	0.0002161	0.0031424	0.0017574	0.006159	-0.0012368	0.0119175	0.0007679	0.308576	0.0040453	0.0205789	0.0166876
91205-20A	30-01-LNE	0.0011366	0.0001199	0.0020968	0.0010187	0.0041097	-0.0058915	0.0103826	0.0004991	0.4112997	0.0024315	0.018406	0.0092941
91211-01A	31-01-LE	0.0001257	0.0007295	0.0005813	0.0070803	0.0011394	-0.0069422	0.0098299	0.0019492	0.0524177	0.0120832	0.0036501	0.0562823
91211-02A	31-01-LE	0.0003229	0.0015221	0.000764	0.0087351	0.0014974	-0.0035984	0.01102	0.0031403	0.1410143	0.0206273	0.0113298	0.1173755
91211-03A	31-01-LE	0.000635	0.0008806	0.0067539	0.0062716	0.0132378	-0.0012017	0.0119051	0.0023444	0.2161488	0.0131462	0.006798	0.0679224
91211-04A	31-01-LE	0.0013549	0.0011353	0.0029125	0.0073508	0.0057084	-0.0226888	0.0046317	0.002328	0.1942813	0.0175015	-0.054436	0.0875807
91211-05A	31-01-LE	0.000371	0.0013077	0.0031431	0.0092078	0.0061604	-0.0035197	0.0110561	0.0031344	0.1573539	0.0193973	0.0118858	0.1008622
91211-06A	31-01-LE	0.0013181	0.0010746	0.0034802	0.0064327	0.0068213	-0.004278	0.0109732	0.0021081	0.1846846	0.0126301	-0.0540132	0.0828562
91211-07A	31-01-LE	0.0002961	0.0011512	0.0057484	0.0078256	0.011267	0.0013058	0.0127059	0.0026812	0.0717141	0.0169193	-0.0043777	0.0887941
91211-08A	31-01-LE	0.0006912	0.0015704	0.005644	0.0112746	0.0110622	0.0007242	0.0125798	0.0039073	0.3149234	0.0255862	0.0279412	0.1211583
91211-09A	31-01-LE	0.0010065	0.0012011	9.67E-06	0.0088531	0.0000189	-0.0016931	0.0118059	0.0023624	0.2676912	0.0174846	-0.0086613	0.0926393
91211-10A	31-01-LE	0.0017822	0.0017356	0.0058256	0.0114546	0.0114181	-0.018442	0.0061765	0.0036201	0.158989	0.0286783	-0.0963876	0.1339241
91211-11A	31-01-LE	0.0002212	0.000118	0.0013324	0.0007763	0.0026115	-0.0022152	0.0114778	0.0003946	0.1584154	0.0019778	0.0236687	0.0091084
91211-12A	31-01-LE	0.0004375	0.0001392	0.0013441	0.0010552	0.0026343	-0.0037203	0.0109996	0.0004852	0.1067724	0.0023811	-0.0063227	0.0107466
91211-13A	31-01-LE	0.0003056	0.0001131	0.0009373	0.0009533	0.001837	-0.0025502	0.0113782	0.0003535	0.0972186	0.0018524	0.0013665	0.0087289
91211-14A	31-01-LE	0.0030656	0.0002172	0.0008538	0.0012178	0.0016734	-0.0021142	0.0120488	0.0004228	1.001019	0.0045862	0.0219524	0.0169113
91211-15A	31-01-LE	0.0001627	0.0001773	0.0008427	0.0010523	0.0016517	-0.0037943	0.0109223	0.0004937	0.1013168	0.0025443	0.0134295	0.0136744
91211-16A	31-01-LE	0.0011762	0.0002365	0.0006361	0.00133	0.0012468	-0.002601	0.0115248	0.0005733	0.5155549	0.0039909	0.0422299	0.0182684
91211-17A	31-01-LE	0.0003552	0.0001046	0.000959	0.0009024	0.0018797	0.0008625	0.0125643	0.0004743	0.1233142	0.0018299	0.0042854	0.0080751
91211-18A	31-01-LE	0.0001267	0.000184	0.0021936	0.0011725	0.0042994	-0.0039588	0.0108587	0.0005292	0.1149816	0.0023995	0.0197556	0.0141856
91211-19A	31-01-LE	0.0000918	0.0001498	0.0012169	0.0009877	0.0023851	-0.0025165	0.0113495	0.0004522	0.0777114	0.0021032	0.0128084	0.0115532
91211-20A	31-01-LE	0.0001278	0.0002131	0.0003657	0.0013692	0.0007169	-0.00348	0.0110241	0.0005031	0.1553275	0.0022721	0.0300383	0.0164287
91200-01A	ACs 7 J1	0.0014425	0.0001752	0.0113249	0.001135	0.022197	0.0019337	0.0131382	0.0006813	5.085378	0.0180451	1.20068	0.0144258
91200-02A	ACs 7 J1	0.0003116	0.0001273	0.0099642	0.00085	0.0195299	-0.0008332	0.0119711	0.000516	4.798197	0.0154316	1.213656	0.0106166
91200-03A	ACs 7 J1	0.0013531	0.0001766	0.008433	0.0010473	0.0165288	-0.0049318	0.0107541	0.0005592	5.059544	0.0177553	1.200825	0.0144847
91200-04A	ACs 7 J1	0.0013005	0.0003258	0.0114218	0.0022112	0.0223869	-0.0044657	0.0109048	0.0009701	5.061867	0.0280817	1.205535	0.0261818
91200-05A	ACs 7 J1	0.0076117	0.0001751	0.0139573	0.0013997	0.0273566	0.0000443	0.0136494	0.0006611	6.87245	0.0271785	1.186601	0.0165447
91207-01A	ACs 7 J2	0.0007727	0.000167	0.0081597	0.0009844	0.0159931	0.0028026	0.0133117	0.0005553	4.917783	0.0164029	1.208969	0.013626
91207-02A	ACs 7 J2	0.1578208	0.0007037	0.0083235	0.0014715	0.0163141	0.001403	0.0424303	0.0012296	52.54133	0.171934	1.398544	0.1283459
91207-03A	ACs 7 J2	0.0728648	0.0003652	0.0069537	0.0009276	0.0136292	-0.0028183	0.0249618	0.0004588	26.51136	0.0844512	1.226918	0.062694
91207-04A	ACs 7 J2	0.0038523	0.0002591	0.0102699	0.0015672	0.0201291	-0.0083225	0.0100559	0.0006864	6.046083	0.0269456	1.262841	0.0214726
91207-05A	ACs 7 J2	0.0008008	0.0002281	0.0091739	0.0014608	0.017981	-0.0053659	0.0105003	0.000646	4.930497	0.0266858	1.210081	0.0189156
91214-01A	ACs 7 J3	0.0012284	0.0002512	0.0110586	0.0015395	0.021675	-0.0094876	0.0091596	0.0009171	5.123064	0.0258782	1.226852	0.0205333
91214-02A	ACs 7 J3	0.0232162	0.0002665	0.0102489	0.0012256	0.0200881	-0.0023033	0.0157813	0.0007948	11.70281	0.0485357	1.230731	0.029013
91214-03A	ACs 7 J3	0.0006873	0.000301	0.0080869	0.0017661	0.0158503	-0.0053024	0.0105008	0.0008655	4.820486	0.026096	1.190432	0.0241656
91214-04A	ACs 7 J3	0.0013639	0.0001959	0.0104281	0.0011558	0.0204392	-0.0029849	0.0114274	0.0007537	4.982622	0.0244158	1.180208	0.0164592
91214-05A	ACs 7 J3	0.0003717	0.0001719	0.0078213	0.0011554	0.0153298	-0.0053167	0.0104364	0.0006932	4.841807	0.0217099	1.220224	0.0143984

Table A3.1. $^{40}Ar/^{39}Ar$ age data table for Aluto (analysis conducted at SUERC).

T(^{0}C)	Age (ka)	% 40Ar*	K/Ca	K/Cl	*Moles40Ar	40Ar	39Ar	38Ar	37Ar	36Ar
Fuse	200.0±16.0	75.37	688.68	-10639	3.16E-15	0.028334±0.000076	0.044447±0.000047	0.000570±0.000018	0.000034±0.000029	0.000023±0.000006
Fuse	151.0±24.1	54.76	177.35	-3031	1.58E-15	0.019442±0.000079	0.029356±0.000052	0.000350±0.000014	0.000087±0.000033	0.000030±0.000006
Fuse	187.1±11.4	46.94	-18152.82	-5463	4.46E-15	0.064261±0.000093	0.067143±0.000071	0.000851±0.000011	-0.000002±0.000019	0.000115±0.000006
Fuse	214.3±36.1	4.77	-2723.5	-6735	2.61E-15	0.370224±0.000195	0.034308±0.000052	0.000652±0.000015	-0.000007±0.000031	0.001193±0.000010
Fuse	191.5±16.7	40.22	402.69	-6376	2.85E-15	0.047794±0.000076	0.041794±0.000070	0.000539±0.000021	0.000054±0.000020	0.000097±0.000006
Fuse	153.0±20.0	42.18	218.71	8889	1.80E-15	0.028877±0.000072	0.033149±0.000046	0.000462±0.000017	0.000080±0.000028	0.000056±0.000005
Fuse	178.4±14.8	40.87	408.85	-17113	3.19E-15	0.052786±0.000092	0.050367±0.000065	0.000669±0.000020	0.000065±0.000023	0.000105±0.000006
Fuse	175.5±17.7	37.34	427.72	-4528	2.60E-15	0.047118±0.000083	0.041741±0.000054	0.000528±0.000013	0.000051±0.000039	0.000100±0.000006
Fuse	162.4±14.4	37.41	597.38	-25909	2.88E-15	0.051985±0.000084	0.049870±0.000067	0.000668±0.000013	0.000044±0.000025	0.000100±0.000006
Fuse	148.3±21.3	57.99	766.68	-38326	1.65E-15	0.019168±0.000074	0.031196±0.000049	0.000412±0.000013	0.000021±0.000036	0.000027±0.000005
Fuse	145.5±23.1	53.32	411.95	1182945	1.75E-15	0.022227±0.000066	0.033917±0.000069	0.000452±0.000019	0.000043±0.000028	0.000035±0.000006
Fuse	184.3±49.7	13.71	193.15	3127	1.13E-15	0.055895±0.000097	0.017311±0.000046	0.000282±0.000016	0.000047±0.000033	0.000163±0.000007
Fuse	160.0±28.3	41.54	2248.92	7794	1.60E-15	0.025978±0.000075	0.028073±0.000039	0.000394±0.000015	0.000007±0.000030	0.000051±0.000006
Fuse	150.2±35.7	31.38	-1396.24	4050	1.23E-15	0.026395±0.000075	0.022960±0.000056	0.000337±0.000014	-0.000009±0.000051	0.000061±0.000007
Fuse	176.1±20.4	5.58	613.21	-11374	4.05E-15	0.490333±0.000251	0.064705±0.000068	0.001119±0.000027	0.000055±0.000031	0.001567±0.000011
Fuse	196.4±22.8	55.81	-2799.52	-6943	2.22E-15	0.026837±0.000060	0.031753±0.000053	0.000405±0.000020	-0.000006±0.000023	0.000040±0.000006
Fuse	250.5±66.0	57.4	699.88	-147191	8.79E-16	0.010345±0.000064	0.009870±0.000027	0.000132±0.000014	0.000007±0.000025	0.000015±0.000005
Fuse	198.7±52.9	43.05	1104.08	6037	9.35E-16	0.014667±0.000054	0.013230±0.000040	0.000189±0.000014	0.000006±0.000028	0.000028±0.000006
Fuse	174.3±29.6	50.92	289.47	-3539	1.42E-15	0.018861±0.000064	0.022950±0.000041	0.000280±0.000017	0.000042±0.000042	0.000031±0.000006
Fuse	166.0±13.7	52.97	783.05	-7260	3.03E-15	0.038637±0.000072	0.051321±0.000070	0.000655±0.000021	0.000034±0.000032	0.000061±0.000006
Fuse	202.6±22.9	49.61	546.89	-22045	2.15E-15	0.029258±0.000077	0.029832±0.000043	0.000395±0.000019	0.000029±0.000025	0.000050±0.000006
Fuse	220.5±24.7	74.9	8554.85	-19448	2.05E-15	0.018512±0.000064	0.026180±0.000051	0.000341±0.000016	0.000002±0.000025	0.000016±0.000005
Fuse	242.2±87.5	46.38	-281.06	-2198	6.64E-16	0.009669±0.000058	0.007710±0.000028	0.000090±0.000010	-0.000014±0.000029	0.000018±0.000005
Fuse	178.1±35.5	52.04	176.25	-3225	1.24E-15	0.016080±0.000073	0.019557±0.000039	0.000236±0.000014	0.000058±0.000048	0.000026±0.000006
Fuse	154.9±43.4	33.32	-514.39	-17294	8.43E-16	0.017098±0.000080	0.015317±0.000039	0.000205±0.000011	-0.000016±0.000017	0.000039±0.000005
Fuse	527.9±43.5	67.18	424.79	-2471	2.92E-15	0.029327±0.000071	0.015535±0.000034	0.000183±0.000014	0.000019±0.000044	0.000033±0.000005
Fuse	163.4±18.1	35.7	213.92	-5680	2.22E-15	0.042054±0.000094	0.038255±0.000054	0.000491±0.000023	0.000094±0.000026	0.000091±0.000006

Table A3.2 a) ^{40}Ar/^{39}Ar age data table for Corbetti (analysis conducted at USGS). COI2E – Sanidine.

Packet IRR333-AA, experiment #15Z0030, Sanidine, all errors ±1 sigma, recalculated to FCs = 28.294 Ma. J value = 0.0002308020±4.774E-07.

40Ar* is radiogenic argon, isotopes in volts (1.48e-13moles/volt), corrected for blank, background, discrimination, and decay.

Total Gas Age = 184.3 ± 4.5 ka.

Weighted Mean Age = 176.8 ± 4.1 ka (±1 sigma, including ±J). MSWD = 0.86 (Good fit, MSWD < 2.40). Grains: 27 of 28.

T(^{0}C)	Age (ka)	% 40Ar*	K/Ca	K/Cl	*Moles40Ar	40Ar	39Ar	38Ar	37Ar	36Ar
Fuse	28.7±12.5	12.49	252.88	-17506	6.04E-16	0.032691±0.000065	0.060769±0.000083	0.000802±0.000012	0.000126±0.000030	0.000097±0.000005
Fuse	2.9±20.0	0.38	1378.85	-16929	2.58E-17	0.046230±0.000066	0.041387±0.000062	0.000562±0.000009	0.000016±0.000014	0.000156±0.000006
Fuse	3.5±14.1	0.91	240.76	-6167	5.33E-17	0.039422±0.000060	0.056652±0.000077	0.000730±0.000019	0.000123±0.000016	0.000132±0.000005
Fuse	24.2±29.8	5.07	183.2	-9693	2.10E-16	0.028015±0.000042	0.026392±0.000048	0.000352±0.000012	0.000076±0.000030	0.000090±0.000005
Fuse	12.6±22.0	3.75	167.89	92689	1.43E-16	0.025805±0.000052	0.035831±0.000070	0.000488±0.000025	0.000112±0.000027	0.000084±0.000005
Fuse	41.4±17.2	5.71	-8671.64	-13147	2.02E-16	0.023921±0.000052	0.041317±0.000065	0.000544±0.000017	-0.000003±0.000034	0.000076±0.000005
Fuse	37.2±18.5	1.59	207.49	-11696	1.30E-16	0.055144±0.000070	0.040437±0.000079	0.000551±0.000019	0.000102±0.000028	0.000184±0.000006
Fuse	148.3±37.2	13.03	174.1	-3781	5.07E-16	0.026276±0.000051	0.017318±0.000041	0.000222±0.000016	0.000052±0.000044	0.000077±0.000005
Fuse	71.0±12.0	19.1	264.98	-11580	1.07E-15	0.037922±0.000061	0.058540±0.000056	0.000767±0.000018	0.000116±0.000030	0.000104±0.000005
Fuse	71.9±33.2	3.13	262.84	-6521	1.18E-16	0.025380±0.000060	0.020475±0.000039	0.000271±0.000014	0.000041±0.000037	0.000083±0.000005
Fuse	4.2±15.3	1.01	251.1	-21436	3.99E-17	0.026680±0.000044	0.044266±0.000071	0.000589±0.000018	0.000092±0.000032	0.000089±0.000005
Fuse	26.5±27.4	6.29	358.47	-9191	2.13E-16	0.022847±0.000046	0.025302±0.000045	0.000334±0.000014	0.000037±0.000029	0.000072±0.000005
Fuse	32.5±11.3	17.81	317.82	-15954	6.65E-16	0.025221±0.000049	0.059663±0.000071	0.000781±0.000015	0.000098±0.000027	0.000070±0.000005
Fuse	82.0±16.2	20.62	259.76	-29137	1.17E-15	0.038320±0.000058	0.040996±0.000061	0.000552±0.000018	0.000083±0.000024	0.000103±0.000005
Fuse	19.3±12.5	8.52	826.17	-9289	3.51E-16	0.027821±0.000061	0.054799±0.000073	0.000711±0.000017	0.000035±0.000035	0.000086±0.000005
Fuse	1.1±27.3	6.38	530.27	-6224	3.08E-16	0.032637±0.000060	0.029743±0.000049	0.000390±0.000011	0.000029±0.000026	0.000103±0.000005
Fuse	-26.6±16.6	-3.97	5066.73	-6135	-1.33E-16	0.022651±0.000050	0.045404±0.000080	0.000580±0.000011	0.000005±0.000015	0.000080±0.000005
Fuse	-4.1±13.4	4.82	245.13	-12376	2.14E-16	0.029946±0.000044	0.056207±0.000069	0.000737±0.000010	0.000120±0.000040	0.000096±0.000005
Fuse	38.9±37.1	17.64	174.8	56420	5.70E-16	0.021823±0.000053	0.019739±0.000045	0.000272±0.000016	0.000059±0.000024	0.000061±0.000005
Fuse	19.8±25.4	8.68	504.72	-44758	5.22E-16	0.040622±0.000060	0.032006±0.000062	0.000441±0.000015	0.000033±0.000021	0.000125±0.000005
Fuse	13.1±20.5	2.6	322.07	-10523	9.99E-17	0.025978±0.000048	0.032113±0.000045	0.000425±0.000012	0.000052±0.000029	0.000086±0.000005

Table A3.2 ^{40}Ar/^{39}Ar age data table for Corbetti (analysis conducted at USGS). b) Chabbi 7 – Sanidine.

Packet IRR333-ZZ, experiment #15Z0029, Sanidine, all errors ±1 sigma, recalculated to FCs = 28.294 Ma. J value = 0.0002306854±4.772E-07.

40Ar* is radiogenic argon, isotopes in volts (1.48e-13moles/volt), corrected for blank, background, discrimination, and decay.

Total Gas Age = 23.7 ± 3.3 ka.

Weighted Mean Age = 18.4 ± 4.3 ka (±1 sigma, including ±J). MSWD = 0.76 (Good fit, MSWD < 2.40).